NBS SPECIAL PUBLICATION 637
Volume 1

U.S. DEPARTMENT OF COMMERCE/National Bureau of Standards

# Optical Fiber Characterization

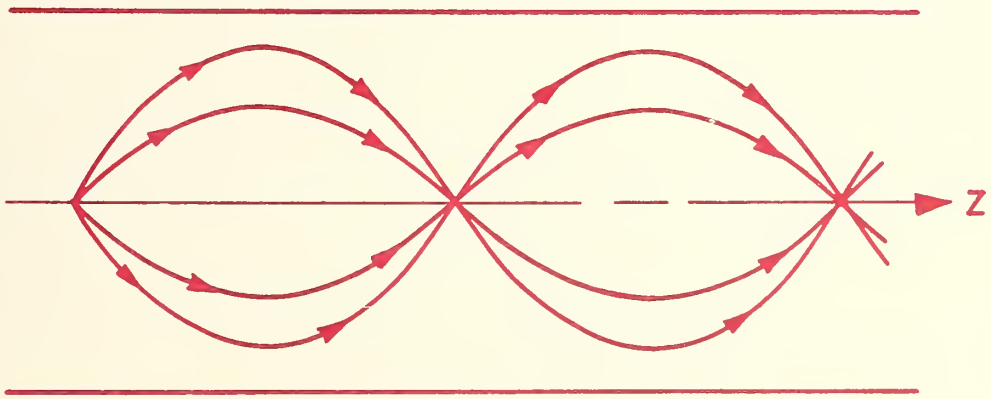

# NATIONAL BUREAU OF STANDARDS

The National Bureau of Standards[1] was established by an act of Congress on March 3, 1901. The Bureau's overall goal is to strengthen and advance the Nation's science and technology and facilitate their effective application for public benefit. To this end, the Bureau conducts research and provides: (1) a basis for the Nation's physical measurement system, (2) scientific and technological services for industry and government, (3) a technical basis for equity in trade, and (4) technical services to promote public safety. The Bureau's technical work is performed by the National Measurement Laboratory, the National Engineering Laboratory, and the Institute for Computer Sciences and Technology.

**THE NATIONAL MEASUREMENT LABORATORY** provides the national system of physical and chemical and materials measurement; coordinates the system with measurement systems of other nations and furnishes essential services leading to accurate and uniform physical and chemical measurement throughout the Nation's scientific community, industry, and commerce; conducts materials research leading to improved methods of measurement, standards, and data on the properties of materials needed by industry, commerce, educational institutions, and Government; provides advisory and research services to other Government agencies; develops, produces, and distributes Standard Reference Materials; and provides calibration services. The Laboratory consists of the following centers:

Absolute Physical Quantities[2] — Radiation Research — Chemical Physics — Analytical Chemistry — Materials Science

**THE NATIONAL ENGINEERING LABORATORY** provides technology and technical services to the public and private sectors to address national needs and to solve national problems; conducts research in engineering and applied science in support of these efforts; builds and maintains competence in the necessary disciplines required to carry out this research and technical service; develops engineering data and measurement capabilities; provides engineering measurement traceability services; develops test methods and proposes engineering standards and code changes; develops and proposes new engineering practices; and develops and improves mechanisms to transfer results of its research to the ultimate user. The Laboratory consists of the following centers:

Applied Mathematics — Electronics and Electrical Engineering[2] — Manufacturing Engineering — Building Technology — Fire Research — Chemical Engineering[2]

**THE INSTITUTE FOR COMPUTER SCIENCES AND TECHNOLOGY** conducts research and provides scientific and technical services to aid Federal agencies in the selection, acquisition, application, and use of computer technology to improve effectiveness and economy in Government operations in accordance with Public Law 89-306 (40 U.S.C. 759), relevant Executive Orders, and other directives; carries out this mission by managing the Federal Information Processing Standards Program, developing Federal ADP standards guidelines, and managing Federal participation in ADP voluntary standardization activities; provides scientific and technological advisory services and assistance to Federal agencies; and provides the technical foundation for computer-related policies of the Federal Government. The Institute consists of the following centers:

Programming Science and Technology — Computer Systems Engineering.

[1]Headquarters and Laboratories at Gaithersburg, MD, unless otherwise noted; mailing address Washington, DC 20234.
[2]Some divisions within the center are located at Boulder, CO 80303.

# Optical Fiber Characterization

## Backscatter, Time Domain Bandwidth, Refracted Near Field, and Interlaboratory Comparisons

B.L. Danielson
G.W. Day
D.L. Franzen
E.M. Kim
M. Young

Electromagnetic Technology Division
Center for Electronics and Electrical Engineering
National Bureau of Standards
Boulder, CO 80303

First of a series on optical fiber technology.

U.S. DEPARTMENT OF COMMERCE, Malcolm Baldrige, Secretary
NATIONAL BUREAU OF STANDARDS, Ernest Ambler, Director

Issued July 1982

Library of Congress Catalog Card Number: 82-600563

National Bureau of Standards Special Publication 637 Volume 1

Nat. Bur. Stand. (U.S.), Spec. Publ. 637 Vol. 1 205 pages (July 1982)

CODEN: XNBSAV

U.S. GOVERNMENT PRINTING OFFICE
WASHINGTON: 1982

# CONTENTS

# PREFACE

The characterization of optical fiber waveguides has been an important topic ever since the first low-loss fiber was fabricated in 1970. Fiber measurements remain a frequent meeting topic and several books have been written on the subject. During the past several years, a number of measurement systems have been developed at the National Bureau of Standards. This book is the first volume of a series intended to describe the design and performance of these systems. Volume I includes a description of systems to measure the backscatter, bandwidth (time domain), and index profile (refracted near field) of optical fibers. Chapters describing these systems are minor revisions of former NBS Technical Notes many of which are now out of print. Descriptions are representative of current practice in the industry and much of the material will be relevant to future systems. Each chapter contains a brief tutorial on the particular subject and a detailed description of the system. This level of engineering detail is not usually found in other books on the subject. Chapter 4 gives a comprehensive description of a series of interlaboratory comparisons with manufacturing members of the Electronic Industries Association. The results are important because they serve to document practices being considered as industry standards. Comparisons cover a complete set of parameters (attenuation, bandwidth, numerical aperture, and core diameter) used in the specification of multimode, graded-index, telecommunications fiber.

The authors would like to thank M. E. DeWeese for preparing the manuscript and providing editorial assistance. Partial support for the work reported here was provided by the Department of Defense, Calibration Coordination Group (CCG) and the U.S. Army Communications R & D Command, Fort Monmouth, New Jersey.

Boulder, Colorado
1982

# ABSTRACT

Optical fiber waveguide measurements are described. Systems to determine the backscatter, bandwidth, and index profile are covered in detail. Measurement comparisons between laboratories are given for fiber attenuation, bandwidth, numerical aperture, and core diameter.

Key words: attenuation; backscatter; bandwidth; index profile; measurements; optical fiber.

# Chapter 1

# Backscatter Measurements on Optical Fibers

**B. L. Danielson**

An optical time domain reflectometer (OTDR) and its components are described in detail. The system performance for this device is examined. Experimental methods are described for the measurement of several parameters of interest in the characterization of optical fibers using the OTDR. These parameters include scattering loss and capture fractions for unperturbed fibers. Experimental capture-fraction values are reported for several step and graded-index fibers and these results are compared with theoretical predictions. Rayleigh backscatter signatures are also presented for several fibers from different manufacturers. Fault signatures are shown for some intrinsic and extrinsic fiber perturbations.

CONTENTS

Table 1. List of symbols, nomenclature and units

| Symbol | Nomenclature | Units |
|---|---|---|
| a | Sellmeier coefficient | |
| A | Absorption coefficient | $m^{-1}$ |
| b | Sellmeier coefficient | um |
| B | Bandwidth | Hz |
| C | Velocity of light | $ms^{-1}$ |
| $C(\lambda)$ | Wavelength dependent absorption | $m^{-1}$ |
| D | Rayleigh scattering coefficient | $m^{-1}\lambda^{+4}$ |
| E | Wavelength independent loss | $m^{-1}$ |
| F | Capture fraction | |
| i | Detector current | A |
| IVPO | Inside vapor phase oxidation | |
| K | Attenuation constant for NDF | |
| L | Fiber length | m |
| n | Index of refraction | |
| $n_1$ | Index of refraction on fiber axis | |
| $n_2$ | Index of refraction of fiber cladding | |
| N | Group index | |
| NA | Numerical aperture | |
| NDF | Neutral density filter | |
| OVPO | Outside vapor phase oxidation | |
| P | Degree of polarization | |
| R | Reflectivity | |
| SNIR | Signal-to-noise improvement ratio | |
| SNR | Signal-to-noise ratio | |
| t | Time | s |
| $v_g$ | Group velocity | $ms^{-1}$ |
| W | Pulse width | s |
| X | Parameter equal to $2\alpha_s L$ | |
| $\alpha_a$ | Absorption loss coefficent | $m^{-1}$ |
| $\alpha_n$ | Non-Rayleigh scattering loss coefficient | $m^{-1}$ |
| $\alpha_s$ | Rayleigh scattering loss coefficient | $m^{-1}$ |
| $\alpha_T$ | Total loss coefficient = $\alpha_a+\alpha_n+\alpha_s$ | $m^{-1}$ |
| $\Delta$ | Relative index difference $\Delta = (n_1^2-n_2^2)/2n_1^2$ | |
| $\theta$ | Half vertex angle of fiber output radiation | |
| $\lambda$ | Wavelength | um |
| $\Phi$ | Power | W |

## 1. INTRODUCTION

The Optical Time Domain Reflectometer (OTDR) is an instrument that was developed in 1976 [1,2] which has proved to be very useful in testing optical fibers. It is similar in operation to the time domain reflectometer that has been used for many years to examine and locate irregularities and mismatches in cables. In the optical case, the inherent Rayleigh backscattering which occurs in the fiber material also provides a visualization of the attenuation and scattering properties of the waveguide as a function of length. Not only can the attenuation of the fiber be estimated, but anomalies may be located and characterized. An excellent review article by Rourke [3] contains much useful information on the OTDR system and its application to a number of optical fiber measurement problems.

If a rectangular optical pulse of width W and peak power $\Phi_0$ is injected into a fiber, the time-dependent response of the backscatter power at the input end of the fiber $\Phi(t)$ can be shown to be [4]

$$\Phi(t) = 0.5\, \Phi_0 W v_g \left[\alpha_s F_s + \alpha_n F_n\right] \exp\left[-\alpha_T v_g t\right] \qquad (1)$$

where $v_g$ is the group velocity, $\alpha_s$ the Rayleigh scattering attenuation coefficient, and $F_s$ is the Rayleigh capture fraction, that is, the fraction of the scattered radiation which is trapped in the fiber and returned in the backward direction. The quantities $\alpha_n$ and $F_n$ refer to the corresponding variables for non-Rayleigh type scattering processes. The total attenuation coefficient, $\alpha_T$ is the sum of the scattering coefficients, $\alpha_s$ and $\alpha_n$, and the absorption coefficient representing the conversion of pulse energy into heat, $\alpha_a$. Equation (1) applies to a uniform reciprocal fiber. In the more general case, both scattering and absorption coefficients as well as capture fractions may be a function of length.

In this chapter, we will document various experimental techniques for measuring the parameters which occur in eq (1). We will also present examples of the observed characteristic backscatter responses, $\Phi(t)$, for fibers which do not possess uniform properties. These backscatter "signatures" will be presented for fibers as received from the manufacturers as well as for fibers which have aberrations induced by external means. We will attempt to correlate observed signatures with changes in the physical properties of the perturbed fibers.

Values of scattering coefficients, capture fractions, and other parameters appearing in eq (1) can be useful in the identification, characterization and location of anomalies occuring in secure optical fiber communication systems. Also, this information may be helpful in OTDR design work, computer modeling and military fiber and cable specification.

## 2. DESCRIPTION OF THE OTDR

### 2.1 Data Acquisition System

Figure 1 shows a block diagram of the main elements of the OTDR system used to generate the data described in this report. The system was mounted on a bench top and no effort was made toward making the device compact or transportable for field use. The main components will be described separately below. Figure 2 illustrates the nature of the unprocessed oscilloscope display for a graded-index fiber which demonstrates a scattering anomaly. Figure 3 represents the corresponding display from the boxcar integrator, and figure 4 the boxcar output on a logarithmic scale.

### 2.2 Laser Diode Sources

For OTDR applications it is desirable to have optical sources capable of producing high peak radiance and high repetition rate with pulse durations in the general range of 5 to 100 ns. If backscatter responses are to be used to estimate loss at the communication wavelength of interest, then the source should also emit radiation at that wavelength. In the spectral region around 850 nm, a suitable pulsed source is the single heterojunction GaAlAs laser diode which is available from a number of manufacturers [5]. The diode used in the present experiments was a RCA type C30012 [6] which was rated at 4 W peak power at a 1 kHz repetition rate. With this source and 1:1 imaging optics it was possible to get a maximum of about 1 W peak power coupled into most fibers.

Many RCA GaAlAs laser diodes are partially polarized. This property can help reduce the coupling loss if a Glan-Thompson prism or polarizing beam splitter is used. It was found that the degree of polarization depends on the current drive level and also varies from diode to diode. A good sample can have about 80 percent of the output radiation polarized in one direction.

Higher average output powers are possible with thermoelectric cooling of the laser diode [7]. No cooling devices were used in the present work, however.

### 2.3 Detectors

In view of the low signal levels involved in backscatter systems, the detector usually has internal gain. This can be either an avalanche photodiode (APD) or photomultiplier tube (PMT). In our somewhat limited experience with both of these types of detectors, we have found the APD to be preferable from several standpoints. In the present case we used an RCA type C30818E silicon APD [8]. For accurate measurements, the linearity of the detector at the normal operating gain is an important consideration. We checked the linearity in the following manner. A calibrated neutral density filter (NDF) with approximately 3 dB attenuation (neutral density 0.3) was inserted in the backscatter beam and the signal level noted. Comparison between the unattenuated and observed signal levels yields a quantitative measure of the detector linearity. When using this method, the NDF should always be inserted in the

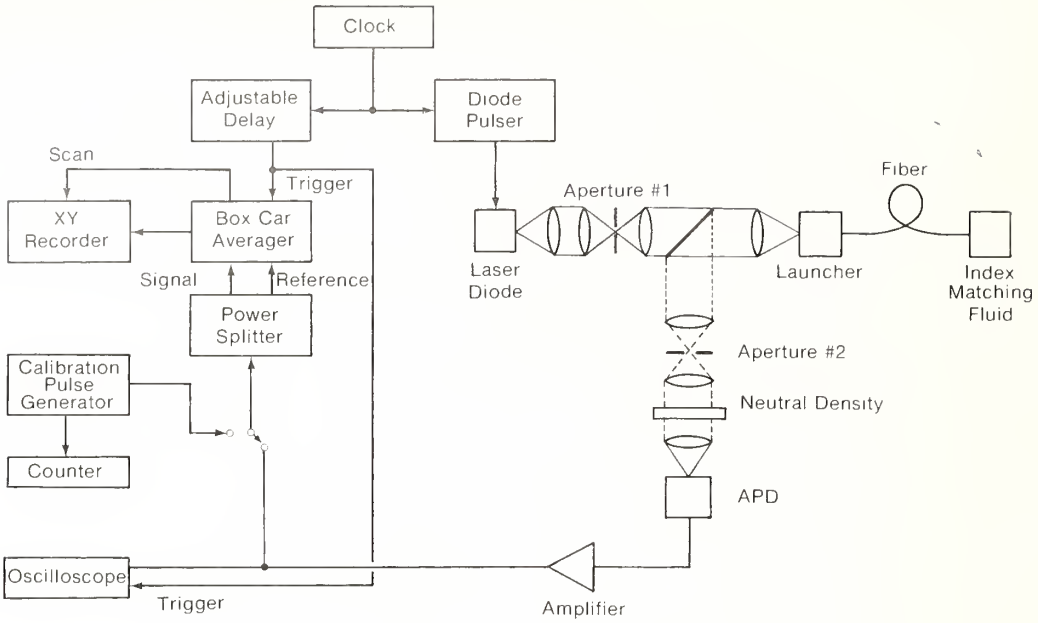


Figure 1. Block diagram of the OTDR system. All lenses are 10X microscope objectives.

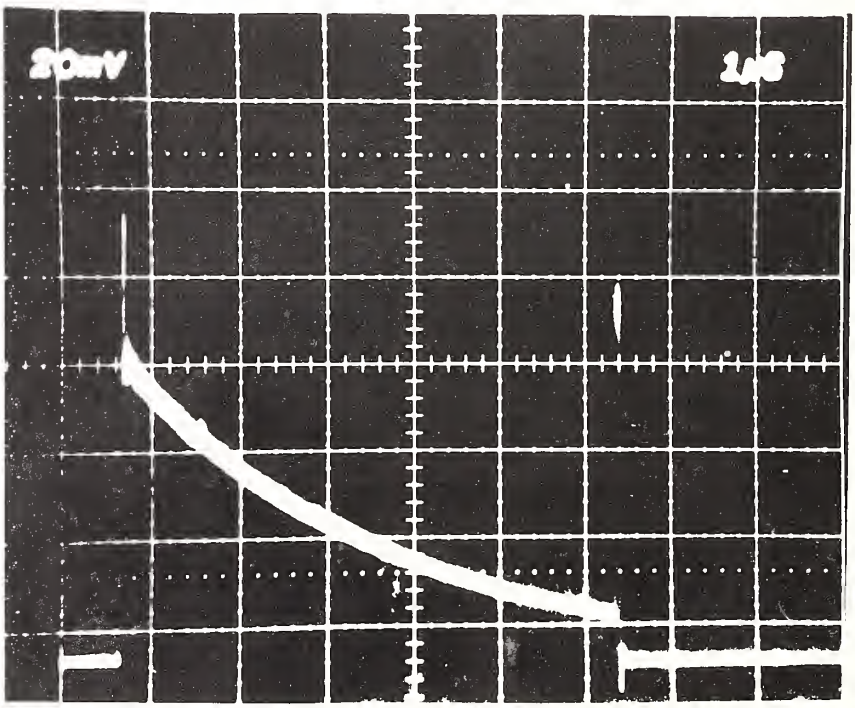

Figure 2. Backscatter signal, oscilloscope display. Fiber H.

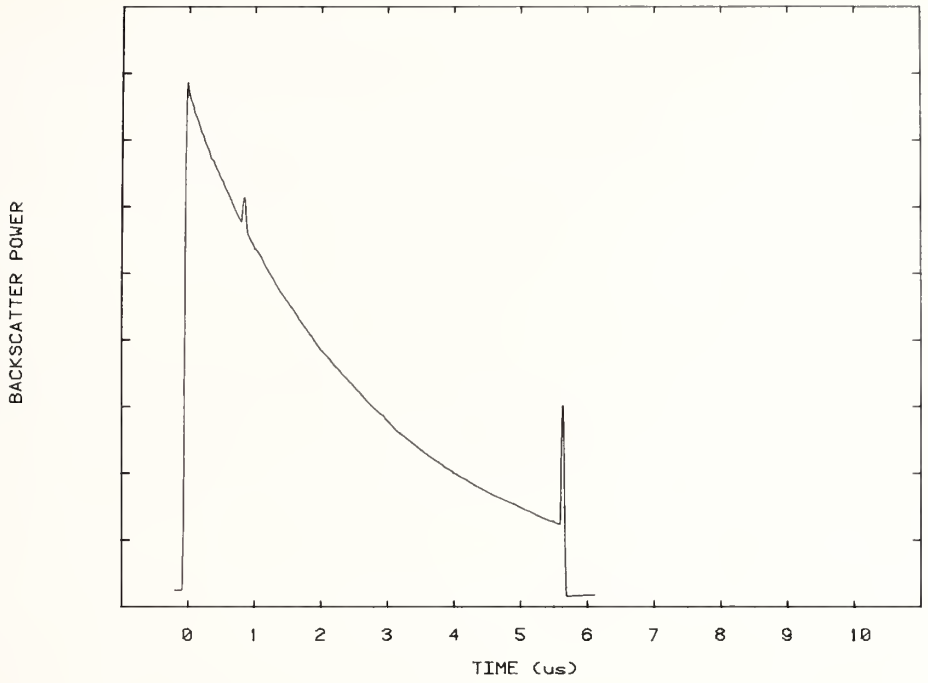


Figure 3. Backscatter signal, boxcar averager display. Fiber H.

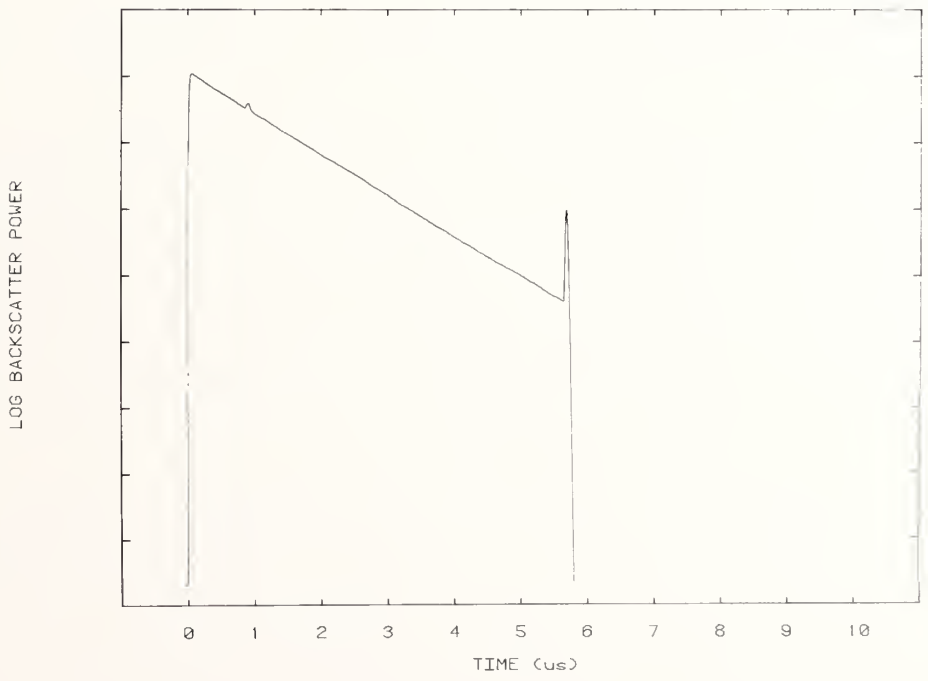


Figure 4. Backscatter signal, boxcar averager display, logarithmic scale. Fiber H.

beam where the rays are parallel and allowance should be made for the fact that the focused beam may be displaced slightly. If the detector response is not uniform across its sensitive area, the apparent detector responsivity may change. This problem may to a large extent be obviated by mounting the detector on a XYZ translator and maximizing all signals prior to reading. Figure 1 shows an appropriate location for insertion of the NDF. Linearity may also be checked over a wider dynamic range with this method by using higher density filters.

## 2.4 Beamsplitters

Several types of possible OTDR beamsplitters and some of their characteristics are illustrated in figure 5. The coupling loss which is listed in the figure is based on the assumption that the backscattered radiation is unpolarized, since few fibers maintain polarization for more than a few meters [9]. The coupling loss is then defined as

$$\text{coupling loss} = 10 \log \frac{\Phi_1}{\Phi_2} \quad \text{(dB)} \tag{2}$$

where $\Phi_1$ is the collimated laser diode output power and $\Phi_2$ is the power that is directed toward the detector after having undergone a lossless reflection. For polarizing beamsplitters this coupling loss will depend on the initial state and degree of source polarization. The minimum loss is for 100 percent polarization in the direction indicated by the arrows in figure 5.

Most commercially available 50:50 (nominal) beamsplitters do not have an exact 50:50 beamsplitter ratio, and this ratio may be a function of wavelength. Figure 6 demonstrates how the coupling loss changes with reflectivity (we assume that transmission + reflection = 1).

Figures 5(b) and 7 indicate that a fairly efficient beamsplitter can be constructed from a glass plate if it is used at a high angle of incidence. The parameter P represents the fraction of the laser diode power which is polarized in the direction perpendicular to the plane defined by the normal to the plate surface and the incoming beam propagation vector. In the calculation of the coupling loss for this device we have taken into account reflections from both the front and back surfaces. The Fresnel equations [10] were used to determine the reflectivity as a function of angle of incidence. A prism may also be used in the same manner.

If space is a consideration, the beam splitter illustrated in figure 5(c) is another possibility. The laser diode, detector and test fiber can be connected together by appropriate pigtails. Since numerical apertures of fibers are independent of their diameters, the diode can couple into the launch fiber with a relatively high efficiency in the forward direction. The coupling loss is calculated from branching ratios determined from the relative fiber cross sections presented to the backward traveling wave. This arrangement apparently has not been described in the literature.

| Beam Splitter Type | | Coupling Loss | Remarks |
|---|---|---|---|
| (a) | 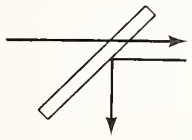 | 6 dB | One surface coated for 50% transmission (see fig. 6). |
| (b) | 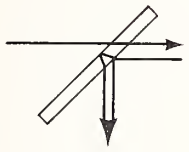 | 5 dB min. | Glass plate, n=1.51 (see fig. 7). |
| (c) | 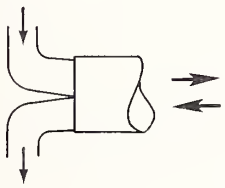 | 6 dB | Optical fiber coupler (see text). |
| (d) | 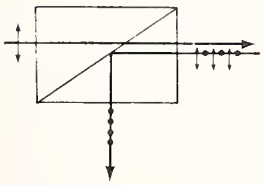 | 3 dB min. | Glan prism polarizer. Polarizer direction indicated by arrows. |
| (e) | 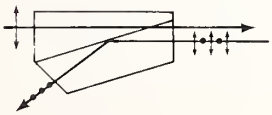 | 3 dB min. | Beam splitting Thompson prism. |
| (f) | 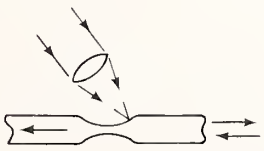 | | Taper coupler [1]. |

Figure 5. Types of OTDR beam splitters.

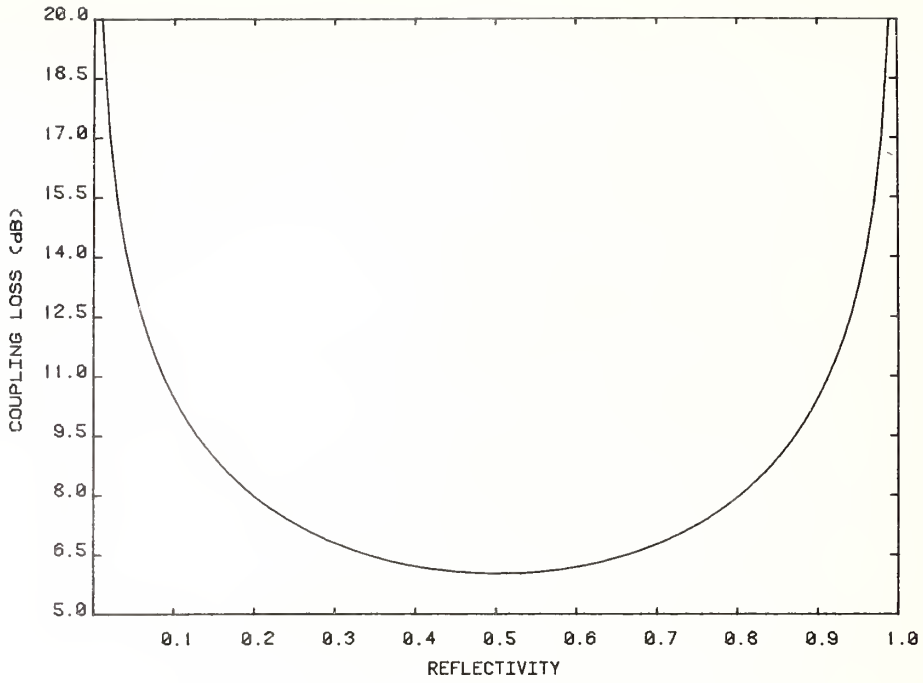


Figure 6. Coupling loss as a function of beam splitter reflectivity.

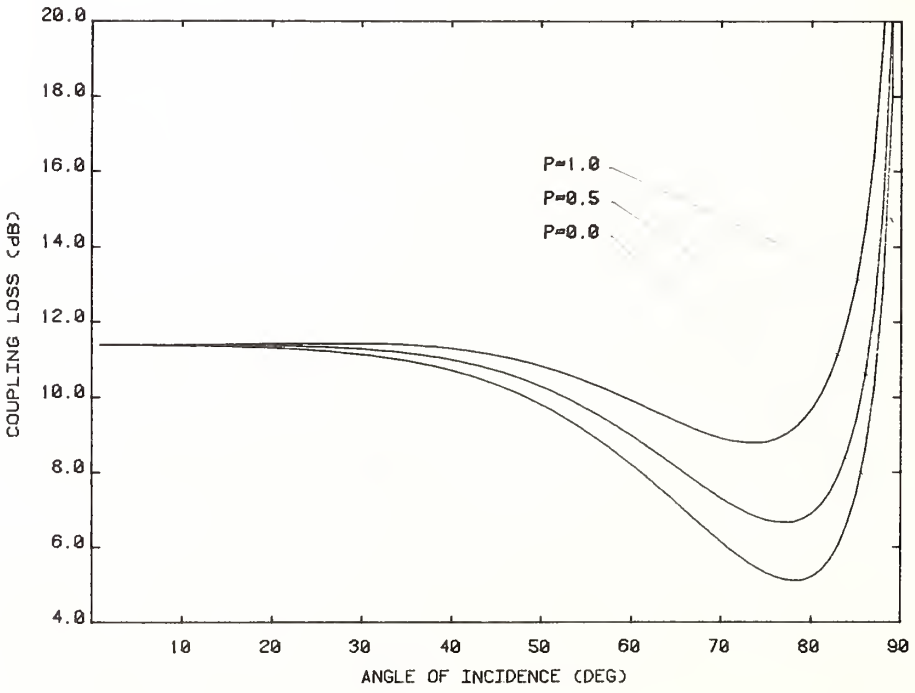


Figure 7. Coupling loss for a glass plate beam splitter as a function of angle of incidence for different degrees of polarization of the incident beam.

We have employed the Glan prism of figure 5(d) in the current work. This beam splitter provides good isolation (-37 dB) to Fresnel reflections from the input end of the fiber, and has a relatively low coupling loss. One disadvantage is the fact that the prism material is dispersive; the backscattered radiation is returned at different angles as the wavelength is changed. Use of different laser sources causes misalignment at the detector. The Foster or beam-splitting Glan-Thompson prism shown in figure 5(e) corrects this problem, but at considerable expense. Polarizing beam splitters do not have this difficulty, but the thin films that comprise the beam splitting surface do not maintain their polarizing properties over a wide spectral interval.

The taper coupler (fig. 5(f)) has been described by Barnoski et al. [1].

Other types of beam splitters have been described in the literature, including bifurcated couplers [11], and a patented coupling cell filled with index-matching liquid and a beam splitter [12]. Optical fiber directional couplers are also available commercially, but have not been evaluated by our laboratories.

## 2.5 Boxcar Averager

The signal averaging device used in the present work was a PAR Model 162 boxcar integrator. This particular instrument has the desirable feature that ratios may be taken of the scanned backscatter signal and an unscanned reference signal. The latter is obtained from a power divider after the first stage of amplification. This type of signal processing minimizes the effect of drift in the laser diode source and detector.

The adjustable delay (fig. 1) allows the boxcar scan to begin at any desired point in time. Since time maps into distance along the fiber, this is equivalent to starting the scan at any desired fiber location.

The time scan of the boxcar averager may be calibrated with markers which are output from a pulse generator. Time intervals are measured with an electronic timer/counter. The display time for a full scale scan is then accurate to within an estimated 0.02 percent.

## 2.6 Launcher

A fiber launcher which we have found to be convenient is shown in figure 8. This is an adaptation of a device originally described by Dakin et al. [13]. It consists of a precision-bore capillary tube [14] which is flared at one end for easy insertion of the fiber. The usual capillary diameter of 0.152 mm will hold 0.125 mm o.d. fibers without creep once the fibers are inserted. The launcher is filled with index-matching oil which also serves as a mode stripper. Once aligned, fibers may be removed and reinserted without significant realignment. However, care must be exercised that dust or foreign matter does not contaminate the bore or launch end. The launcher is demountable so that it can be cleaned if desired.

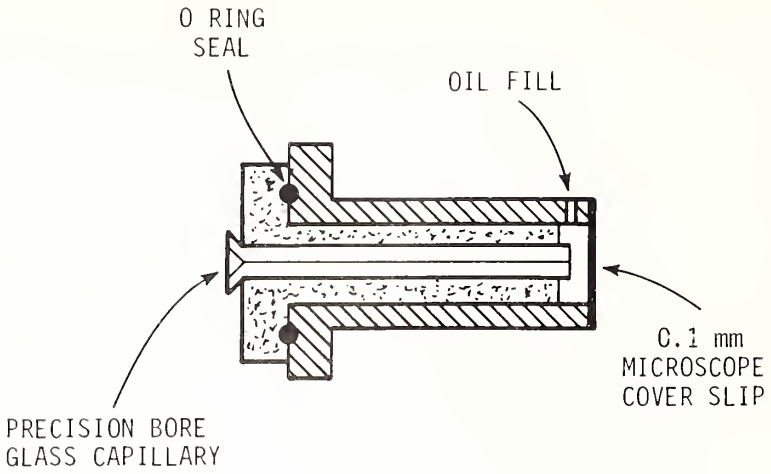


Figure 8. Demountable fiber launcher.

It is not necessary to use antireflection coatings on the glass cover slip on the input end if polarizing optics are used for the beam splitter. The reflection off the front surface is polarized and therefore largely rejected at the Glan prism coupler.

### 2.7 Apertures

The aperture labeled No. 1 in figure 1 is a laser-drilled pinhole and is used to control the spot size on the fiber. In certain cases, for example, with concentric-core fibers, it may be desirable to restrict the set of excited modes which are launched at the input end of the fiber. Alignment is facilitated if the optics have a magnification of one. Here the desired spot size is the same as the pinhole size and is independent of the launch NA. The aperture labeled No. 2 in the same figure is used to reduce the magnitude of the Fresnel reflection from the input end of the fiber. However, in many of the measurements reported on here, both apertures were removed in order to maximize the backscatter signal.

## 3. SIGNAL AND NOISE CONSIDERATIONS

### 3.1 Loss Budget

The ultimate limitation on the OTDR system for obtaining useful information from optical fibers will be associated with the problem of extracting useful signals in the presence of noise. The backscatter power levels are inherently small, and for fibers that are many kilometers in length, the Signal-to-Noise Ratio (SNR) of the returning signal may be degraded to an unacceptable level. We will present here a numerical example of the backscatter signal levels to be expected in a somewhat idealized OTDR system for a special case. We

consider a pure silica fiber whose only loss is due to the intrinsic Rayleigh scattering, and a laser diode whose radiation is 100 percent polarized. Other conditions are assumed as follows:

| | |
|---|---|
| Pulse duration W | 50 ns |
| Electronic bandwidth B | 20 MHz |
| Rayleigh scattering loss (850 nm) | 1.5 dB/km ($3.45 \times 10^{-4}$ nepers/m) |
| Absorption loss $\alpha_a$ | 0 dB/km |
| Peak power input to fiber $\Phi_o$ | 1 W (+30 dBm) |
| Beamsplitter coupling loss | 6 dB |
| Optical losses (lenses, etc.) | 0.2 dB |
| Group velocity $v_g$ | $2.01 \times 10^8$ m/s |
| Capture fraction $F_s$ | 0.005 |

From eq (1) we can calculate the maximum backscatter power in the fiber, at t = 0, to be about -20.6 dBm, or considering the beamsplitter cooling loss and optical loss, a power of about -26.8 dBm at the detector. From design data presented elsewhere [15], we can infer that, for a given SNR, a typical APD requires a power level $\Phi_r$ of approximately

$$\phi_r = 10 \log B - 73 + [SNR-10]\ 0.88\ W. \qquad (3)$$

For a minimum SNR of 0 dB, we have

$$\Phi_r \cong -69\ dBm\ . \qquad (4)$$

This implies a loss margin of about 42 dB, so that a fiber may have a one way loss of 21 dB and still have an observable backscatter feature. For the silica fiber considered here this represents a length of about 14 km. In most cases the loss of commercially available fibers is much greater than 1.5 dB/km at 850 nm so that the critical length is reduced correspondingly.

Figure 9 illustrates the backscatter signal levels expected from eq (1) as a function of fiber length for several probe pulse widths (at constant peak power) for silica at 850 nm. We have converted time to length according to the usual prescription $2L = tv_g$.

### 3.2 Optimum Scattering Levels

An examination of eq (1) shows that the backscatter power is proportional to the Rayleigh scattering loss $\alpha_s$. Being a form of loss, $\alpha_s$ also decreases the signal as a funtion of length through the exponential factor $\exp(-\alpha_T v_g t)$. For a given length, L, then, there is an optimum $\alpha_s$ which maximizes the backscatter signal at that point. This is easily seen to be

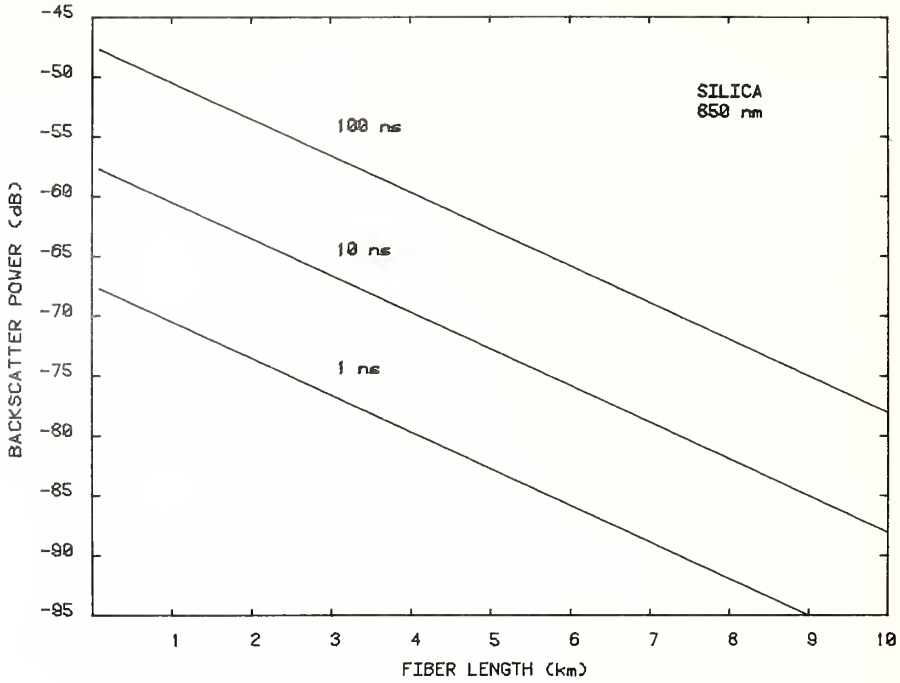


Figure 9. Backscatter power levels for silica at 850 nm. To a first approximation this power is proportional to the probe duration as shown here. Other conditions are given in the text.

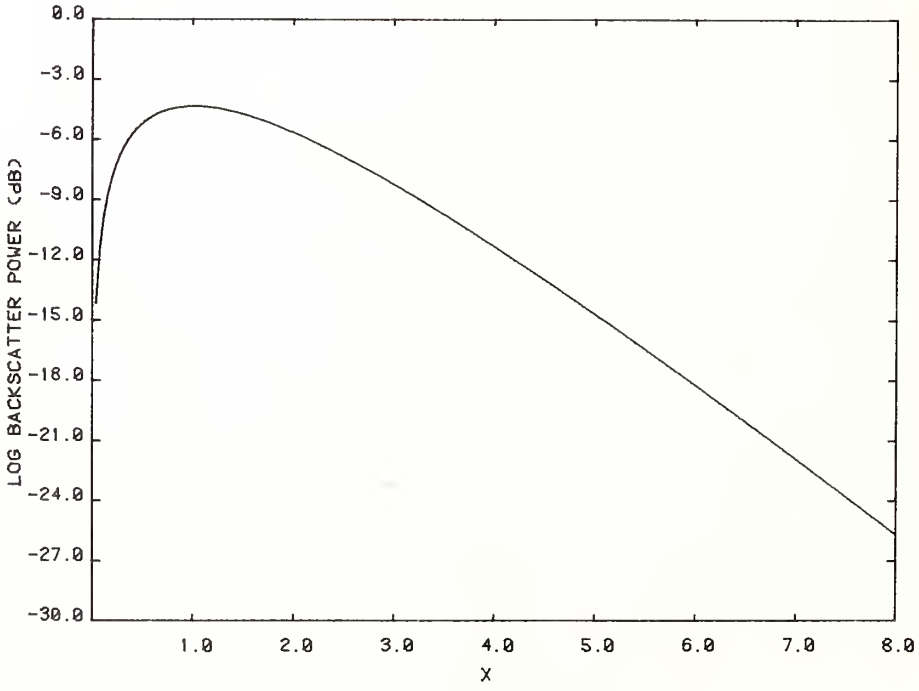


Figure 10. Relative backscatter power as a function of the parameter X (see text).

$$\alpha_s = \frac{1}{2L} . \qquad (5)$$

where $\alpha_s$ has units of nepers/m and L is in meters. Figure 10 shows the relative backscatter signal as a function of the parameter $X = 2\alpha_s L$. We have normalized this plot in such a way that $0.5\ FWv_g = 1$. As an example, for a fiber length of 2.6 km, the maximum backscatter signal occurs for a Rayleigh scattering loss which is just equal to that of pure silica (850 nm).

### 3.3 Signal-to-Noise Ratio Improvement

There are many possible avenues for improving the SNR of the backscatter signal. For example, one can increase the averaging time, peak power, or increase the pulse width at quasi-constant power. However, these strategies often have their limits, and sometimes have deleterious side effects. We will now examine some of these possibilities.

Increasing the peak power, for example with a YAG laser, can result in nonlinear scattering processes, although for multimode fibers the thresholds appear to be very high [16, 17]. Often high peak powers are simply not available at the wavelength of interest.

With many laser diode sources it is possible to increase the pulse width at constant peak power output, without exceeding the maximum drive current specifications. The optical backscatter power is directly proportional to the probe pulse width W according to eq (1). For square-law detectors the corresponding electrical power is proportional to the square of the optical power. Also, in this case, the electronic signal bandwidth can be adjusted to be approximately 1/W (Hz); for white noise the (electrical) noise power will be inversely proportional to pulse width. We then have an apparent signal-to-noise improvement which varies as the third power of the pulse width W. However, fault-location resolution is degraded as a consequence. In addition, if $W > 1/\alpha_T v_g$, the background backscatter signature is distorted, making attenuation measurements less accurate and interpretation of anomalies more difficult.

It is well known that the SNR also can be increased by appropriate averaging. For Gaussian noise processes, averaging N samples will reduce the mean rms current noise by a factor of $N^{-1/2}$, or the mean noise power by a factor of 1/N. One would expect then, that the SNR should increase directly with N or with averaging time. The boxcar integrator operates on this principle. However, these expectations are realized only for certain stationary random noise processes. In real-world systems, flicker noise, drifts, or nonrandom (coherent) types of interference will generally set a limit to the SNR which can be attained with an increase in averaging time.

## 4. MEASUREMENTS WITH UNPERTURBED FIBERS

### 4.1 Fiber Backscatter Signatures

An estimate of the total attenuation of an optical fiber is easily made from an examination of the background backscatter signature, that is the backscatter power versus time profile which is a characteristic of the fiber in question. As used here, the background signature refers to the response due to uniform Rayleigh scattering in the fiber and is distinguished from fault signatures discussed in a later section which arise from fiber irregularities or faults. The degree of agreement between backscatter-derived loss determinations and the conventional cut-back loss values depends on measurement procedures as well as the intrinsic properties of the fiber. The procedures and conditions necessary for good agreement have been discussed at length elsewhere [18]; we will note here only that if the properties of the fiber are uniform (not a function of length) and reciprocal (the same in both forward and backward directions) then the losses determined from the cut-back and backscatter methods sould be equal. In some cases the actual fiber attenuation may be inferred from OTDR measurements when these conditions are not fulfilled [19].

We will show in this section some typical backscatter scans, from which attenuation may be inferred, in order to demonstrate their appearance, the variability between manufacturers, and some possible significance to the fine structure which is often observed. It will sometimes be convenient to display the linear backscatter signature (fig. 11) and at other times the logarithmic signature (fig. 12). The linear display emphasizes irregularities near the launch end of the fiber and can be used to determine attenuation with no Y-axis calibration. The logarithmic display requires a system calculation to calibrate the Y-axis, but has a wider dynamic range and provides for easy visual identification of nonlinear loss regions. These are manifested by changes in slope.

Figures 11 to 13 represent the backscatter scans from a concentric-core fiber [20]. This type of fiber has a special geometry consisting of two step-type channels in one fiber. One of the cores is on axis and the second is in the form of a concentric annulus. It will be noted that there is a high degree of correlation in the irregularities appearing on the scans of both channels. These fluctuations are reproducible and are observed on most of the fibers we have tested. They are most likely due to diameter changes which arise while the fiber is being drawn. Rourke [3] has shown that diameter variations will produce effects of this sort, although other explanations have also been offered [21].

Figures 14 to 22 show the signatures of other fibers which also exhibit irregularities. In all of these samples, the fluctuations are a real effect and are not due to system noise. It is apparent that some fibers manifest much smaller variations than others. Fibers A and E (both from the same manufacturer) are particularly smooth in this regard. It is also clear that, for certain applications, such as secure communications, where it is desired to detect as small a fault signature as possible, these background irregularities should be minimized.

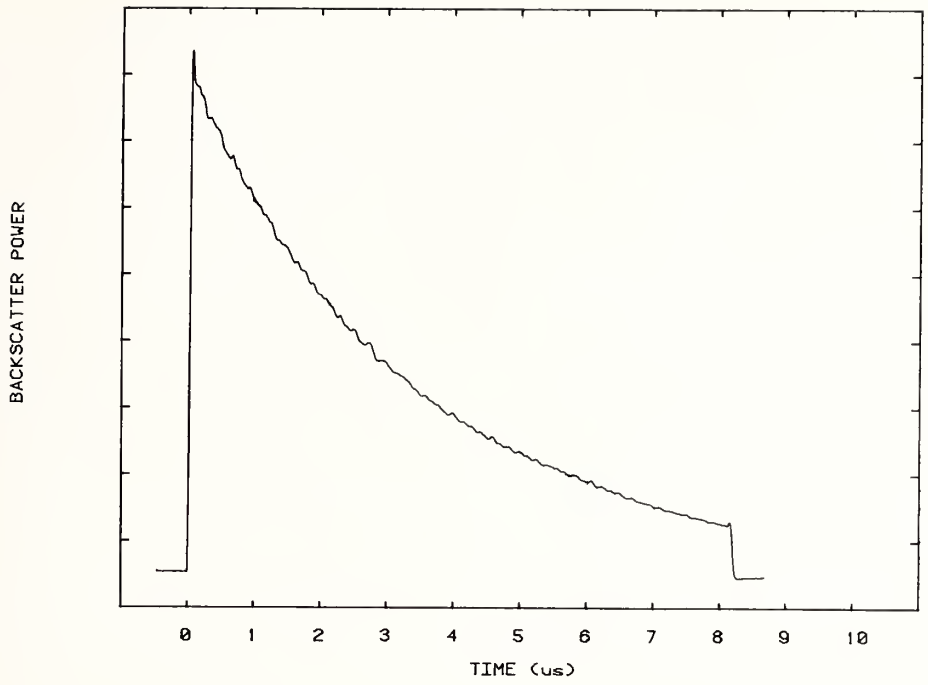


Figure 11. Backscatter response for a concentric-core fiber, center core. Fiber G.

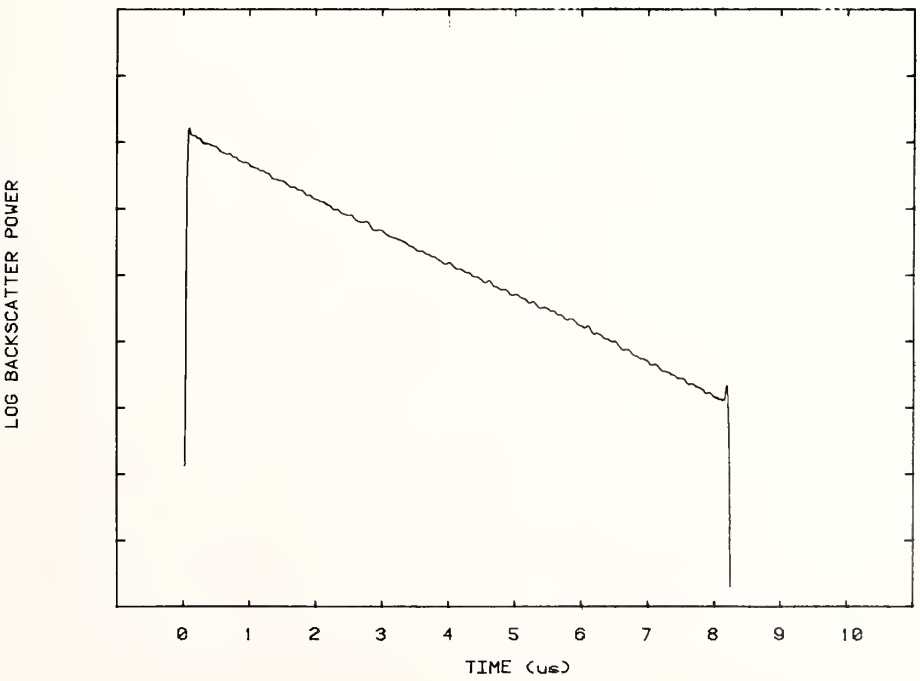


Figure 12. Backscatter response for a concentric-core fiber, center core, logarithmic scale. Fiber G.

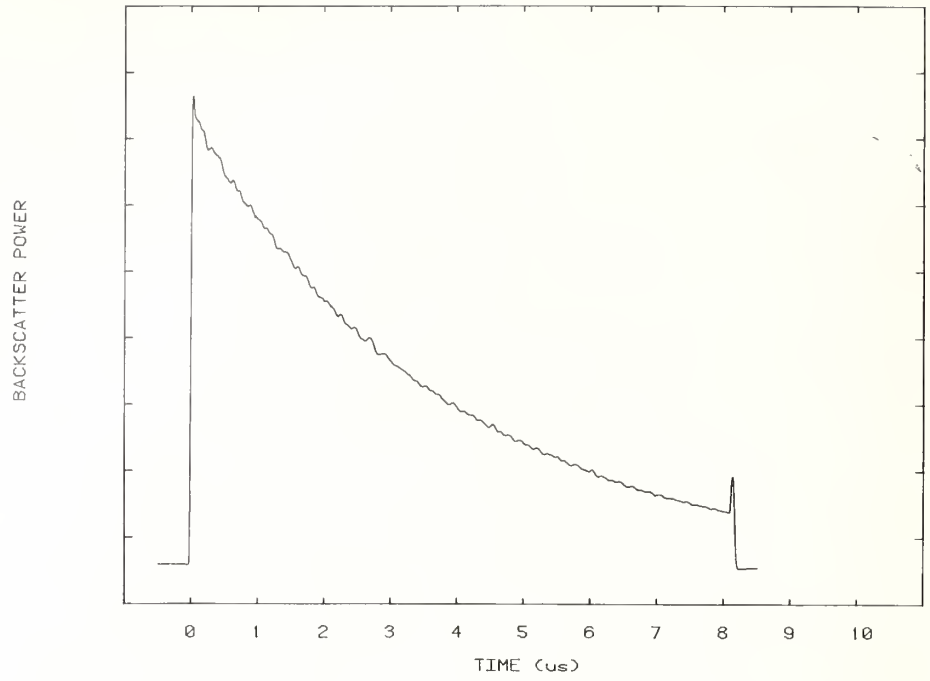


Figure 13. Backscatter response for a concentric-core fiber, outer core. Fiber G.

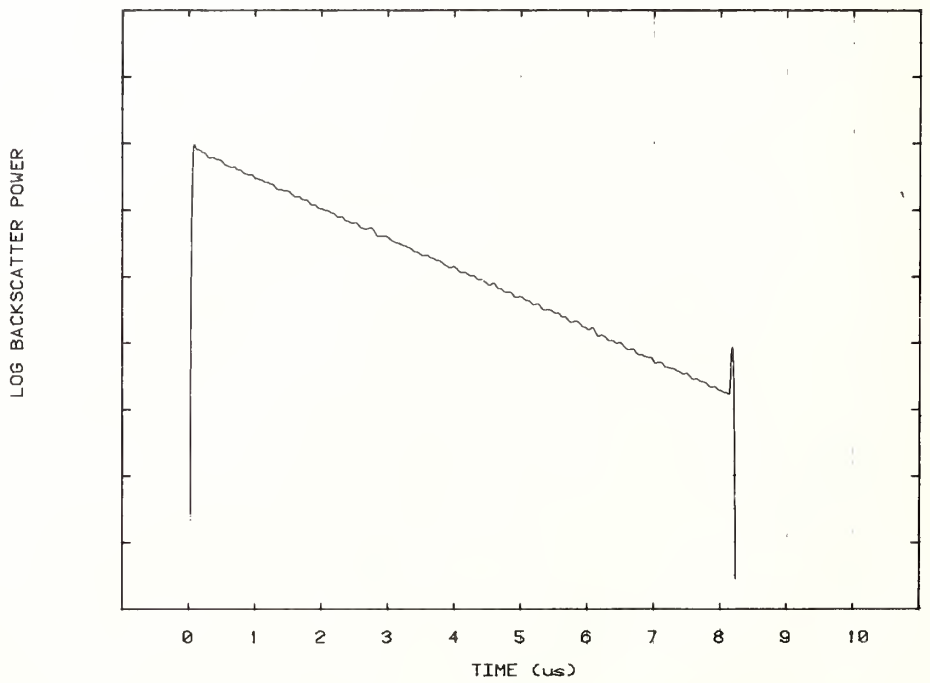


Figure 14. Backscatter response for a concentric-core fiber outer core, logarithmic scale. Fiber G.

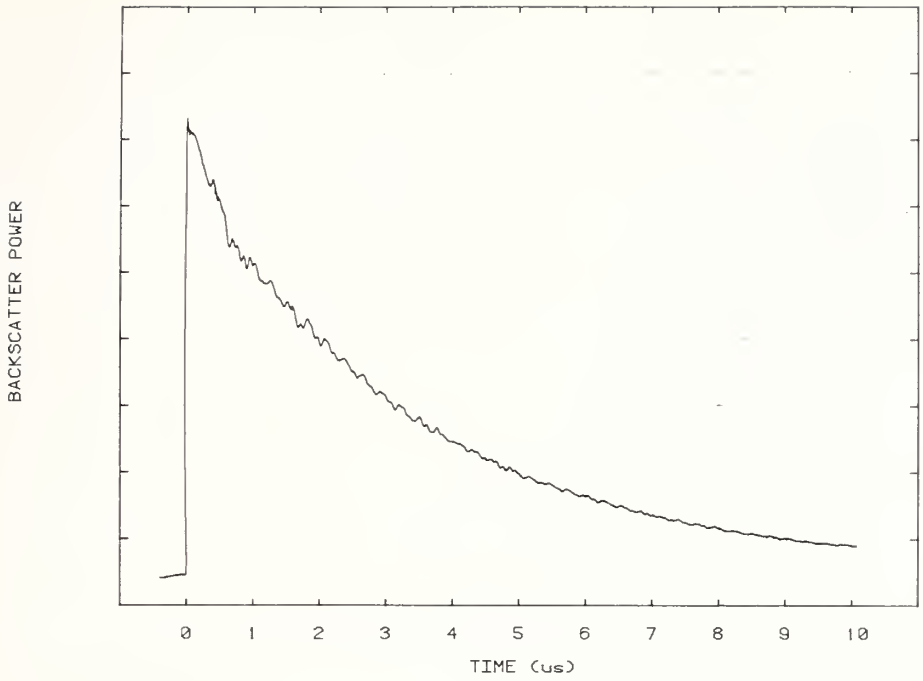


Figure 15. Backscatter response for step-index fiber F.

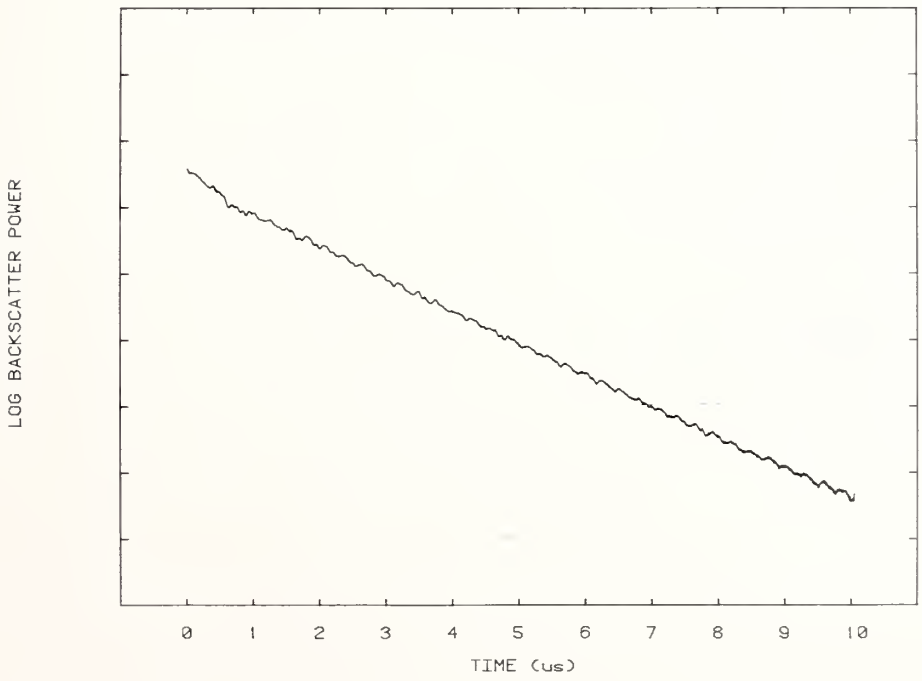


Figure 16. Backscatter response for step-index fiber F, logarithmic scale.

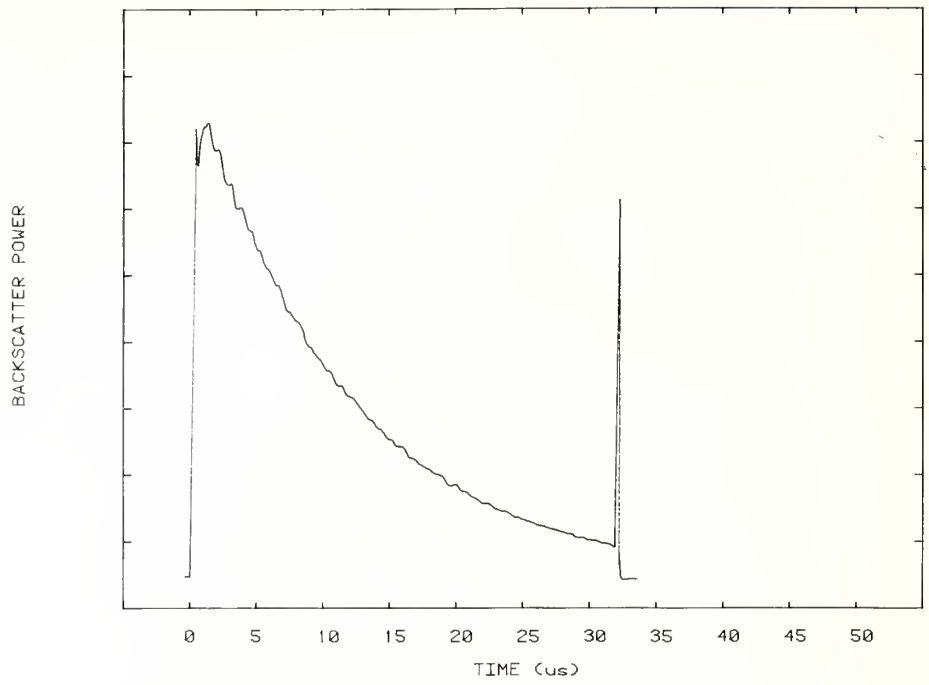


Figure 17. Backscatter response for graded-index fiber I.

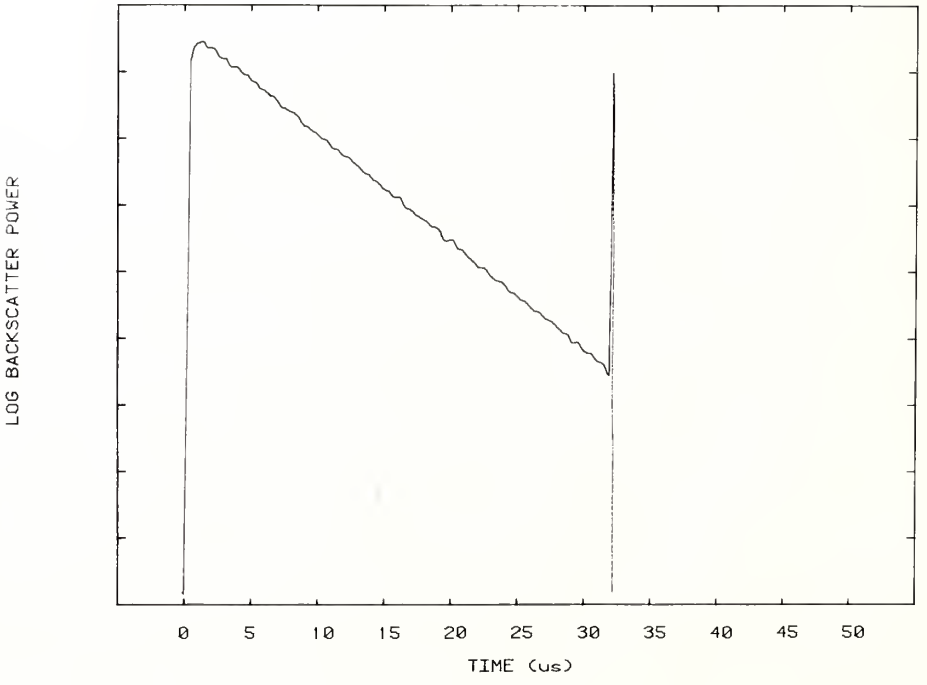


Figure 18. Backscatter response for graded-index fiber I, logarithmic scale.

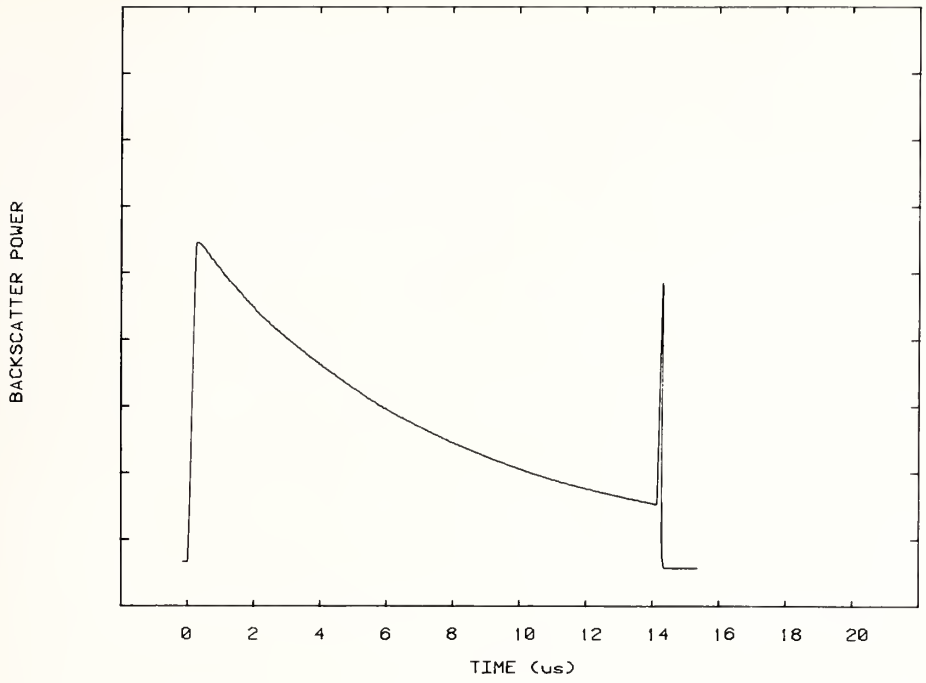


Figure 19. Backscatter response for graded-index fiber A.

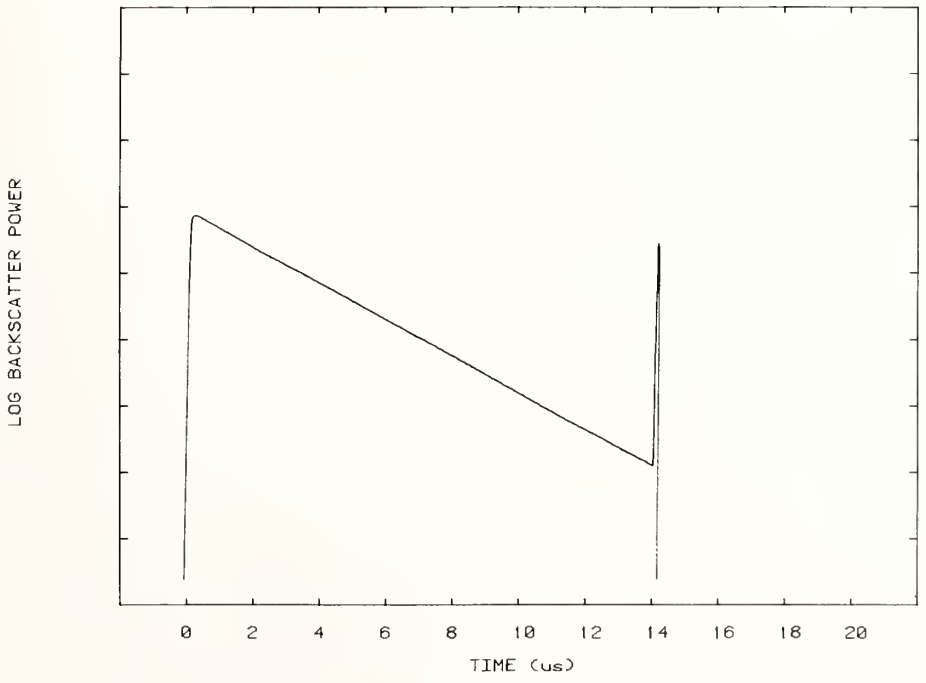


Figure 20. Backscatter response for graded-index fiber A, logarithmic scale.

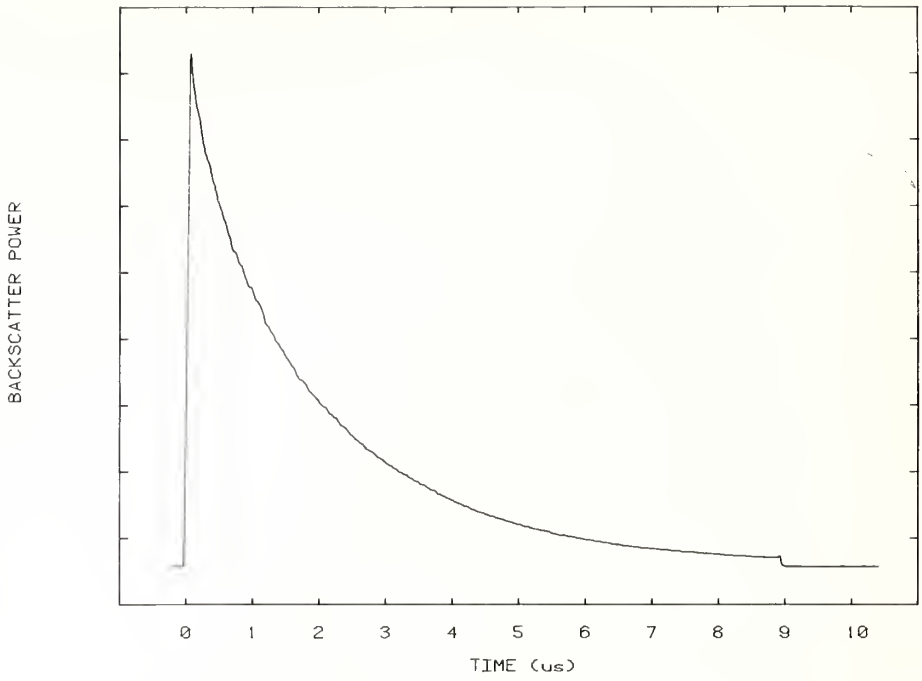


Figure 21. Backscatter response for graded-index fiber D.

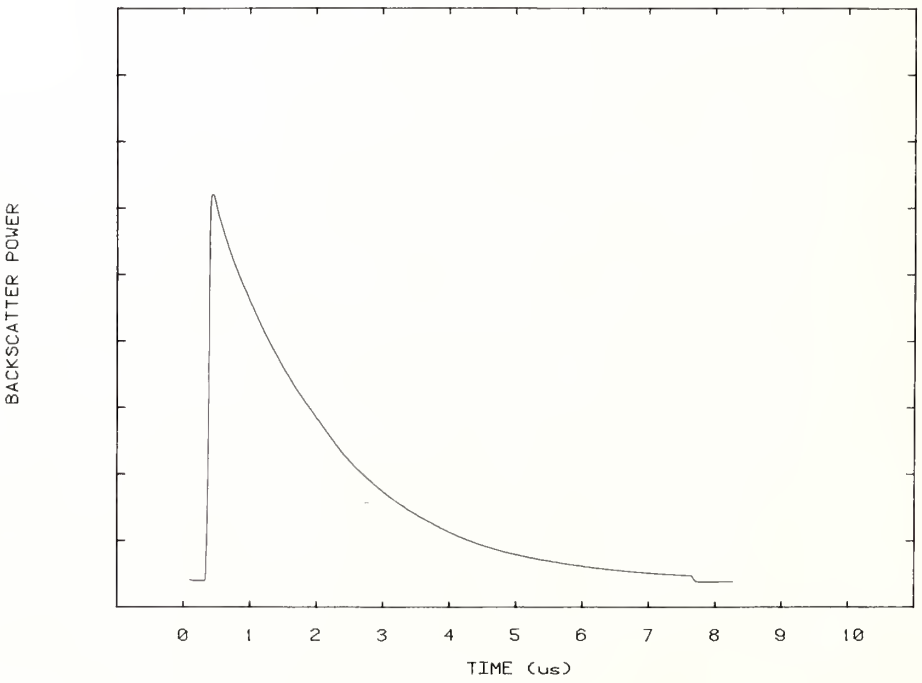


Figure 22. Backscatter response for step-index fiber E.

## 4.2 Scattering Loss Measurements

In eq (1) we have divided the scattering mechanisms in fibers into two different categories, Rayleigh and non-Rayleigh. Rayleigh scattering originates in intrinsic spatial variations in the index of refraction and in fluctuations in the dopant material which occur on a small scale compared with the wavelength. It is characterized by a $(1+\cos\theta)$ angular dependence and is inversely proportional to the fourth power of the wavelength. Olshansky [22] gives an excellent review of Rayleigh scattering in fibers, along with many useful references. Non-Rayleigh scattering includes such processes as microbending, core-cladding interface scattering, Mie scattering, radiation from bends (macrobending), and scattering, or reflection, from fiber imperfections. Most of these mechanisms will scatter radiation predominantly in the forward direction (i.e., $F_n$ is small) so that their effects on the backscatter signature is similar to an absorption process.

Many different methods have been developed for measuring scattering in fibers [23,24, 25]. These are all variants of integrating spheres which have the severe disadvantage, in our application, of measuring forward as well as Rayleigh-type scattering. A technique proposed by Inada [26], and implemented by other authors [27,28], avoids this problem. In this method the spectral loss is plotted as a function of $\lambda^{-4}$. If $\alpha_T$ represents the total loss

$$\alpha_T = \frac{D}{\lambda^4} + E + C(\lambda) \qquad (6)$$

where D is the Rayleigh scattering coefficient in units of $m^{-1}\ \lambda^{+4}$, E is the loss contribution which is independent of wavelength, and $C(\lambda)$ is the wavelength contribution which in our case is dominated by OH absorption. The Rayleigh scattering coefficient can be determined by a least-squares fit to eq (6) by ignoring wavelengths around 950 nm where water absorption is important. The fibers described in section 4.3.5 were measured in this fashion in order to obtain $\alpha_s$ values for capture fraction determinations. Some sample plots are shown in figures 23, 24, and 25 which show the variability of these types of plots. All are graded-index fibers. Fiber A demonstrates a loss dependence on launch NA. However, the Rayleigh scattering coefficient (the slope of the straight-line fit) is independent of launch NA. The difference in total loss has been attributed to excess core-cladding scattering [26]. Fibers B and D do not exhibit this effect. Fiber D has a very small residual loss coefficient E which was unusual in the fibers tested. It is instructive to compare these results with pure silica. Values of scattering coefficients vary somewhat depending on sample preparation and whether measurements are made on bulk material or fibers. Values of 0.80 dB $km^{-1}$ $um^{+4}$ ($1.84 \times 10^{-4}$ nepers $m^{-1}$ $um^{+4}$) are typical [29,30]. The lowest reported loss in a graded-index multimode fiber had a Rayleigh scattering coefficient of 1.0 dB $km^{-1}$ $um^{+4}$ [28]. Scattering levels usually increase with dopant concentration.

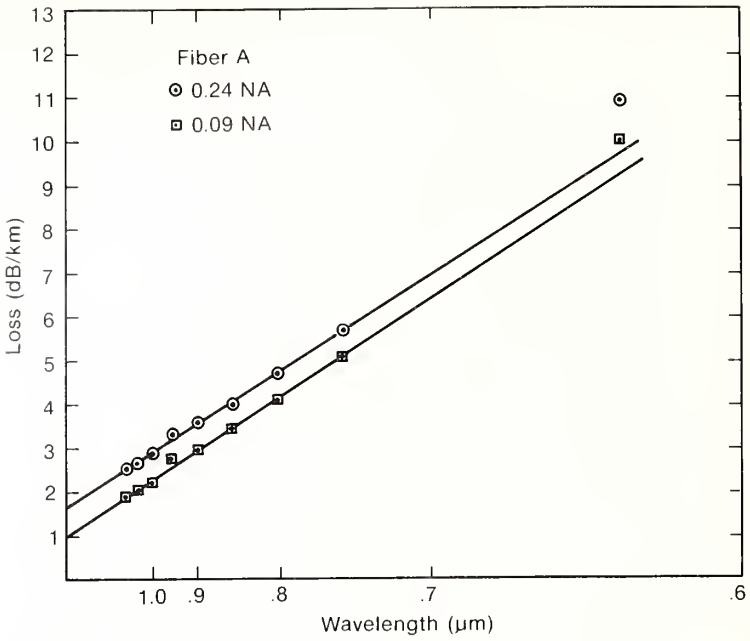


Figure 23. Measured loss spectra, fiber A.

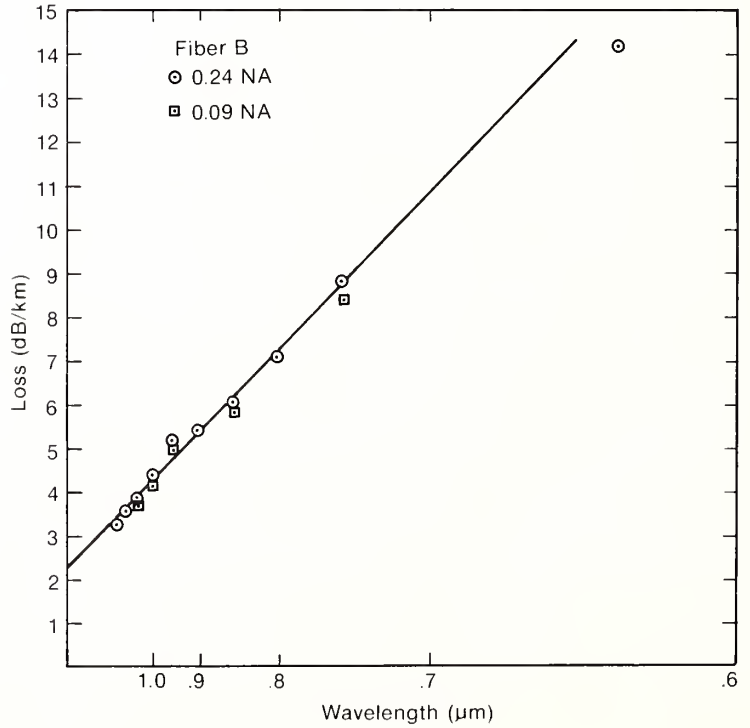


Figure 24. Measured loss spectra, fiber B.

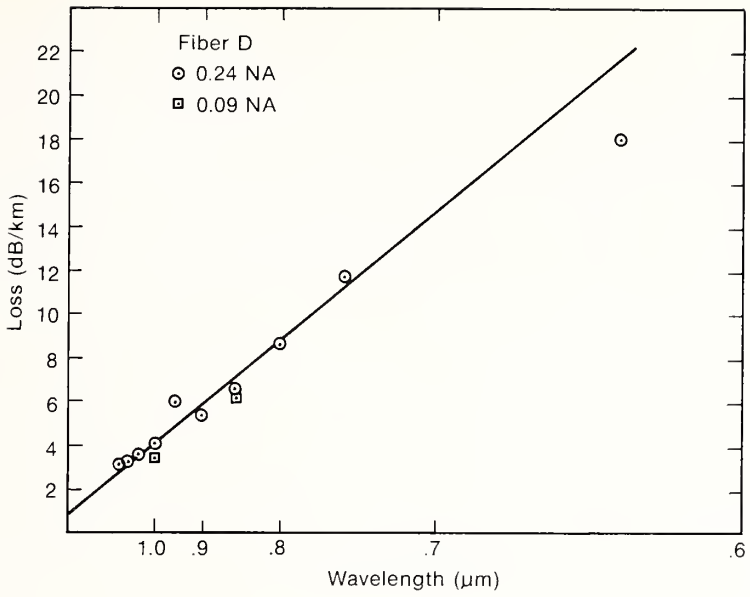


Figure 25. Measured loss spectra, fiber D.

## 4.3 Capture Fraction Measurements

### 4.3.1 Significance of Capture Fractions

The numerical value of optical fiber capture fractions contribute to the data base which is essential to design engineers in the following applications areas:

1. Passive (optical fiber) gyroscopes. The ultimate attainable SNR and accuracy will be dependent on backscatter power levels which are proportional to the capture fractions [31].
2. Full-duplex communication systems. In systems which employ a single wavelength for bidirectional transmission on a fiber, backscatter levels will determine the SNR and crosstalk [32,33].
3. OTDR systems. Backscatter signal levels will determine the allowable fiber loss for location of breaks or defects.
4. Computer simulation studies. Realistic values for F are required for proper computer modeling as described in section 6.

### 4.3.2 Theory and Experimental Methods

The capture fraction F (also referred to as the backscatter factor or trapping factor) represents the fraction of the radiation which is scattered or otherwise removed from the forward propagating pulse which falls within the acceptance cone of the fiber and is therefore confined within the guided wave structure. We will be concerned here only with that radiation travelling in a direction opposite to the probe pulse. The concept of capture

fractions is usually restricted to Rayleigh scattering, but we will use it here in a broader sense; every process or event, discrete or distributed, which removes radiation from the probe pulse and returns at least some of this radiation in the back direction has associated with it a capture fraction. Table 2 lists the capture fractions which can be identified with some scattering and reflection processes in several different types of fibers. We have also included F values of some fiber perturbations which have their characteristic capture fractions. Some of these, as we will see in section 5, are too small to be measured but upper limits can be placed on their magnitude.

We will in the first instance concern ourselves with the actual experimental determination of fiber capture fractions associated with scattering processes which vary inversely with the fourth power of the wavelength: Rayleigh and Brillouin scattering. Brillouin scattering is expected to have the same angular and wavelength dependence as the Rayleigh scattering and will therefore have the same value of F. According to Lin [21], the Brillouin scattering coefficient is about 13 percent as large as the Rayleigh coefficient.

Theoretical values for the Rayleigh scattering capture fractions have been derived by several authors [2,21,33,34,35]; we will use the results of Neumann [4] as follows:

For a step-index fiber

$$F = \frac{3(NA)^2}{8\ n_1^2} \tag{7}$$

and for a graded-index fiber

$$F = \frac{(NA)^2}{4\ n_1^2} \tag{8}$$

In both equations $n_1$ is the value of refraction on the fiber axis. We see than, that for identical NA and $n_1$ values the capture fractions for a graded-index fiber are smaller than the step-index fiber by a factor of 2/3.

The approach we have taken for the experimental determination of F is based on eq (1) where a known signal level is compared with the observed backscatter signal level. A convenient "calibrated" signal level in this case is the Fresnel reflection from a perfect fiber break. The ratio of the power reflected $\Phi_r$ to the power backscattered for an ideal cleave $\Phi_s$ is given by [27]

$$\frac{\Phi_r}{\Phi_s} = \frac{2RN}{\alpha_s cWF} \tag{9}$$

where W is the probe pulse width, R the Fresnel reflectivity, and the other quantities have been defined previously. This relation is independent of the total attenuation and length of the test fiber. The reflectivity is given by the relation

Table 2. Capture fractions associated with various scattering and reflection processes

| Backscatter source | Capture fraction | Remarks |
|---|---|---|
| Isotropic scattering | $\frac{1}{2}\left(\frac{NA}{n_1}\right)^2$ | Single mode fiber, ref. 2 |
| Rayleigh scattering | $0.21\left(\frac{NA}{n_1}\right)^2$ to $0.24\left(\frac{NA}{n_1}\right)^2$ | Single mode fiber, ref. 47 |
| Rayleigh scattering | $\frac{3}{8}\left(\frac{NA}{n_1}\right)^2$ | Multimode step index, ref. 4 |
| Rayleigh scattering | $\frac{1}{4}\left(\frac{NA}{n_1}\right)^2$ | Multimode graded index, ref. 4 |
| Reflection from break | 1 | Fresnel reflection |
| Reflection from break end face tilt angle 4° | 0.46 | Step index, $\Delta = 0.01$, ref. 38 |
| Reflection from break end face tilt angle 4° | 0.26 | Graded index $\Delta = 0.01$, ref. 38 |
| Fiber bends | $<6 \times 10^{-4}$ | Section 5 experimental data |
| Pressure-induced microbending | $<5 \times 10^{-5}$ | Section 5 experimental data |

$$R = \frac{(n_1-1)^2}{(n_1+1)^2}. \tag{10}$$

If we assume that the entire core is of index $n_1$, and the cleave is a mirror surface perpendicular to the fiber axis. We can then relate F to quantities which are observables as follows:

$$F = \frac{2(n_1-1)^2\, N}{(n_1+1)^2\, \alpha_s c W}\ \frac{\Phi_s}{\Phi_r}. \tag{11}$$

In our experiment we measure $\alpha_s$ as described in section 4.2, and estimate N and $n_1$ according to section 4.4. The probe pulse is nearly rectangular and its width W is easily obtained from an oscilloscope trace. The ratio $\Phi_r/\Phi_s$ is determined as follows: The fiber was cleaved and examined for end quality (see section 4.3.3). Since the power level $\Phi_r$ is large compared with $\Phi_s$ (typically +30 dB), it is necessary to place a carefully calibrated neutral density filter with attenuation constant K in front of the detector at the position noted in figure 1. The rays at this point are approximately parallel so that no corrections are necessary for the NDF attenuation, and the location of the focus on the APD is unchanged. The detector is mounted on an XYZ translator so that it is easy to check for a signal maximum. After the signal level $K\Phi_r$ from the fiber break is noted, the fiber end is immersed in an index matching fluid to suppress unwanted reflections and the backscatter signal $\Phi_s$ is observed at the same location in the fiber. If the NDF is chosen correctly the signal level

Table 3. Capture fraction data

| Fiber | Type | $10^3$ F Experimental | $10^3$ F Theory |
|---|---|---|---|
| A | Graded | 3.4 ± 0.6 | 4.56 |
| B | Graded | 6.1 ± 1.2 | 6.74 |
| C | Graded | 6.6 ± 1.3 | 6.83 |
| D | Graded | 2.9 ± 0.6 | 6.49 |
| E | Step | 2.0 ± 0.4 | 7.11 |
| F | Step | 5.7 ± 1.1 | 13.9 |

at the APD will be approximately the same as in the prior measurement of $\Phi_r$. This tends to minimize any nonlinear response effects in the APD. Since K is known, the ratio $\Phi_r/\Phi_s$ is easily deduced. This information is used with eq (11) to determine the values of the capture fraction for six step and graded-index fibers. At least six measurements were made on each fiber in order to obtain an estimate of the statistical errors.

4.3.3 Fiber End Preparation

In order to use eq (11) for the determination of capture fractions, it is essential to have the fiber ends cleaved so that they are perfectly reflecting mirror surfaces. Gloge [37] has shown that, in general, the glass fiber fracture face is composed of three regions known as the mirror, the mist and the hackle zones. If properly cleaved, the surface consists entirely of a mirror zone. In addition to being smooth and flat, the end surface must be perpendicular to the fiber axis. Marcuse [38] has shown that, for end faces tilted with respect to the plane perpendicular to the fiber axis as little as two degrees, the reflectivity can change by 30 percent (parabolic index fiber, $\Delta = 0.01$). Here $\Delta$ is the relative index difference of the fiber, $\Delta = (n_1^2-n_2^2)/2n_1^2$. We have used the scribe-and-pull technique of Chesler and Dabby [39] in order to produce the highest quality of fiber breaks. In this method, the fiber is held between thumb and forefinger, scribed with a silicon carbide razor blade [40], and then pulled until broken. The fiber must be pulled straight without bending. Experience has shown that this method produces fractures of superior quality to those obtained from other breaking techniques [41,42].

The fiber-end quality was determined by microscopic examination and with an He-Ne laser technique described by Reitz [43]. With the latter method, a low power laser illuminates the end of the fiber. The quality of the end break will determine the type of reflection pattern on a remote screen. A small spot indicates a mirror surface fiber end. Diffused or large spots or visible scatter from the end indicates a poor break. The locus of points described by the reflected beam on a calibration target as the fiber is rotated, determines the end-face angle (the axis of rotation is the fiber axis). This rotation is easily done with the fingers if the fiber is held in a precision bore capillary tube [14]. With care, these angles can be kept within a degree or less of being perfectly perpendicular to the fiber axis.

Table 4. Optical fiber data

| Fiber | Length m | NA | $\alpha_s$ @ 819 nm dB/km | $\alpha_s/\alpha_T$ % | $\Phi_r/\Phi_s$ |
|---|---|---|---|---|---|
| A | 975 | 0.20 | 3.27 | 71 | 2386 |
| B | 1300 | 0.24 | 2.07 | 67 | 946 |
| C | 1089 | 0.24 | 1.64 | 71 | 1106 |
| D | 1167 | 0.23 | 3.35 | 91 | 1346 |
| E | 782 | 0.20 | 3.00 | 49 | 1950 |
| F | 1200 | 0.28 | 2.40 | 78 | 883 |

### 4.3.4 Numerical Aperture Measurements

There are a number of interpretations and definitions of the term "numerical aperture" (NA) [44]. We have chosen the far-field equilibrium radiation pattern as the appropriate physical quantity from which we determine the numerical values of NA for use in eqs (7) and (8). Figure 26 is an example of such a radiation pattern from fiber C. The fiber was flooded to excite all possible modes and measurements were taken at the output end (1.2 km) in order to approximate equilibrium conditions. For our purposes we will take NA = $\sin\theta$ where $\theta$ is half the vertex angle at which the output irradiance falls to 0.05 of the on-axis irradiance. In a series of comparisons for graded-index fibers [45], the NA determined in this way has been found to agree (to within about 10 percent) with the NA derived from index measurements according to the equation

$$NA = (n_1^2 - n_2^2)^{1/2} . \qquad (12)$$

This relation is independent of the profile parameter, that is, whether the fiber is of the step or graded-index variety. The exact identification is, however, complicated by the presence of lossy high order modes and leaky modes [46,47].

### 4.3.5 Results

The results of the capture fraction measurements are listed in table 3. We see that experimental F values for three of the four graded-index fiber A, B, and C agree fairly well with the result calculated from eq (8). Fiber D, however, has a value almost a factor of two less than expected. For the step-index fibers all measured values are less than the simple theory, eq (7), predicts.

Fibers A and E were from the same manufacturer, as were fibers B, C, and F. Fiber D was obtained from a third manufacturer. For reference purposes some of the properties of these fibers are listed in table 4. There does not seem to be an obvious correlation of low F values with any other of the measured fiber parameters.

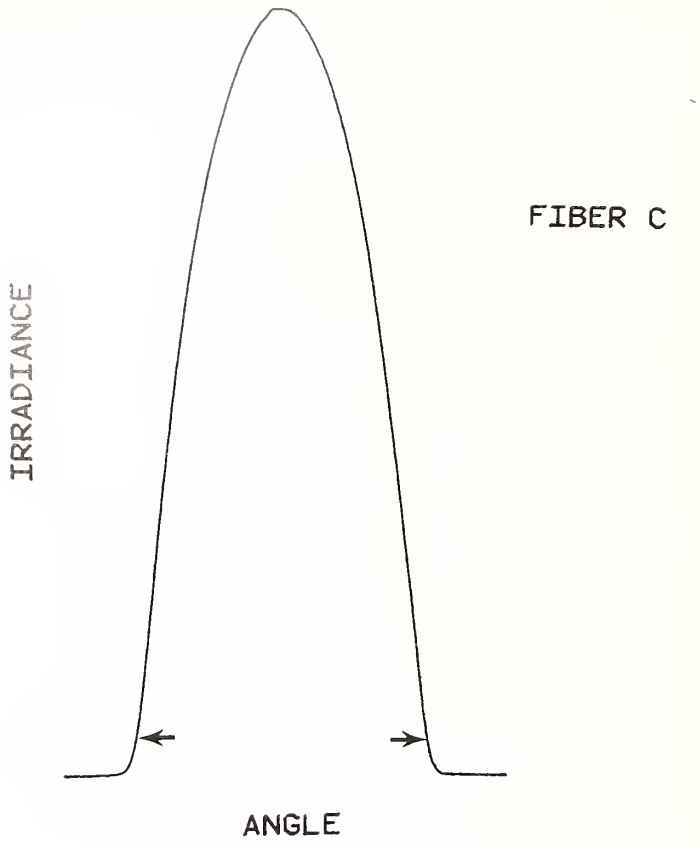


Figure 26. Far-field equilibrium radiation pattern which is used to determine the NA of fiber C. The angle between the 5 percent intensity points is indicated by the arrows.

4.3.6 Error Analysis

The uncertainties in the determination of F values which appear in table 2 were expressed as estimated standard errors evaluated in the following manner. The standard errors $\Delta x_n$ in the independent random variables $x_n$ and the systematic errors $\Delta y_n$ in the variables $y_n$ can be taken to contribute to the total fractional measurement standard error $\Delta F/F$ as

$$\frac{\Delta F}{F} = \sum_{n=1}^{3} \left(\frac{\Delta X_n}{X_n}\right)^2 {}^{1/2} + \sum_{n=1}^{2} \left| \frac{\Delta Y_n}{Y_n} \right| . \qquad (13)$$

where individual measurement variables and their fractional errors are:

| | |
|---|---|
| Power ratio $\Phi$ | 0.12 |
| Group velocity $v_g$ | 0.014 |
| Phase index $n_1$ | 0.02 |
| Pulse width W | 0.03 |
| Rayleigh scattering $\sigma_s$ | 0.10 |

The quantities $\Delta x_n$ (for $\Phi$, W, $\sigma_s$) represent one sigma calculated values. The systematics $\Delta y_n$ (for $n_1$, $v_g$) are best estimates for the limits of error. We have then, from eq (15) $\Delta F/F = 0.19$. This number was used to calculate the tabulated uncertainties appearing in table 2.

### 4.3.7 Significance of Mode Strippers

Since Rayleigh scattering is approximately isotropic, it is possible for some of the rays emerging from the scattering centers on the fiber axis to be captured by the cladding. If the index of refraction of the surrounding medium is smaller than the cladding, rays may be refracted at the air-cladding interface and trapped in the backward direction. This will increase the effective capture fractions. Stone [24] has analyzed this problem and found that the one-way capture fraction $F_c$ for a bare cladding in air is

$$F_c = \frac{1}{2}\left[1 - \frac{3}{4}\left(\frac{1}{n_1} - \frac{1}{3n_1^3}\right)\right] \qquad (14)$$

This quantity is, rather surprisingly, independent of the cladding index of refraction and fiber diameter. The numerical value of $F_c$ can be rather large; for example, for a core index of 1.45, the value of $F_c$ is approximately 0.20 or a factor of approximately 100 larger than a mode-stripped fiber which has no backscattered power propagating in the cladding.

We have conducted an experiment to determine the importance of mode strippers on the backscattered signal. This was done by replacing the usual launcher described in section 2.6 by a holder that contained no index matching fluid. The backscatter signal was recorded by observation on the oscilloscope. A section of fiber close to the launching end was then placed on a mode stripper consisting of 12 cm of felt which was saturated with an oil having index greater than $n_2$. A weight placed on the fiber insured good optical contact with the oil. The backscatter signal was again recorded. For most of the fibers there was no perceptible change in backscatter signal. The maximum observed change represented a 12 percent drop in signal with application of the mode stripper.

These results indicate that, at least for the fibers tested here, there is a negligible amount of backscattered power propagating in the cladding. There are two possible reasons for this. The loss of the cladding is usually very high (100 dB/km) so that the radiation in the cladding is rapidly attenuated. This is particularly true for the Inside Vapor Phase Oxidation (IVPO) process where the soot is deposited on the inside of a lossy silica tube. For other manufacturing processes, for example the Outside Vapor Phase Oxidation (OVPO), the

cladding may not be as lossy. Secondly, if the fiber is in contact with a jacket, coating, or other material of index greater than $n_2$, the rays in the cladding will escape into the surrounding medium. We conclude then, for the fibers we have tested from three different manufacturers, mode strippers do not have a significant effect on backscatter signal levels or capture fraction determinations.

### 4.3.8 Discussion

We see from the capture fraction results in table 2 that slightly over one half the experimental F values do not have limits of error that bracket the values predicted from simple theory. The experimental values are consistantly low. We feel that the experimental determinations of capture fractions described here represent a realistic approach to the measurement of these physical quantities and that the low values are real. This conclusion implies that there are deficiencies in the theoretical model we have used, at least as it applies to certain fiber configurations. Neumann [4] has discussed some of the approximations and physical effects which have been neglected in the derivation of eqs (7) and (8). The presence of leaky modes, mode selective attenuation, variations in the fiber material as a function of length, variations in scattering as a function of fiber radius and changes in modal energy distributions could all effect the simple theoretical predictions.

Pending independent F measurements by other investigators, we tentatively conclude that the magnitude of the capture fraction as given by eqs (7) and (8) may yield excessively large values in some fibers. The discrepancies are largest for the step-index fibers which we tested.

## 4.4 Length Determination and Fault Location

The OTDR also yields a quick estimate of the length of the fiber L from time-of-flight measurements. This distance is determined from observations of the time interval between Fresnel reflections at the front and far ends of the fiber according to the relation

$$L = \frac{cT}{2N}, \tag{15}$$

where T is the time interval, c the velocity of light, and N the group index of the fiber. In order to measure time intervals with precision, it is necessary to have a source capable of emitting a fast-risetime pulse. Measurement accuracy requires a knowledge of the group index N. This information may be available from manufacturers. Experimentally, group velocities, c/N, can be fixed for a short sample of a given fiber, by means of a shuttle-pulse technique with a precision of about 0.1 percent and accuracies of approximately 0.2 percent [48]. A more convenient, though less accurate, method of estimating L from backscatter scans is by assuming a representative value of N for use in eq (17). We will now examine a possible way of accomplishing this.

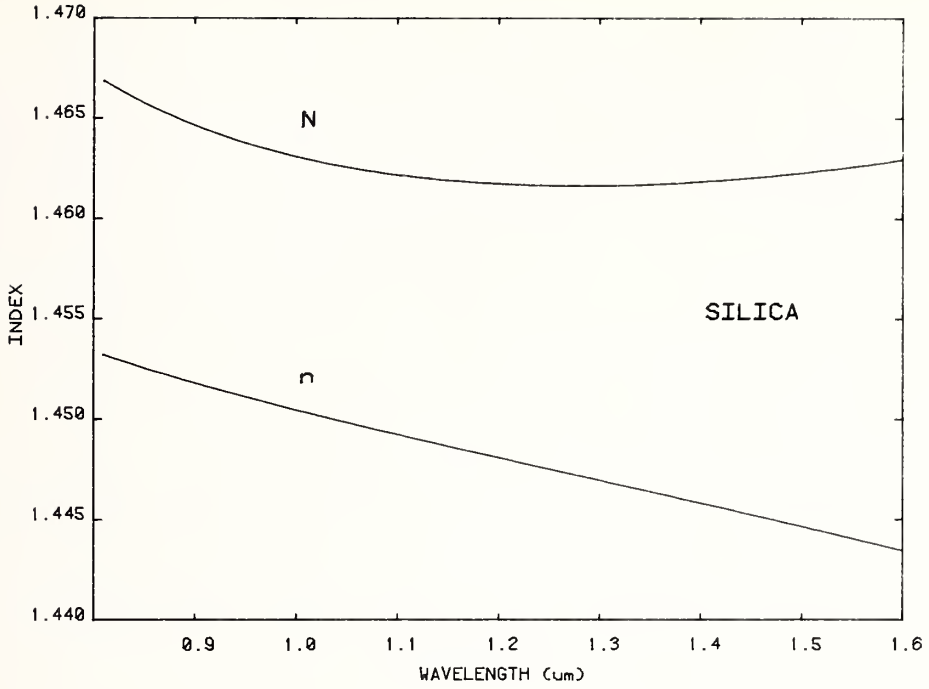


Figure 27. Index of refraction and group index for silica.

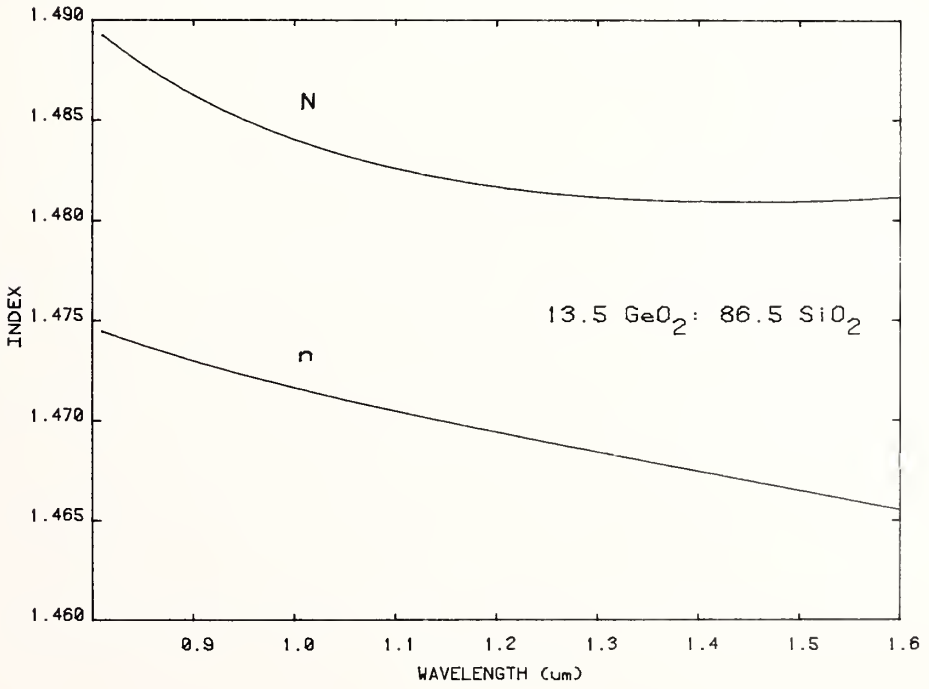


Figure 28. Index of refraction and group index for 13.5 $GeO_2$:86.5 $SiO_2$ glass.

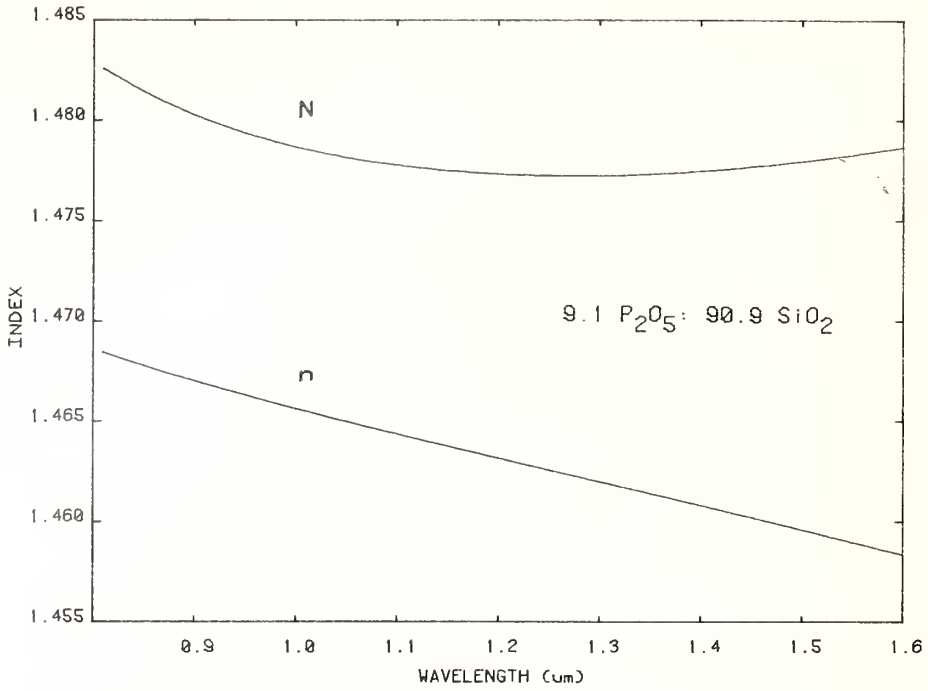


Figure 29. Index of refraction and group index for 9.1 $P_2O_5$:90.9 $SiO_2$ glass.

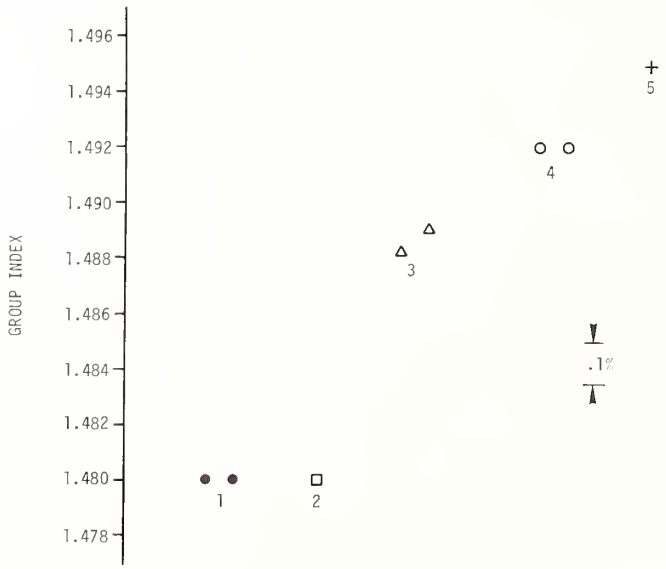


Figure 30. Group index measurements for five commercial fibers. Measurements on on three fibers repeated to within 0.1 percent. From Franzen and Day [48].

The value of N can be calculated from the equation

$$N = n_1 - \lambda \frac{dn_1}{d\lambda} \tag{16}$$

if the wavelength dependence of the index of refraction is known. The required dispersion data for silica and a number of doped silica glasses used in optical fibers has been tabulated by Malitson [49], and Fleming [50,51]. The dispersion information may be expressed as a three-term Sellmeier relationship of the form

$$n_1^2 = 1 + \frac{a_1\lambda^2}{\lambda^2 - b_1^2} + \frac{a_2\lambda^2}{\lambda^2 - b_2^2} + \frac{a_3\lambda^2}{\lambda^2 - b_3^2} \tag{17}$$

where the coefficients a are related to the material oscillator strength, and b the corresponding oscillator wavelengths. We have calculated N and $n_1$ as a function of wavelength for three typical fiber materials using the data of Fleming and eqs (15) and (16); these appear in figures 27, 28 and 29. For our purposes we will assume that the 13.5 $GeO_2$:86.5 $SiO_2$ sample represents a fairly typical on-axis material for a high-bandwidth telecommunicaions fiber.

Some experimental values of N at 824 nm have been reported by Franzen [48] for a number of high-bandwidth graded-index fibers. These are reproduced in figure 30. It can be seen that they are consistent with the above approximation scheme.

We have been concerned above with fiber length measurements. The same considerations also apply to fault location.

## 5. MEASUREMENTS WITH PERTURBED FIBERS

In this section we will consider the effect that various local perturbations have on the backscatter response of an otherwise uniform and reciprocal fiber. These perturbations may be either extrinsic, for example bends, or intrinsic, for example an impurity region of high loss in the fiber. We will refer to the characteristic backscatter features as "fault signatures" which generate a change in the background Rayleigh response. It will be convenient to divide the signal returns into two categories which will be referred to as absorption-like and scatter-like fault signatures. The distinction is made clear from an examination of the computer-generated plots shown in figures 31 and 32. Scatter-like signatures are defined as those which have an increase in backscatter signal larger than the associated decrease (fig. 31). Likewise figure 32 illustrates an absorption-like signature, from which defect loss may be inferred as shown. The most general form of fault signature is a combination of both (fig. 33). It should be noted that there is always some absorption associated with scatter-like signatures, even though this can be rather small. Also the decrease in backscatter power on a decibel scale is twice the actual fault loss.

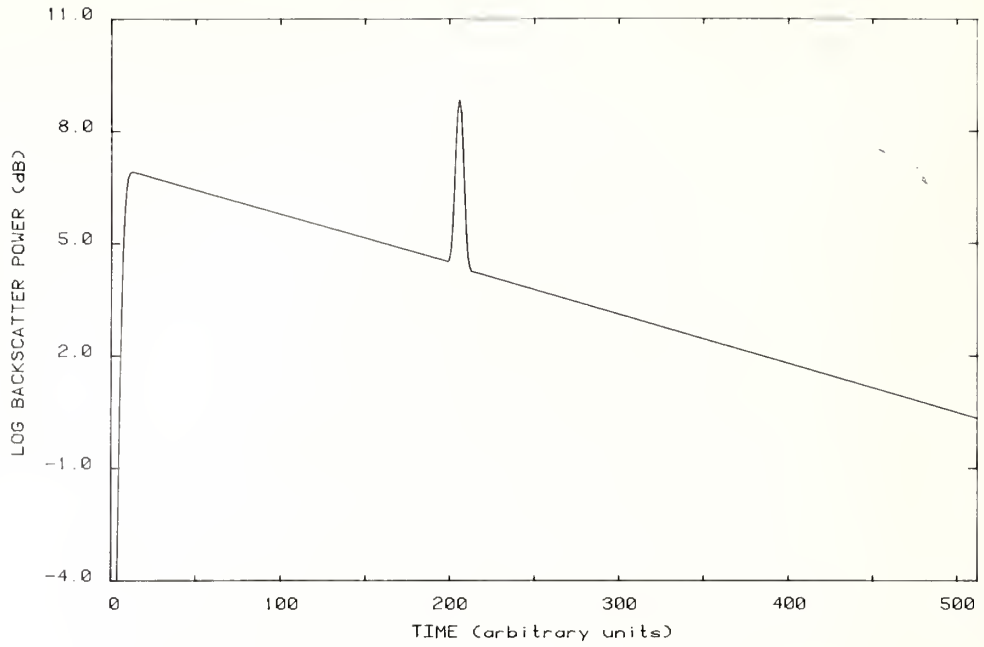


Figure 31. Example of a scatter-like fault signature. Gaussian probe pulse.

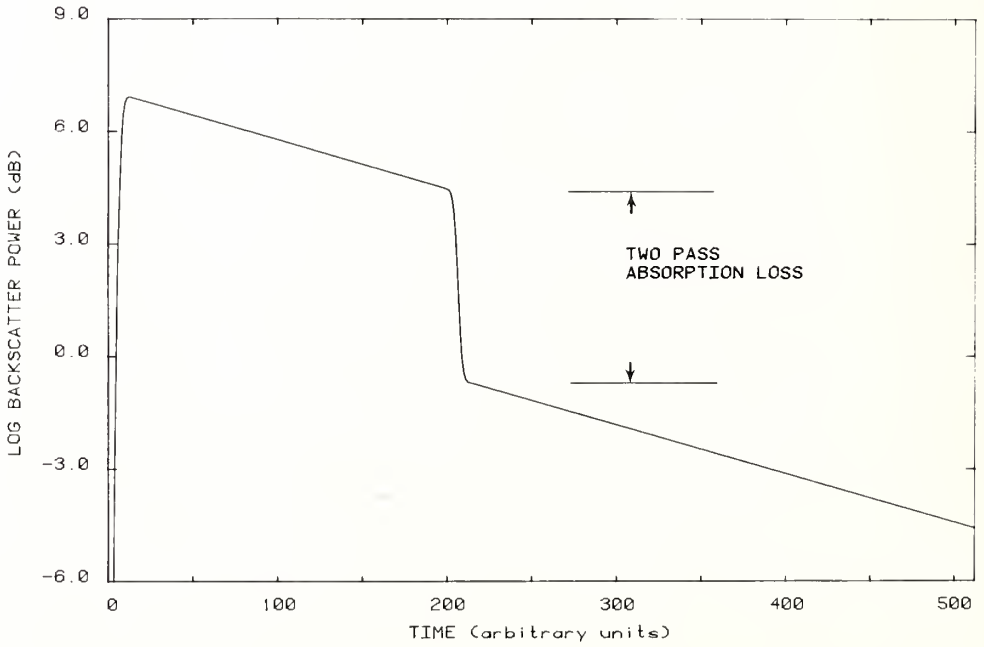


Figure 32. Example of an absorption-like fault signature. Gaussian probe pulse.

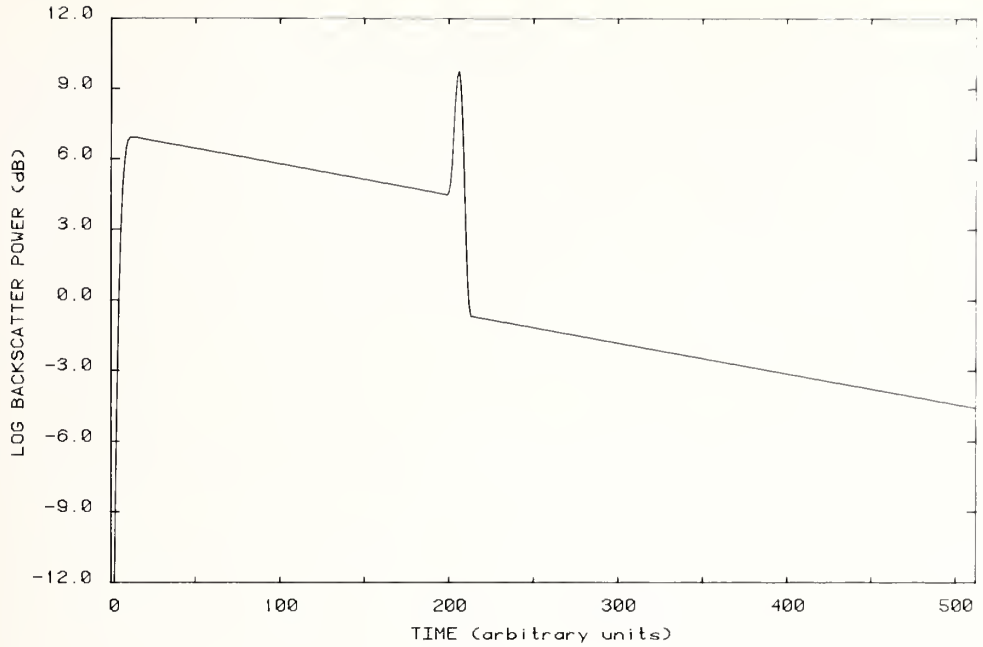


Figure 33. Example of a composite fault signature consisting of both scattering and absorption loss. Gaussian probe pulse.

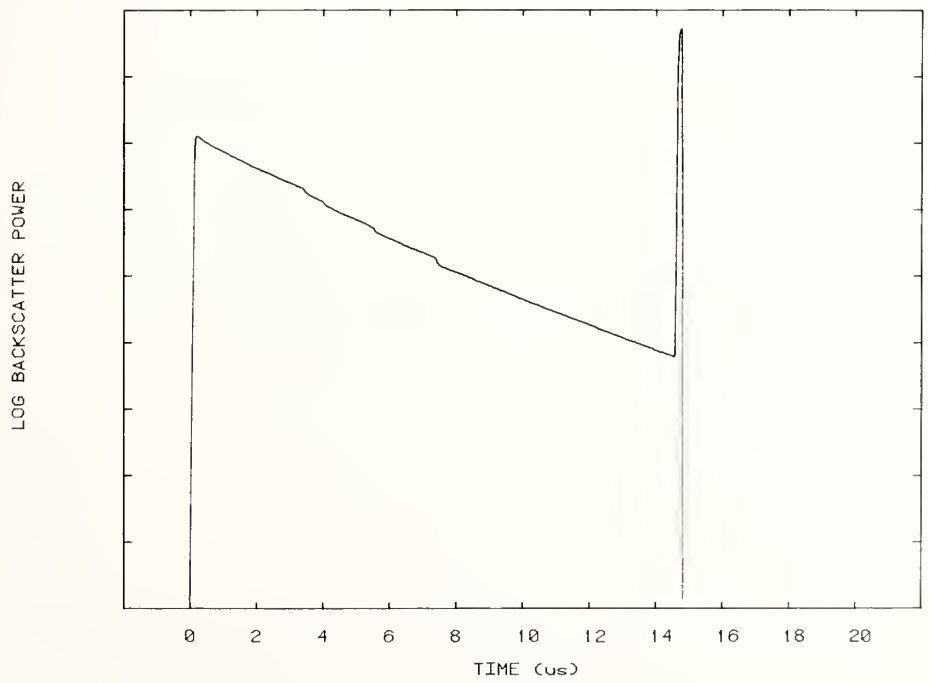


Figure 34. Backscatter signature for a graded-index fiber with a fusion splice at the midpoint. The three other irregularities are unidentified. Fiber J.

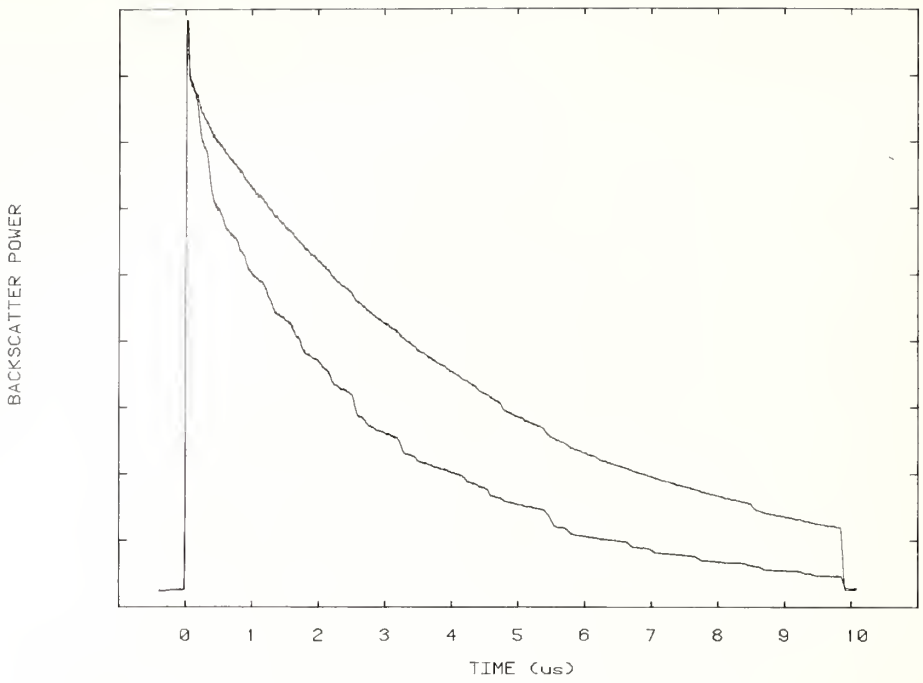


Figure 35. Backscatter signatures resulting from a microbending experiment (see text). Lower curve exhibits effect of pressure-induced microbending. Upper curve represents the response in the relaxed state. Fiber K.

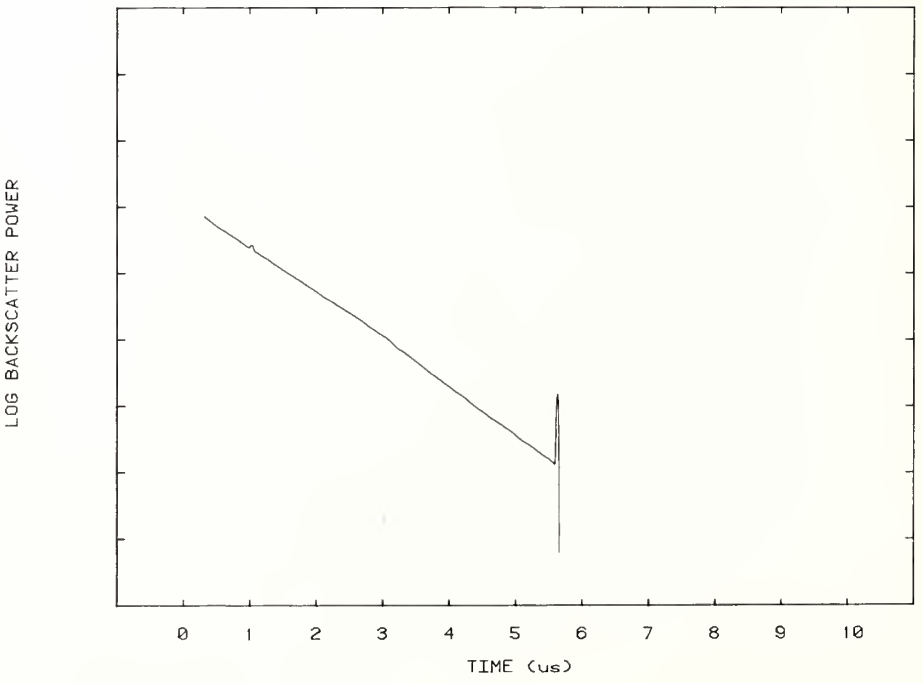


Figure 36. Backscatter signature for a fiber wrapped on drums of differing diameter. The input half of the fiber is wound on a drum of diameter 30 cm, the output half of the fiber is wound on a drum of 10 cm diameter. Fiber H.

## 5.1 Absorption-Like Signatures

Absorption-like fault signatures are produced by perturbations which convert the radiation in the probe pulse into heat energy, or by perturbations which scatter the radiation exclusively in the forward direction. Figure 34 shows the absorption-like fault signature for a fusion splice which exists at the center of the fiber. The one-way loss is approximately 0.18 dB at the splice. The cause of the other irregularities which can be seen, has not been identified. Fusion splices are known to weaken the fiber, and the backscatter technique is the only practical means of detecting the presence of these flaws once the fiber is cabled.

Microbending signatures are also absorption-like. The capture fraction associated with radiation loss due to microbending was estimated in the following experiment. We wound a 1 km graded-index fiber loosely in several layers on a felt-covered, 20 cm diameter drum. Ten plastic rods, each 6 mm in diameter, were positioned transverse to the winding. Lateral pressure was applied to the layers of fiber by pressing them against the rods using an adjustable strap concentric to the drum. The effect on the fiber is shown in figure 35. The lower curve represents the backscatter response with tension applied to the strap. Increased loss (about 3.1 dB total) occurs at locations where the rods were in contact with the fiber. The upper curve represents the response when the tension was removed. Some residual stress effects can still be observed. It will be noted that, in the stressed state the backscatter signal is a monotonically decreasing function of time. This implies that the capture fraction associated with the removed radiation is very small. A more quantitative estimate of the microbending capture fraction $F_n$ may be obtained from a comparison of the two backscatter scans at t=0. From eq (1), the backscatter power in the stressed state differs from the corresponding power in the unstressed state only in the term $\alpha_n F_n$. Then, assuming the excess loss in figure 35 is a uniformly distributed radiation loss, $\alpha_n$ is about $7 \times 10^{-4}$ $m^{-1}$, about the same as $\alpha_s$. However, the stressed t = 0 signal does not increase within an uncertainty of about one percent. This implies that $F_n < 0.01\ \alpha_s F_s/\alpha_n$, or $F_n < 5 \times 10^{-5}$. This is the basis of the estimate given in table 2.

A third example of an absorption-like signature is given by the effect of radiation from fiber bends. The magnitude of the capture fraction associated with macrobending of this sort was inferred from the following experiment. A graded-index fiber, which was loosely cabled in a plastic tube, was wound on drums of different diameters. Figure 36 shows the resulting signature when the input half of the 570 m cable was wrapped on a drum of 30 cm diameter and the remaining cable wrapped on a drum of 10 cm diameter. There is a small change in slope at the midpoint which implies an excess loss of about 0.9 dB/km. Most of this loss can be attributed to radiation whih is emitted as a result of the decreased bend radius. Figure 37 is a similar scan where the final 40 m of the cable is wound on the smaller drum, and a change in slope is also apparent. To obtain an upper limit on the macrobending capture fraction we modeled the backscattering process on a computer using the

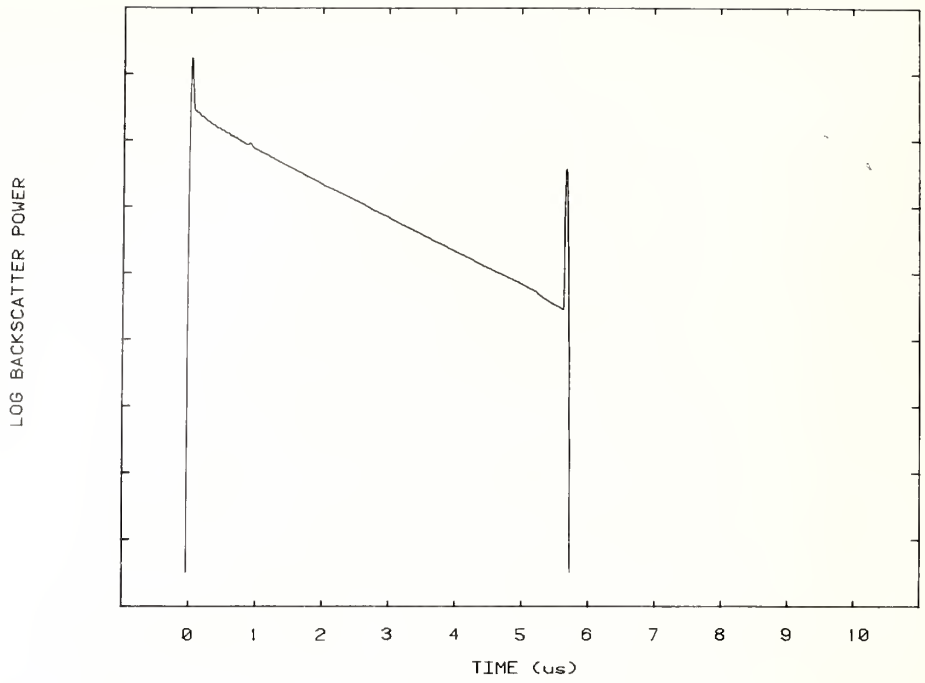


Figure 37. Backscatter signature under conditions similar to figure 36, except the final 7 percent of the fiber is on the smaller drum. Fiber H.

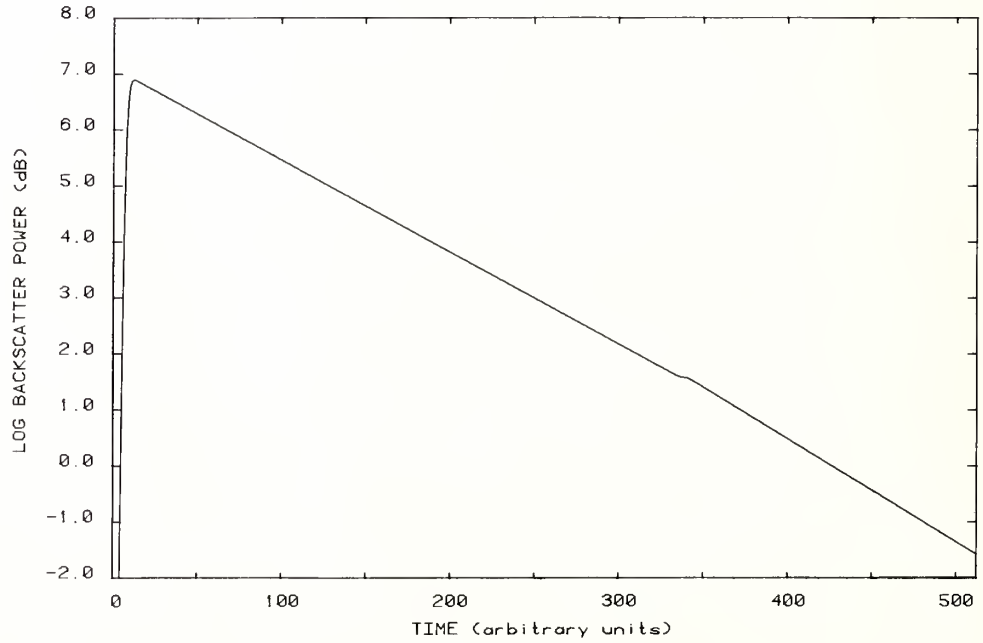


Figure 38. Computer simulation of radiation loss with an excess F value of 0.0006, other parameters similar to fiber H. Excess radiation loss begins at time 345.

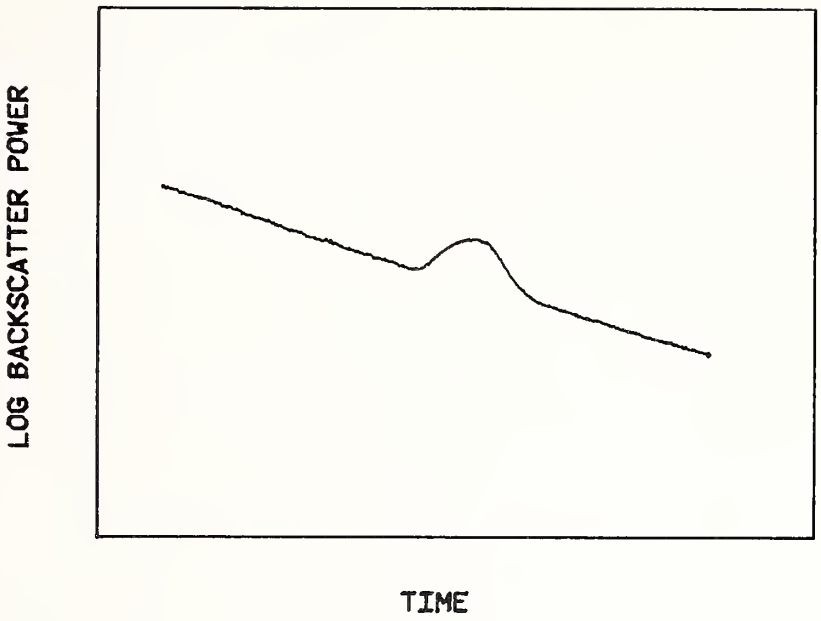


Figure 39. Fault signature for a bubble in a graded-index fiber. This is an expanded scale of figure 4. Fiber H.

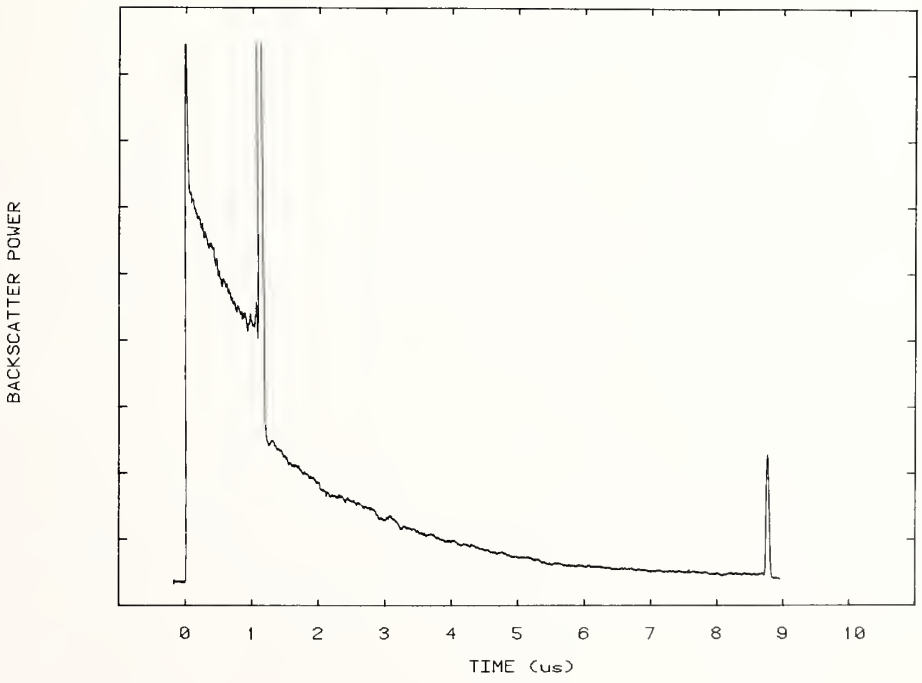


Figure 40. Signature for a commercial coupler. The scatter signal at 1.2 μs is off scale. Fiber E.

known parameters for fiber H, and assuming a value of $F_n$ which was judged to produce a barely perceptible change in the backscatter signature. If the observed increase in radiation loss had one photon in 1700 returned in the backward direction, the signature would appear as in figure 38. The backscatter response in this case exhibits a signal increase at the location corresponding to the junction of the two drums. Since no such signal can be detected experimentally, we conclude that, for this fiber, $F_n < 0.0006$. This result is also given in table 2.

### 5.2 Scatter-Like Signatures

We have seen previously, in figures 2 to 4, an example of a localized scatter-like fault signature. The scan is also reproduced in figure 39 on an expanded scale. The magnitude of the feature depends somewhat on the launching spot size and its location on the input face of the fiber. It is possible to observe a small decrease in the slope of the log backscatter signal following the fault. This could possibly be explained by a redistribution of probe pulse energy into less-lossy modes. The most likely explanation for the origin of the fault is an elongated bubble or dielectric filament of the type described by Rawson [52].

Figure 40 represents the scatter-like signature due to a commercial coupler which joins two identical step-index fibers. The signal at the junction interface is off scale. The one-way loss at the connector is about 1.4 dB. This represents a rather extreme example of a scatter-like signature.

## 6. COMPUTER SIMULATIONS

One of the main motivations for the experimental determination of backscatter parameters is to obtain a realistic data base for purposes of computer modeling. The actual backscatter display signatures can represent a rather complex interaction of many variables. For example, the Rayleigh as well as fault signatures will depend on absorption loss, scattering loss, capture fractions, input pulse shape, input pulse duration, wavelength, SNR, type of backscatter display (direct, logarithmic, differential logarithmic), fiber type (single mode, multimode) and the spatial distribution of any perturbations along the length of the fiber. Computer generated displays which can independently vary these parameters can greatly assist in interpreting and understanding experimental signatures. Also, we may be led to a preferred display scheme for backscatter signatures.

Some of these computer-generated signatures have appeared in this report. A much more comprehensive atlas of backscatter signatures is in preparation for a future report in this series.

## 7. CONCLUSIONS

We have described a laboratory OTDR in some detail, indicated its potentialities and limitations, and suggested ways in which the SNR may be improved. We have also described experimental techniques for estimating fiber Rayleigh scattering, capture fractions, and group velocities. The OTDR system was used to examine the backscatter signatures of a number of fibers and fiber perturbations. Some of the main conclusions from the experimental work may be summarized as follows:

1. Fibers from some manufacturers exhibit much smaller irregularities in background backscatter than similar type fibers from other manufacturers. These signal variations are probably due to diameter fluctuations. It is much easier to observe a perturbation or fault signature on a uniform background. Therefore, in some applications, for example secure communications, it may be desirable for military agencies to specify tolerances on the oscillatory swings in the Rayleigh backscatter signature.
2. Measured capture fractions were often smaller than predicted from simple theoretical considerations. There was a large variability in the agreement of theory and experiment from fiber to fiber. The reason for this is not fully understood, but is believed to be related to the oversimplified nature of the formulae used to predict $F_s$ values.
3. The presence of a mode stripper does not alter the backscatter signal level appreciably in the fibers we have tested. This experience may not apply to fibers manufactured with low-loss cladding materials.
4. Many types of defects and anomalies can be observed with backscatter techniques. We have classified the observed backscatter features as absorption-like and scatter-like signatures. Among the former are those due to good fusion splices, microbending, and macrobending. Among the latter are those due to some couplers, dielectric filaments, gross fractures, and breaks.
5. Upper limits have been placed on the capture fractions due to macrobending and microbending in sample fibers (table 2). The small values are due to the fact that the radiation associated with these processes is largely scattered in the forward direction.

## 8. REFERENCES


[1] Barnoski, M. K.; Jensen, S. M. Fiber waveguides: A novel technique for investigating attenuation characteristics. Appl. Opt. 15(9):2112-2115; September 1976.

[2] Personik, S. D. Photon probe--an optical time domain reflectometer. Bell Sys. Tech. J. 56(3):355-366; March 1977.

[3] Rourke, M. D. An overview of optical time domain reflectometry. Conference on the Physics of Fiber Optics; April 28-30, 1980; Chicago, IL.

[4] Neumann, E. G. Analysis of the backscattering method for testing optical fiber cables. AEU, Electron. and Commun. 34(4):157-160; 1980.

[5] Elion, G. R.; Elion, H. A. Fiber optics in communication systems. New York, NY: Marcel Dekker, Inc.; 1978. Chapter 3 lists specifications for laser diodes from several manufacturers.

[6] Certain trade names are used in this report in order to specify the experimental conditions used in obtaining the reported data. Mention of these products in no way constitutes endorsement of them. Other manufacturers may have products of equal or superior specifications.

[7] Riad, S. M. Optical fiber dispersion characterization study. NASA Final Report, Contract No. NAS10-9455; December 1979.

[8] Reference 5, chapter 4 lists a number of commercially available APDs along with device specifications and much useful information.

[9] Kaminow, I. R. Polarization in fibers. Laser Focus; June 1980. 80-84.

[10] Born, M.; Wolf, E. Principles of optics, Second edition. New York, NY: McMillan Co.; 1964. 39-40.

[11] Straus, J.; Few, I.; Conrad, J. Measurement of frequency dependence of Rayleigh backscattering in bidirectional optical systems. Electron. Lett. 15:306-307; 1979.

[12] Costa, B.; Sordo, B. Experimental study of optical fiber attenuation by a modified backscattering technique. Digest of the Third European Conference on Optical Communication; September 14-16, 1977; Munich, Germany. 69-71.

[13] Dakin, J. P.; Gambling, W. A.; Payne, D. N.; Sunak, H. R. D. Launching into glass-fiber optical waveguides. Opt. Commun. 4(5):354-357; January 1972.

[14] Wilmad Glass Co., Buena, NJ 08310.

[15] Reference 5, p. 172.

[16] Smith, R. G. Optical power handling capacity of low loss optical fibers as determined by stimulated Raman and Brillouin scattering. Appl. Opt. 11(11):2489-2494; November 1972.

[17] Crow, J. D. Power handling capacity of glass fiber lightguides. Appl. Opt. 13(3):467-468; March 1974.

[18] Danielson, B. L. An assessment of the backscatter technique as a means for estimating loss in optical waveguides. Nat. Bur. Stand. (U.S.) Tech. Note 1018; February 1980. 76.

[19] DiVita, P.; Rossi, U. Backscattering measurements in optical fibers: Separation of power decay from imperfection contribution. Electron. Lett. 15(15):467-469; July 1979.

[20] Bender, A.; Salisbury, G.; Akers, F. Concentric-core optical fiber, Paper THC4, Topical Meeting on Optical Fiber Communications, Technical Digest; Washington, DC; Mar. 6-8, 1979.

[21] DiVita, P.; Rossi, U. The backscattering technique: Its field of applicability in fibre diagnostics and attenuation measurements. Opt. Quantum Electron. 11:17-22; 1980.

[22] Olshansky, R. Propagation in glass optical waveguides. Rev. Mod. Phys. 51(2):341-367; April 1979.

[23] Olshansky, R.; Oaks, S. M. Differential mode attenuation measurements in graded-index fibers. Appl. Opt. 17(11):1830-1835; June 1978.

[24] Tynes, A. R. Integrating cube scattering detector. Appl. Opt. 9(12):2706-2710; December 1970.

[25] Ostermayer, F. W.; Benson, W. W. Integrating sphere for measuring scattering loss in optical fiber waveguides. Appl. Opt. 13(8):1900-1902; August 1974.

[26] Inada, K. A new graphical method relating to optical fiber attenuation. Opt. Commun. 19(3):437-439; December 1976.

[27] Yoshida, K.; Sentsui, S.; Shii, H.; Kurona, T. Optical fiber drawing and its influence on fiber loss. Paper D9-3, 1977 International Conference on Integrated Optics and Optical Fiber Communication; July 18-20, 1977; Tokyo, Japan.

[28] Blankenship, M. G.; Keck, D. B.; Levin, P. S.; Love, W. F.; Olshansky, P.; Sarkar, A.; Schultz, P. C.; Sheth, K. D.; Siegfried, R. W. High phosphorus containing $P_2O_5$-$GeO_2$-$SiO_2$ optical waveguide. Post-deadline paper PD3-1, Topical Meeting on Optical Fiber Communications, Technical Digest; March 6-8, 1979; Washington, DC.

[29] Miller, S. E.; Chynoweth, A. G., eds. Optical fiber telecommunications. New York, NY: Academic Press, 1979. 357.

[30] Midwinter, J. E. Optical fibers for transmission. New York, NY: John Wiley & Sons; 1979. 159.

[31] Lin, S.; Giallorenzi, T. G. Sensitivity analysis of the Sagnac-effect optical fiber ring interferometer. Appl. Opt. 18(6):915-931; March 1979.

[32] Rourke, M. D. Maximum achievable crosstalk isolation in full-duplex single strand fiber-optic systems. Opt. Commun. 25(1):40-42; April 1980.

[33] Wells, W. H. Crosstalk in a bidirectional optical fiber. Fiber and Integrated Optics 1(3):243-287; 1978.

[34] Stone, J. Measurement of Rayleigh scattering in liquids using optical fibers. Appl. Opt. 12(8):1824-1827.

[35] Dakin, J. P.; Gambling, W. A. Theory of scattering from the core of a multimode fiber waveguide. Opt. Commun. 10(2):195-199; February 1974.

[36] Neumann, E. G. Optical time domain reflectometer: Comment. Appl. Opt. 17(11):1675; June 1978.

[37] Gloge, D.; Smith, P. W.; Bisbee, D. L.; Chinnock, E. L. Optical fiber end preparation for low-loss splices. Bell Sys. Tech. J. 52(9):1579-1588; November 1973.

[38] Marcuse, D. Reflection losses from imperfectly broken fiber ends. Appl. Opt. 14(12):3016-3020; December 1975.

[39] Chesler, R. B.; Dabby, F. W. Simple testing methods give users a feel for cable parameters. Electronics. August 5, 1976. 90-92.

[40] Deane Carbide Products Inc., P.O. Box 118, Trevose, PA 19047.

[41] Gordon, K. S.; Rawson, E. G.; Nafarrate, A. B. Fiber-break testing by interferometry: A comparison of two breaking methods. Appl. Opt. 16(4):818-819; April 1977.

[42] Saunders, M. J. Torsion effects on fractured fiber ends. Appl. Opt. 18(10):1480-1481; May 1979.

[43] Reitz, P. R. A quality check for fiber end faces. Optical Spectra. December 1979. 39-40.

[44] Hanson, A. G.; Bloom, L. R.; Day, G. W.; Gallawa, R. L.; Grat, E. M.; Young, M. Optical waveguide communications glossary. NTIA Spec. Publ. NTIA-SP-79-4; September 1979.

[45] Franzen, D. L., private communication.

[46] Kim, E. M.; Franzen, D. L. Measurement of far-field and near-field radiation patterns from optical fibers. Nat. Bur. Stand. (U.S.) Tech. Note 1032; January 1981.

[47] Brinkmeyer, E. Backscattering in single-mode fibers. Electron. Lett. 16(9):329-330; April 1980.

[48] Franzen, D. L.; Day, G. W. Measurement of propagation constants related to material properties in high-bandwidth optical fibers. IEEE J. Quantum Electron. QE-15(12):1409-1414; December 1979.

[49] Malitson, I. H. Interspecimen comparison of the refractive index of fused silica. J. Opt. Soc. Am. 55(10):1205-1209; October 1965.

[50] Fleming, J. W. Material and mode dispersion in $GeO_2 \cdot B_2O_3 \cdot SiO_2$ glasses, J. Am. Ceram. Soc. 59(11/12):503-507; November/December 1976.

[51] Fleming, J. W. Material dispersion in lightguide glasses. Electron Lett. 14(11):326-328; May 1978.

[52] Rawson, E. G. Measurement of the angular distribution of light scattered from a glass fiber optical waveguide. Appl. Opt. 11(11):2477-2481; November 1972.

# Chapter 2

# Measurement of Optical Fiber Bandwidth in the Time Domain

**Douglas L. Franzen**
**G. W. Day**

A system is described for determining optical fiber bandwidth from time domain information. A measurement gives the optical fiber transfer function (or frequency response) relating the output waveform to the input. An analysis is given of the variables affecting the measurement. This includes a discussion of such input related topics as launching conditions, mode scramblers, and laser diode sources; output related topics include a discussion of optical detectors. Laser diodes are evaluated with respect to short pulse performance, near field emission, material dispersion limits, and other spectral behavior like chirping; detectors are evaluated with respect to time response, linearity, and uniformity. Overall system architecture, precision, and dynamic range are discussed. A number of bandwidth related topics are briefly presented and typical experimental results given. This includes examples of: mode mixing via microbending, profile compensation, profile dispersion, intramodal broadening, material dispersion constants, relative magnitude-phase behavior, and Gaussian predictions of frequency response.

## CONTENTS

## 1. INTRODUCTION

Attenuation and bandwidth are the important parameters used to describe the propagation characteristics of optical fiber waveguides. Measurement practices with regard to these parameters continue to evolve as accumulated practical experience and the efforts of standards groups lead toward uniformly accepted procedures. This chapter describes the design and capabilities of a fiber measurement system used at the National Bureau of Standards. This system is perhaps representative of current practice in the industry and many of the present techniques and methods will be relevant to future systems. The emphasis is on the bandwidth measurement of multimode, silica, telecommunications-type fibers over the 0.8 to 0.9 μm wavelength region. Much of the discussion is general and can be applied to most optical fiber bandwidth measurement systems.

## 2. BANDWIDTH CONSIDERATIONS IN OPTICAL FIBERS

### 2.1 Pulse Broadening in Optical Fibers

Bandwidth is related to the information carrying capacity of a fiber and includes the various sources of signal distortion. In multimode optical fibers, differences in mode group velocity result in pulse broadening or spreading; i.e., different modes arrive at the output at different times. This is commonly called "intermodal" broadening, and in multimode fibers is often the most significant bandwidth limitation [1]. Due to coupling between modes, the intermodal broadening of multimode fibers does not necessarily scale linearily with fiber length. In fact, a square root dependence is observed in cases of strong mode coupling [2].

Other sources of pulse broadening affect all of the fiber modes together. This contribution to pulse broadening is commonly called "intramodal" broadening [1]. While different modes are affected in different amounts, it is often useful to think of an average intramodal term to describe a given fiber. Intramodal broadening is directly proportional to source linewidth and arises because different spectral components of the source travel with different velocities. Intramodal broadening results from both material and waveguide dispersion. Material dispersion is related to the optical properties of the fiber core material, in particular, to the second derivative of the refractive index with respect to wavelength. Waveguide dispersion is related to the physical dimensions of the core, to the index profile, and to wavelength. Because of the dependence of intramodal broadening on source linewidth, some authors have chosen the terms "monochromatic" and "chromatic" to distinguish intermodal and intramodal effects. Presently, there is no standard terminology to describe the various contributions to pulse broadening. Perhaps this is because in a strict mathematical sense the terms cannot be clearly separated.

The concept of rms pulse broadening is useful in describing the time domain behavior of pulse propagation in optical fibers [1]. The rms duration $\sigma$, of a waveform $p(t)$ is given by

$$\sigma = \left[ \int_{-\infty}^{+\infty} p(t)(t-T_0)^2 \, dt \right]^{1/2}, \tag{1}$$

where p(t) is normalized according to

$$\int_{-\infty}^{+\infty} p(t)dt = 1, \tag{2}$$

and $T_0$ is the central time given by

$$T_0 = \int_{-\infty}^{+\infty} tp(t)dt. \tag{3}$$

The rms pulse duration of the fiber impulse response, $\sigma_T$, for a fiber with input and output waveforms $p_1(t)$ and $p_2(t)$, respectively, is

$$\sigma_T = \sqrt{\sigma_2^2 - \sigma_1^2}, \tag{4}$$

where $\sigma_1$ and $\sigma_2$ are the corresponding rms values for the input and output waveforms. In practice, rms pulse broadening is difficult to implement because low-level values near the baseline receive a large weighting in eq (1). The total rms broadening, $\sigma_T$, for a fiber can also be expressed in terms of the inter and intramodal contributions by

$$\sigma_T^2 = \sigma^2_{\text{intermodal}} + \sigma^2_{\text{intramodal}}, \tag{5}$$

where $\sigma_{\text{intermodal}}$ and $\sigma_{\text{intramodal}}$ represent the rms broadenings due to the individual components.

When intramodal broadening is dominated by material dispersion, the term is given by

$$\sigma_{\text{intramodal}} = \frac{\lambda}{c} \frac{d^2n}{d\lambda^2} \sigma_s L, \tag{6}$$

where n is the on-axis refractive index of the core, $\sigma_s$ is the rms value for the spectral lineshape of the source, and L the length of the fiber. In the 0.8 to 0.9 μm wavelength range, the intramodal term is dominated by material dispersion and, for silica fibers, the waveguide dispersion does not become important until the wavelength is longer than approximately 1.1 μm.

In general, the importance of the various contributions to measured fiber bandwidth depends on the type of fiber, wavelength, and source linewidth. For laser diode sources and multimode silica fibers in the 0.8 to 0.9 μm wavelength region, the intermodal term usually dominates. As the bandwidth approaches multi-GHz-km values, however, the material dispersion term becomes more important.

## 2.2 The Transfer Function

The rms pulse broadening concept was widely used in early fiber work. Specifications are now generally based on the transfer function. In this approach, which is analogous to conventional linear network analysis, the fiber is described by a transfer function, which is assumed to be linear in optical power; i.e., if $p_1(t)$ is the input optical power as a function of time averaged over many optical periods, $p_2(t)$ is the output similarly averaged, and $P_1(f)$ and $P_2(f)$ the corresponding Fourier transforms, then the output is related to the input by

$$P_2(f) = H(f)P_1(f), \tag{7}$$

where H(f) is the transfer function or frequency response in baseband frequency f describing the fiber. In general, the quantities in eq (7) are complex, and the transfer function can be written in polar form as

$$H(f) = M(f)e^{i\phi(f)} \tag{8}$$

with M(f) and $\phi(f)$ being real functions of frequency f.

The validity of eq (7) has been examined by others [3], [4]. Theoretical work shows that it is valid as long as the source is sufficiently incoherent; i.e., if frequency width of $P_1(f)$ is much less than the linewidth of the source. No actual experiments have been performed to check the range of validity of eq (7) in this respect. As practical sources like laser diodes become more coherent [5], the question becomes more than academic.

If eq (7) holds, conventional linear system analysis can be used. In this work, the bandwidth is determined by measuring M(f), the magnitude of the transfer function and, $\phi(f)$ the phase response, from ratios of the fast Fourier transform of output and input waveforms. Alternatively, the bandwidth could be completely specified by giving the impulse response which is just the inverse transform of H(f). Algorithms exist to accomplish this calculation if it is desired.

It is useful to derive relationships assuming Gaussian shapes for the input pulse and fiber frequency response. We shall see later (section 6.3) that this is an acceptable approximation for some fibers. Since the Gaussian shape is invariant under Fourier

transformation, simple relationships result. If the input $p_1(t)$ and output $p_2(t)$ are given by

$$p_1(t) = e^{-4\ell n2(t/\tau_1)^2}, \tag{9}$$

and

$$p_2(t) = e^{-4\ell n2(t/\tau_2)^2} \tag{10}$$

which are Gaussians having a FDHM (Full Duration at Half Maximum) of $\tau_1$ and $\tau_2$, respectively, then the fiber frequency response is also Gaussian with the 3 dB roll-off frequency given by

$$f_{3dB} = \frac{0.44}{\sqrt{\tau_2^2 - \tau_1^2}} \tag{11}$$

$$= \frac{0.44}{\tau_T}. \tag{12}$$

where $\tau_T$ is the half width broadening of the fiber. Also, the rms pulse duration for a Gaussian is a simple expression with

$$\sigma_1 = 0.43 \ \tau_1 \tag{13}$$

and

$$\sigma_2 = 0.43 \ \tau_2. \tag{14}$$

Using eq (13) with eq (11), an expression can be found relating the 3 dB frequency of the transfer function, $f_{3dB}$, to the rms pulse broadening, $\sigma_T$, for the fiber with

$$f_{3dB} \ \sigma_T = 0.19. \tag{15}$$

## 2.3 Important Parameters Affecting Bandwidth Measurements

Precision of fiber bandwidth measurements can be quite good for repeated measurements with the same system (e.g., section 5.1). However, certain parameters can vary among systems to cause rather large measurement discrepancies or offsets. These parameters include launching conditions, receiving conditions, and source spectral properties. Other factors representing the limitation of commercial equipment, such as sampling oscilloscope time base nonlinearity, sampling head aberration, etc. are important, but not as significant as the former problems.

Launching conditions are particularly important, because in multimode fibers the modes exhibit differential delay and attenuation. Thus the output pulse shape depends on the specific modes excited at the input (see section 3.3). Nearly as significant as the launching conditions are the receiving conditions which determine how the modes are differentially detected (see section 3.2.4).

Source spectral properties influence the measured bandwidth via intramodal broadening (material dispersion). For normally encountered laser diode linewidths, at wavelengths of 800 to 900 nm, this does not become important until the fiber bandwidth exceeds 1 GHz/km (see sections 3.1.4 and 5.3). Measurements on high bandwidth fibers will therefore reflect the varability commonly encountered in laser diode linewidths.

## 3. DESCRIPTION OF MEASUREMENT SYSTEM

### 3.1 Laser Diode Sources

#### 3.1.1 Short-Pulse Performance

Laser diodes are the most commonly used sources for optical fiber bandwidth measurements. They are relatively inexpensive, compact, and usually sufficiently incoherent to satisfy the transfer function validity requirement. Moreover, pulses that are much shorter than the electrical driving current pulses can be generated at repetition rates useful for sampling oscilloscopes. This "Q-switching" behavior is still poorly understood but is believed to be related to a saturable absorption or self-relaxation oscillation in the optical cavity of the laser diode.

Gloge and other early workers generated short pulses from GaAs single heterojunction laser diodes by using mercury wetted reed relays to switch charged transmission lines [6,7]. In this manner, pulses of 100 ps FDHM were produced at repetition rates of a few hundred hertz. Transistors operating in the avalanche mode can also be used as fast switches [8,9,10]. Andrews describes a useful avalanche transistor circuit for switching a charged transmission line to produce 110 ps FDHM pulses from a GaAs laser diode [9]. Dannwolf et al. report a similar circuit with a ceramic chip capacitor as the energy storage element that produced pulses of 190 ps FDHM [10].

Compared to mercury wetted relays, avalanche transistors have the advantage of high repetition rate and external trigger capability. In the present study, avalanche transistor switching circuits using both silver mica capacitors and transmission lines as the energy storage element were examined. Transmission lines were found to be preferable producing slightly narrower pulses with less tendency toward multiple pulsing.

The circuit, using five miniature coaxial cables (RG-174U), is shown in figure 1. When a single cable is switched across a low impedance, the current delivered is approximately $\Delta V/R$, where R is the cable characteristic impedance and $\Delta V$ the voltage swing available from the avalanche transistor. With an R of 50 $\Omega$, a $\Delta V$ of 150 V, the current delivered is 3 A. Thus, five cables are necessary to supply up to 15 A to a diode. Two different avalanche

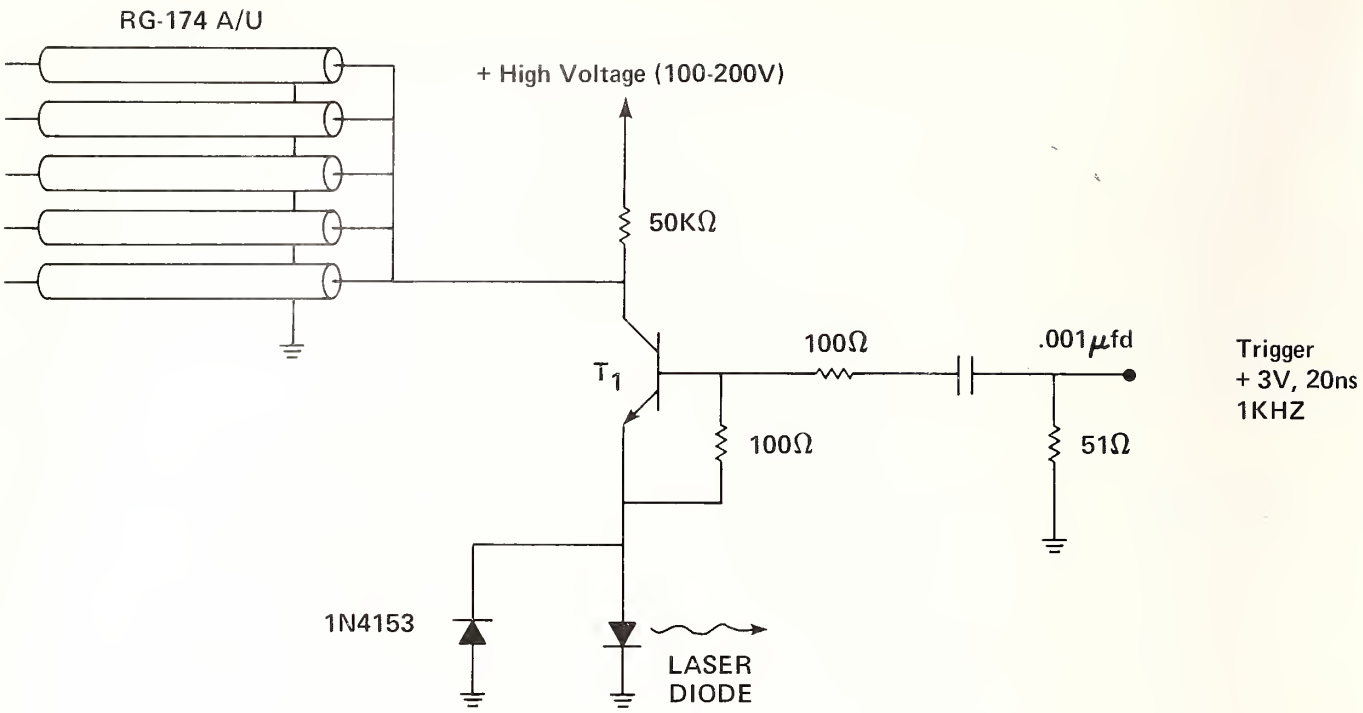


Figure 1. Circuit for pulsing GaAlAs and GaAs single heterojunction laser diodes.

transistors were used, a 2N3700 for high ΔV and a 2N3904 for lower ΔV. The only other circuit element requiring explanation is the diode shunting the laser diode which is intended to protect it from excessive reverse bias. The whole circuit, except for cables, is packaged in a 3 x 3 x 6 cm instrument box.

The repetition rate was arbitrarily limited to 1 kHz. While these circuits may be operated at several tens of kilohertz, the lower repetition rate was chosen to guard against diode aging. Several diodes have been in routine operation for over one year and no circuit failures or changes in pulse shape, threshold, jitter, wavelength, etc. have been observed.

The main factor affecting short-pulse performance is the choice of a specific laser diode; significant differences are observed among diodes of the same type and manufacturer. The objective in short pulsing is to drive the diodes sufficiently far above threshold without generating multiple pulses. Shortest pulses and least tendency toward multiple pulsing were achieved by operating near the maximum voltage for a particular transistor and with cable lengths short enough to obtain a single pulse.

Four diodes selected from a large number of RCA C30012 (GaAlAs), Laser Diode LA-63 (GaAlAs), and RCA SG2001 (GaAs) single heterojunction diodes [11] were chosen to cover the 0.8 to 0.9 μm wavelength region. These diodes had wavelengths of 803, 824, 866, and 902 nm.

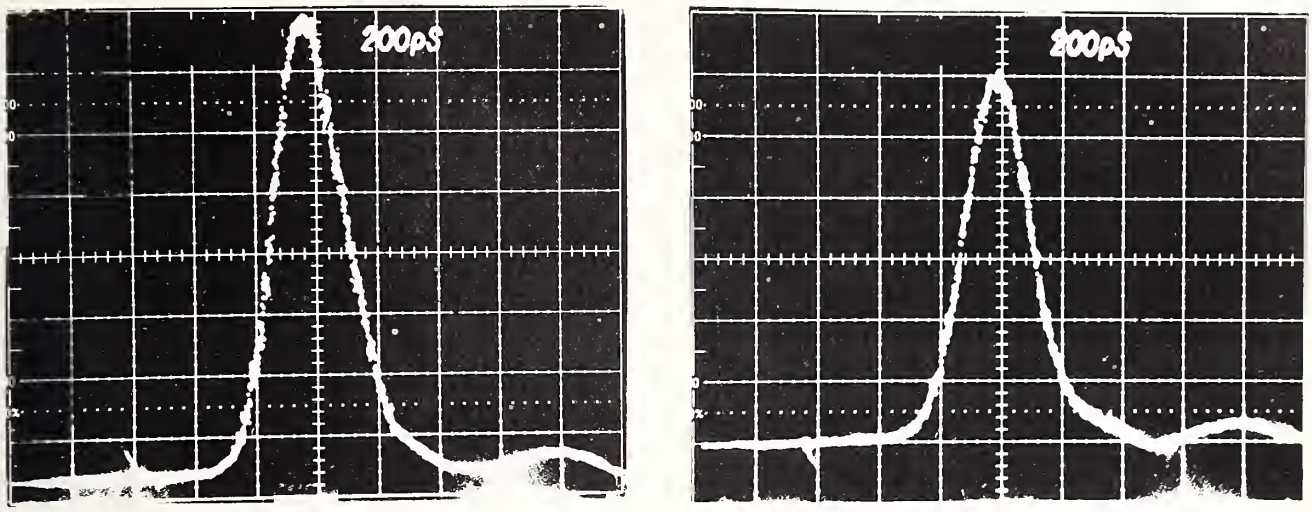


(a) (b)

Figure 2. Typical pulses from single heterojunction laser diodes, 200 ps per division, (a) 824 nm GaAlAs diode, (b) 902 nm GaAs diode.

A typical pulse shape is shown in figure 2 and consists of a nearly Gaussian-shaped main pulse of nominally 250 ps FDHM followed by a tail at 5 to 10 percent of the peak level. Table 1 gives the tabulated performance for all of the diodes. The frequency spectrum of the pulse is of prime importance; figure 3 shows a typical Fourier transform of one of the diode pulses. In obtaining this data, a delay line was used with the sampling

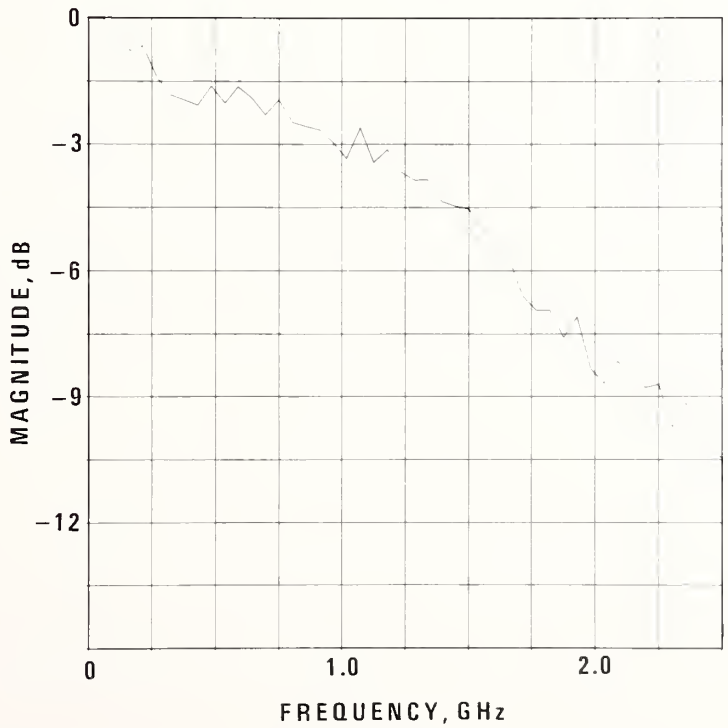


Figure 3. Frequency content for a typical laser diode pulse, 902 nm GaAs 3 dB frequency approximately 1 GHz.

Table 1. Laser diode pulse durations

| Diode | Pulse duration, ps (FDHM) |
|---|---|
| 803 nm, GaAlAs | 250 |
| 824 nm, GaAlAs | 240 |
| 866 nm, GaAlAs | 290 |
| 902 nm, GaAs | 250 |

oscilloscope; consequently, the detected pulses were broadened to about 330 ps FDHM. The 3 dB frequency is approximately 1 GHz. Observed pulse shapes do contain some broadening from the detector (section 3.2) and in some cases are probably less than 200 ps in actual duration.

It should be mentioned that the above temporal behavior and the spectral emission reported in section 3.1.4 were determined from the power exiting a short length of fiber and are therefore representative of actual system use.

### 3.1.2 Near-Field Radiation Patterns

The emission region in laser diodes consists of a narrow strip at the PN junction interface. In the case of C30012 and LA-63 GaAlAs diodes the junction dimension is 150 x 2 μm while for SG2001 GaAs diodes it is slightly smaller (75 x 2 μm). We find that the emission characteristics vary among diodes and cannot be accurately predicted. In the short-pulse mode the emission generally occurs over only a small segment of the junction. This is because the diodes are operated close to threshold and only the lowest loss regions of the junction oscillate. Typical behavior is given in figure 4 for the 803 nm diode. Figure 4a is an image of the junction showing low level spontaneous emission along the entire 150 μm junction length. Laser emission is restricted to a 16 μm segment of the total length. However, if the diode is driven further above threshold, other parts of the junction will eventually oscillate, as shown in figure 4b. All of the diodes exhibit this behavior except for the 824 nm diode which oscillates over a 40 μm length of the junction immediately from threshold.

### 3.1.3 Launched Power

The amount of power launched into a fiber is important since it affects signal-to-noise ratio. Power launched into a fiber with the diodes operating in the short-pulse mode was determined using two different types of calibrated detectors. One detector responded to individual pulse energy (in the 10 pJ range) while the other measured total average power (10 nW range). Measurements on the 825 nm diode differed by less than 10 percent. Peak

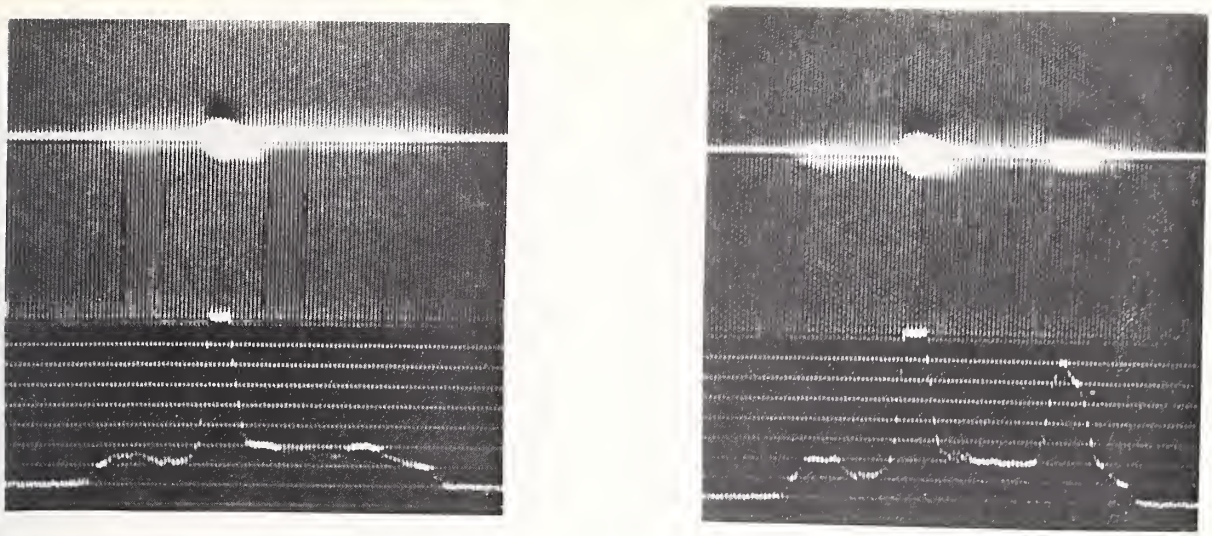

(a) (b)

Figure 4. Near-field emission characteristics: (a) 803 nm GaAlAs diode operating in short-pulse mode; quantitative curve relates to intensity along scan bar (oriented along junction image). Note low-level spontaneous emission along entire junction length with laser emission over a small segment; (b) same as (a) but with increased drive current causing other junction segments to exceed threshold.

power launched into a short section of step index fiber (55 μm dia. core, 0.25 NA) for the different diodes is tabulated in table 2 and is between 30 and 300 mW.

### 3.1.4 Spectral Emission

Spectral emission properties of the source are important because they determine the extent of intramodal pulse broadening in the fiber. The output of laser diode source consists of both spontaneous emission (linewidth about 30 nm) and stimulated emission (linewidth about 1 to 2 nm). For measurement purposes, it is important that the spectrally narrow stimulated emission dominate. Figure 5a shows the pulse shape which is coupled into a short length of fiber with the diode operated just below threshold. The pulse width is about 5 ns and the cusp represents the short pulse starting to form from stimulated

Table 2. Peak power from laser diodes exiting a short length of step index fiber with mode-scrambler

| Diode | Peak Power, mW |
|---|---|
| 803 nm, GaAlAs | 150 |
| 824 nm, GaAlAs | 300 |
| 866 nm, GaAlAs | 65 |
| 902 nm, GaAs | 35 |

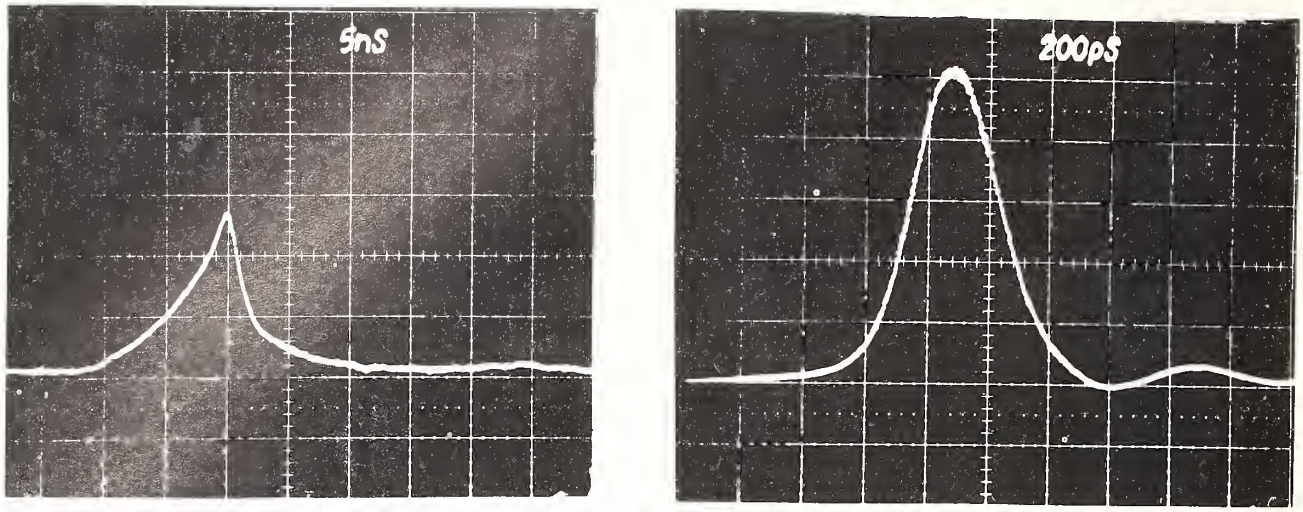


(a) (b)

Figure 5. (a) Spontaneous emission coupled into fiber (laser diode below threshold), 5 ns per division. (b) Laser emission coupled into fiber (laser diode above threshold); 200 ps per division; peak power in (b) is 70 times that in (a).

emission. Above threshold (fig. 5b) the short pulse is fully produced with the peak power exceeding the spontaneous emission by a factor of 70 for this particular diode. Contributions from spontaneous emission were judged to be insignificant for all diodes tested.

Spectral lineshapes were determined using time resolved measurements. This was necessary to determine the extent of "chirping," a shift of instantaneous spectral emission with time that can affect bandwidth measurements [12]. Radiation from the diodes was coupled into a short length of fiber containing a mode scrambler (section 3.3); after relaunching into a second fiber, the radiation was passed through a monochrometer and onto a detector (BPW-28, section 3.2). By triggering the sampling oscilloscope externally with a signal derived from the electrical trigger to the laser diode, a dc signal was obtained that was proportional to optical power at a selected point in time. Optical power was recorded on a strip chart recorder while the monochrometer was scanned. Line shapes were recorded on the leading half-height of the pulse and on the trailing half height. Only the 824 nm diode showed a significant shift of line center during the pulse (fig. 6). During the pulse, the peak of the spectral emission moved 0.7 nm toward longer wavelength. This rate of chirping, 0.0027 nm/ps, is not very different from the 0.0018 nm/ps previously reported for subnanosecond pulses from a particular single heterojunction laser diode [12]. The 824 nm diode differed from the rest in that it was driven higher above threshold with more of the junction stripe oscillating. This observation seems to be consistent with the evidence in [12] that chirping results from filaments in the junction stripe having different wavelengths and time delays.

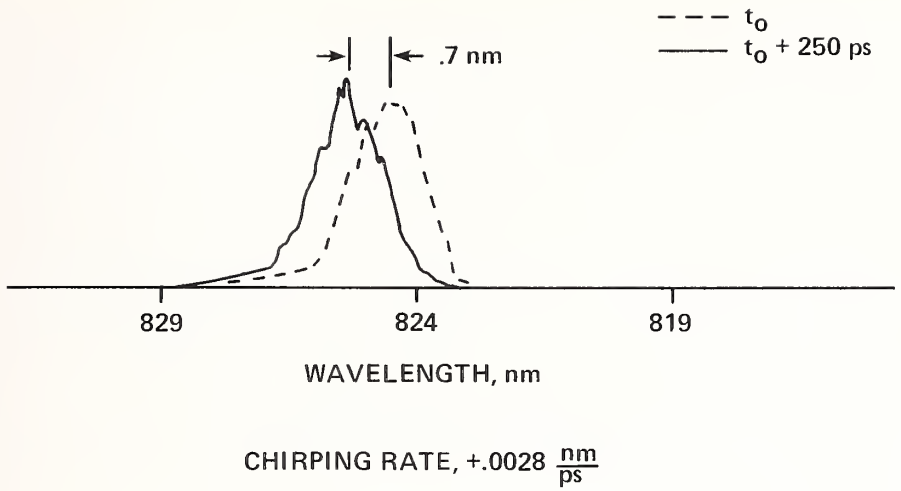


Figure 6. Time-resolved spectral emission showing chirping behavior of 824 nm GaAlAs diode under normal short-pulse conditions. Dashed curve is a spectrum at time $t_o$ at the front half height while solid curve is a spectrum 250 ps later at back half height (note wavelength increase to left).

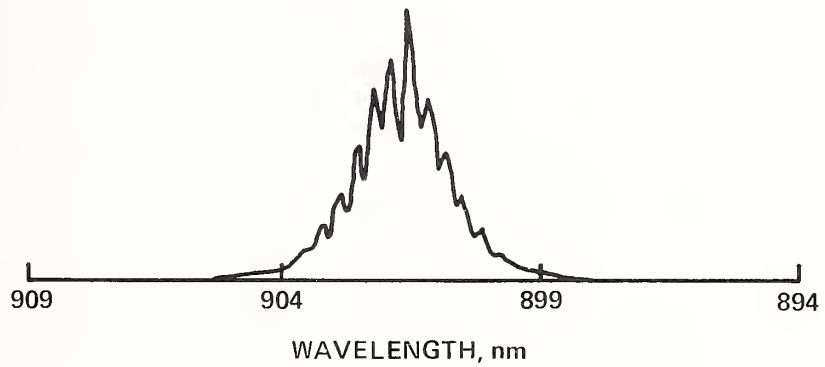


Figure 7. Time-integrated spectral emission from 902 nm GaAs diode showing partially resolved modes.

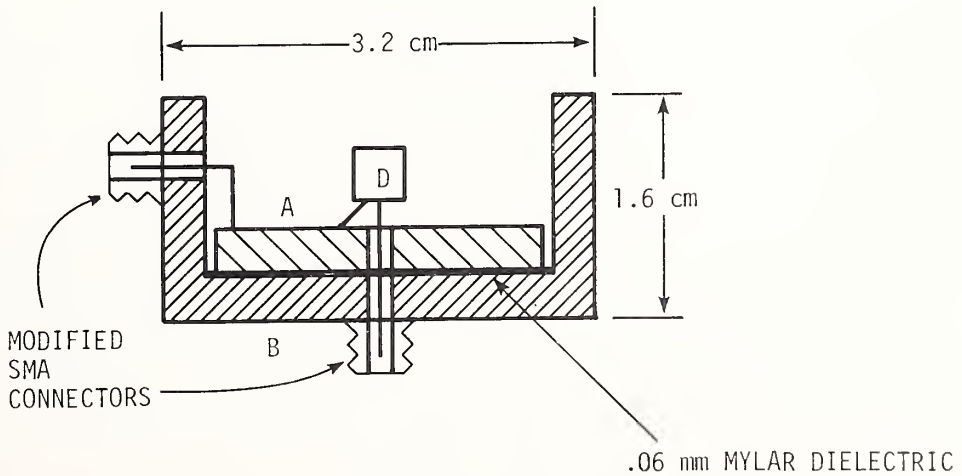


Figure 8. Mounting structure for optical detector, diode indicated by part D.

Table 3. Laser diode spectral lineshapes

| Diode | Linewidth, nm (FWHM) | General Features |
|---|---|---|
| 803 nm, GaAlAs | 1.2 | Smooth with some mode structure |
| 824 nm, GaAlAs* | 1.6 | Smooth, Gaussian like |
| 866 nm, GaAlAs | 0.9 | Two completely resolved cavity modes |
| 902 nm, GaAs | 1.5 | Several partially resolved cavity modes |

* Only diode which exhibited measurable chirping.

The spectral shapes from the four diodes showed different behavior; some were smooth Gaussian-like while others consisted of several partially resolved cavity modes. An example of the latter behavior was the 902 nm diode (fig. 7) where several modes of the diode were partially resolved by the monochrometer. Figure 7 was obtained using a detector having a 5 ns FDHM impulse response and therefore represents pulse energy.

Lineshapes for a given diode with a fixed alignment showed good reproducibility. However, fine structure changes within a nominal shape could be observed with different alignments of the diode. Nominal behavior for the four diodes is summarized in table 3.

## 3.2 Detectors

### 3.2.1 Mounting Configuration and Electrical Circuit

A number of different detectors are available for optical fiber bandwidth measurements. In the 800 to 900 nm region these principally include silicon PIN and APD (Avalanche PhotoDiode) devices.

A detector which performed satisfactorily was an AEG Telefunken BPW-28, silicon APD [11]. This detector was mounted in a structure similar to that described by Green [13] (fig. 8). In this structure the photodiode is mounted directly on the end of a coaxial transmission line which is also coaxial with a disc capacitor. The low inductance disc capacitor, $C_1$, is formed by pieces A and B which are separated by a thin dielectric (0.06 mm mylar). This capacitor is charged through 17 m of RG-58AU coaxial cable. Any reflections from the bias supply are therefore delayed by 160 ns and do not appear in the time window of interest. Figure 9 shows the complete electrical schematic. The cable is charged through resistor $R_1$ and ammeter M. $R_1$ is typically 50 kΩ and limits the current in case of an accidental short circuit. The value of $R_1$ and the capacitance of the cable are low enough so the cable is completely charged between pulses. Ammeter M measures the average current being supplied to the diode and is a useful monitor when approaching avalanche breakdown. Under typical operating bias, however, the average current is too low to be measured by the meter.

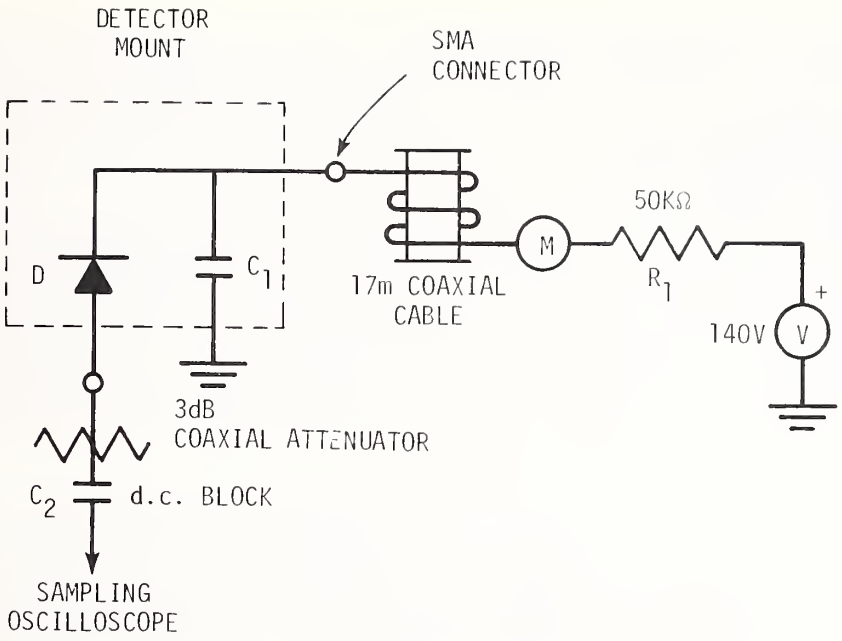


Figure 9. Detector electrical schematic, parts integral to mounting structure are enclosed by dashed line.

The detector load is a 3 dB SMA attenuator followed by an SMA series blocking capacitor. This attenuator is permanently attached to the detector and provides a constant 50 Ω load; thus, sensitive electronics can be reconnected to the detector without danger from excessive dc voltages which could occur under open circuit conditions. Blocking capacitor $C_2$ assures no dc voltage appears aross the sampling oscilloscope. $C_2$ is sufficiently large so normally encountered pulse shapes are not distorted.

### 3.2.2 Time Response

Ideally, detector time response should be fast compared to source pulse duration. Additional pulse broadening due to the detector will limit the upper bandwidth capability of the measuring system. Since the Fourier transform of the input pulse is the important quantity, the total pulse shape including half-duration, tail, ringing, etc., is important. It is of little use to obtain a small half-duration and yet have significant ringing. A well-matched detector is better for bandwidth measurements, and also for differential mode delay measurements where reflections could be confused with mode delay information.

A BPW-28 detector in the previously described mount was evaluated using a 1.06 μm, CW, modelocked Nd:YAG laser [14]. This laser produced pulses of 100 ps FDHM as measured with a fast detector based on a Shottky barrier-switching diode [13]. Although this detector is fast, it was not sensitive enough to use for fiber measurements with laser diode sources.

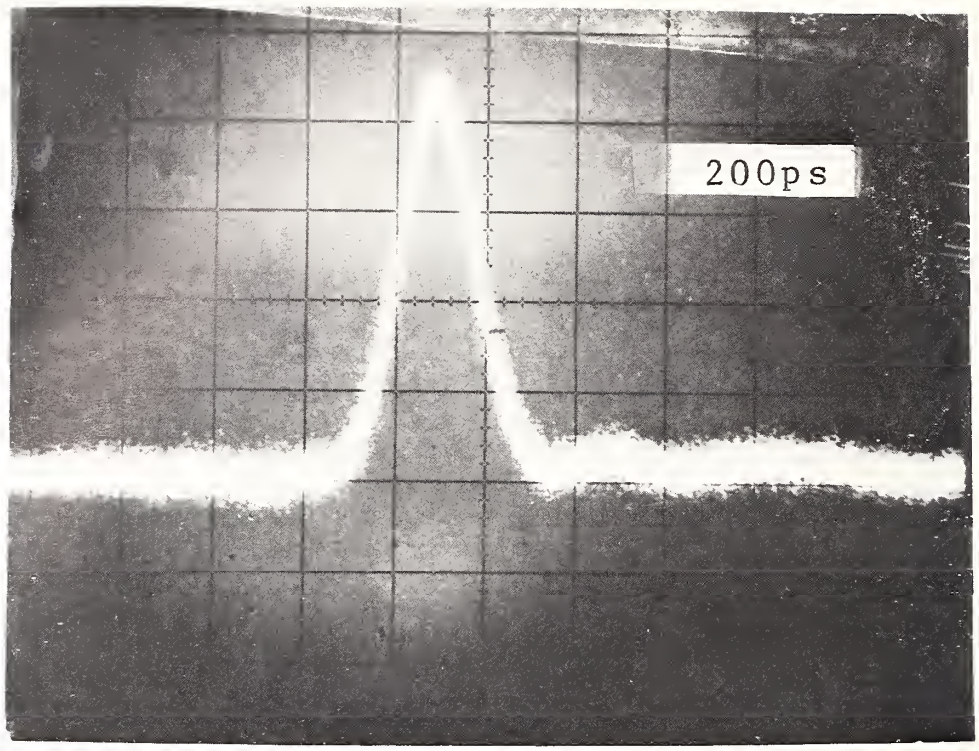


Figure 10. Response of BPW-28 detector to 100 ps FDHM pulse from CW modelocked, 1.06 μm, Nd:YAG laser, 200 ps per division.

Response of the BPW-28 to the modelocked pulses is shown in figure 10. The inferred impulse response is less than 200 ps FDHM. Notice that there is no evidence of a significant tail or ringing. These measurements were made at the 140-V bias voltage used in normal operation. The value of bias was selected by increasing the voltage until the pulse exhibited additional broadening; this yielded an avalanche gain of less than 10. This is substantially below the maximum available gain and is consistent with the gain-bandwidth trade-off in APD detectors.

### 3.2.3 Linearity

To obtain the frequency response of optical fibers, the output pulse must be compared to the input pulse. This requires that all components be linear, and in particular that the optical power levels involved not saturate the detector. Since the power of the input pulse is substantially higher than that of the output, a variable optical attenuator is used in front of the detector to control peak power. Thus, the detector is not used over a very large range of powers. It is also positioned in the exit optics so its aperture is filled; therefore, the power density (irradiance) on the detector is minimized.

The detector was tested for linearity at the highest levels used in the measurement system (8 ma peak diode current). This was done by varying the optical power by a factor of

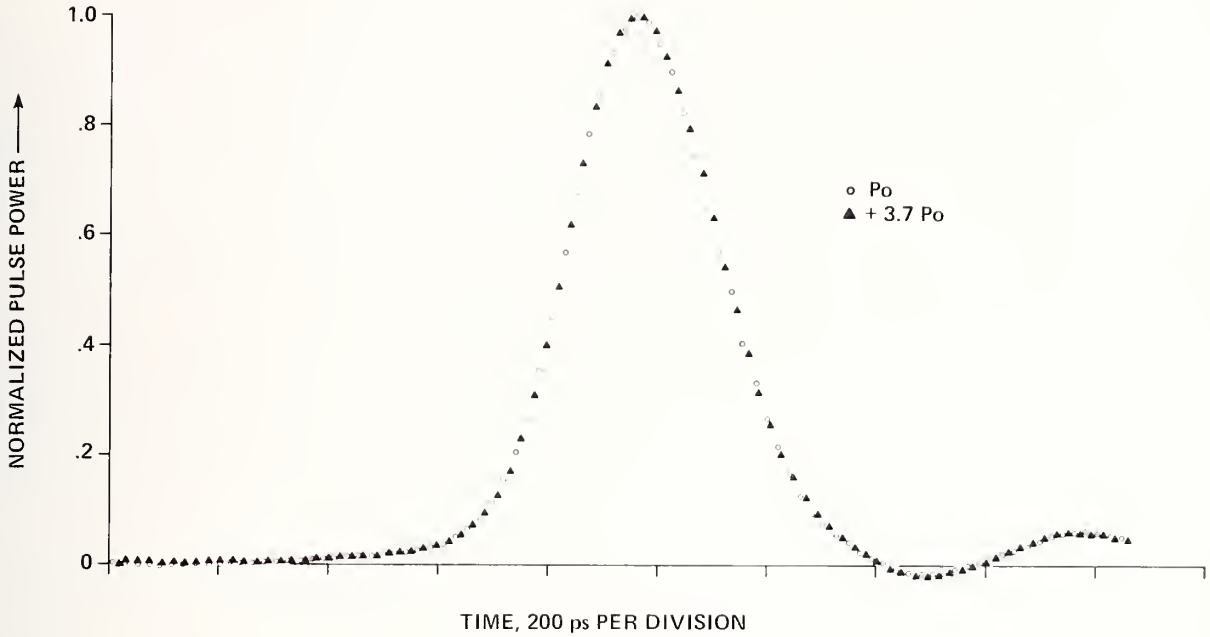


Figure 11. Verification of detector linearity; pulses at two different power levels show good super-position.

more than three and comparing the detected pulse shapes at the different powers. The whole pulse shape is checked for saturation. Figure 11 shows the normalized comparison; each pulse was digitally acquired from the sampling oscilloscope with each point being the analog average of several hundred pulses. As indicated, there is no appreciable difference between the pulses at the two power levels. Linearity of this particular detector was thus judged to be adequate.

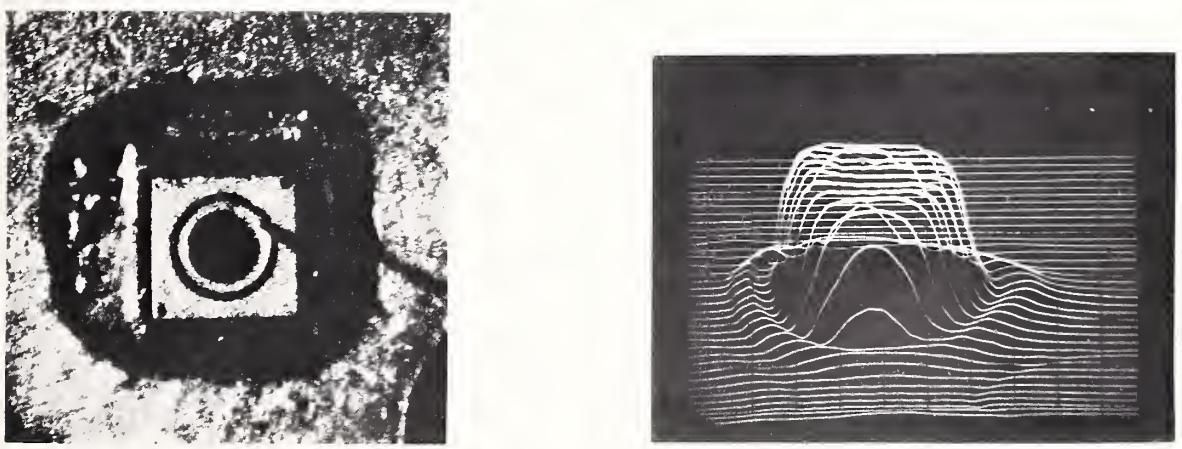

(a) (b)

Figure 12. (a) BPW-28 detector, 200 μm sensitive area inside ring electrode.
(b) Detector uniformity, two-dimensional dc scan at 0.63 μm wavelength.

### 3.2.4 Uniformity

The detector response should be uniform across the sensitive area. If this is not the case, then preferential mode detection can take place. Concern is usually expressed over launching conditions to a fiber; however, in the absence of much mode coupling, the receiving conditions are just as important. In fact, the spatial information at the output using an overfilled input is often used to make differential mode delay measurements [15]. Recent studies have shown that the responses of several commercial APD detectors are not necessarily uniform [16]. Consequently, the detector uniformity was investigated.

The BPW-28 detector has a circular sensitive area 0.2 mm in diameter surrounded by a ring electrode (fig. 12a). A two-dimensional raster scan of dc responsivity was made at 0.63 μm (fig. 12b). The response was constant to ±5 percent across the sensitive area. A low-level annulus was also present and corresponds to the area outside of the ring electrode.

Responsivity was also measured at high frequency. To accomplish this, a 300 ps FDHM pulse from a laser diode was focused to a 25 μm spot. This spot was scanned in one dimension across the detector and the peak power was obtained as a function of radial position (fig. 13). As indicated, the response was flat to better than 5 percent. Other parts of the detector were manually scanned and similar results obtained. Detector uniformity was judged to be adequate for the present system.

## 3.3 Launching Conditions

Launching conditions determine the initial modes excited in a fiber. Because of differential mode attenuation and delay, the results of bandwidth measurements depend upon launching conditions. As was discussed in section 3.1.2, the emission pattern from short pulse, single heterojunction laser diodes cannot be accurately predicted and would give non-quantifiable launching conditions. To circumvent this problem, a mode scrambler is used in a 2 m section of step index fiber and the radiation relaunched to provide a well-defined launching condition [17]. A distinction should be made between a mode filter and a mode scrambler. The former strips out specific modes (usually high order) while the latter is a device for inducing mode coupling.

The mode scrambler, which is conceptually similar to previous serpentine designs [18], consists of 7 nylon posts 1 cm in diameter, placed on 1.3 cm centers (fig. 14a). Three of the posts are positioned on a translation stage and can be moved into alignment with the rest. In this manner a fiber can be placed in the mode scrambler without breaking since the bending radius is never less than that of the posts. It should be pointed out that macroscopic bends in the step fiber not only induce mode coupling from low-order modes but also filter high-order modes so the far-field angle becomes slightly restricted from the full fiber NA. If desired, the launch numerical aperture to the test fiber can be adjusted by using appropriate launch optics.

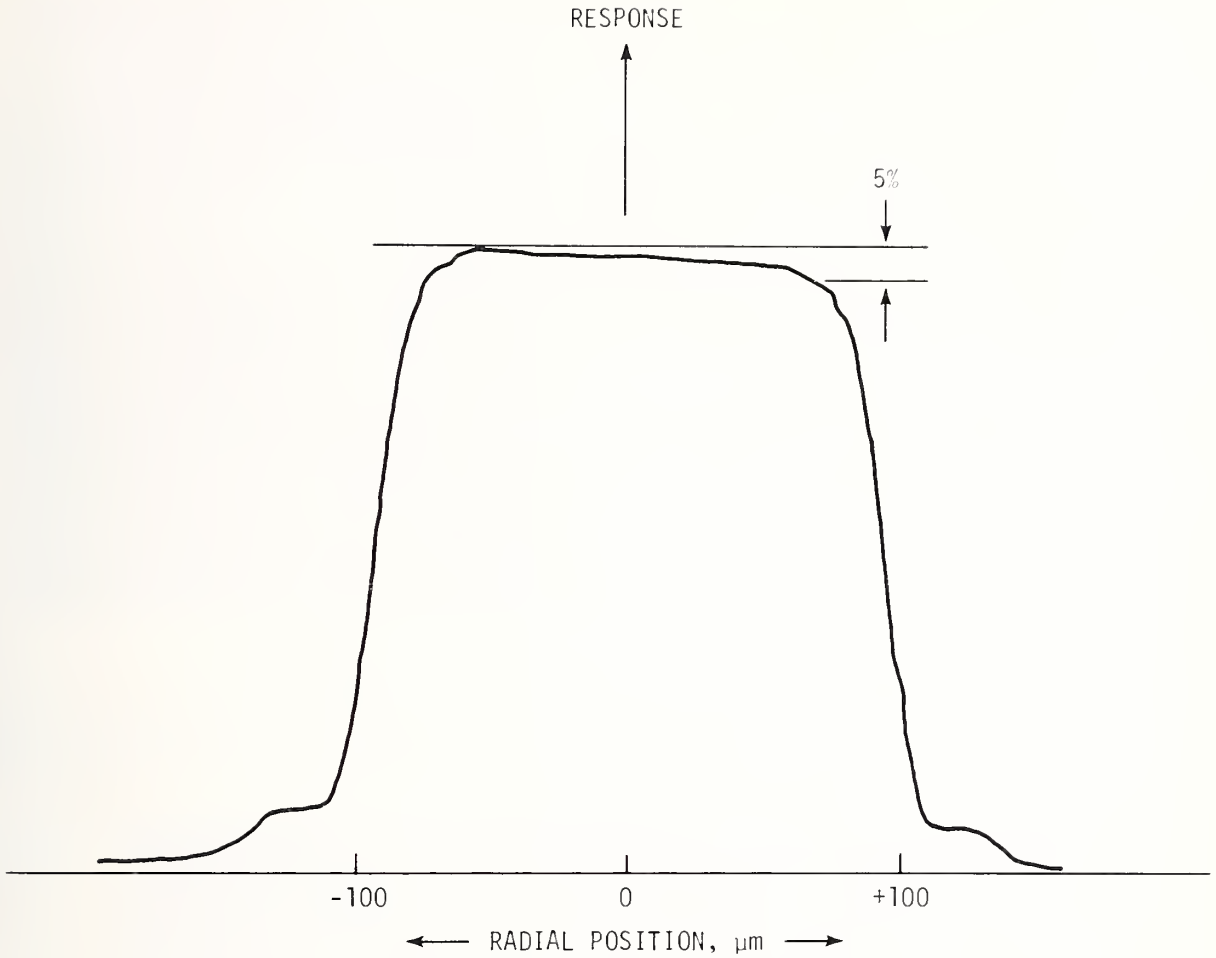


Figure 13. Detector uniformity, detected peak pulse power as a function of radial position.

Without the mode scrambler, various near-field patterns could be obtained from the step fiber depending upon diode alignment. Patterns ranged from on-axis maximums to annular shapes. With the mode scrambler, the near-field patterns were more uniform and not as sensitive to diode alignment. With proper alignment, the near-field emission could be made very uniform (fig. 4b). The resulting emission from the step fiber (55 μm, 0.25 NA) was imaged 1:1 by two microscope objectives and relaunched into the fiber under test with peak transmitted power being the alignment criterion. For this alignment, the image of the step fiber is not necessarily exactly at the input end of the test fiber; however, for overfilled launching conditions, this does not represent a significant uncertainty. This launching overfills the modes of most graded-index fibers and results in a bandwidth which is generally lower than that obtained with small spot excitation. The advantages of the overfilled launching condition are: (1) it can be reproduced in other laboratories and (2) it is the starting point for other types of launching conditions which make use of equilibrium mode simulators on the fiber under test.

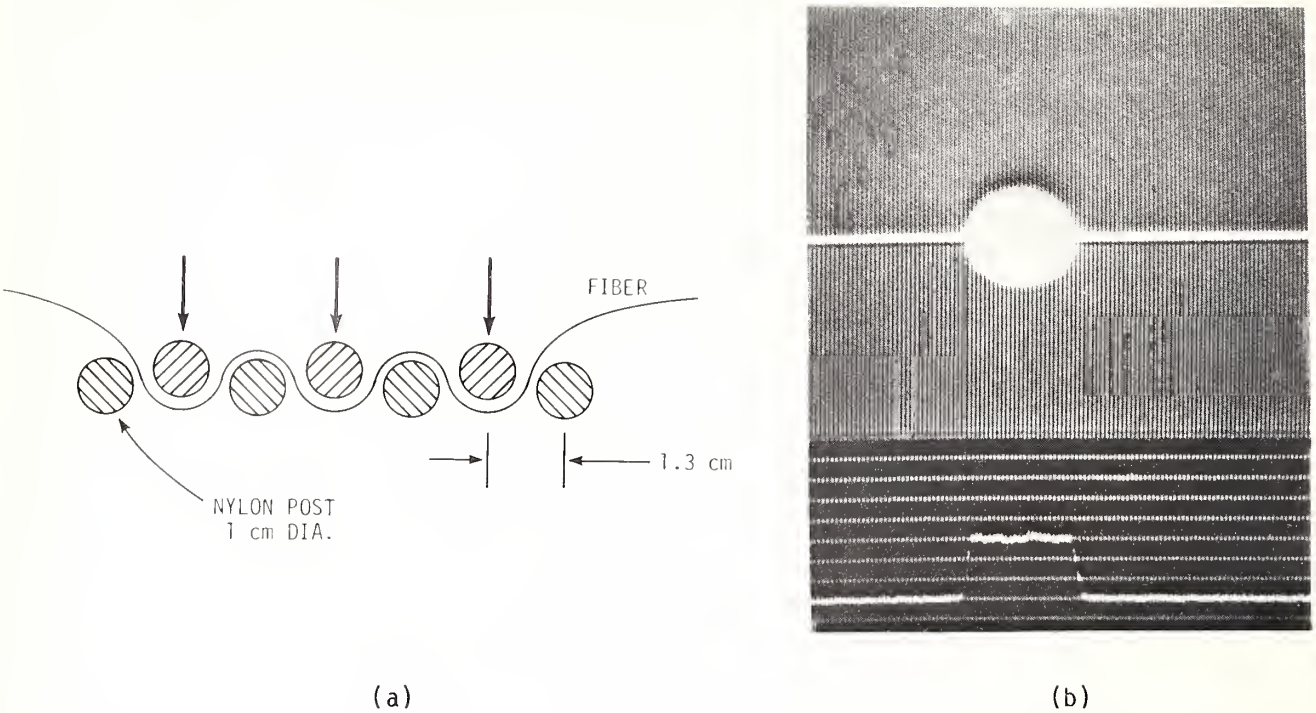


(a) (b)

Figure 14. (a) Serpentine mode scrambler used in a 2 m section of step index fiber (55 μm, 0.25 NA). (b) Near-field emission from step fiber with mode scrambler adjusted to give most uniform pattern--curve relates to intensity along scan bar.

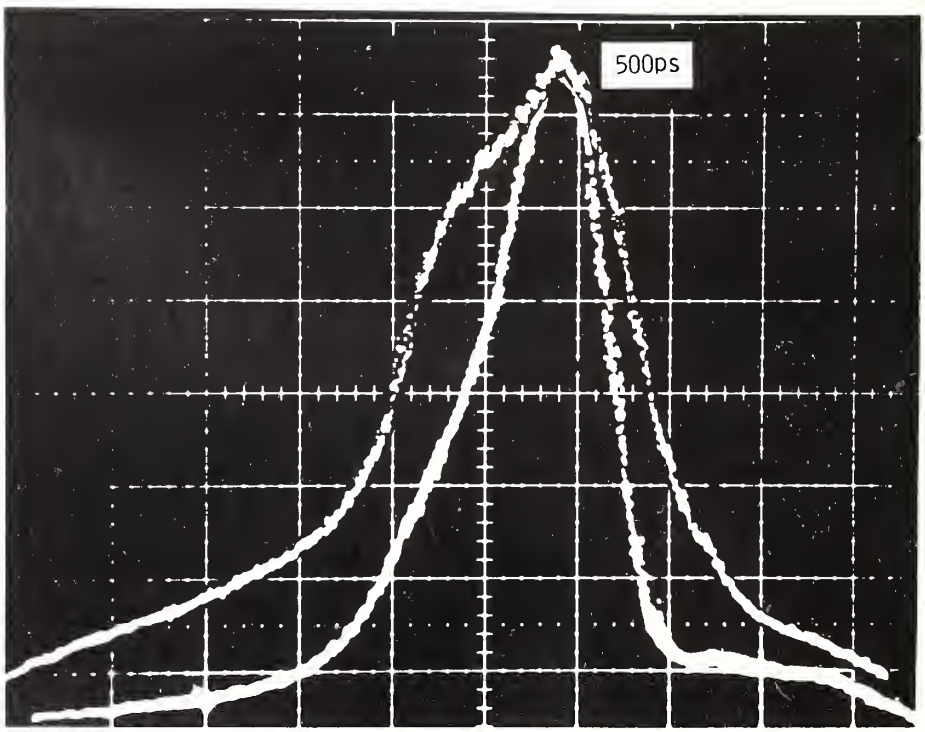


Figure 15. Superimposed output pulses from 1.3 km, graded-index fiber using the same source (300 ps FDHM) but with different launching conditions, 500 ps per division. Narrow pulse is from directly imaging laser diode onto fiber, whereas broad pulse results from use of the mode scrambler-step fiber. In both cases peak detected power was used as the alignment criteria.

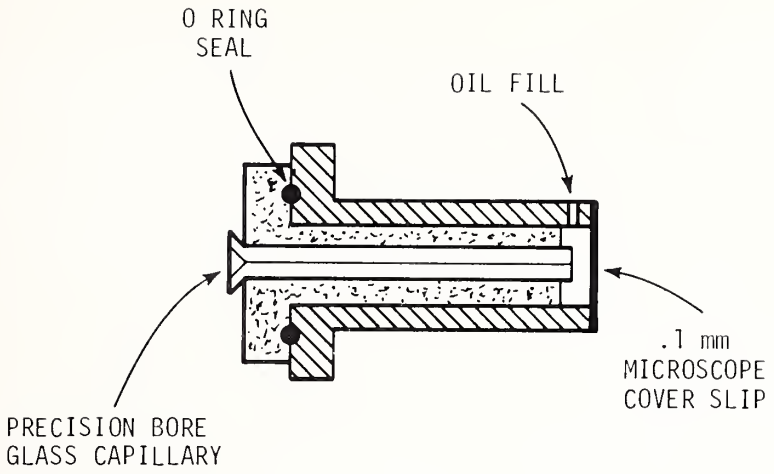


Figure 16. Oil-filled, precision 150 μm bore, capillary fiber holder.

A comparison was made using two different launching conditions on the same fiber with peak transmitted power being the alignment criteria. In one case, the laser diode output was directly imaged onto the fiber, while in the other it was first passed through the mode scrambler-step fiber filter. A superposition of the output pulses (fig. 15) shows that the small spot from the laser diode excites fewer modes (narrower pulse) than the mode scrambler-step fiber launch which fills the mode volume of the fiber. For the two different launching conditions, the fiber half-duration broadening differs by a factor of 1.8.

An oil-filled capillary is utilized to hold fibers (fig. 16) [19]. The capillary bore is 150 μm in diameter and readily accepts standard 125 μm o.d. fibers. One end of the capillary is flared to accept the fiber while the other end has an oil reservoir covered by a thin microscope cover slip. This holder has the following advantages: (1) it acts as a cladding mode stripper, (2) the oil index matches the fiber end, and (3) it aligns the fiber stabily in the system with little readjustment required when fibers are changed. The main disadvantage is the possible accumulation of dirt and other foreign material in the capillary. For this reason the holder is demountable and the capillary can be cleaned by a thin wire.

## 3.4 System Architecture

The previously described components are assembled in the following manner (fig. 17). Multiple laser diodes are mounted on a translation stage enabling different wavelengths to be easily launched into the step fiber-mode scrambler. The output from the step fiber is collimated, passed through an aperture wheel, and relaunched into the fiber under test.

A bandwidth measurement on a fiber is made by aligning the fiber for peak transmitted power and then acquiring the output waveform. Next, without disturbing the launching, the

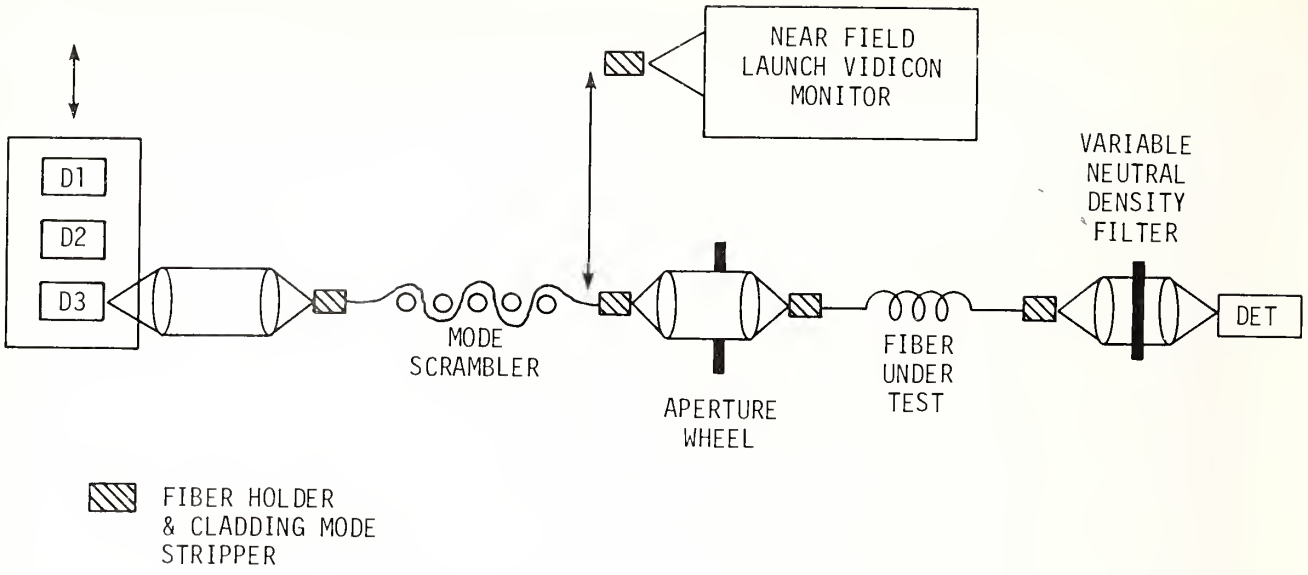


Figure 17. Configuration of bandwidth measurement system.

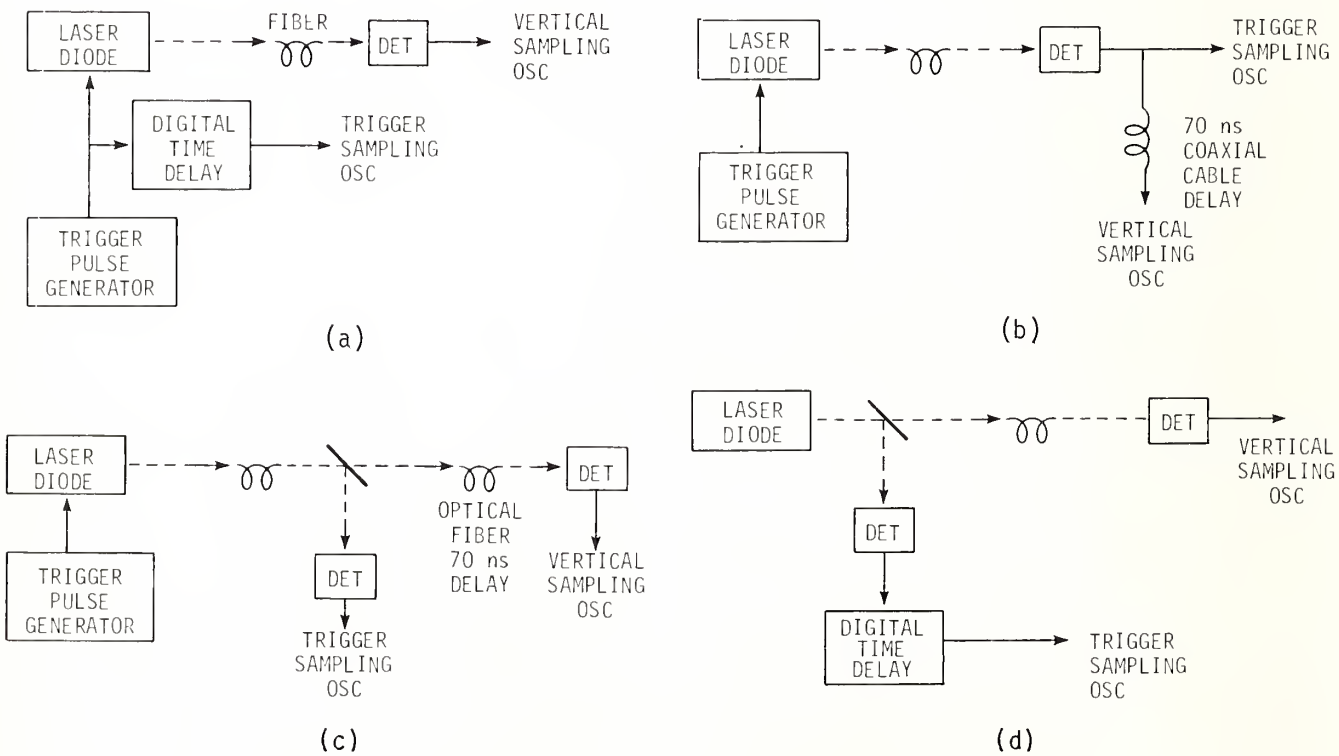


Figure 18. Possible choices for triggering sampling oscilloscope: (a) digital time delay generator, (b) electrical delay line, (c) optical delay line, and (d) digital time delay generator scheme when source exhibits excessive trigger jitter. Dashed lines refer to optical paths while solid lines are electrical.

fiber is cleaved approximately 1.5 m from the input end and the waveform exiting the short length measured. This waveform is used as the input to the fiber under test.

At the receiving end, the output is collimated by a X10, 0.25 NA microscope objective. At this point neutral density filters are inserted to attenuate the power until it is within the linear range of the detector. Also, to minimize detector dynamic range requirements, the peak power from the short length is made equal to the power detected from the full length. Finally, the collimated output is focused on the detector by a X5 microscope objective.

Waveforms are acquired using a sampling oscilloscope. A number of choices (fig. 18) are available for triggering the oscilloscope. First (fig. 18a), a digital time delay generator can be used to produce an electrical trigger pulse which just precedes the arrival of the optical output pulse. For this method to be successful, the delayed trigger signal must have low jitter and what jitter remains should be random so it can be averaged out. Also, the range of available delays should cover all fiber length encountered. Second (fig. 18b), an electrical delay line can be used at the output to delay the detected electrical signal while providing an advanced trigger signal. The delay line should have sufficient bandwidth to not appreciably distort the pulse. Third (fig. 18c), the optical output can be divided to provide an advanced trigger signal and then delayed optically in another fiber. This has the advantage of high bandwidth in the delay line but care must be taken to prevent the loss of modes on relaunching. Fourth (fig. 18d), the optical input can be divided to trigger a digital time delay generator. This configuration is useful when a digital delay is required but, the laser diode exhibits excessive trigger jitter. In the present system we utilize figure 18b with a Tektronix 7M11 delay line. To observe differential mode delay, however, figure 18b is not applicable and the method of figure 18a is used.

To digitally record a waveform, the sampling oscilloscope time base is swept by a ramp voltage while two four and one-half digit, digital voltmeters read the vertical out signal and the time base ramp. Analog averaging is used to increase the signal-to-noise ratio and is accomplished with a capacitor in parallel with the vertical output to give a time constant of 0.2 s. Consequently, a vertical data point is the result of several hundred pulses averaged. A number of choices involving different levels of automation are available for storing data points and taking Fast Fourier Transforms (FFT). A description of these is beyond the intended scope of this report [20,21]. The system, in its present state, uses a large general purpose computer to compute the transforms.

## 4. DATA TRANSFORMATION AND ANALYSIS

### 4.1 General Description

Data from the acquisition system appears in the form of a 2 x N integer array identified as Y(I), T(I) where Y(I) is related to the pulse amplitude and T(I) is related to time.

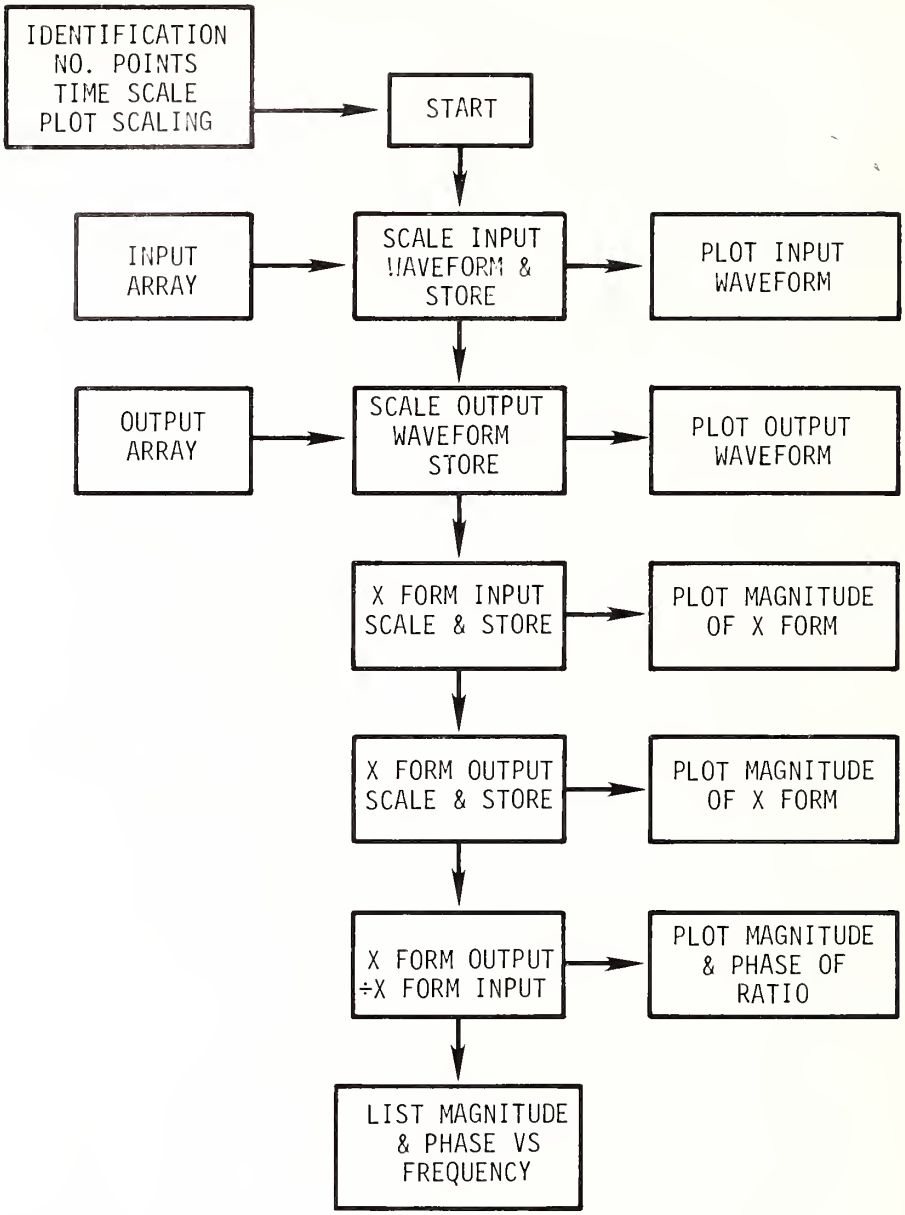


Figure 19. Flow diagram showing various computer program outputs.

In most cases the array is 256 elements long, a choice resulting from several compromises. Y(I) varies from about -7200 to +7200 and T(I) from +0000 to +9500 so that, in each case, the resolution in sampling the waveform is about $1{:}10^4$.

Two such arrays result from a single measurement, one representing the input waveform and the other the output waveform. These arrays are stored in the mass storage of a large, multipurpose computer for subsequent processing.

The analysis program provides for the scaling of both waveforms, the Fourier transformation of each, and the computation of the complex ratio of the transform of the output to

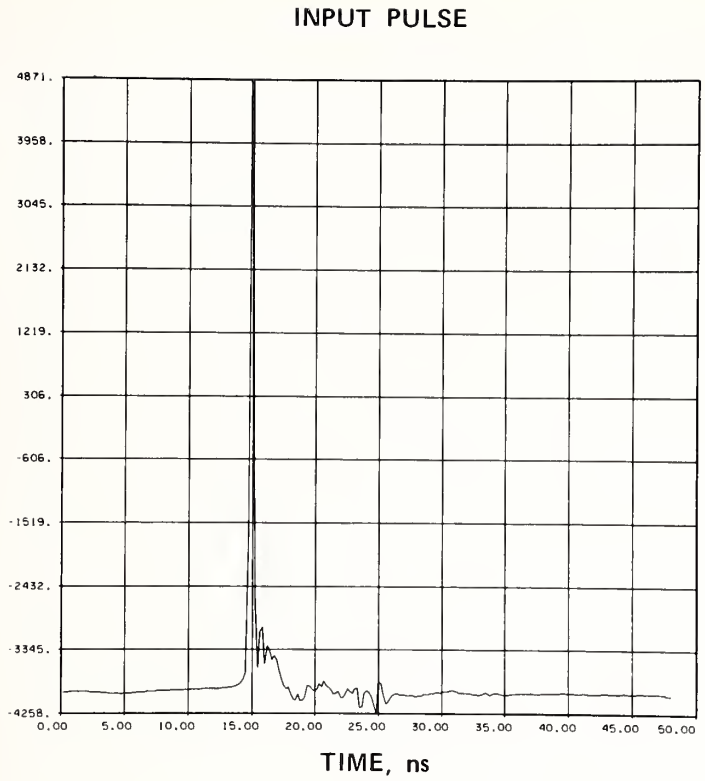


(a)

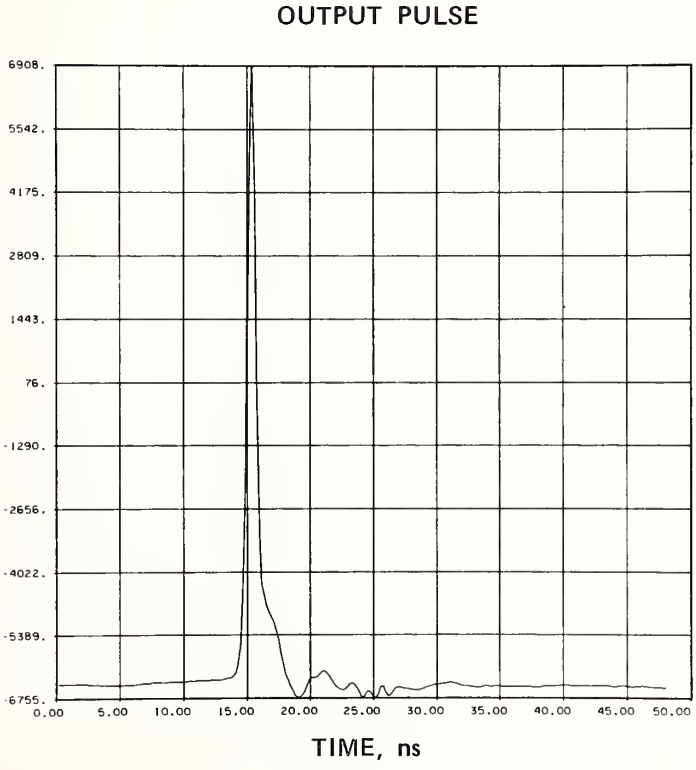


(b)

Figure 20. Typical set of computer-generated output for a fiber bandwidth measurement: (a) input pulse (time), (b) output pulse (time).

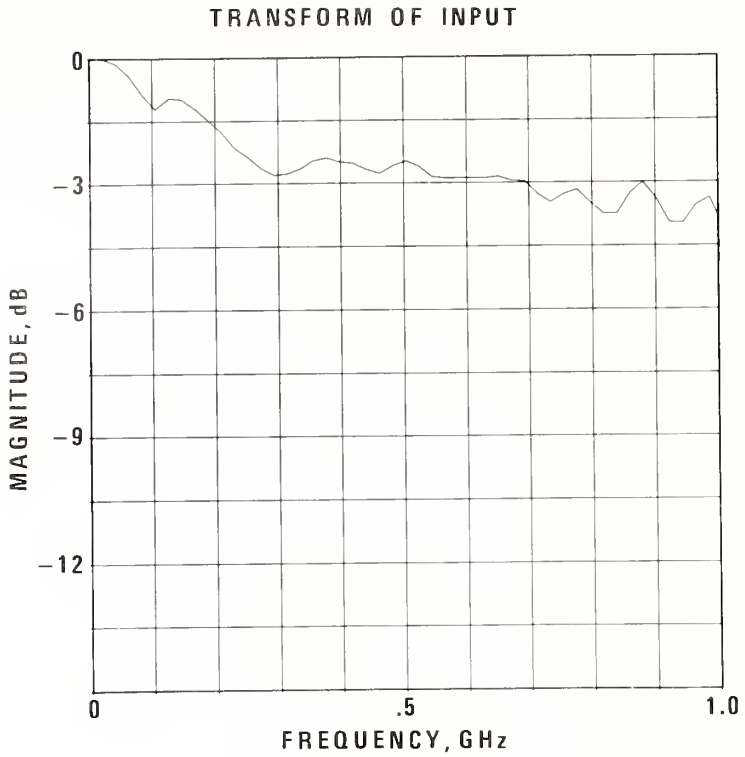


(c)

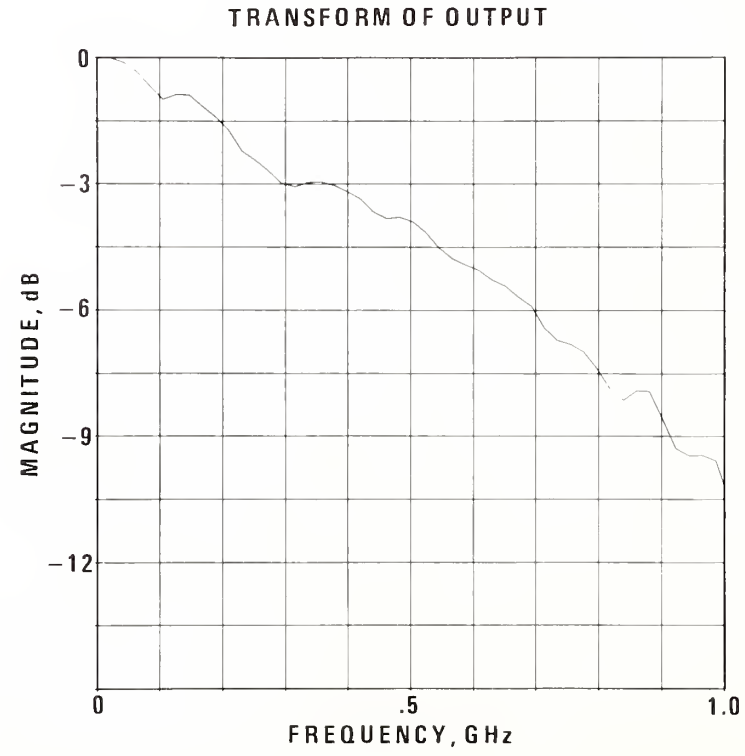


(d)

Figure 20, continued. (c) Fourier transform of input pulse, (d) Fourier transform of output pulse.

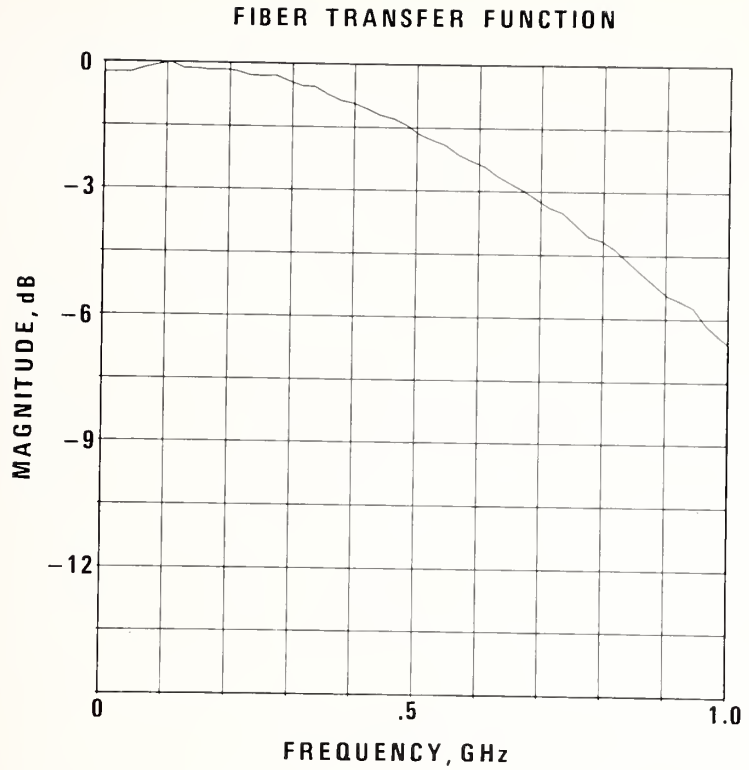


(e)

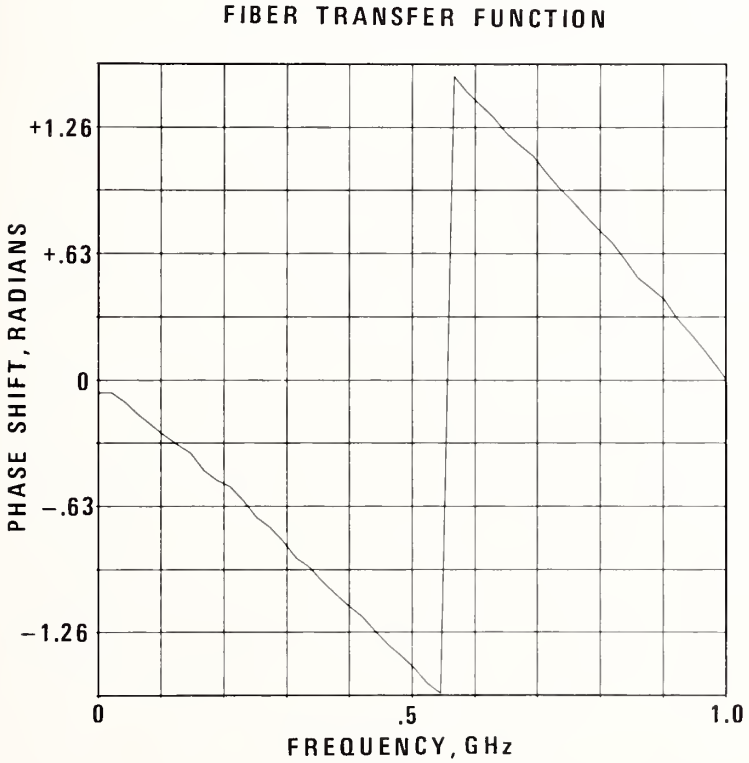


(f)

Figure 20, continued. (e) Magnitude of fiber transfer function, (f) phase of fiber transfer function.

the transform of the input (the transfer function). Figure 19 indicates the order in which these functions are carried out. Typical outputs for one fiber are shown in figure 20.

The FFT subroutine is a general purpose routine locally available. It is distinguished by its general versatility and by the fact that the input array need not be an integer power of two long, although that restriction greatly increases the efficiency.

## 4.2 Accuracy Considerations

The principal factor in assuring accurate computation of the transfer function is the choice of appropriate sampling parameters, specifically N, the number of samples, and T, the time interval between samples. The time interval must be chosen so that the transform is effectively zero at frequencies greater than $f = 1/2T$. Errors resulting from a failure to satisfy this condition are known as aliasing. Resolution in the frequency domain, that is, the frequency interval betweens points is given by $\Delta f = 1/NT$. Maintaining good resolution without introducing significant aliasing errors or requiring a particularly large number of samples thus requires certain compromises.

Because the system in its present configuration uses slow data acquisition equipment, the number of samples is generally limited to no more than 256. These samples are spaced across about 95 percent of the sweeptime of the sampling oscilloscope. Most fibers measured with this system have a 3 dB bandwidth below 800 MHz. In this case a 50 ns sweep is used so that $T = 0.186$ ns and $\Delta f = 21$ MHz. For higher bandwidth fibers, a 20 ns or 10 ns sweep is used.

The greatest problem with aliasing errors occurs when transforming the input waveform using the longest sweep time. Figure 21(a) shows the transform of a typical input pulse with the frequency range expanded to $f = 1/2T$ or 2.7 GHz. At this frequency the magnitude is approximately 10 dB below its value at low frequency.

To estimate the magnitude of the aliasing error in this waveform, a sampled Gaussian pulse having a similar 10 dB bandwidth was generated and transformed. Figure 21(b) shows the magnitude of the transform and the difference between that magnitude and an analytically computed transform. At frequencies below about 1250 MHz the difference is less than about 0.1 dB. At frequencies below 800 MHz where these sampling parameters are used, the maximum difference is 0.045 dB, which is within the observed precision of the complete system. Some caution in interpreting these numbers is necessary, however, because the shape of the transform is different in the two cases.

One approach to decreasing the aliasing error without decreasing the resolution or requiring excessive measurement time is to artificially extend the baseline. One might, for example, take 256 samples over about 10 ns and artificially extend the data to include 1024 points over 40 ns. The aliasing error would be substantially reduced while the resolution

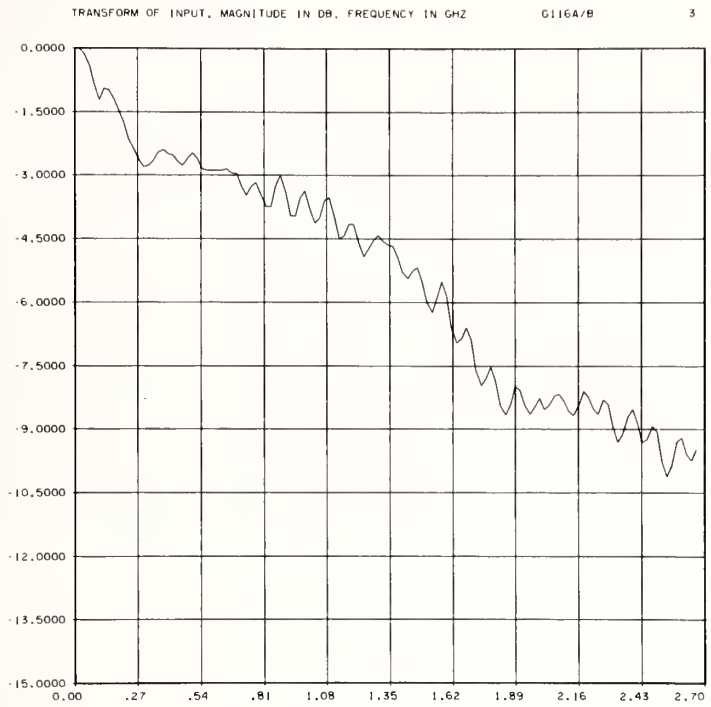


(a)

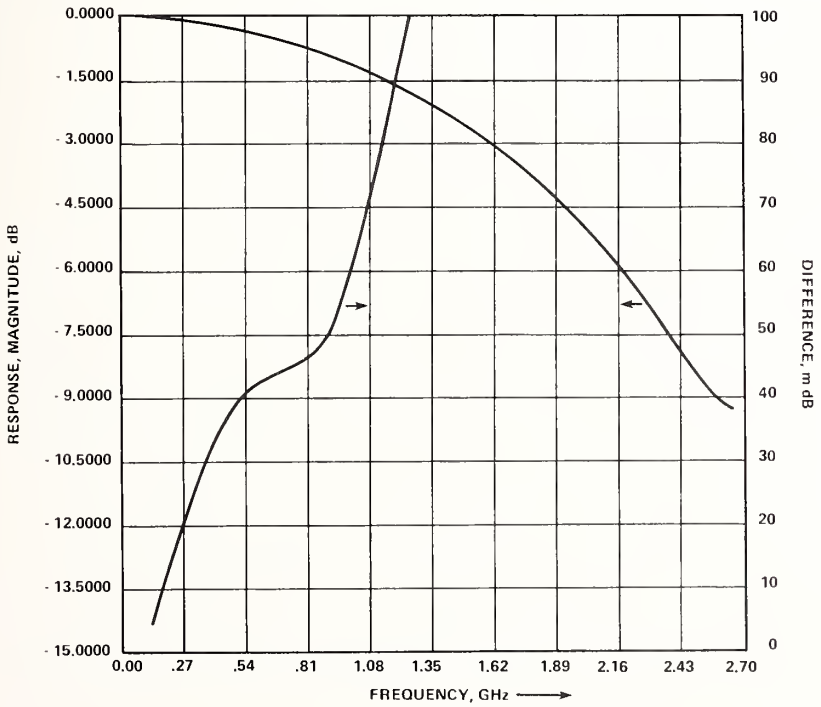


(b)

Figure 21. (a) Transform of input pulse out to 2.7 GHz using 50 ns sweep and 256 point FFT. (b) Estimation of aliasing error, left ordinate is FFT of a Gaussian having the same 10 dB frequency as (a) and the same sampling parameters, right ordinate is difference between FFT and exact, analytically computed transform.

would be only about 20 percent worse. This aproach has not yet been used in this system because of uncertainty in the procedure for creating the simulated data, in particular, because the low frequency part of the transform is strongly dependent on the data in the baseline.

Another concern is the manner in which the transforms are scaled. The zero frequency point has no meaning in this system since dc levels in the data are arbitrary. One choice is to reference the entire transform to the first point in the frequency domain. Thus, it is important to maintain good frequency resolution, even for high bandwidth fibers because any variation between zero frequency and the first point is lost. Furthermore, the transform does not necessarily decrease monotonically with frequency, which sometimes can be the case for the first few points in the low frequency range; consequently, the apparent value of the transform can have values greater than unity. Presently, this system normalizes the transforms to the largest value and the interpretation of such effects is left to the user.

## 5. SYSTEM PERFORMANCE

### 5.1 Precision

Precision refers to the reproducibility of a measurement. A precision statement, however, says nothing about "systematic" error which is the offset of the average of a large

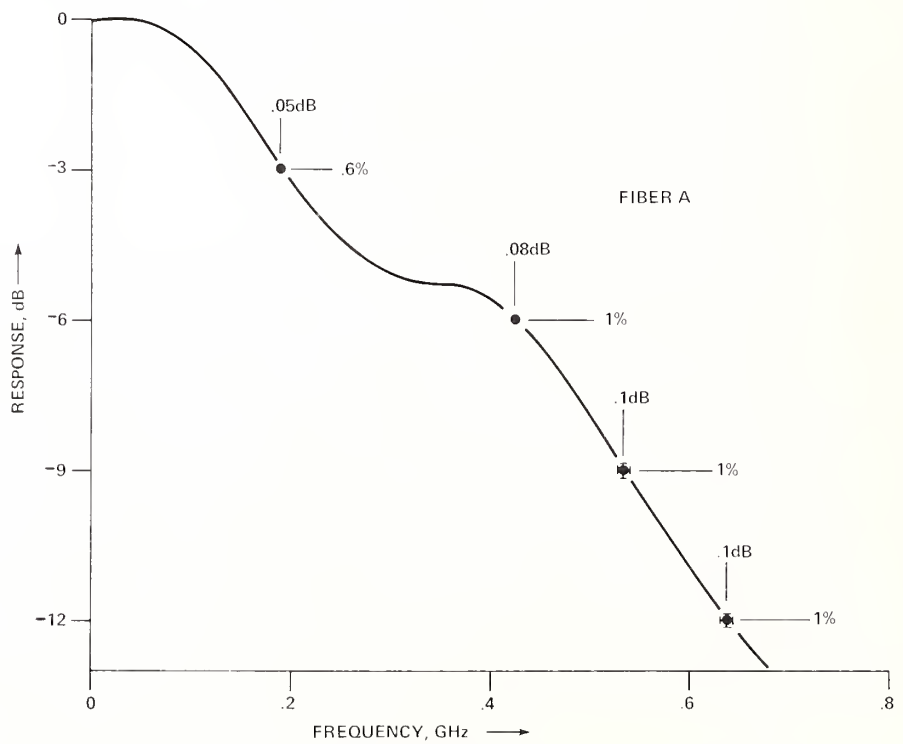


Figure 22. System precision, 824 nm diode; error bars are ±1 standard deviation (2 standard deviations in length) for five repeated bandwidth measurements. Fiber A: graded index, 50 μm core, 125 μm o.d., 0.25 NA, plastic jacketed, 6.0 dB/km attenuation at 850 nm, 1.3 km length.

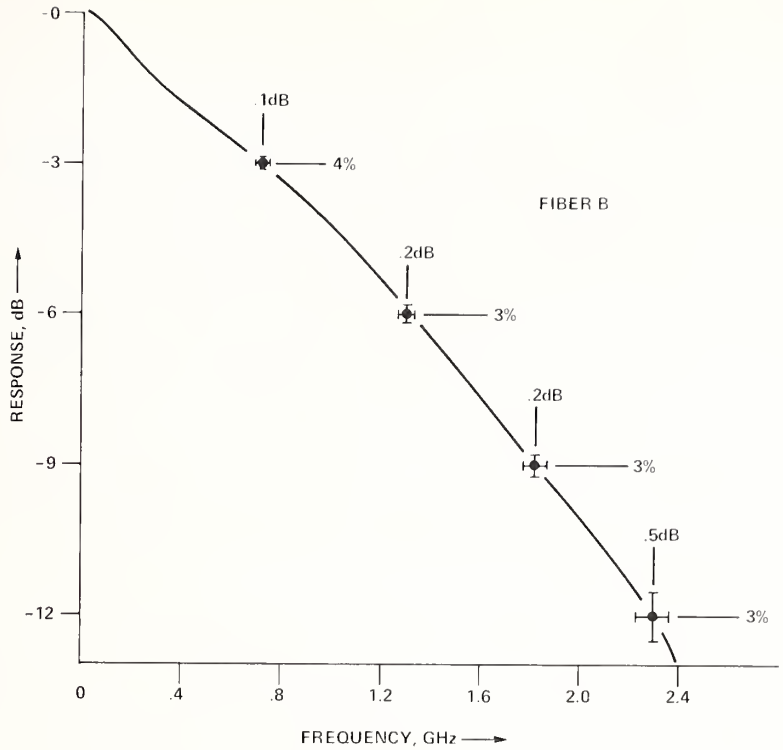


Figure 23. System precision, 902 nm diode; error bars are ±1 standard deviation (2 standard deviations in length) for five repeated bandwidth measurements. Fiber B: graded index, 50 μm core, 125 μm o.d., 0.25 NA, plastic jacketed, 4.6 dB/km attenuation at 850 nm, 1.1 km length.

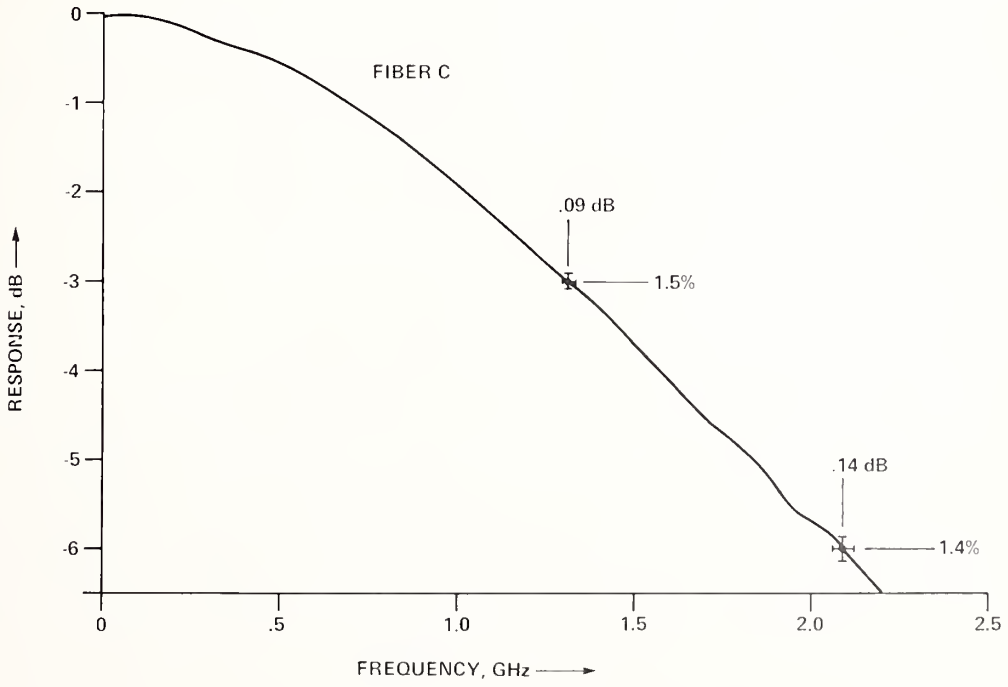


Figure 24. System precision, 824 nm diode; error bars are ±1 standard deviation (2 standard deviations in length) for five repeated bandwidth measurements. Fiber C: graded index, 62 μm core, 125 μm o.d., 0.25 NA, plastic jacketed, 4.0 dB/km attenuation at 850 nm, 1 km length.

number of measurements from the true value. In the case of optical fibers it is difficult to assign systematic errors since launching condition have yet to be standardized.

Precision is defined here as the reproducibility of the frequency response curve (magnitude). To determine this, measurements were repeated five times on the same fiber. For each measurement the fiber was recleaved and the necessary parts of the measurement system realigned. Three multimode, graded index, telecommunications type fibers with a range of bandwidths were chosen for this set of measurements and represent fiber from two different manufacturers. Also, measurements were made using two different laser diodes. The results therefore represent typical system performance.

Results are given in figures 22, 23, and 24 with two-dimensional error bars representing an estimate of plus or minus one standard deviation determined from the five measurements. To summarize the results, error bars are displayed at the 3, 6, 9, and 12 dB points on the frequency response curve. These frequencies were determined by interpolating between discrete FFT points and this precision is indicated by the horizontal error bars. The closest discrete frequencies to the average 3, 6, 9, and 12 dB frequencies were used to determine the precision in the vertical axis. In all cases, a 256 point FFT was used and the time base chosen so that the separation between frequency points was 21 MHz for fiber A and 54 MHz for fibers B and C. In plotting the figures, a smooth curve was drawn through the points.

Some fibers gave better measurement precision than others. Fiber A with the lowest bandwidth (200 MHz) gave the best precision with the frequency at a given response being determined to ~1 percent and the response at a given frequency being determined to ~0.1 dB. For fiber B with medium bandwidth (720 MHz), the corresponding numbers varied from 2 to 4 percent and 0.1 to 0.5 dB with the highest frequency part of the curve showing the poorest reproducibility. Fiber C with the highest bandwidth (1.3 GHz), gave corresponding precisions of 1 to 2 percent and 0.1 to 0.2 dB, respectively.

## 5.2 Dynamic Range

Dynamic range applies to both the maximum fiber bandwidth and attenuation that can be accommodated by the system. If only the intermodal contribution is to be determined from a measurement, the upper bandwidth limit is determined by the spectral properties of the laser diodes and is in the 1 to 2 GHz•km, 3 dB frequency range depending upon the specific diode. Although higher bandwidths can be measured, the material dispersion contributions become too large and accurate corrections become difficult (section 4.3). Limitations due to source pulse width (260 ps FDHM) do not become important until the 3 dB frequency exceeds 3 GHz.

Maximum attenuation limits depend upon the amount of signal averaging done or on the signal level available to the sampling oscilloscope trigger for good stability. Present sources, attenuated with a 1.0 neutral density filter and detected with a BPW-28 APD

(section 3.2), produce from 0.2 to 2 V at the detector for short lengths of fiber having negligible attenuation and high bandwidth.

If an advanced-trigger, electrical-delay line is used with the output signal, figure 18b, we find about 15 mV of signal should be available for the oscilloscope trigger to provide good long-term stability. If the trigger level is not a problem, for example, with a digital time delay generator (fig. 18a), then the amount of signal averaging determines the attenuation limits. For the present amount of analogue averaging (section 3.4), the noise level is less than 0.1 mV. Both the fiber attenuation and bandwidth will determine the peak voltage level available at the detector output. Signal level in the present system has not been a problem for most of the currently available telecommunications type fibers at the 1 to 1.5 km length.

## 5.3 Material Dispersion Limits

In characterizing the bandwidth of multimode fibers, it is desirable to know the intermodal contribution. If the measurement contains significant intramodal broadening, the result depends upon the source spectral properties and does not represent the ultimate bandwidth potential of the fiber.

Material dispersion results in intramodal pulse broadening with the RMS contribution to total pulse broadening given by eq (6), section 2. From the observed diode lineshapes and occasional chirping behavior, it seems unlikely that eq (6) could be used to calculate a significant correction term with a high degree of confidence. A more prudent approach would be to place an upper bandwidth limit on measurements made with a particular diode; i.e., for measured fiber bandwidths below a certain maximum 3 dB bandwidth, $f_m$, the contribution from intramodal effects for a given diode would be less than 6 percent of the measured bandwidth.

Material dispersion constants were measured for a number of commercial fibers with the apparatus described in the appendix. The results give M (-M plotted) in the appendix, where

$$M = -\frac{\lambda}{c}\frac{d^2n}{d\lambda^2}. \tag{16}$$

Since the M values at a given wavelength show little variation among fibers (a ±10 percent variation would nearly bracket the data), the value of $f_m$ determined is, roughly a property of a given diode. Using a Gaussian approximation for spectral, pulse and fiber frequency response shapes along with the M values from the appendix, eqs (5) and (6) predict an $f_m$ of 1.0, 2.0, and 1.4 GHz·km for the 803, 866, and 902 nm diodes, respectively. Chirping observed in the 824 nm diode should partially compensate the material dispersion broadening for fibers exceeding a critical length [12]. From the linear chirping theory of reference 12, a critical length of 1.1 km is predicted. For shorter lengths, pulse compression would

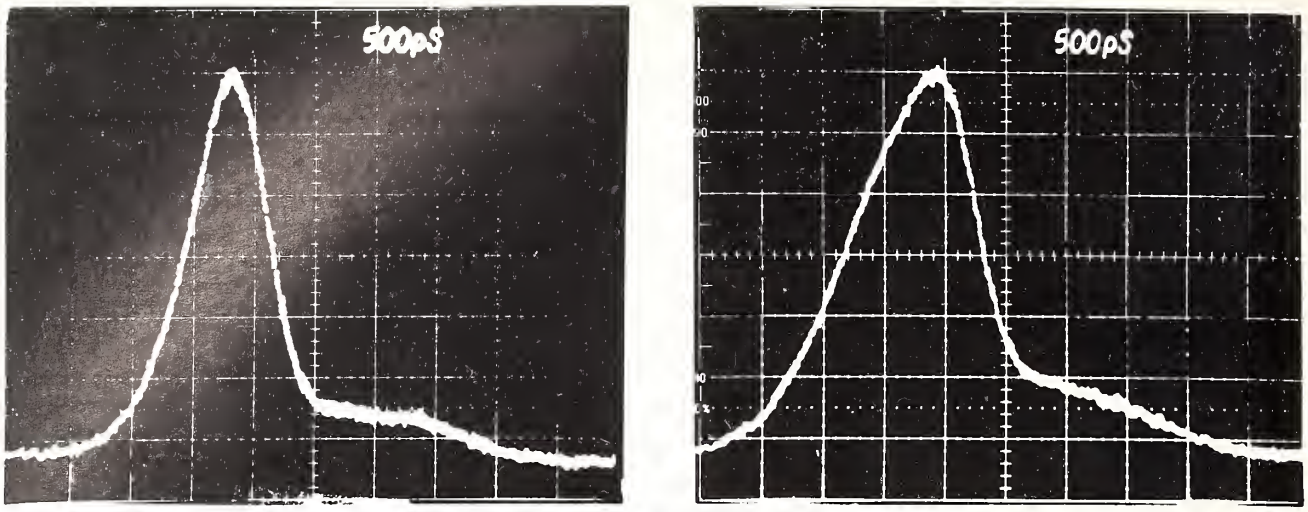


(a) (b)

Figure 25. Output pulses from 1.5 km, graded-index optical fiber at two wavelengths, (a) 803 nm, (b) 902 nm for nearly identical shaped input pulses of 330 ps FDHM.

occur. For the pulse widths involved (260 ps), and the fiber lengths measured (1 km or more), intramodal broadening effects are negligible for the 824 nm diode if fiber bandwidth is below 1.1 GHz•km.

For a measurement at the bandwidth limit $f_m$, the 6 percent correction could be handled in the following manner. Add 8 percent to the measured bandwidth in the frequency domain and then take a ±4 percent error. This allows for nearly a ±40 percent uncertainty in determining $f_m$. Such a generous uncertainty is possible since at $f_m$ the intramodal contribution represents a small correction to the bandwidth.

## 6. RESULTS OF BANDWIDTH RELATED MEASUREMENTS

The purpose of this section is to demonstrate typical fiber bandwidth behavior in a quantitative manner. Results were selected from about 20 fibers and represent a diverse mix of properties.

### 6.1 Wavelength Dependence of Bandwidth

Differences in the refractive index dispersion of the dopants used in making graded index optical fibers results in an index profile that is wavelength dependent. This "profile dispersion" directly affects the optical fiber bandwidth which depends critically on the shape of the index profile. Cohen has shown that bandwidth may increase or decrease with wavelength depending upon the profile characteristics [22].

Figure 25 shows a 1.6 km fiber with a rather large wavelength dependence in the bandwidth. Figure 25a gives the output at 803 nm while figure 25b is the output at 902 nm. The inputs were 330 ps FDHM for both wavelengths. Measurements of the transfer functions indicated the 3 dB bandwidth decreased from 0.90 GHz·km at 803 nm to 0.61 GHz·km at 902 nm.

## 6.2 Mode Mixing

In a multimode optical fiber, power can be coupled between modes as a result of perturbations in the optical characteristics induced by physical changes. If fast and slow modes are mixed, the delay times tend to be equalized and the bandwidth increases. Figure 26a shows the output from a 1 km lightly buffered fiber, loosely wound in a single layer on a measurement spool. The input pulse duration was about 300 ps. Figure 26b shows the output using the same source but now with the fiber under tension and wound in multiple layers so as to introduce microbending. The bandwidth has now increased so that the output pulse is barely distinguishable from the input and is largely representative of the intramodal broadening occuring in the fiber. Fiber attenuation also increased between these two cases; an additional microbending loss of more than 10 dB was incurred to achieve the above bandwidth enhancement.

## 6.3. Accuracy of Gaussian Predictions

If the fiber frequency response and input pulse are assumed to be Gaussian, the 3 dB bandwidth may be predicted by a simple deconvolution of the input pulse duration from the

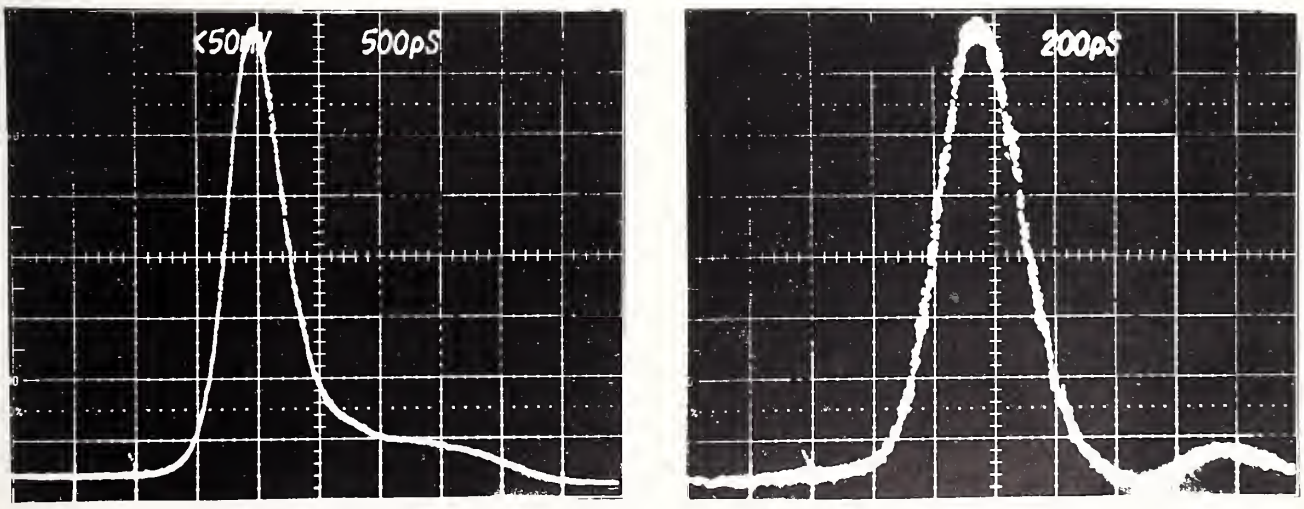


(a) (b)

Figure 26. Influence of microbending on bandwidth of a lightly buffered, graded-index optical fiber, 1 km length, (a) output pulse with fiber wound loose in a single layer, (b) output pulse with fiber wound under stress in multiple layers (824 nm diode). In (b) the output pulse shape is barely distinguishable from the input; due to microbending bandwidth has been increased by approximately a factor of four.

Table 4. Accuracy of Gaussian assumption for determining 3 dB bandwidth from half-duration pulse broadening

| Graded index fiber | Length, km | Bandwidth, Gaussian prediction, MHz | Actual bandwidth, MHz | Percentage difference, percent |
|---|---|---|---|---|
| 308 | 1.4 | 256 | 198 | +29 |
| 223 | 1.1 | 846 | 732 | +16 |
| 116 | 1.6 | 612 | 673 | -9 |
| 206 | 1.0 | 713 | 752 | -5 |
| 1206 | 1.4 | 280 | 325 | -14 |
| 1208 | 1.4 | 189 | 210 | -10 |
| 1212 | 0.7 | 467 | 402 | +16 |
| 207 | 1.0 | 1048 | 1062 | -1 |
| 156 | 1.0 | 164 | 184 | -11 |

output pulse duration [section 2, eq (11)]. The accuracy of this assumption was checked using the present system to measure the actual bandwidth. All fibers measured over a given period of time with the system are included with no preselection. Output pulse shapes ranged from symmetric to assymmetric (usually the latter), some with long leading edges others with long trailing edges; however, none of the pulses exhibited multiple peaks. The results are given table 4. The agreement is close enough for some purposes and is in accord with similar statements made by Midwinter [23].

### 6.4 Fiber Response Pathologies

The impulse-response, transfer-function characteristics of multimode fibers show a rich variability. The purpose of this section is to demonstrate the range of behavior that can be observed.

#### 6.4.1 Pulse Shapes

In some cases, output waveforms from multimode fibers exhibit multiple pulses or peaks. Results similar to those reported by Eickhoff have been observed where energy is

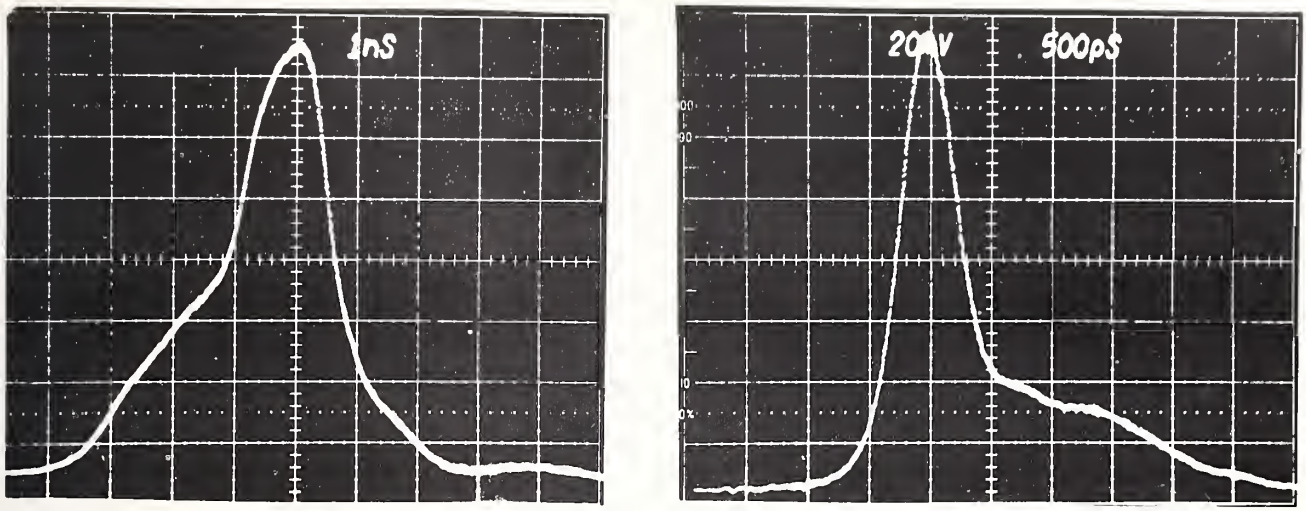


(a) (b)

Figure 27. Opposite pulse broadening behavior in graded-index optical fibers, (a) 1.1 km fiber (fiber B, 902 nm) with some modes arriving too early, (b) 1.3 km fiber (fiber A, 824 nm) with some modes arriving too late.

carried in an on-axis index peak and for a 1 km fiber arrives over 10 ns later than the main pulse [24]. In another instance, we measured a fiber having 20 multiple peaks resolved to the half-widths in its impulse response. In most situations, however, the fiber response has a single maximum which is frequently asymmetric about the peak. The asymmetry is

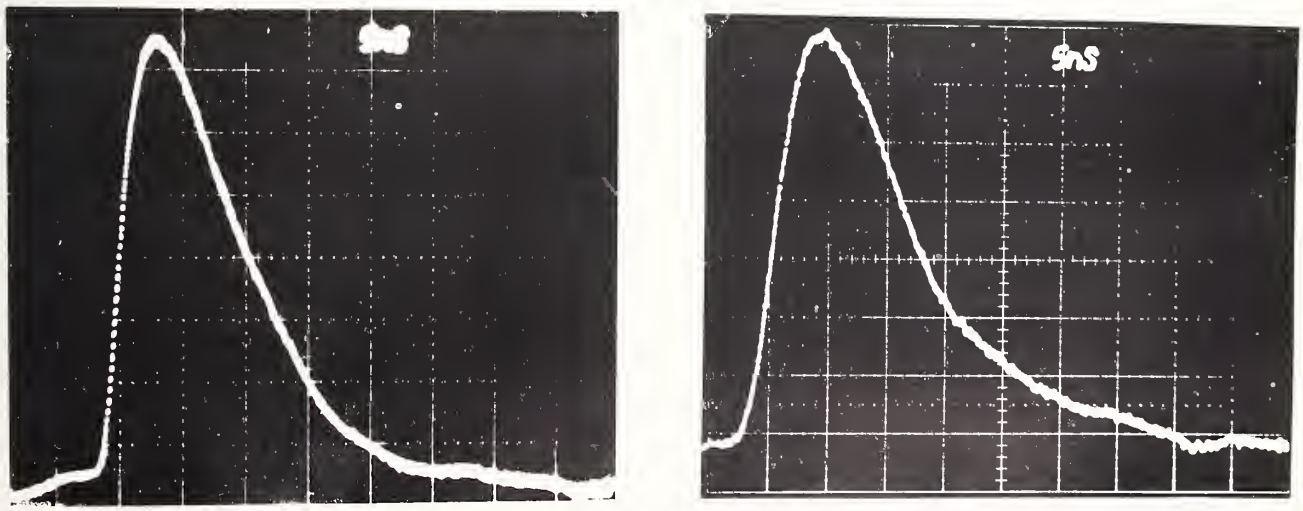


(a) (b)

Figure 28. Characteristic impulse response for step index fibers (a) 85 μm core, 0.18 km length, 824 nm and (b) 55 μm core, 0.25 NA, 1.2 km length, 824 nm.

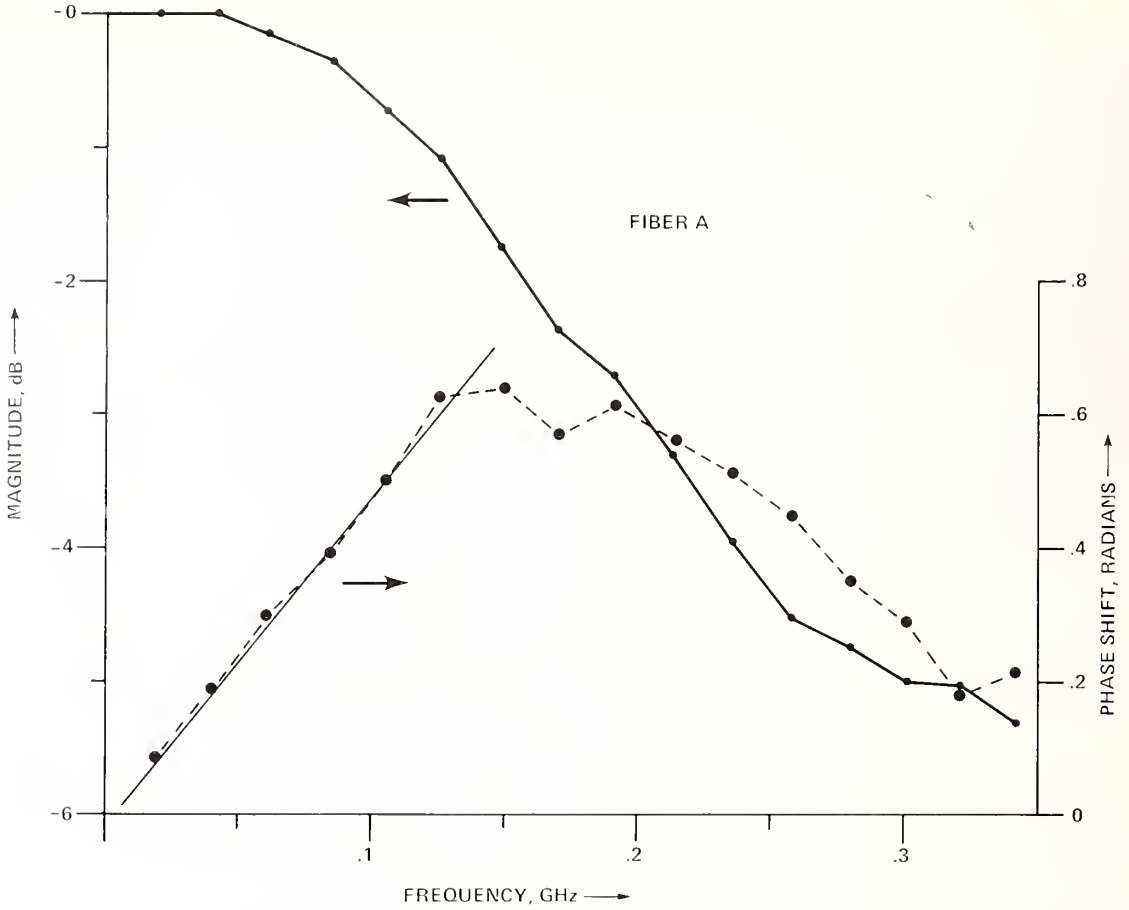


Figure 29. Magnitude and phase of the transfer function versus frequency for a graded-index fiber exhibiting large phase distortion (Fiber A, 1.3 km length, 824 nm).

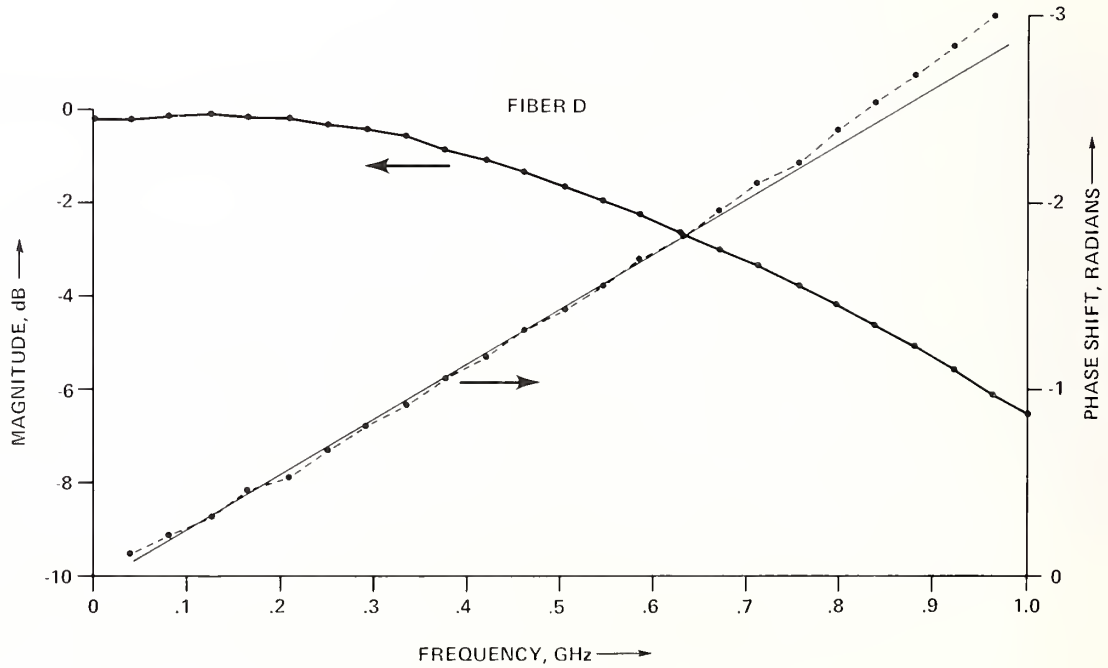


Figure 30. Magnitude and phase of the transfer function versus frequency for a graded-index fiber exhibiting low phase distortion (Fiber D, 1.5 km length, 824 nm).

characterized by either a low-level leading edge or a low-level trailing edge; this results from an index profile which does not adequately equalize mode arrival time. Figure 27 is typical of this behavior. If one assumes most of the energy is carried in low to medium order modes, then the fiber in figure 27a represents a profile with insufficient doping near the cladding (high order modes arrive too early and are overcompensated with respect to group velocity) while the opposite (too much doping and undercompensation) would be true in figure 27b.

While graded index fibers exhibit great variations in behavior, multimode step fibers have a characteristic impulse response. The impulse response has a rapid rise with a nearly ramp-like decay lasting for a longer time (fig. 28). This general behavior is roughly predicted by simple mode propagation models [25].

### 6.4.2 Frequency-Phase Characteristics

Since output pulses from fibers show diverse behavior, it is not surprising that the frequency response characteristics also exhibit a diversity. This is evident in a comparison of the magnitude and phase responses for fibers. Fibers have been observed where the significant distortion in the phase has occurred both before and after the frequency where the magnitude is down by 3 dB. Examples of both kinds of behavior are given in figures 29 and 30. No distortion in the phase is represented by a straight line on these plots; i.e., linear phase shift with frequency. For the fiber of figure 29, the phase distorts significantly before the 3 dB frequency; while in figure 30, the phase is fairly linear out to the 5 dB frequency.

## 7. CONCLUSIONS

Perhaps the greatest uncertainty in making bandwidth measurements on multimode fibers is the lack of standardized launching conditions. This makes a discussion of systematic error difficult because at the present one cannot say that one launching condition is more "correct" than another. The launching conditions presently employed with this system tend to over fill the fiber under test. A spot size of 55 μm and a launch NA of 0.25 will fill the mode volume of most graded-index fibers meeting the proposed standard core size of 50 μm. Such a launching condition has the following merits. (1) It will give a lower estimate for most fibers to the bandwidth encountered in actual systems use and therefore could be used in "worst case" calculations. (2) It is the starting point for the use of Equilibrium Mode Simulators (EMS). An EMS would strip away specific high loss modes which do not propagate very far in the fiber. (3) It can be reproduced by other laboratories and is independent of a particular diode radiation characteristic.

Some additional work needs to be done by standards groups on the terminology used in reporting bandwidth. For multimode fibers, reporting the intermodal contribution seems appropriate. The intramodal part could be specified as a function of wavelength by the manufacturer based on refractive index data and specified per unit fiber length and source linewidth. Also, a problem remains on reporting the bandwidth per unit length where the actual measurement length is quite different from the unit length.

With improved fiber characteristics at the longer wavelengths, more emphasis will be placed on bandwidth measurements over the 1.1 to 1.5 μm region. Many of the points emphasied in this chapter still remain valid. Material dispersion however will not be as important since the material broadening is approximately 40 ps/km•nm at 1.1 μm and even less for longer wavelength.

## 8. REFERENCES


[1] Olshansky, R.; Keck, D. B. Pulse broadening in graded-index optical fibers. Appl. Opt. 15(2):483-491; February 1976.

[2] Cohen, L. G. Shuttle pulse measurements of pulse spreading in an optical fiber. Appl. Opt. 14(6):1351-1356; June 1976.

[3] Cohen, L. G.; Astle, H. W.; Kaminow, I. P. Frequency domain measurements of dispersion in multimode optical fibers. Appl. Phys. Lett. 30(1):17-19; January 1977.

[4] Vassallo, Linear power responses of an optical fiber, IEEE Trans. Microwave Theory Tech. MTT-25(7):572-576; July 1977.

[5] Machida, S.; et al. Interference of an AlGaAs laser diode using a 4.15 km single mode fiber cable. IEEE J. Quantum Electron. QE-15(7):535-537; July 1979.

[6] Gloge, D.; Chinnock, E. L.; Lee, T. P. Self-pulsing GaAs laser for fiber-dispersion measurements. IEEE J. Quantum Electron. QE-8(11):844-846; November 1972.

[7] Keck, D. B. Spatial and temporal power transfer measurements on a low-loss optical waveguide. Appl. Opt. 13:1882-1888; August 1974.

[8] Hansen, J. B.; Schmidt, W. A. A fast risetime avalanche transistor pulse generator for driving injection lasers. Proc. IEEE 55(2):216-217; February 1967.

[9] Andrews, J. R. Inexpensive laser diode pulse generator for optical waveguide studies. Rev. Sci. Instrum. 45(1):22-24; January 1974.

[10] Dannwolf, J. W.; et al. Optical-Fiber impulse-response measurement system. IEEE Trans. Instrum. Meas. IM-25(4):401-406; December 1976.

[11] In order to describe adequately the experimental procedure and permit reproduction of this work, certain commercial components are mentioned here and elsewhere; in no way does this represent an endorsement by NBS. Other components may work equally well or better.

[12] Wright, J. V.; Nelson, B. D. Pulse compression in optical fibers. Electron. Lett. 13(12):361-363; June 1977.

[13] Green, S. I. 50 picosecond detector pulse monitor. Rev. Sci. Instrum. 47(9):1083-1085; September 1976.

[14] The authors would like to thank Matt Young of the Time-Domain Metrology Section of NBS for use of the mode-locked Nd:YAG laser.

[15] Costa, B.; et al. Wavelength dependence of differential group delay in graded-index optical fibers: Application to fiber-links characterization. Paper ThG5, Topical Meeting on Optical Fiber Communications, March 6-8, 1979, Washington, DC.

[16] Green, S. I. Wideband 1.064 micrometer detector evaluation. McDonnell Douglas Astronautics Co. Final Report NA55-20616 (NTIS # N77-32459/8wz).

[17] Love, W. F. Novel mode scrambler for use in optical-fiber bandwidth measurements. Paper ThG2, Topical Meeting on Optical Fiber Communications, March 6-8, 1979, Washington, DC.

[18] Tokuda, M.; et al. Measurement of baseband frequency response of multimode fibre by using a new type of mode scrambler. Electron. Lett. 13(5):146-147; March 1977.

[19] Dakin, J. P.; et al. Launching into glass fibre optical waveguides. Opt. Commun. 4(5):354-357; January 1972.

[20] Andrews, J. R.; Young, M. Time domain pulse measurements and computed frequency responses of optical communications components. NBSIR 79-1620; 1979.

[21] Ramirez, R. W. Evaluating fibers digitally. Laser Focus 15(4):46-52; April 1979.

[22] Cohen, L. G.; et al. Profile dispersion effects on transmission bandwidths in graded index optical fibers. IEEE J. Quantum Electron. QE-14(1):37-41; January 1978.

[23] Midwinter, J. E. Optical fibers for transmission. New York, NY: John Wiley & Sons; 1979.

[24] Eickhoff, W.; Krumpholtz, O. Pulse response and microbending losses of an optical glass-fibre waveguide with a bump in its index profile. Electron. Lett. 13(9):256-257; April 1977.

[25] Gallawa, R. L. A user's manual for optical waveguide communications. NTIA Report #OTR 76-83.

[26] Gloge, D.; Chinnok, E. L.; Lee, T. P. GaAs twin-laser setup to measure mode and material dispersion in optical fibers. Appl. Opt. 13(2):261-263; February 1974.

[27] Sordo, B.; Esposto, F.; Costa, B. Proceedings of the Fourth European Conference on Optical Communications; September 12-15, 1978; Genova, Italy.

[28] Payne, D.N. and Hartog, A.H. Determination of the wavelength of zero material dispersion in optical fibers by pulse-delay measurements. Electron. Lett. 13(21): 627-629; October 1977.

[29] Cohen, L.G.; Chinlon, L. Pulse delay measurements in the zero material dispersion wavelength region for optical fibers. Appl. Opt. 16(12):3136-3139; December 1977.

## APPENDIX

This appendix describes measurements of optical fiber material dispersion constants. Material dispersion was measured by a technique described by Gloge et al. [26]. In this method, the dispersion is determined by noting the differential delay between pulses from two different wavelength laser diodes. This work utilizes the same method with the following extensions: (1) four laser diodes with appropriate wavelengths to cover the whole 0.8 to 0.9 mm wavelength region, (2) shorter pulse widths to provide good resolution, (3) a mode scrambler to reduce effects of differential launching conditions, and (4) the use of high-bandwidth fibers to minimize intermodal contributions.

An experimental configuration for determining material dispersion is shown in figure 31. By pulsing pairs of diodes, pulses at two different wavelengths were launched down the test fiber. Diodes at 803, 824, 866, and 902 nm were used to cover the 0.8 to 0.9 mm region. Pulses were separated slightly in time before launching to avoid overlap which would shift the positions of the peaks. A pulse pair before and after traversing a 1 km fiber length is shown in figure 32a and 32b. In this case, a wavelength difference of 21 nm gives a differential delay of 2.4 ns. Measurements of differential delay between pulses were repeatable within ±100 ps.

Material dispersion was determined for fibers labeled 2, 4, and 5, figure 33. These fibers had lengths of 1.0, 1.5, and 1.4 km and exhibited pulse FDHM broadenings of 0.42, 0.74, and 1.1 ns, respectively. Bandwidth (3 dB optical) determined in the frequency domain by the FFT ratio of output to input pulses was 1.1, 0.9, and 0.4 GHz-km, respectively. A

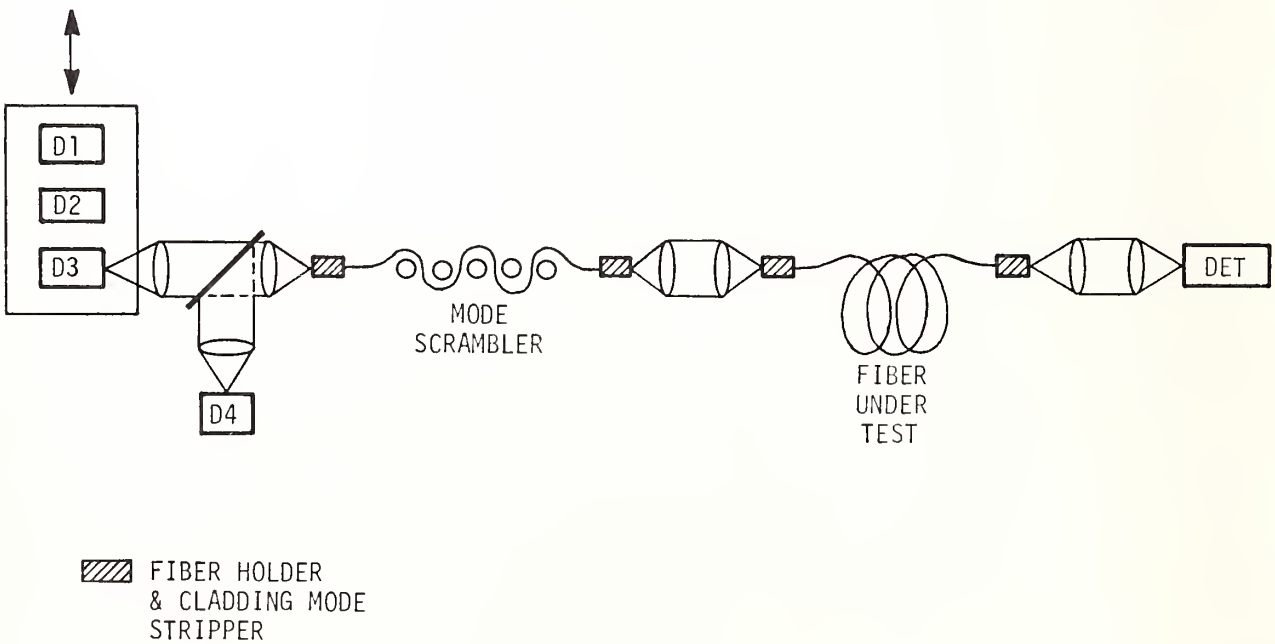


Figure 31. Apparatus for measuring material dispersion by simultaneous propagation of pulses from pairs of laser diodes.

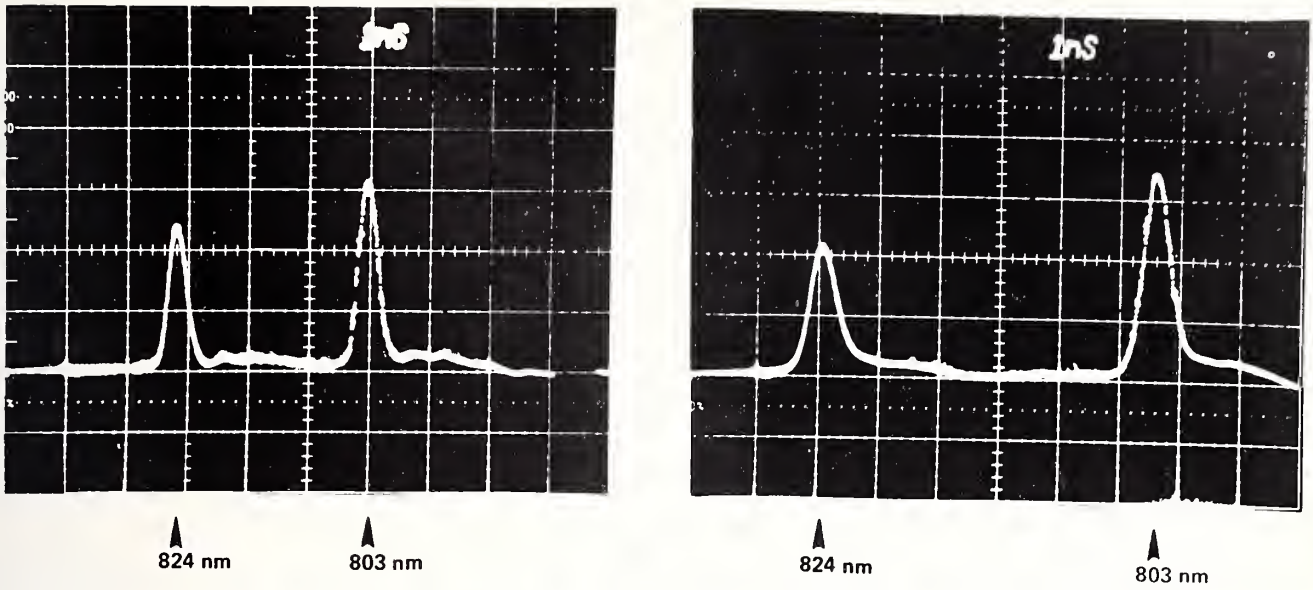


(a) (b)

Figure 32. Example of group delay material dispersion in an optical fiber showing a pulse pair (a) before and (b) after propagating through a 1 km length of fiber.

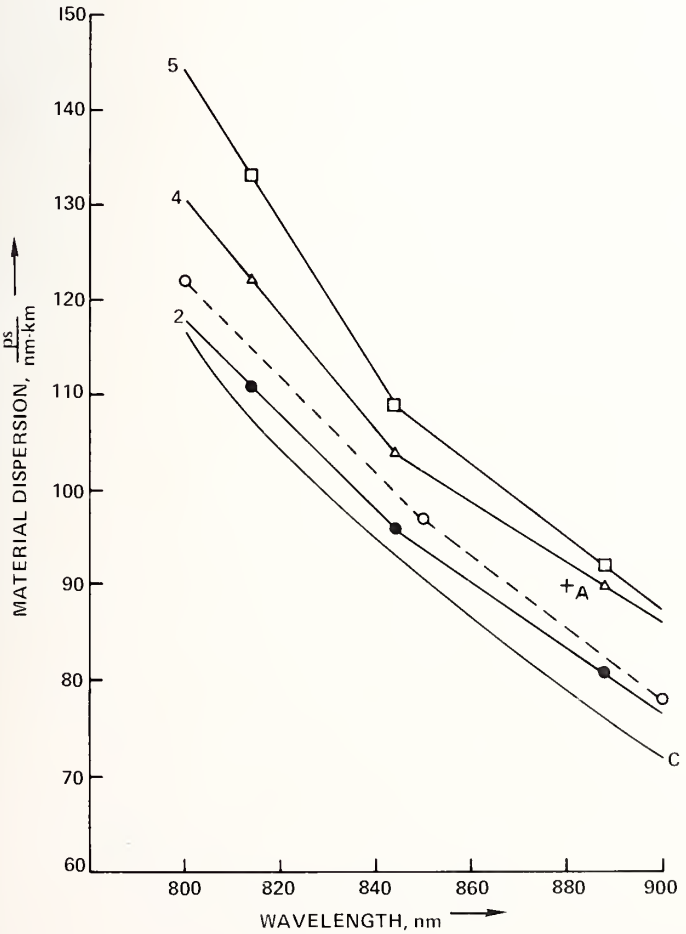


Figure 33. Material dispersion constants for a number of commercially available graded-index fibers labeled 2, 4, and 5. Curve C and point A are measurements from the literature while the dashed curve is calculated from index data supplied by the manufacturer of fiber 2.

single point, A, inferred from the data of reference 26 is also shown in figure 33. Other data from the literature representing fibers measured at another laboratory using similar techniques is included (curve C) [27]. Overall, results do indicate significant, measurable differences between fibers. However, at any one wavelength, a ±10 percent variation would nearly bracket the data. The result on fiber 2 has the least influence from intermodal delay of the fibers measured. This fiber exhibited the highest bandwidth and the least variation of bandwidth with wavelength. Also, the manufacturer of fiber 2 provided sufficient representative index data to determine eq (16), at 800, 850, and 900 nm. Values of M from this data are indicated by the dashed curve and are slightly above the experimental values. While the above measurements were limited to the 800-900 nm wavelength region, other experimental results are available from the literature for longer wavelengths [28,29].

# Chapter 3

# Refracted-Ray Scanning (Refracted Near-Field Scanning) for Measuring Index Profiles of Optical Fibers

**M. Young**

The purpose of this work is twofold. First, it provides an elementary description and tutorial overview of the refracted-ray method of measuring fiber-index profiles. Second, it presents new results concerning the theoretical foundation, the linearity and precision, and other aspects of the method. In particular, we find that index differences may be measured to 5 percent or better and spatial resolution is diffraction limited. We conclude by showing about 3 percent agreement with another laboratory, good agreement with numerical-aperture measurements performed by participants in a round-robin experiment, and good agreement on single-mode fiber measurements.

## CONTENTS

## 1. INTRODUCTION

Roughly a half-dozen methods have been proposed and implemented for determining the refractive-index profile of an optical-fiber waveguide. At least half of these will no doubt find use in one or another application.

One of the more promising techniques for a simple high-resolution measurement is known as refracted near-field scanning or, preferably, refracted-ray scanning. It is one of the few measurement systems capable of generating the profile of a single-mode fiber. First proposed and demonstrated by Stewart [1], the method was further developed by White [2]. In addition, I have analyzed the precision and other aspects [3-6], Saunders has compared his results with other methods [7], and Reid and Stewart have developed an extremely high resolution scanner [8].

The purpose of this chapter is to describe refracted-ray scanning in detail, to analyze it as a measurement system, to document a particular system for implementing it, and to show some exemplary results, including application to single-mode fibers with depressed cladding. First, however, let us examine some of the alternate approaches that are either in use or have been proposed.

Certain methods illuminate the fiber in a direction perpendicular to the axis; that is, they look through the fiber sides rather than at its end face. These transverse-illumination methods have the advantage that they can be used to examine a fiber in real time, as it is being produced. Likewise, these methods may be used to determine the fiber's properties at several points without having to cut the fiber to prepare an end.

One of the simplest techniques is that developed by Liu, who used an oil-immersion method similar to that used in crystallography [9]. By placing a short piece of fiber in a microscope and varying the index of a matching fluid, Liu was able to measure the indices of the core and cladding of a step fiber.

Later workers illuminated immersed fibers transversely with a laser and placed the apparatus in an interference microscope or interferometer [10-15]. The index difference between core and cladding can be obtained fairly readily and without detailed calculation [10-12], as can the alpha parameter of a fiber that is assumed to have a power-law profile [13]. In addition, formulas can be derived for calculating the full index profile from measurements of the fringe intensity [14,15]. The overall accuracy of these measurements is on the order of 10 percent, and spatial resolution is not great because the finite width of the fringes limits resolution.

Transverse-scattering methods, including backscatter, have been implemented by several groups [16-18]. With these techniques, a fiber (also immersed in oil) is illuminated transversely by a laser, and the far-field diffraction pattern is observed. A great deal of data is required, so that an automatic data-acquisition scheme is almost mandatory; the index

profile is calculated by computer. The accuracy of the method is greater than of transverse interferometry, but no simple or direct methods for determining alpha or core-cladding index difference have been developed.

More recently, Marcuse and Presby have developed a focusing method that uses transverse illumination and may be used to examine either fibers or preforms [19-21]. This technique scans the near field of the transversely illuminated fiber and calculates the index profile from data acquired by a computer. Because circular symmetry is assumed in the calculation, the calculated profile is necessarily symmetric, even if the fiber is not.

Presby and Marcuse have also developed a fluorescence method for determining the index profile of fibers or preforms [22]. They illuminate a germania-doped sample with ultraviolet light and observe the germania fluorescence in a direction transverse to the axis. They assume that the fluorescent intensity is proportional to germania concentration and therefore to index profile. A computer calculates the profile.

Other methods illuminate the fiber along the axis; either a thin, specially prepared sample or a flat, properly prepared end is required. While not amenable to real-time measurement as a fiber is drawn nor to nondestructive testing, these methods provide a more direct evaluation of the index profile, and certain of them offer resolution that is comparable with conventional optical microscopy.

Axial or slab interference microscopy (as opposed to transverse interference microscopy) requires a thin slice of fiber to be placed in an interference microscope or interferometer [23,25]. The interferogram is generally interpreted by computer. In any case, the slab is treated as a pure-phase object for the purpose of interpreting the interference pattern; because a graded-index fiber has focusing properties, it should not be regarded as a phase object unless the sample is extremely thin, say of the order of tens of micrometers. Further, it is difficult to determine what errors arise from the effects of polishing; these may include changes of the surface composition of the material and deviation from flatness as a result of the polishing rate's varying with glass composition. As with transverse interferometry, the number of fringes is small, so the spatial resolution is apt to be relatively low.

Fresnel reflection from the cleaved or polished end of a fiber has been used to measure the index profile [26-28]. This method is direct and precise and has high resolution. It is difficult because the changes in reflectance are typically less than 1 percent; highly stable radiometric techniques must be employed. This method has recently been improved with an index-matching technique [27]. However, the reflectance of the face may change as the result of contamination or exposure to the atmosphere.

Other methods that have been discussed in the literature depend on examination of the far-field interference pattern [29-31], on special properties of self-focusing fibers [32] and on the spatial coherence of the light emerging from an optical fiber [33]. See also

reference 34 for a more detailed review of index-profile measurements and reference 41 for a comparison of several techniques.

## 2. NEAR-FIELD SCANNING

Near-field scanning depends on the existence of a local acceptance angle (or numerical aperture) at any point on the entrance face of the fiber [36]. That is, the vertex angle of the cone that can enter the fiber and be guided depends on the index of the core at the point of illumination.

The fact was first exploited by Sladen, Payne, and Adams [37,38]. This group illuminated the end of a short fiber with a uniform, lambertian source. They scanned the exit face of the fiber with a detector and thereby generated a plot of the output power as a function of position along a diameter of the fiber.

The exact proportionality between the local numerical aperture and the power coupled into the fiber holds only for guided rays. Therefore, Adams, Payne, and Sladen had to derive correction factors for the leaky-ray contribution to the power that propagates into the fiber [39]. With these correction factors, they are able to calculate the index profile to a high degree of accuracy.

A modification of near-field scanning has also been developed [40]. In this modification, the low-index jacket layer is not removed from the fiber and cladding modes are deliberately excited. The fiber behaves something like a step fiber with a perturbation near the center; the leaky-mode problem is at least to a degree shifted to the cladding-jacket boundary, and the entire core region may be visualized, relatively free of leaky modes. Whether the profile may be measured sufficiently precisely by modified near-field scanning has yet to be determined. In addition, the application to fibers that are not suitably jacketed may be somewhat cumbersome.

Other workers devised a similar scheme for measuring the index profile [41,42]. Rather than illuminate the entire entrance face of the fiber, these groups focused a laser beam to a point and observed the total power radiated at the far end of the fiber as a function of the position of the point on the entrance face. This variation of near-field scanning also requires correction for leaky modes; in principle, it differs only slightly from the original technique.*

*For simplicity of nomenclature and for avoiding confusion, I shall refer to both these methods as near-field scanning. When it is necessary to distinguish between them, I shall use the terms entrance-face scanning and exit-face scanning. Likewise, I will not use the term refracted near-field scanning, but rather will refer to this method as refracted-ray scanning.

In practice, entrance-face scanning may be preferable to exit-face scanning because an absolute calibration is possible. In addition, imperfections or mode coupling along the fiber will have minimal effect on the relative powers transmitted by excitations at different points on the entrance face. The same is not necessarily true of the exit-face scan (the original method); although I know of no detailed studies to this effect, it seems quite possible that such factors as mode coupling will distort the results in an unpredictable way, particularly in a fiber with fine structure like the characteristic index dip along the axis (see section 8, below). On the other hand, exit-face scanning is somewhat simpler because the detector actually scans a magnified image of the exit face.

There is another difficulty with both methods of near-field scanning. This is the problem of making the leaky-mode corrections with confidence. Microbending or slight deviations of the fiber from circularity may drastically alter the leaky-mode propagation; indeed, Petermann has suggested that the leaky-mode correction may be unnecessary for fibers with nearly square-law profiles [43]. Thus, whereas near-field scanning is both simple and elegant, it may be that its major use will be to measure the fiber diameter or give excellent, qualitative information about the index profile.

## 3. REFRACTED-RAY SCANNING

Stewart's innovation was to illuminate a fiber with a focused beam whose vertex angle greatly exceeds the acceptance angle of the fiber and to observe not the rays that are trapped by the fiber, but the rays that are refracted at the core-cladding interface [1]. With this method, it is often possible to eliminate entirely the deleterious effects of the leaky modes and to develop a system that generates the index profile directly, without the need for a correction factor.

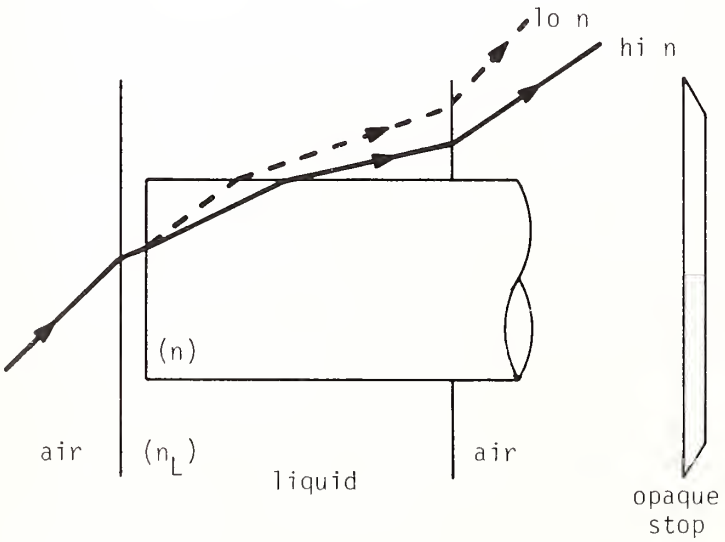


Figure 1. The lower the index of the fiber, the greater the vertex angle of the emergent cone.

To understand the principle of the method, it is helpful to examine figure 1. In that figure, a fiber whose index is n is surrounded by a liquid whose index is $n_L$. The fiber is illuminated by a focused cone of rays; the ray that is drawn in the figure represents the most-oblique ray in the cone, a marginal ray for the lens that focuses the beam. Because the angle of incidence exceeds the acceptance angle of the fiber, the ray is refracted both at the entrance face of the fiber and at the periphery.

Suppose now that we alter the index of the fiber in some way, for example by changing the fiber entirely. The ray that emerges is now represented by the dashed line in figure 1; as the index of the fiber is decreased, the angle formed by the marginal ray's intersection with the axis increases accordingly.

Now we introduce an opaque, circular stop directly behind the fiber; the stop is designed to intercept all but the outermost rays of the emergent cone. A conical shell is transmitted beyond the stop. In the plane of the stop, the inner radius of the shell is always equal to the radius of the stop. The outer radius, however, varies with the index of the fiber. Therefore, the power that is transmitted around the stop also varies with index. The heart of refracted-ray scanning lies in the fact that, under the right conditions, the change of transmitted power is precisely proportional to the change of index of the fiber.

Figure 1 used a uniform, unclad fiber for tutorial purposes. In practice, all that is required is a fiber whose index variation is a function of radius only. The vertex of the incident cone is scanned across the entrance face of the fiber; the power transmitted by the stop is a linear function of the index of the fiber at the point of illumination.

## 4. STEP FIBER

For illustrative purposes, we begin by examining a meridional ray in a step fiber. The extension to the general case is straightforward.

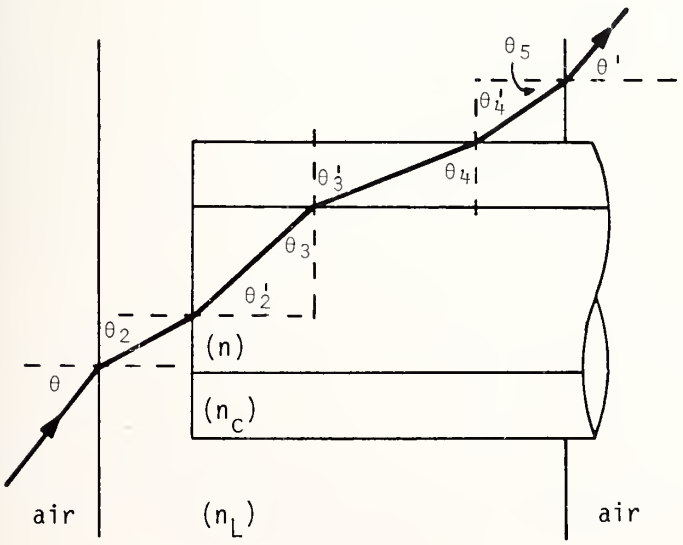


Figure 2. The path of a meridional ray through a step fiber.

Figure 2 traces the path of the marginal ray that is focused onto the face of the fiber. The fiber is immersed in a fluid whose index is $n_L$. The index of the fiber core is n; that of the cladding is $n_c$.

The ray enters the system at angle $\theta$ to the axis of the fiber. It suffers a couple of refractions through a microscope coverslip (whose thickness is not shown) before reaching point 2. Because the coverslip makes a right angle to the axis of the system, we may easily show that

$$\sin \theta = n_L \sin \theta_2. \tag{1}$$

$n_L \sin \theta_2$ is the numerical aperture (NA) of the cone that converges onto the face of the fiber and is equal to the NA of the microscope objective used to focus the light.

If we apply Snell's law at points 2 and 3, we find that

$$n_L \sin \theta_2 = n \sin \theta_2', \tag{2}$$

and

$$n_c \sin \theta_3' = n \cos \theta_2'. \tag{3}$$

If we square and add these equations and use eq (1), we find that

$$\sin^2 \theta + n_c^2 \sin^2 \theta_3' = n^2. \tag{4}$$

We may eliminate the term in $\theta_3'$ by applying Snell's law at points 4 and 5:

$$n_c \sin \theta_3' = n_L \sin \theta_4', \tag{5}$$

and

$$\sin \theta' = n_L \cos \theta_4'. \tag{6}$$

Finally, we square and add eqs (5) and (6) and combine with eq (4) to learn that

$$n^2 = n_L^2 + \sin^2 \theta - \sin^2 \theta'. \tag{7}$$

Equation (7) shows how the vertex angle $\theta'$ of the emergent conical shell of rays is related to the core index n of the fiber.

## 5. A MORE-GENERAL CASE

Consider the general case of a skew ray incident on a graded-index fiber with angle of incidence $\theta$ and arbitrary azimuthal angle $\phi$; this is shown in figure 3, with the cover slip omitted for clarity.

Snell's law may be written as

$$n \sin i = \text{constant}, \tag{8}$$

where i is the angle of incidence at an arbitrary interface. Equation (8) is valid whether the index change is sudden or gradual. If $\lambda$ is the vacuum wavelength of light, then the magnitude k of the wavevector in a medium is $2\pi n/\lambda$; therefore, Snell's law may also be written in the equivalent form,

$$k \sin i = k_{\perp} = \text{constant}. \tag{8a}$$

That is, the component of the wave vector perpendicular to the index gradient is conserved as the ray propagates. White has used this principle to derive a general form of eq (7). It is applicable to any fiber whose index variations are purely radial.

Let us number points 1 through 5 as in figure 2, remembering, however, that the ray path inside the fiber is in general curved and need not lie in a plane. Using eq (8a), we find that

$$\sin \theta = n_L \sin \theta_2 = n(r) \sin \theta_2'. \tag{9}$$

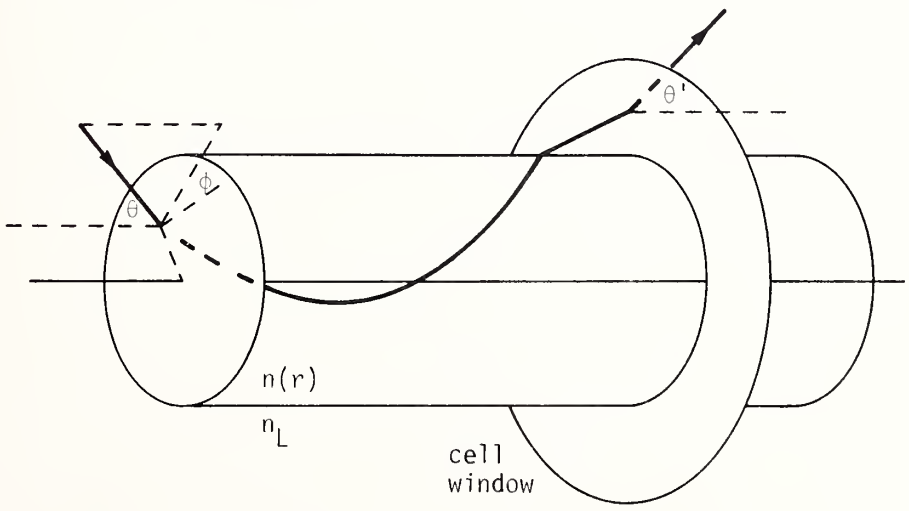


Figure 3. The path of a skew ray through a graded-index fiber. $\theta$ is the angle of incidence, and $\phi$, which lies in a plane perpendicular to the axis, is the azimuthal angle. The coverslip at the front of the cell is suppressed for clarity.

where $n(r)$ is the index of the fiber at a distance $r$ from the axis of symmetry. From point 2 until point 4, the index variations become purely radial, so the axial component of the wave vector remains constant; that is,

$$n(r) \cos \theta_2' = n_L \cos \theta_5. \tag{10}$$

Finally, at point 5,

$$n_L \sin \theta_5 = \sin \theta'. \tag{11}$$

Combining eqs (9) through (11) as before, we find that

$$n^2(r) = n_L^2 + \sin^2 \theta - \sin^2 \theta'. \tag{12}$$

This is the same as eq (2) of reference 2. When $n(r)$ is nearly equal to $n_L$ we may rewrite eq (12) in the form

$$2n_L \Delta n(r) = \sin^2 \theta - \sin^2 \theta'. \tag{12a}$$

$\Delta n(r) = n(r) - n_L \ll n(r), n_L$; it is <u>not</u> the delta parameter of the fiber. We discuss the importance of eqs (12) and (12a) in the following sections.

## 6. RADIOMETRIC ANALYSIS

A lambertian source is one whose radiance is independent of angle. Many thermal sources approximate lambertian sources; lasers and many light-emitting diodes do not. We begin this section by assuming that the source is lambertian and later generalize to a non-lambertian case.

A lambertian source emits total power proportional to $\sin^2 \theta$ into a cone whose vertex angle is $\theta'$ [44]. In the refracted-ray technique, we insert an opaque stop behind the fiber to block some of the rays refracted by the fiber, as in figure 1. If the source is lambertian, then the power transmitted around the stop may be expressed as

$$P(\theta') = A (\sin^2 \theta' - \sin^2 \theta_s), \tag{13}$$

where $\theta_s$ is the angle subtended by the stop and A is a constant of proportionality.

If we let $n(r) = n_L$ (no fiber in the system), then we find from eq (12) that $\theta' = \theta$. If we call the power transmitted around the stop $P_o$, then we find that

$$A = P_o/(\sin^2 \theta - \sin^2 \theta_s). \tag{14}$$

Finally, if we combine eqs (12a), (13) and (14), we find that

$$2\, n_L\, \Delta n(r) = \frac{P(\theta') - P_o}{P_o} (\sin^2 \theta - \sin^2 \theta_s). \tag{15}$$

All the terms in this equation are constants except $P(\theta')$ and $\Delta n(r)$. Thus, when $\Delta n$ is small, the power that propagates beyond the stop is in principle almost precisely proportional to the index profile of the fiber. (The derivation has been made for guided rays only; see reference 2 and below for a discussion of leaky rays.)

Equation (15) could be used for calibration of the system if the two angles, $\theta$ and $\theta_s$, could be measured with sufficient precision. In particular, it is difficult to measure $\theta_s$, because this is the angle subtended by the stop at a point inside the fiber--that is, at the virtual image of the point source as seen from the rear of the cell. In part for this reason, it may be preferable to devise a direct calibration method (see section 11, below).

Many sources are not lambertian. For example, a laser beam that is expanded and passed through a small-diameter lens more nearly approximates a uniform point source than a lambertian source. In contrast, edge-emitting diodes and semiconductor lasers emit their radiation more strongly in the forward direction than does a lambertian source. Such sources can be approximated at least roughly by writing their radiance $L(\theta)$ in the form,

$$L(\theta) = L_o \cos^m \theta\ , \tag{16}$$

where we assume circular symmetry. A lambertian source is described by m = 0 and a uniform point by m = -1. Other sources, such as edge-emitting diodes, may be approximated by using eq (16) with m an integer between, say, 5 or 10, depending on the specific source.

As noted above, the power radiated by a lambert source into a cone is proportional to $\sin^2 \theta$; see, for example, eq (3.17) of reference 41. If we follow the derivation leading to that equation, we find that the fraction of the total power radiated into a cone is

$$1 - \cos^{m+2} \theta, \tag{17}$$

which reduces to $\sin^2 \theta$ when m = 0. (This relationship and all subsequent ones are also valid when m = -1.) Equation (13) becomes, in the general case,

$$P(\theta') = A\, (\cos^{m+2} \theta_s - \cos^{m+2} \theta'), \tag{18}$$

and eq (14) becomes

$$A = P_o/(\cos^{m+2} \theta_s - \cos^{m+2} \theta). \tag{19}$$

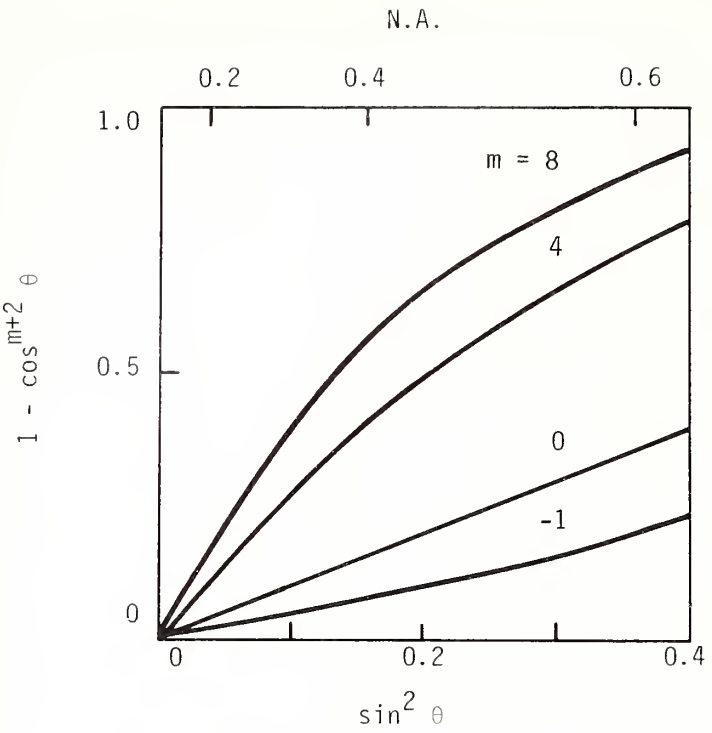


Figure 4. A function useful for describing the power transmitted by a non-lambertian source.

If eq (18) is to describe the fiber index profile, it must be linear in $\sin^2\theta'$, because eq (12a) shows that $\Delta n(r)$ is linear with $\sin^2\theta'$. I have not found it fruitful to try to relate eq (18) directly with $\sin^2\theta$; however, it is instructive to plot $(1 - \cos^{m+2}\theta)$ [eq (17)] as a function of $\sin^2\theta$. This is shown in figure 4 for several values of m.

The most-important cases are the lambertian source and the uniform point source, for which m is equal to 0 and -1. The former case is obviously linear, and the latter is nearly so for numerical apertures up to 0.6 or more. Fortunately, what is important is that the curves be linear only over the small range of angles defined by the stop diameter and the numerical aperture of the focusing lens.

As m increases, the curves become less linear. Also, they deviate substantially from the line m = 0. Therefore, unless m is precisely 0, a calibration based on eq (15) will be invalid.

## 7. LEAKY-RAY ANALYSIS

Suppose that a circular fiber is illuminated off axis by a focused cone of rays. Geometric optics predicts that certain rays will be trapped by the fiber, whereas certain others will be refracted out of the fiber; we refer to these cases as guided and refracted rays (or bound and radiation modes).

Snyder and his colleagues have shown that certain rays are guided but nevertheless suffer high loss and therefore are greatly attenuated after transmission along a relatively short length of fiber; they called these leaky rays [45-47]. The presence of leaky rays invalidates a guided-ray analysis such as that of sections 4, 5 and 6.

Adams, Payne and Sladen have derived correction factors to be used with the near-field scanning technique [39]. However, as noted above, there is some doubt as to the utility of these correction factors in some cases. The refracted-ray technique in many cases avoids the necessity for a correction factor by adjusting the angular subtense of the stop so that the leaky-ray power transmitted by the fiber is intercepted by the stop; only truly refracted rays are passed by the stop. When the leaky-ray contribution is excluded, the guided-ray analysis becomes valid [39].

If a fiber is excited at a point at a distance r from the center, leaky rays will be excited only for angles of incidence $\theta$ given by [2,47]

$$(n^2(r) - n_c^2) / (1 - \rho^2 \cos^2 \phi) \geq \sin^2 \theta > n^2(r) - n_c^2. \tag{20}$$

$\phi$ is the azimuthal angle shown in figure 3, a is the core radius and $\rho$ is (r/a); all other terms have been defined before.

Following White, we exclude leaky rays by restricting angles of incidence to values larger than the largest value of the left side of eq (20). That is, we make the opaque stop large enough that rays pass the stop only if their angle of incidence is larger than that given by

$$\sin^2 \theta > (n^2(r) - n_c^2)/(1 - \rho^2). \tag{21}$$

The right side of this equation defines the largest angle of incidence at which leaky rays will be excited at a given radius.

If we apply eq (11) to eq (21), we find that leaky rays will be excluded provided that $\theta_s$ exceeds the value of $\theta'$ given by

$$\sin^2 \theta_s > \sin^2 \theta' = n_L^2 - n^2(r) + [(n^2(r) - n_c^2)/(1 - \rho^2)] . \tag{22}$$

White has applied eq (22) to a fiber with a power-law profile and quoted his results [2]. A power-law profile may be described by the equations

$$n^2(r) = n_o^2 (1 - 2\rho^{\alpha}\Delta) , \tag{23a}$$

and

$$n_c^2 = n^2(a) = n_o^2 (1 - 2\Delta) , \tag{23b}$$

where

$$n_o = n(0) \text{ and } \Delta = (n_o^2 - n_c^2)/2n_o^2. \tag{23c}$$

If we use these equations in eq (22), we find after a few lines of algebra that

$$\sin^2 \theta_s > (n_L^2 - n_c^2) + 2n_o^2 \rho^2 \Delta (1 - \rho^\alpha)/(1 - \rho^2), \tag{24}$$

which is the same as White's eq (10) [2].

To eliminate the leaky rays entirely, we must examine eq (24) when the $\rho$ term on the right side is largest. Physical arguments show that this term must be a maximum when $\rho = 1$, because leaky rays are excited in greater numbers as we move away from the axis toward the core-cladding interface. We may also show this analytically by differentiating $F(\rho^2)$ with respect to $\rho^2$, where

$$F(\rho^2) = \rho^2(1 - \rho^\alpha)/(1 - \rho^2). \tag{25}$$

The derivative is equal to

$$dF/d\rho^2 = [1 - (1+\alpha/2) \rho^\alpha + (\alpha/2)\rho^{\alpha+2}](1 - \rho^2)^{-2}, \tag{26}$$

which is indeterminate when $\rho = 1$. We may evaluate the limit by substituting $\rho^2 = 1 - \varepsilon$ and letting $\varepsilon \to 0$. We find in this way that the derivative is indeed 0 when $\rho = 1$, and that $F(\rho^2)$ is a maximum at the core-cladding boundary.

Returning now to eq (24), we evaluate $F(\rho^2)$ in the limit $\rho \to 1$ by applying l'Hôpital's rule. The calculation is straightforward and leads to the conclusion that $F(\rho^2)$ approaches $\alpha/2$ as $\rho$ approaches 1.

Thus, the angular subtense of the stop must exceed

$$\sin^2 \theta_s > (n_L^2 - n_c^2) + n_o^2 \alpha \Delta , \tag{27}$$

which is equivalent to eq (13) of reference 2.

If the parameters in eq (27) are reasonably well known, then it is an easy matter to calculate the minimum stop diameter. In the event that all the parameters are not known, then it is possible to measure the first term on the right side of eq (27). Let I be the axial acceptance angle of the fiber. Then, according to reference 2 or reference 44, section 2.8,

$$\sin^2 I = n_o^2 - n_c^2. \tag{28}$$

We now return to eq (11) and replace $\theta$ and $\theta'$ with I and I', where I' is the angle at which the guided ray emerges from the cell. Combining eqs (11) and (27) in this way shows that

$$\sin^2 I' = n_L^2 - n_c^2. \tag{29}$$

Thus, the term $(n_L^2 - n_c^2)$ in eq (27) is equal to $\sin^2 I'$, where I' is the inner vertex angle of the hollow cone of light that is refracted by the fiber. An alternate way of writing eq (27) is therefore to replace $(n_L^2 - n_c^2)$ with sin I'.

Finally, $2n_o^2\Delta$ is equal to $\sin^2 I$, where sin I is sometimes called the theoretical numerical aperture of the fiber. Therefore, eq (27) may be rewritten

$$\sin^2 \theta_s > \sin^2 I' + (\alpha/2) \sin^2 I. \tag{30}$$

The stop must subtend an angle larger than the value of $\theta'$ given by eq (27) or (30). By way of example, let us choose a fiber for which $n_c = 1.46$ (approximately the value for vitreous silica), sin I = 0.25, and $\alpha = 2.3$. Assume further that $n_L$ is one-half percent larger than $n_c$ (it is preferable to choose $n_L > n_c$ to avoid exciting cladding modes). I have chosen these values deliberately to overestimate sin $\theta$.

Using eqs (29) and (30), we find that $\sin^2 I' = 0.021$ and therefore that $\sin \theta_s > 0.3$. A microscope objective with a numerical aperture in the neighborhood of 0.5 will be required; fortunately these are quite common.

A profile with an index step may be thought of as a power-law profile for which $\alpha$ approaches infinity. According to eq (30), there is no value of $\theta_s$ for which leaky rays can be completely excluded if $\alpha$ is unbounded.

When r = 0, $\theta'$ is a minimum (we exclude from this discussion the possibility of an index dip at the center). Therefore, to allow observation of the complete index profile, the angular subtense of the opaque stop must not exceed the value of $\theta'$ given from eq (11) by

$$\sin^2 \theta_s < \sin^2 \theta' = \sin^2 \theta + n_L^2 - n_o^2, \tag{31}$$

which is just eq (11) with r = 0. We may write $n_o$ in terms of $\Delta$ by manipulating eq (23c), which yields

$$n_o^2 = n_c^2 + N_F^2, \tag{32}$$

where $N_F^2 = \sin^2 I = 2n_0^2\Delta$. The second equality holds because $\Delta$ is very small. Using eq (32) in eq (31), we find that

$$\sin^2 \theta_s < \sin^2 \theta + n_L^2 - n_c^2 - N_F^2, \tag{33}$$

which is White's eq (15) [2].

Equation (31) or (33) delimits the angular subtense of the largest stop that may be used with a given fiber. Equation (24) delimits the greatest angle of refraction at which leaky modes will be found. This angle increases with radius. Following White, let us assume that the subtense of the stop is precisely that given by eq (33); in fact, it must be slightly less than this value. If we scan a fiber, leaky modes will not appear beyond the stop until the radius is sufficiently large that the angle $\theta'$ defined by eq (24) exceeds the subtense of the stop as given in eq (33). To find an implicit expression for this radius, we set the right sides of these two equations equal and find that

$$N^2/N_F^2 = (1 - \rho^{(\alpha+2)})/(1 - \rho^2) \tag{34}$$

where $\rho = (r/a)$, and $N = \sin \theta$ is the numerical aperture of the incident cone.

We calculate the limit of eq (34) as $\rho$ approaches 1 and solve for $\alpha$. Because $\rho = 1$ at the core-cladding interface, this procedure yields the largest value of $\alpha$ for which leaky modes will not be a factor. The calculation is carried out using l'Hôpital's rule; the result is

$$\alpha = 2[(N^2/N_F^2) - 1] , \tag{35}$$

which is eq (18) of reference 2. For a fiber for which sin I is 0.25 illuminated by a microscope objective whose NA is 0.5, $\alpha = 6$; $\alpha$ increases to 10.5 if sin I decreases to 0.2. Thus, leaky rays can be handled for nearly all practical fibers except possibly step fibers.

For step fibers, we examine eq (34) in the limit as $\alpha \to \infty$. Because $\rho$ is at most 1, the right side simply approaches $1/(1 - \rho^2)$. Therefore,

$$r/a < (1 - N_F^2/N^2)^{1/2} \tag{36}$$

for leaky rays to be excluded by the stop. This relation is precise only when $\theta_s$ has been optimized for each fiber. For the examples used in connection with eq (35), $\rho = 0.87$ and 0.92, in that order. Beyond these radii, an indeterminate fraction of the leaky-ray power is blocked by the stop; therefore, it is not possible to calculate a correction factor. Thus, the refracted-ray method is not useful for scanning step fibers beyond about nine tenths of their radius.

## 8. RESOLUTION LIMIT, EDGE RESPONSE, AND DEPTH OF FOCUS

References 2 and 5 reported that the scanner was diffraction-limited as long as $\varepsilon$ remained <0.7 or so. Both authors observed a loss of resolution with larger values of $\varepsilon$. Although we interpreted our results differently, we assumed that the edge response due to an opaque straightedge adequately described the system.

Stewart [48] has shown that the response of the system to an index step differs from that to a straightedge. This comes about because the index step has finite thickness; the Fresnel reflection from the boundary between the two dissimilar materials interferes with the directly transmitted wave. Pursuing his argument further, Stewart found that there is a decrease of resolution at values of $\varepsilon$ smaller than those examined in references 2 and 5.

Using information theory, Stewart showed additionally that resolution is best when the numerical aperture of the opaque stop is a factor of $\sqrt{2}$ less than the numerical aperture of the microscope objective or when $\varepsilon$ is ~0.7 [49]. Reid and Stewart have used this result to design a scanner with a numerical aperture of 1.5 and resolution limit of 0.34 μm [8].

To check the edge-response width of the present system (to be described shortly), I cleaved some silica fibers, immersed them in oil, and scanned across the edge along a diameter that was roughly at right angles to the direction along which the fiber had been cleaved. Figure 5 shows a typical set of such scans for several values of $\varepsilon$. This parameter varies by about 10 percent depending upon whether the light is focused into the fiber or the oil; the numbers in figure 5 are the averages of these two values.

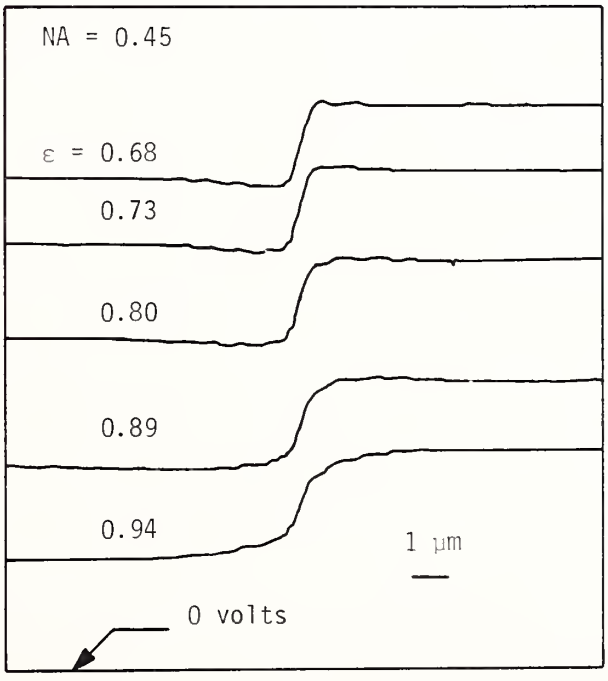


Figure 5. Measured edge response of refracted-ray scan for various values of $\varepsilon$.

The scans are diffraction limited as long as $\varepsilon$ is 0.7 or thereabouts; resolution suffers when $\varepsilon$ is increased. (The system was not designed to operate with smaller values of $\varepsilon$.) The edge ringing seen in the top three scans is characteristic of the diffraction-limited response of the system; the over- and undershoot are the result of the Fresnel reflection noted by Stewart.

Depth of focus is related to resolution limit and is one factor that may determine the precision with which the end of the fiber must be perpendicular to the axis of the system. For a diffraction-limited optical system such as a microscope objective, depth of focus may be written

$$DF = n\lambda/2(NA)^2. \tag{37}$$

If NA = 0.5 and $\lambda$ = 633 nm, the depth of focus DF is about 2 μm. If we focus on the center of a 100-μm diameter fiber, then the edges will be in sharp focus only if the face of the fiber deviates from perpendicularity by less than (2/50) rad, or about 2°.

## 9. CONDENSING LENS

With no fiber in the cell, the hollow cone transmitted through the cell will have a numerical aperture NA equal to that of the microscope objective. If the fiber index is slightly less than that of the matching fluid, then the emergent cone is noticeably larger than the incident cone. The hollow emergent cone must be focused by a condensing lens onto a detector.

Lenses (other than microscope objectives) are more commonly described in terms of their F number $\phi$ than numerical aperture. Figure 6 shows the geometry used for calculating the relationship between NA and F number. In air, the NA is given by

$$NA = \sin U = D/2(f'^2 + D^2/4)^{1/2} \tag{38}$$

from which we may readily calculate that

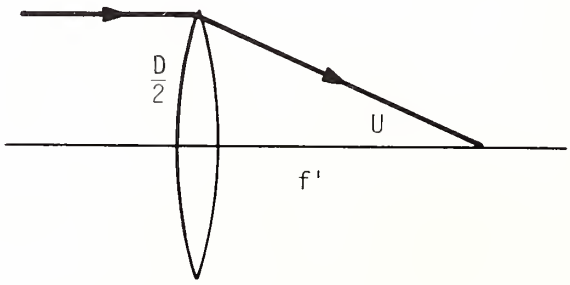


Figure 6. Vertex angle of a lens.

Table 1. F number, numerical aperture, and vertex angle

| NA | $\phi$ | U |
|---|---|---|
| 0.15 | 3.3 | 8.6° |
| 0.20 | 2.4 | 12 |
| 0.25 | 1.9 | 15 |
| 0.40 | 1.15 | 23.5 |
| 0.50 | 0.87 | 30 |
| 0.65 | 0.58 | 41 |

$$\phi = f'/D = (1/2)(NA^{-2} - 1)^{1/2} \tag{39}$$

Thus, an NA of 0.5 is equivalent to an F number of about 0.9. (Table 1 compares NA and F number.) We must design a condensing lens with an effective F number $\phi$(1 + magnification) less than 1.

Aspheric Fresnel lenses are available from more than one manufacturer with F numbers as low as 0.7. These lenses are corrected for spherical aberration, generally provided that one conjugate is located at infinity. Therefore, two lenses with adequate diameter (but not necessarily equal focal length) will be required: The first roughly collimates the beam, and the second focuses onto the detector. The F number of 0.7 implies that the numerical aperture of the microscope objective may exceed 0.5 if necessary.

To make the lens out of glass elements is more difficult; also, the glass lens is thick and allows less working distance than the pair of Fresnel lenses. A prescription for designing a glass condensing lens made from planoconvex elements is left to appendix D.

## 10. APPARATUS

The experimental apparatus is sketched in figure 7. The HeNe-laser beam is expanded by the first microscope objective MO and focused by the second 40X microscope objective through a microscope cover slip onto the fiber. The fiber is held in the moveable cell, whose cross section is shown in figure 8 and which is discussed below. The fiber passes through a hole in the opaque stop OS. The refracted rays escape the fiber and are focused by the condensing lens CL onto a uniform, 1-cm-diameter silicon detector. (The lens is shown as a three-element glass condenser, although it has long since been replaced with two 7.1-cm aspheric Fresnel lenses.) Because the laser is polarized, the $\lambda/4$ plate is used to reduce the dependence of various reflectances on angle.

Figure 9 shows two rear views of the apparatus, with the lens and detector removed. The cell is constructed of aluminum. The glass window is fastened with a good grade of epoxy. The cover slip is fastened to a mounting plate with a fast-setting epoxy that may be removed with a razor blade if the cover slip has to be replaced; the plate is screwed to the

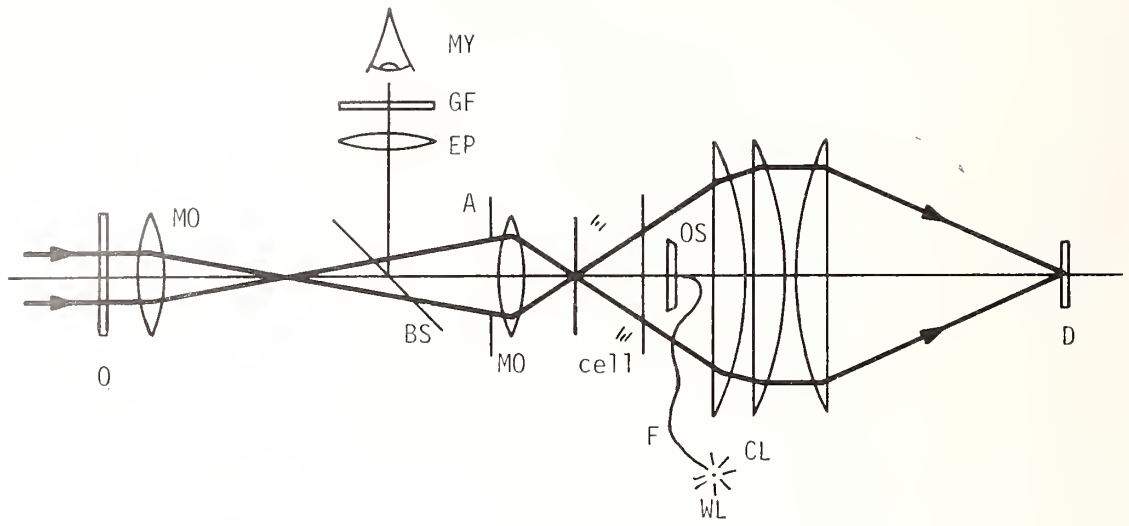


Figure 7. Experimental setup. Q--quarter-wave plate. MO--microscope objective. BS--beam splitter. A--aperture stop. OS--opaque stop. F--fiber. WL--white-light source. CL--condensing lens. D--detector. EP--eyepiece. GF--green filter. MY--experimenter.

cell housing in case the cover slip must be removed and cleaned. The fiber is introduced through a 0.25-mm capillary tube that is fastened to the window with the same rapidly setting epoxy, so that the capillary tube may be removed easily with a heat gun. The outer end of the tube has been formed into a funnel to guide the fiber. The stop is made of aluminum by turning it on a lathe and is fixed in place with piano wire, as shown in figure 10. Stray light that passes through the hole in the stop is intercepted by a piece of black tape fastened to the center of the lens.

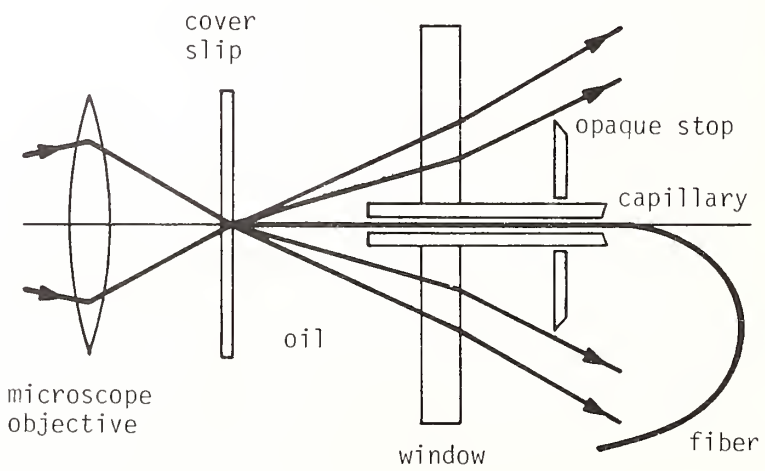


Figure 8. Detail of cell assembly and focusing optics. Outside the capillary, the fiber is confined to the plane perpendicular to the direction of scan.

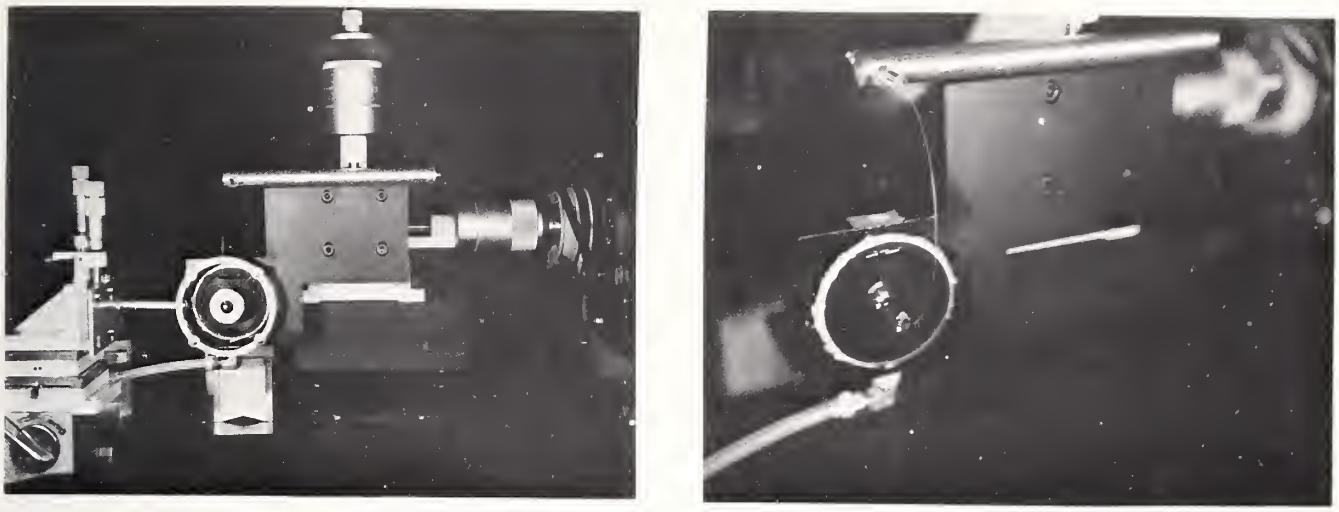

(a) (b)

Figure 9. Photographs of the cell and translation stage, condensing lens removed.

In addition, I illuminate the fiber with a white light placed directly behind the cell (or sometimes at the far end) and inspect the entrance face with the beam splitter and eyepiece assembly shown in figure 7. The green filter is used to eliminate stray laser light. Once the beam splitter and eyepiece are fixed in place, they may be used to locate the fiber and focus on it by manipulating the cell position. This procedure is accurate to better than 25 μm; I adjust the focus further by scanning across the index dip or other sharp feature and examining the profile for sharpness. The white-light source at the far end of the fiber may be replaced with a detector for transmitted near-field scanning.

In its present form, the system uses a three-axis manipulator whose precision is 2.5 μm (0.0001 in) or better. The manipulator is used to focus onto the fiber end and to locate the fiber so the incident beam hits the index depression at the center of the core. The entire assembly sits atop a translation stage driven by a digital stepping motor with 0.4 μm steps. The digital drive may be useful for computer analysis, but I simply connect the shaft of the stepping motor to a continuous, precision potentiometer by means of toothed

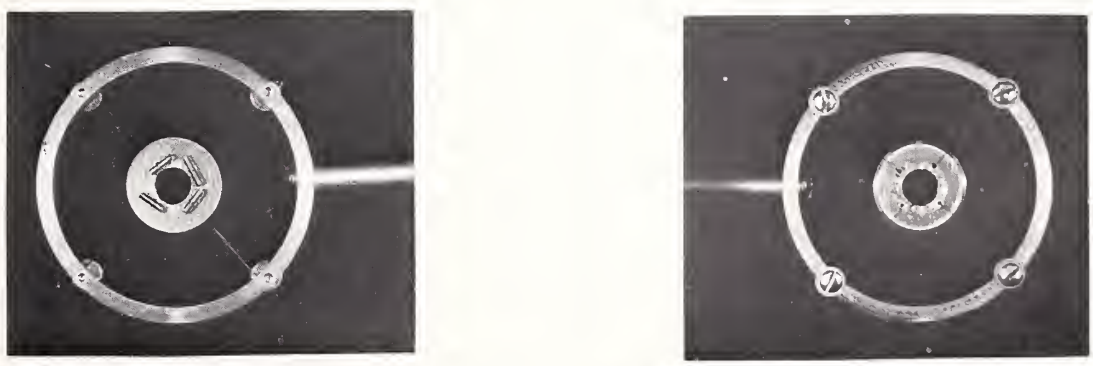

(a) (b)

Figure 10. Photographs of the opaque stop.

drive wheels and matching belts. The potentiometer is used in a voltage-divider circuit with a plus-and-minus 15-V power supply and drives the horizontal axis of an xy recorder. (It is also possible to connect one of the micrometers of the manipulator directly to the potentiometer and to a clock motor with the toothed belt and wheels. I have not found this method fully satisfactory because, in my manipulator, there is slight interaction between orthogonal axes.) Coupling between the stepping motor and the stage is sufficiently precise that the position of the cell need not necessarily be detected directly.

With one exception, the optical alignment of the apparatus is not critical. I introduce the laser beam by means of two mirrors (not shown). After rough alignment, I center the opaque stop by eye; the aperture stop creates pronounced diffraction rings that make the visual alignment fairly precise. After introducing the condensing lens and positioning the detector by maximizing its output, I use the mirrors to maximize the power through the system; this ensures that the laser beam is centered about the aperture stop that precedes the microscope objective. The opaque stop may be adjusted further at this time, but such adjustment does not seem necessary.

The location of the aperture stop, however, is critical. The aperture stop determines the axis of the cone that focuses onto the face of the fiber. If that axis is not very nearly parallel to the axis of the fiber, then the scans will be skewed slightly. In a graded-index fiber, the cladding index shows a slight upward or downward slope that is consistently in the same direction on both sides of the core. To correct for this error, I found that the aperture stop must be positioned horizontally to an accuracy of 25 μm or so. With a 40X microscope objective (4-mm focal length), this corresponds to a pointing accuracy of about 6 mrad or one third of a degree. The adjustment is best made by scanning a fiber repeatedly until the cladding or the oil levels on either side of the scan are equalized. In addition, to avoid creating an angular error in the horizontal plane, I introduce the fiber by holding it in place directly above the capillary, rather than to one side.

## 11. CALIBRATION

Data are taken on an xy recorder. The output of the photodetector passes through a trans-impedance amplifier (current-to-voltage converter) whose output enters the vertical amplifier of the recorder. I checked the overall linearity of the electronic system by first calibrating a set of neutral-density filters at 633 nm on a spectrophotometer. Introducing the filters into the beam ahead of the first MO yielded the curve shown in figure 11. Electrical linearity is therefore good over a factor of at least 5.

White [2] has calibrated his system by translating the stop to different positions along the axis. I sought a more-direct calibration scheme, which might be more amenable to analysis [3-6]. Ideally, one or more fibers with known core and cladding indices would make calibration an easy matter. Unfortunately, such a set of fibers is not available; neither

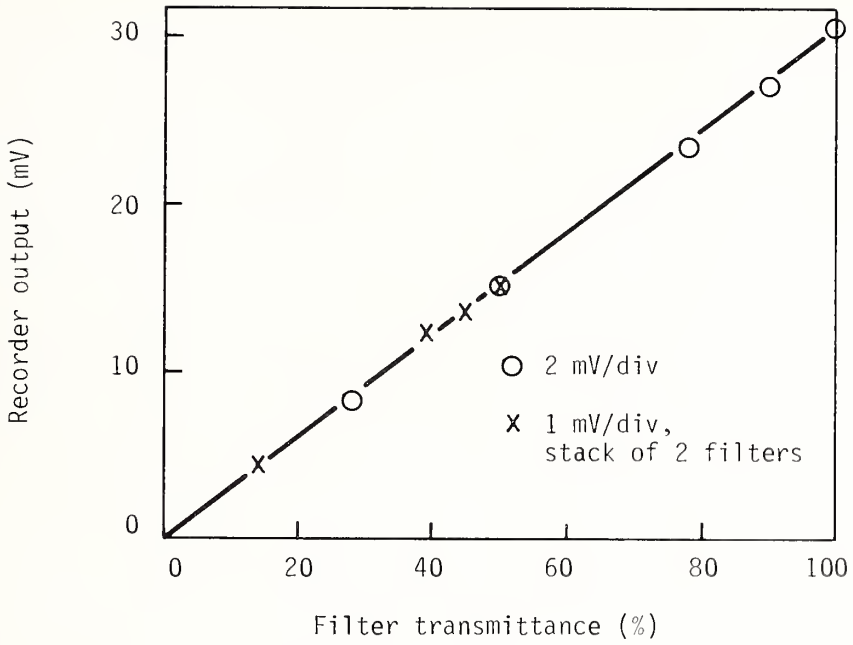


Figure 11. Electrical linearity of the system, determined by placing calibrated filters into the laser beam.

is there a guarantee that the index of a fiber is precisely that of the preform from which the fiber was drawn.

Malitson has shown that vitreous silica is manufactured with sufficient purity that the index variation from sample to sample or manufacturer to manufacturer is, for our present purposes, negligible [50]. He has also derived Sellmeier coefficients that allow calculation of the index at any wavelength up to 3.71 μm. However, Fleming has criticized the use of Malitson's numbers for calculating the index of a fiber; fibers are not annealed, but rather are chilled or quenched and may not have the same index as the annealed, bulk material [51,52]. Hence, Fleming has determined the Sellmeier coefficients relevant to quenched silica.

At the wavelength 632.8 nm, the Malitson formula gives the result that the index of the silica at 20°C is 1.457018; the Fleming formula gives 1.457334 at 23.5°C (see table 2). Malitson quotes a temperature coefficient of $10.0 \times 10^{-6}$ $K^{-1}$; thus at 23.5°C, the index of vitreous silica is 1.457053. At this temperature, the Malitson and Fleming values differ by 0.00028, an amount that is significant when compared with the accuracy to which the indices of the immersion fluids are known. I chose the average value of 1.45719 and assigned an error of ±0.00014.

For calibration, I used several fibers drawn by hand from vitreous-silica rods as well as the naked core of a plastic-clad silica fiber. (Although the latter was more convenient, I wanted to verify that it was truly silica.) I compared these fibers with each of five oils sequentially. The indices of the oils were supplied by the manufacturer, who claimed an accuracy of ±0.0005 [53].

Table 2. Sellmeier coefficients for vitreous silica (0.21-3.71 μm and 20°C) and for quenched silica (0.44-1.53 μm and 23.5°C). All wavelengths are expressed in micrometers.

| | $A_1$ | $A_2$ | $A_3$ |
|---|---|---|---|
| vitreous silica | 0.6961663 | 0.4079426 | 0.8974794 |
| quenched silica | 0.696750 | 0.408218 | 0.890815 |
| | $\lambda_1$ | $\lambda_2$ | $\lambda_3$ |
| vitreous silica | 0.0684043 | 0.1162414 | 9.896161 |
| quenched silica | 0.069066 | 0.115662 | 9.900559 |

$$n^2 - 1 = \frac{A_1\lambda^2}{\lambda^2-\lambda_1^2} + \frac{A_2\lambda^2}{\lambda^2-\lambda_2^2} + \frac{A_3\lambda^2}{\lambda^2-\lambda_3^2}$$

Figure 12 shows a typical calibration run with the silica core. When the laser is focused into the oil rather than the fiber, the rays should emerge parallel to their original direction; we might expect the power transmitted to be independent of the index of the fluid. The slight variation in figure 12 may be accounted for by the change in reflectance at various oil-glass interfaces. Because of this variation, it is necessary to normalize the results to the power transmitted through the oil alone.

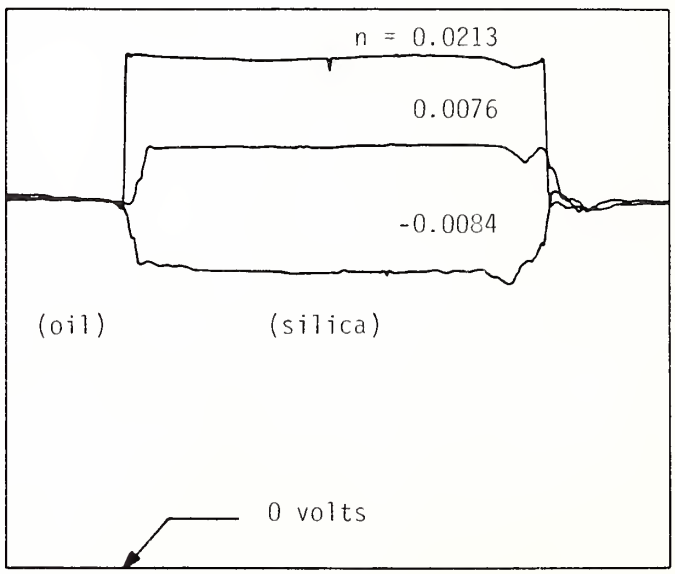


Figure 12. Calibration scans with unclad PCS fiber. Structure near right edge is a result of the fracture and does not represent true index data.

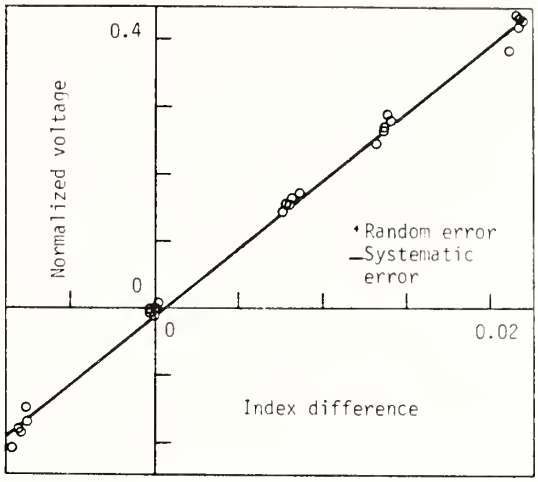


Figure 13. Normalized voltage as a function of index difference between silica and oil, for a particular stop position. Estimates of random and systematic error are indicated.

Figure 13 shows the results of some calibration runs similar to those reported in references 3 through 5. The vertical axis is $(V_s - V_o)/V_o$, where V is the voltage read by the xy recorder and s and o stand for silica and oil. The horizontal axis is $n_o - n_s$, where n is index of refraction.

The greatest barrier to a linear calibration may be ensuring the absence of vignetting when the highest-index oil is in the cell (and the emergent cone was largest). It is important to verify the linearity of the system over a large range of indices in case, for example, some of the fibers to be tested have cladding indices less than that of vitreous silica. Because of the possibility of vignetting, or other effect, an extrapolation may be dangerous if linearity over a sufficient range has not been demonstrated.

A calculation along the lines described by Natrella showed linearity at the 99 percent confidence level [54]. However, I did not calculate a conventional line of best fit because the points have uncertainty in the horizontal direction as well as the vertical. Rather, I used a method similar to another suggested by Natrella. The center of mass of all the points as well as the means of each of the four sets are calculated. Three line segments join adjacent means, and their slopes are calculated. The best-fit line is taken to be the one that passes through the center of mass and whose slope is equal to the average of the slopes of the three line segments. This is the line shown in figure 13.

The vertical error bar in figure 13 is an estimate of the instrumental limit of error (or resolution) of the xy recorder; the actual vertical errors are also of this order. The horizontal error is the sum of the index uncertainties just mentioned, as well as an additional ± 0.0001 owing to the effect on the oils of the uncertainty of the oil temperature measurement. Because the large horizontal error bar is not reflected in large vertical

Table 3. Error budget

| | | |
|---|---|---|
| | Vertical | |
| Instrumental limit of error | ±0.01 | random |
| | Horizontal | |
| Temperature coefficient of refractive index, ±0.25 K | ±0.0001 | random |
| Index of silica | ±0.00014 | systematic |
| Index of oils at 25°C | ±0.0005 | assumed systematic |
| SUBTOTALS | ±0.0001<br>±0.00064 | random<br>systematic |
| Projection of vertical error | ±0.0005 | random |
| TOTALS | ±0.0006<br>±0.0006 | random<br>systematic |

scatter, I conclude that most if not all of the horizontal error (except the temperature component) is a systematic error that is common to each oil and has approximately constant magnitude and sign; the two horizontal error bars show the random and systematic errors separately. (See table 3 for a compilation.)

When running an unknown sample, I usually choose the oil whose index at 25°C is about 1.464; generally this value is slightly higher than the cladding index, and the values of $\Delta V/V$ for the scan remain within the range defined by figure 13. In the unusual event that some of the values fell outside that range, the oil would have to be changed to avoid having to extrapolate the line in figure 13.

After running the scan, I remove the fiber to determine the voltage corresponding to the index of the oil without the complicating effect of the shadow of the fiber. (It is equivalent to continue to scan for several fiber radii beyond the cladding.) I measure the voltage difference corresponding to the core-cladding index difference and compute $\Delta V/V$ for the fiber. The value can be converted directly to index difference by using the slope of the calibration curve of figure 13. For relative measurements, it is not necessary to know the precise index of the oil; therefore, $\Delta n$ should be accurate to ±0.0006, as detailed in table 3. This procedure eliminates the index of the oil from the measurement and relies on a calibration line derived from many points (rather than one or two). Therefore it should

be more accurate than calibrating each measurement with a vitreous silica fiber and monitoring the temperature of the oil; this may be especially important when examining single-mode fibers, whose values of $\Delta n$ are relatively small compared to the accuracy with which the index of silica may be known.

The approximate index of the fiber is needed to calculate the numerical aperture, $NA = \sqrt{(2n^2\Delta n)}$. However, because n is large, an error in n is not nearly so severe as an error in $\Delta n$, and the NA may be calculated precisely with only approximate knowledge of the index of the fluid.

The index of any of the oils is significantly temperature dependent; for the D line, the coefficient is of the order of $4 \times 10^{-4}\ K^{-1}$. Thus, with slight increase in complexity, we could calibrate the system using only a single oil and varying its temperature by a few tens of kelvins while measuring to a precision of a few tenths of a kelvin.

With this scheme, we could get many more points along the calibration curve, but would have to measure the index of the oil as a function of temperature at precisely the wavelength of interest. Further thoughts on index measurements of liquids are detailed in appendices A and B.

## 12. MEASUREMENTS ON MULTIMODE FIBERS

In this section, I report the results of refracted-ray scans of a number of actual communication fibers, on a comparison with conventional near-field scans, and on a comparison with another laboratory.

I obtained a step fiber, designated DF-1, that had been subjected to an exit-face scan and a far-field scan by other workers in this laboratory. I performed additionally a refracted-ray scan and an entrance-face scan on this fiber.

Figure 14a shows the refracted-ray scan. The scan reveals a central structure that is actually an index dip surrounded by a nearly circular index dip (as may be verified with the eyepiece). In addition, the scan shows that the fiber has a low-index cladding layer surrounded by what is evidently silica.

Incidentally, if we knew that the outermost layer of a fiber were in reality silica, then we could use the index of that layer as a calibration level. Most of the fibers I have tested had cladding indices that were (within experimental accuracy) equal to that of silica; some, however, had substantially lower index. It is therefore unwise to presume anything about the fiber in the absence of a priori knowledge that it is clad with pure silica.

The apparently high-index region near the edge of the core of the fiber DF-1 is an artifact that results from the presence of leaky rays. That the structure is not real may be verified by translating the opaque stop either in or out and noticing that the relative

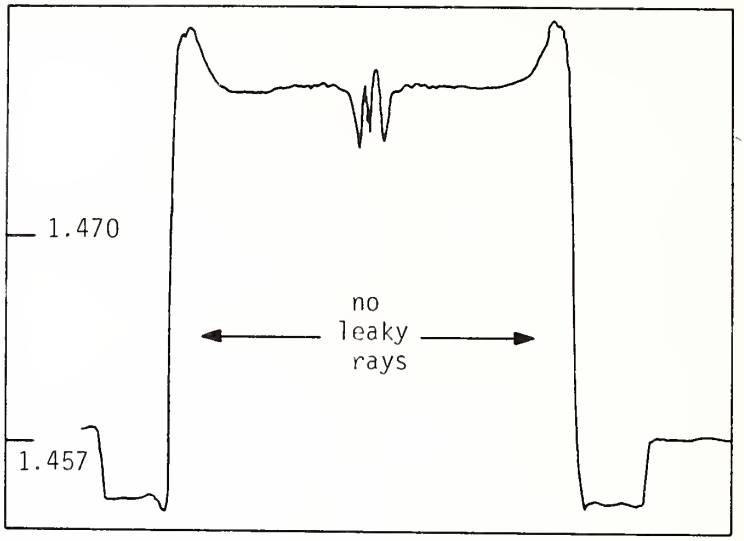


Figure 14a. Refracted-ray scan of step fiber. Arrowheads show region calculated to be free of leaky rays.

magnitude of the peaks varies with stop position (not shown in a figure). These artifacts may be eliminated by translating the stop axially to the proper position, but at the expense of having to recalibrate the system and probably losing resolution.

We may also use the data to calculate the core-cladding index difference $\Delta n$ and employ eq (36) to determine the portion of the core that is free of leaky rays; this region in indicated in figure 14a and corresponds well with the appearance of the artifacts.

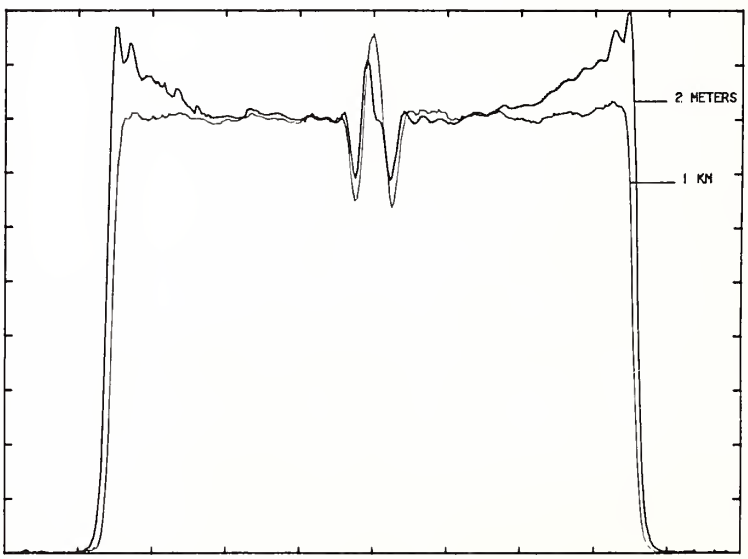


Figure 14b. Exit-face scans of step fiber at 857 nm.

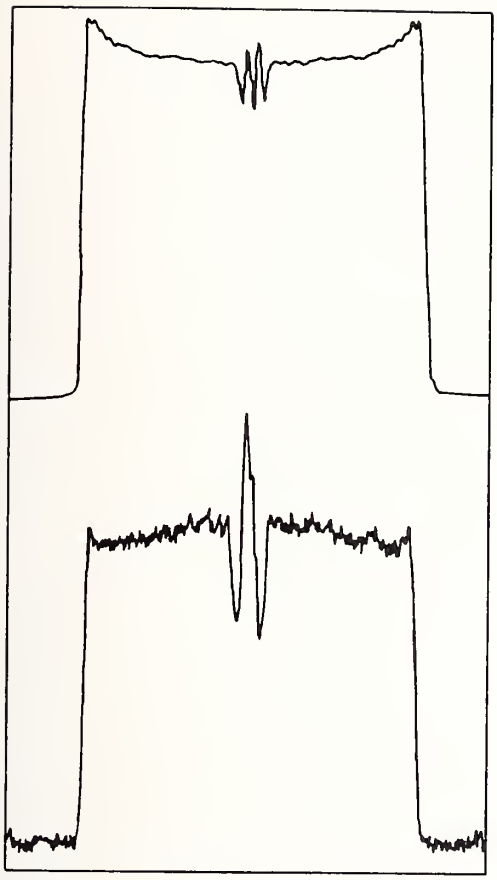

Figure 14c. Entrance-face scan of step fiber at 633 nm. Upper--short length; lower--kilometer length.

Figure 14b shows exit-face scans of both a short length and a kilometer length of this fiber, both performed at 857 nm. The scan of the short length nearly resolves the index dip but suffers from the leaky-ray problem. The second scan, on the other hand, is free of leaky rays and suggests that the fiber core does indeed have a nearly constant index of refraction. However, the index dip has been greatly exaggerated (compared with figure 14a), probably because of mode coupling by scattering or diffraction out of the core center as a result of the long propagation distance. (Because of mode coupling, the scan of the long piece should not be considered a reliable representation of the profile.)

Figure 14c shows entrance-face scans of short and long pieces of this fiber. To make these scans, I simply removed the condensing lens from the system and placed the output end of the fiber into an oil-filled capillary tube and brought it nearly into contact with the detector. As before, the scan of the short length shows the index dip with what is evidently its proper magnitude but suffers from the leaky-ray problem near the core edge. The scan of the longer piece, however, distorts the index dip substantially, not only by exaggerating its magnitude, but also by injecting a spike into the center of the pattern. (This spike is easily explained by noticing that, because of the oscillatory nature of the index dip, the center of the fiber contains a tiny annular waveguide. Apparently this waveguide has lower loss than the fiber as a whole. The scan does not resolve the waveguide, which appears as a sharp spike.)

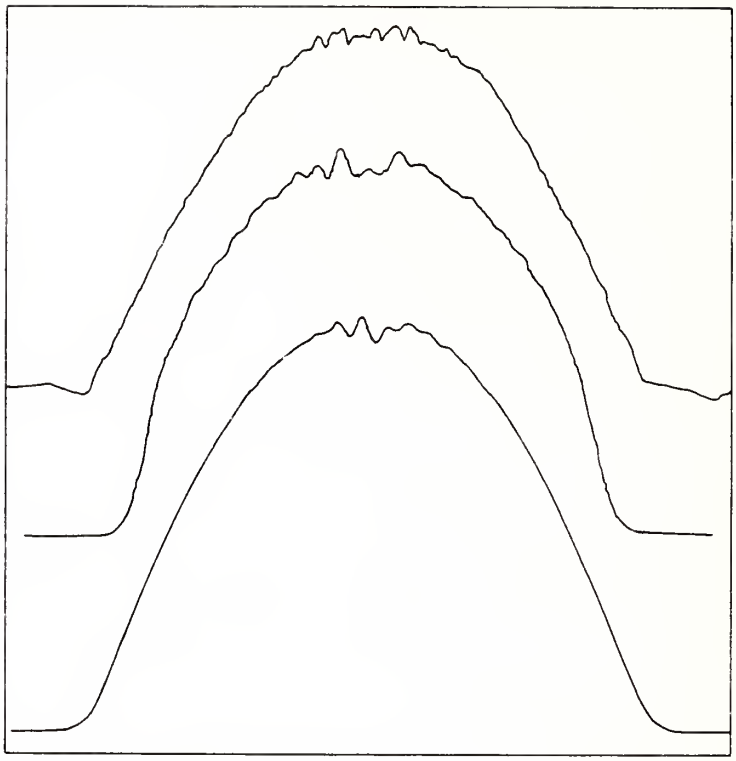

Figure 15. Scans of a graded-index fiber. Upper--refracted-ray scan; center--entrance-face scan, short length; lower--entrance-face scan, kilometer length.

The refracted-ray scan shows details of the step fiber that are not shown or are distorted by conventional near-field scanning. However, the refracted-ray scan suffers from the presence of leaky rays near the periphery of the step-fiber core. It may therefore be prudent, when examining step fibers, to supplement the scan with, say, entrance face scans taken with different numerical apertures.

To assess the leaky-ray problem in graded-index fibers, I performed a refracted-ray scan and an entrance-face scan of a 56-cm length of fiber DF-D; these are shown in figure 15. (Because the refracted-ray scan has to be inverted to make the positive n axis vertical, the upper scan is in the opposite direction from the lower two.) The horizontal scales are the same for the two scans; the vertical scales have been adjusted to give nearly the same amplitude. The cladding of fiber DF-D is not uniform, as I have determined by scanning several freshly cleaved ends; the structure in the cladding of figure 15 (upper) is real and not an artifact of the apparatus. Figure 15 (lower) is an exit-face scan of a long piece of the same fiber; the horizontal scale is not the same as those of figure 15 (upper) and (center).

Even a casual inspection shows the two near-field scans to be substantially more rounded than the refracted-ray scan.

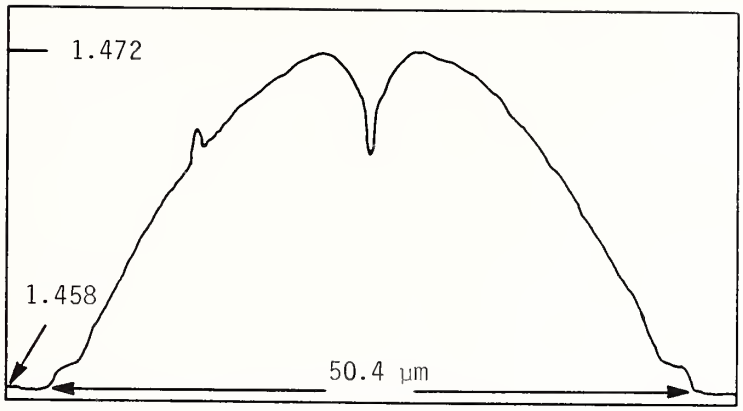


Figure 16. Refracted-ray scan of fiber DF-E. Glitch to left of center is likely due to contamination by dirt or shard of glass.

Among the other fibers I scanned were graded-index fibers designated DF-A, B, D and E. These fibers had been used in a round robin to intercompare radiation-angle or numerical-aperture measurements made in each of several laboratories [55]. Figure 16 shows a scan of one of these fibers, DF-E. This curve is chosen deliberately to show the glitch to the left of the center, which is probably the result of a speck of dirt or a shard of glass too small to be seen with the eyepiece.

The maximum acceptance angle U for meridional rays may be calculated from the formula

$$\sin^2 U = n_o^2 - n_c^2 \cong 2n\,\Delta n, \tag{40}$$

where n is the average of $n_o$ and $n_c$. sin U is sometimes called the numerical aperture of the fiber. Table 4 compares calculated values of sin U with the means of the values obtained for each fiber by the laboratories in the round robin. (The same data are shown graphically in figure 17.)

Table 4. Comparison with a round robin

Numerical Aperture

| Fiber | Round-robin average | Calculated, this report |
|---|---|---|
| DF-A | 0.235 ± 2.9%* | 0.264 |
| DF-B | 0.163 ± 2.4% | 0.174 |
| DF-D | 0.202 ± 1.6% | 0.208 |
| DF-E | 0.195 ± 0.9% | 0.202 |

*One standard deviation, expressed in percent of mean.

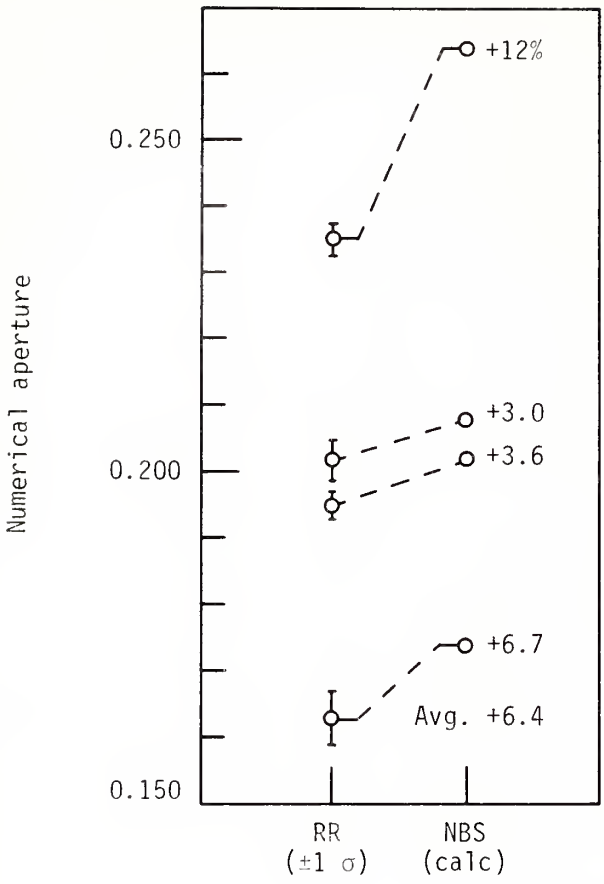


Figure 17. Comparison of numerical-aperture measurements by round robin (RR) with calculation based on index-profile measurements (NBS).

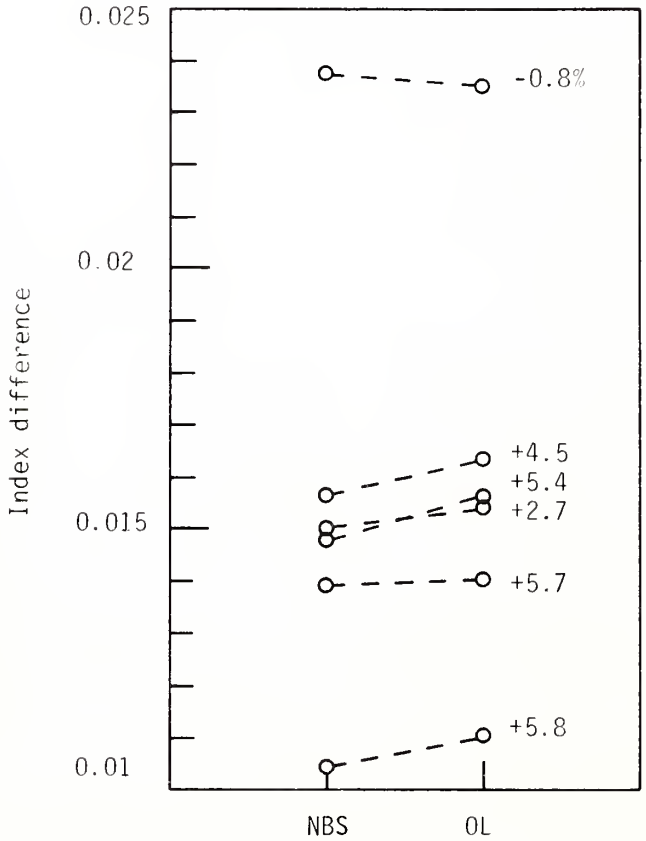


Figure 18. Core-cladding index difference measured by NBS and by other laboratory (OL) that also uses refracted-ray scanning. Average difference between measurements is 3 percent.

Table 5. Interlaboratory comparison of index difference Δn

| Fiber | This report | Other laboratory | Difference |
|---|---|---|---|
| DF-A | 0.0237 | 0.0235 | -0.8% |
| DF-B | 0.0104 | 0.0110 | +5.8 |
| DF-D | 0.0148 | 0.0156 | 5.4 |
| DF-E | 0.0139 | 0.0140 | 0.7 |
| MJ-A | 0.0150 | 0.0154 | 2.7 |
| MJ-B | 0.0156 | 0.0163 | 4.5 |
| | | Average | +3% |

In all four cases, the values calculated from index data are slightly larger than the sample-average numerical aperture. This is so because the participants in the round robin were instructed to measure the angle between the points at which the intensity was 5 percent of the peak, whereas the calculated numerical aperture will include all the light transmitted by the fiber. Therefore, we expect the calculated values to exceed slightly the measured values, and this is precisely the case.

Finally, I was fortunate to be able to make an informal comparison with refracted-ray scans by M. J. Saunders of Bell Laboratories [57]. Owing to the round robin, which was going on at the same time, we were easily able to exchange a total of six fibers. We measured the index differences shown in table 5 and figure 18. The other laboratory's value is generally slightly higher than that of NBS, but the arithmetic-average difference between our measurements is 3 percent even though we used different calibration techniques.

## 13. MEASUREMENTS ON SINGLE-MODE FIBERS

Single-mode fibers are a different breed from multimode fibers, whether graded or step index. The core of the single-mode fiber may be as small as a few micrometers, and the index difference Δn may be several times less than typical values for near-parabolic fibers. Therefore, profiling of single-mode fibers requires a method that is sensitive and has high spatial resolution.

In addition, the distribution of power at the output of a single-mode fiber is that characterized by the mode itself and not by the local numerical aperture or the index profile. Consequently, conventional near-field scanning will not generate the index profile of a single-mode fiber; it will, rather, generate the power distribution of the mode. Whereas this distribution may be important for certain problems (like that of connecting fibers together), it gives no information about the index profile.

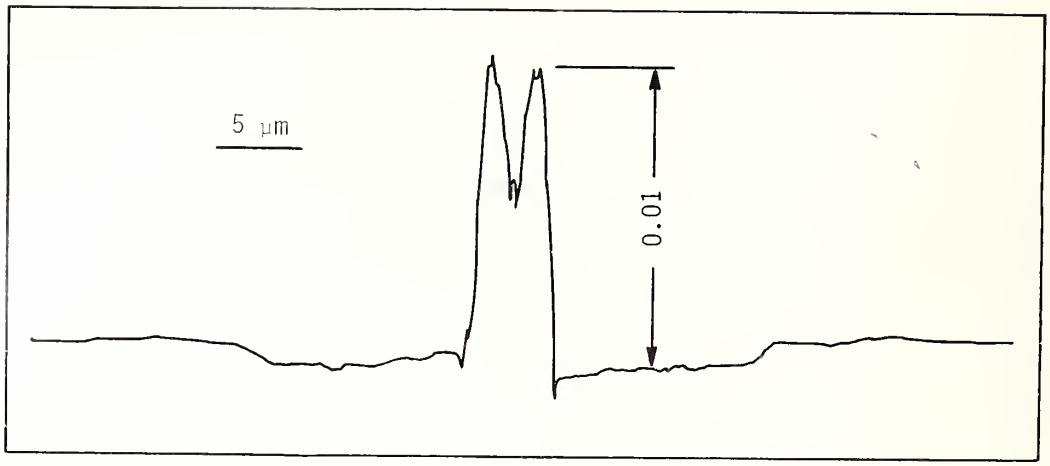


Figure 19. Refracted-ray scan of single-mode fiber. Outermost layer is cladding; asymmetry of inner cladding layer is real, as may be verified by repeating scan on freshly cleaved ends.

The refracted-ray method, on the other hand, does not depend on the radiation-trapping properties of the fiber; it can therefore generate the index profile of even a single-mode fiber. Indeed, because of its precision and resolving power, refracted-ray scanning is probably the method of choice for profiling such fibers.

I was able to obtain two single-mode fibers and exchange them also with Saunders. Figure 19 shows a scan of one such fiber. The horizontal and vertical axes are as labeled. This fiber has been designed with a compound cladding that consists of two layers; the inner layer has the lowest index of any layer in the fiber [56]. The index difference between that layer and the core center is only about 0.011. The diameter of the core is about 3 μm.

Table 6 shows a comparison between the measurements of $\Delta n$ taken in this laboratory and the other. Expressed as a percent, agreement is somewhat poorer than before; this is so because $\Delta n$ is significantly smaller than before. Some of the discrepancy can be accounted for by noting that the other laboratory used a calibration method that assumed a particular value for the index of vitreous silica; an error in the fourth decimal place is significant compared to the value of $\Delta n$ for these single-mode fibers. Nevertheless, most of the discrepancy is just experimental error; both values fall well within the precision and accuracy claims in table 3.

Refracted-ray scanners generally use HeNe lasers. Most single-mode fibers are designed for 850 nm or longer wavelengths. Therefore, some of them may support more than one mode at the HeNe-laser wavelength of 633 nm. One fiber, a step fiber with about four modes at 633 nm, showed evidence of leaky rays near the core-cladding interface. If there is doubt, these fibers should be checked for leaky rays by translating the opaque stop along the axis of the system and inspecting the recorded profiles for changes.

Table 6. Interlaboratory comparison of index difference $\Delta n$ of single-mode fibers

| Fiber | This report | Other laboratory | Difference |
|---|---|---|---|
| EK | 0.0110 | 0.0114 | +3.6% |
| JW | 0.0034 | 0.0041 | 20.6% |

## 14. ADDITIONAL REMARKS

One of the major practical problems with refracted-ray scanning is the accumulation of dirt particles or shards of glass on the inside of the microscope cover slip. Probably these particles are deposited by the fiber onto the inside of the capillary; they are later picked up by other fibers and deposited in turn onto the cover slip. In any case, such particles accumulate on the cover slip and eventually interfere with the measurement.

The problem may be less severe in a laboratory environment, where relatively few fibers are tested than, say, in a production environment. I simply clean the fibers in an ultrasonic cleaner that contains the same oil as the cell. When the cover slip becomes contaminated with particles, I wash or replace it.

K. I. White of British Telecom informs me that they insert their fibers by using a tube within a tube, rather than a single capillary. They push the fiber through a fine tube, cleave it, and place the tube and the fiber in an ultrasonic cleaner. They then withdraw the fiber into the tube and insert the tube into a larger tube that is fixed to the cell. They feel that much of the contamination problem is eliminated in this way.

White further informed me that their cell is cylindrical and mounted in a V block for easy removal and accurate replacement. Such a design will greatly simplify the removal and cleaning of the cover slip.

Another problem is that the fiber drifts slightly within the cell. The rate of drift varies but is often as large as a micrometer or so per minute. With multimode fibers, this is not important unless we are interested in examining the index dip or other fine features; however, a micrometer of drift may cause significant error in a scan of a single-mode fiber.

The drift can be arrested by clamping the fiber just outside the cone of refracted rays; I simply use an alligator clip, suitably padded with a soft rubber gasket (not shown in the figures). Because the total motion of the capillary is only 100 μm or so, the alligator clip need not be fixed to the translation stage. With the fiber thus clamped, drift is very slight, whereas without clamping the fiber sometimes drifts unacceptably before a full scan can be completed.

---

Although I am the sole author of this chapter, it has been in certain ways a cooperative venture, and it is my very great pleasure to acknowledge Ernest Kim for supplying the exit-face scans; M. J. Saunders of Bell Laboratories, Norcross, Georgia, for supplying his excellent data; Saunders, K. I. White, R. L. Gallawa, and G. W. Day for very careful and perceptive reviews of the earlier edition; D. L. Franzen for supplying the round-robin fibers; Edie DeWeese for her infinite patience preparing and then revising the manuscript; and Aaron A. Sanders for providing means, motive, and opportunity.

## 15. REFERENCES

[1] Stewart, W. J. A new technique for measuring the refractive index profiles of graded optical fibers. Proc. Conf. Integrated Optics and Optical Communication, Japan; 1977. 395-398.

[2] White, K. I. Practical application of the refracted near-field technique for the measurement of optical fibre refractive index profiles. Opt. Quantum Electron. 11:185-196; 1979.

[3] Young, M. Calibration technique for refracted near-field scanning of optical fibers. Appl. Opt. 19:2479-80; 1980.

[4] Young, M. Linearity and resolution of refracted near-field scanning. Technical Digest --Symposium on Optical Fiber Measurements. Nat. Bur. Stand. (U.S.) Spec. Publ. 597; 1980.

[5] Young, M. Refracted-ray scanning (refracted near-field scanning) for measuring index profiles of optical fibers. Nat. Bur. Stand. (U.S.) Tech. Note 1038; 1981.

[6] Young, M. Optical fiber index profiles by the refracted-ray method (refracted near-field scanning). Appl. Opt. 20:3415-3422; 1981.

[7] M. J. Saunders. Optical fiber profiles using the refracted near-field technique: a comparison with other methods. Appl. Opt. 20:1645; 1981. Optical fiber profiles using using the refracted near-field technique: a comparison with interferometry. Technical Digest--Symposium on Optical Fiber Measurements, Digest Supplement; 1980.

[8] Reid, D. C. J.; Stewart, W. J. Ultrahigh resolution refractive near-field profiling. Technical Digest, Third International Conference IOOC, paper TUG6; 1981.

[9] Liu, Y. S. Direct measurement of refractive indices for a small numerical aperture cladded fiber: A simple method. Appl. Opt. 13:1255-1256; 1974.

[10] Marhic, M. E.; Ho, P. S.; Epstein, M. Nondestructive refractive-index profile measurements of clad optical fibers. Appl. Phys. Lett. 26:574-575; 1975.

[11] Saunders, M. J.; Gardner, W. B. Nondestructive interferometric measurement of the delta and alpha of clad optical fibers. Appl. Opt. 16:2368-2371; 1977.

[12] Stone, F. T. Rapid optical fiber delta measurement by refractive index tuning. Appl. Opt. 16:2738-2742; 1977.

[13] Hanson, A. G.; Bloom, L. R.; Cherin, A. H.; Day, G. W.; Gallawa, R. L.; Gray, E. M.; Kas, C.; Kapron, F. P.; Kawasaki, B. S.; Reitz, P.; Young, M. Optical waveguide communications glossary. Nat. Bur. Stand. (U.S.) Handb. 140; 1982.

[14] Maruyama, Y.; Iwata, K.; Nagata, R. Determination of axially symmetric refractive index distribution from directions of emerging rays. Appl. Opt. 16:2500-2503; 1977.

[15] Iga, K.; Kokobun, Y. Formulas for calculating the refractive index profile of optical fibers from their transverse interference patterns. Appl. Opt. 17:1972-1974; 1978.

[16] Okoshi, T.; Hotate, K. Refractive-index profile of an optical fiber: Its measurement by the scattering-pattern method. Appl. Opt. 15:2756-2764; 1976.

[17] Chu, P. L.; Whitbread, T. Nondestructive determination of refractive index profile of an optical fiber: Fast Fourier transform method. Appl. Opt. 18:1117-1122; 1979.

[18] Saekeang, C.; Chu, P. L. Nondestructive determination of refractive index profile of an optical fiber: Backward light scattering method. Appl. Opt. 18:1110-1116; 1979.

[19] Marcuse, D. Refractive index determination by the focusing method. Appl. Opt. 18: 9-13; 1979.

[20] Marcuse, D.; and Presby, H. M. Focusing method for nondestructive measurement of optical fiber index profiles. Appl. Opt. 18:14-22; 1979.

[21] Presby, H. M.; Marcuse, D.; French, W. G. Refractive-index profiling of single-mode optical fibers and preforms. Appl. Opt. 18:4006-4011; 1979.

[22] Presby, H. M.; Marcuse, D. Preform core diameter measurement by fluorescence. Appl. Opt. 20:4324-4328; 1981.

[23] Presby, H. M.; Kaminow, I. P. Binary silica optical fibers: Refractive index and profile dispersion measurements. Appl. Opt. 15:3029-3036; 1976.

[24] Martin, W. E. Refractive index profile measurement of diffused optical waveguides, Appl. Opt. 13:2112-2116; 1974.

[25] Wonsiewicz, B.; French, W.; Lazay, P.; Simpson, J. Automatic analysis of interferograms: optical waveguide refractive index profiles. Appl. Opt. 15:1048; 1976.

[26] Eickhoff, W.; Weidel, E. Measuring method for the refractive index profile of optical glass fibers. Opt. Quantum Electron. 7:109-113; 1975.

[27] Calzavara, M.; Costa, B.; Sordo, B. Stability and noise improvement in reflectometric index measurement. Post-deadline paper, Symposium on Optical Fiber Measurements, 1980, Nat. Bur. Stand. (U.S.) Spec. Publ. 597; 1980.

[28] Tateda, M., Single-mode-fiber refractive-index profile measurement by reflection method. Appl. Opt. 17:475-478; 1978.

[29] Maeda, K.; Hamasaki, J. A method of determining the refractive index profile of a lenslike medium. J. Opt. Soc. Amer. 67:1672-1680; 1977.

[30] Brinkmeyer, E. Refractive-index profile determination of optical fibers from the diffraction pattern. Appl. Opt. 16:2802-2803; 1977. Refractive index profile determination of optical fibers by spatial filtering. Appl. Opt. 17:14-15; 1978.

[31] Jeunhomme, L.; Pocholle, P. Selective mode excitation of graded index optical fibers. Appl. Opt. 17:463-468; 1978.

[32] Rawson, E. G.; Murray, R. G. Interferometric measurement of SELFOC dielectric constant coefficients to sixth order. IEEE J. Quant. Electron. QE9:1114-1118; 1973.

[33] Daino, B.; Piazzola, S.; Sagnotti, A. Spatial coherence and index-profiling in optical fibers. Opt. Acta 26:923-928; 1979.

[34] Marcuse, D.; Presby, H. M. Index profile measurements of fibers and their evaluation. Proc. IEEE 68:666-688; 1980.

[35] Presby, H. M. Profile characterization of optical fibers--A comparative study. Bell Syst. Tech. J. 60:1335-1362; 1981.

[36] Gloge, D.; Marcatili, E. A. J. Multimode theory of graded-core fibers. Bell Syst. Tech. J. 52:1563-1578; 1973.

[37] Payne, D. N.; Sladen, F. M. E.; Adams, M. J. Index profile determination in graded index fibres. Proc. First Conf. on Optical Fibre Communication, London. IEE Pub. 132: 43-45; 1975.

[38] Payne, D. N.; Sladen, F. M. E.; Adams, M. J. Determination of optical fiber refractive index profiles by a near-field scanning technique. Appl. Phys. Lett. 28:255-258; 1976.

[39] Adams, M. J.; Payne, D. N.; Sladen, F. M. E. Correction factors for the determination of optical-fibre refractive-index profiles by the near-field scan technique. Electron, Lett. 12:281-283; 1976. Length-dependent effects due to leaky modes on multimode graded-index optical fibers. Opt. Commun. 17:204-209; 1976.

[40] Irving, D. H.; Donaghy, F. A.; Sabine, P. V. H. Fibre light acceptance for modified near field technique. Electron. Lett. 17:250-252; 1981. Sabine, P. V. H.; Donaghy, F.; Irving, D. Fibre refractive-index profiling by modified near-field scanning. Electron. Lett. 16:882-883; 1980.

[41] Arnaud, J. A.; deRosier, R. M. Novel technique for measuring the index profile of optical fibers. Bell Syst. Tech. J. 55:1489-1508; 1976.

[42] Sumner, G. T. A new technique for refractive index profile measurement in multimode optical fibres. Opt. Quantum Electron. 9:79-82; 1977.

[43] Petermann, K. Uncertainties of the leaky mode correction for near-square-law optical fibers. Electron. Lett. 13:513-514; 1977.

[44] Young, M. Optics and lasers, an engineering physics approach (chapter 3). New York, Berlin, Heidelberg: Springer; 1977.

[45] Snyder, A. W. Leaky-ray theory of optical waveguides of circular cross section. Appl. Phys. 4:273-298; 1974.

[46] Snyder, A. W.; Mitchell, D. J.; Pask, C. Failure of geometric optics for analysis of circular fibers. J. Opt. Soc. Am. 64:608-614; 1974.

[47] Snyder, A. W.; Mitchell, D. J. Leaky rays on circular optical fibers. J. Opt. Soc. Am. 64:615-623; 1974.

[48] Stewart, W. J. Detail resolution in optical fibre index profiling methods. AGARD Conf. Proc. 219:28-1; 1977.

[49] Stewart, W. J. Resolution of near-field optical fibre refractive index profiling methods. Proc. International Meeting on Scanned Image Microscopy, London, 1980, New York:Academic Press; 1981. 233-239.

[50] Malitson, I. H. Interspecimen comparison of the refractive index of fused silica. J. Opt. Soc. Am. 55:1205,1209; 1965.

[51] Fleming, J. W. Material dispersion in lightguide glasses. Electron. Lett. 14:326-329; 1978.

[52] Fleming, J. W. Dispersion in step-index silicone-clad fibers. Appl. Opt. 18:4000-4002; 1979.

[53] I am indebted to Michael Liva and William Sacher of Cargille Laboratories for providing the liquids along with their indices, their Sellmeier coefficients and a statement of accuracy.

[54] Natrella, M. G. Experimental Statistics. Nat. Bur. Stand. (U.S.) Handb. 91; 1963. 5-22, 5-23, 5-27.

[55] Kim, E.; Franzen, D. L. Interlaboratory measurement comparison to determine the radiation angle (NA) of graded-index optical fibers. Appl. Opt. 20:1218-1220; 1981.

[56] Cohen, L. G.; Mammel, W. L.; Lumish, S. Tailoring the shapes of dispersion spectra to control bandwidths in single-mode fibers. Opt. Lett. 7:183-185; 1982; and references therein.

[57] Longhurst, R. S. Geometrical and physical optics, third ed., chapter 5. London: Longmans Group; 1973.

[58] Tilton, L. W. Standard conditions for precise prism refractometry. J. Res. Nat. Bur. Stand. 14:393-418; 1935. Tilton, L. W. Prism refractometry and certain goniometrical requirements for precision. J. Res. Nat. Bur. Stds. 2:909-930; 1929.

## APPENDIX A. MEASUREMENT OF INDEX OF REFRACTION

It may be desirable to measure the index of the matching fluids directly, for example if the calibration is to be carried out by varying the temperature of a single fluid. If a refractometer is not available, the measurement may be carried out using one of several methods that employ a prism spectrometer. The theory and practice of these methods are described in detail by Longhurst [57]. In this appendix, I will discuss several factors that limit the precision of liquid-prism and total-internal-reflection methods of measuring the index of a liquid. I include this material here because I have been unable to find similar calculations elsewhere.

There is no need to repeat Longhurst's description of the minimum-deviation method. The index is determined from the formula,

$$n = \frac{\sin\ (\alpha + \theta)/2}{\sin\ \alpha/2}\ , \tag{A1}$$

where $\alpha$ is the prism angle and $\theta$ is the angle of minimum deviation. At minimum deviation, $\alpha + \theta = 2I_1$, where $I_1$ is the angle of incidence at the first prism face, and a ray travels through the prism perpendicular to the bisector of angle $\alpha$. To analyze the errors inherent in this method, we first differentiate with respect to both $\alpha$ and $\theta$. The results are

$$\Delta n_\alpha = (n/2)[\cot\ \alpha/2 - \cot\ (\alpha+\theta/2]\Delta\alpha \tag{A2}$$

and

$$\Delta n_\theta = (n/2)[\cot\ (\alpha+\theta)/2]\Delta\theta, \tag{A3}$$

where $\Delta n_\alpha$ is the error that results in n if $\alpha$ is known to an accuracy of $\Delta\alpha$ and where $\Delta n_\theta$ is defined similarly. $\Delta\alpha$ and $\Delta\theta$ are instrumental errors and may be taken as one half the finest divisions on the divided circles of the spectrometer (see also reference 58).

For mathematical convenience, we may treat these errors as correlated and add their magnitudes to estimate the total instrumental error. Paying careful attention to sign, we find that eqs (A2) and (A3) are positive as written; therefore, the sum $\Delta n_1$ of the instrumental errors $\Delta n_\alpha$ and $\Delta n_\theta$ is

$$\Delta n_1 = (n/2)\ \Delta\alpha\ \cot\ (\alpha/2), \tag{A4}$$

where we assume that $\Delta\theta$ and $\Delta\alpha$ are equal. This is so because near minimum deviation $\theta$ is a slowly varying function of angle of incidence. The orientation of the prism need be accurate no better than several minutes to measure $\theta$ precisely. Therefore, we take $\Delta\theta$ as well as $\Delta\alpha$ to be one-half division of the scale.

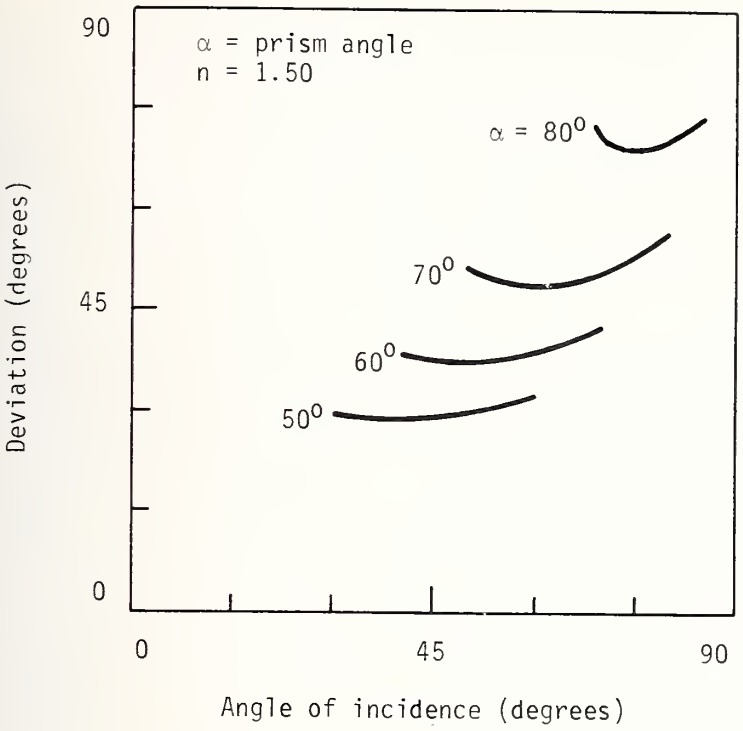


Figure A1. Deviation as a function of angle of incidence for various prism angles.

For a 1-minute spectrometer, $\Delta\alpha$ = 0.5' or about 0.15 mrad; if $\alpha$ = 60° and n = 1.5, $\Delta n_1$ is consequently about 0.0002. This is about the precision required for index-profile measurements.

Taken by itself, eq (A4) suggests that $\alpha$ should be made as large as possible, provided that it is not so large that light will not pass through the prism. Figure A1, however, shows that as $\alpha$ increases, the deviation becomes a stronger function of angle of incidence. As a result, measurement of the minimum deviation $\theta$ becomes more dependent on the precise orientation of the prism. Inasmuch as increasing $\alpha$ from 60° to 80° can be expected to reduce experimental error by only about 30 percent, little or nothing will be gained by making $\alpha$ much larger than the common value of 60°.

The prism must also be levelled; that is, the edge of the prism must be made parallel to the axis of rotation of the prism table. For the degree of accuracy required here, levelling error is potentially significant, as may be shown by referring to figure A2. In that figure, the yz plane is the plane that contains the face of the prism. The incident ray OB strikes the prism with angle of incidence i = AOB. However, because OB is inclined to the xy plane with angle $\varepsilon$ = COB, the spectrometer will measure angle i' = AOC. We wish to calculate the difference between the measured value i' and the true value i.

We construct a vector OB whose magnitude is 1 and apply the law of cosines to the triangle OAB:

$$x^2 + 1 - 2x \cos i = x^2 + y^2. \qquad \text{(A5)}$$

x, y, and z are the line segments indicated on the figure and $y^2 + z^2$ is the length of AB. We express x and y in terms of the angles $\varepsilon$ and i', and then demand that $\varepsilon$ be sufficiently small that cos $\varepsilon$ = 1 and sin $\varepsilon$ = $\varepsilon$. eq (A5) therefore becomes

$$\cos^2 i' + 1 - 2 \cos i' \cos i = \sin^2 i' + \varepsilon^2. \qquad \text{(A6)}$$

When $\varepsilon$ = 0, eq (A6) may be written in the form,

$$\cos^2 i + 1 - 2 \cos i \cos i = \sin^2 i. \qquad \text{(A7)}$$

We may combine eqs (A6) and (A7) by subtracting and writing the result in the form,

$$\Delta(\cos^2 i) - 2 \cos i \, \Delta(\cos i) = \Delta(\sin^2 i) + \varepsilon^2 \qquad \text{(A8)}$$

Carrying out the differentiation indicated by the symbol $\Delta$, we find that

$$\Delta i = -\varepsilon^2/(2 \sin i \cos i). \qquad \text{(A9)}$$

At minimum deviation, $\alpha$, i, and $\theta$ are related by the equation

$$\theta + \alpha = 2i. \qquad \text{(A10)}$$

The error in measuring $\theta$ is consequently twice $\Delta i$. Likewise, figure A2 shows that a levelling error will cause a similar error in measuring $\alpha$.

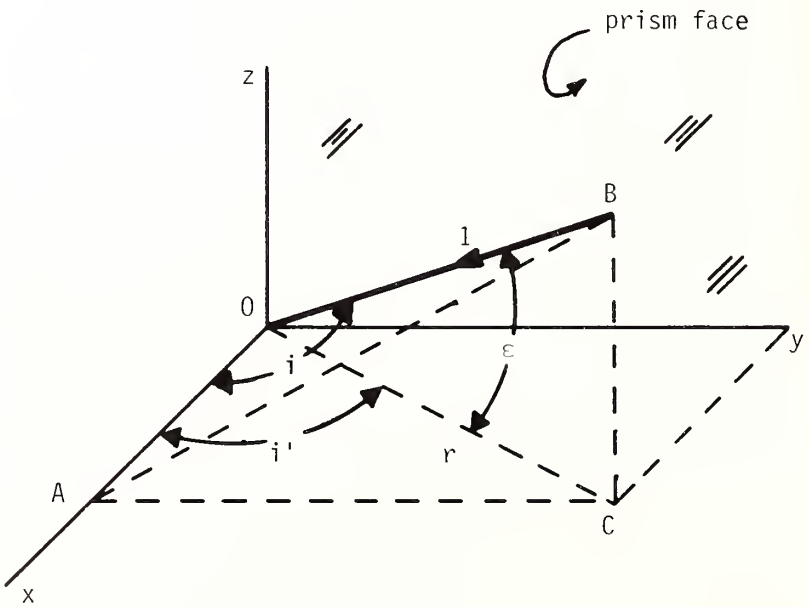


Figure A2. Geometry for calculation of error resulting from improper leveling of prism.

Suppose that the prism has index 1.5 and that the prism angle is 60°. If we take $\varepsilon$ to be 0.1°, then we find from eq (A9) that $\Delta i$ is about 0.1' and therefore that $\Delta\alpha$ and $\Delta\theta$ are each about 0.2'. This is nearly comparable to the precision of the instrument used in the previous examples. Levelling must consequently be precise to better than 0.1°.

Levelling error is a systematic error and is always negative because $\Delta i$ is always negative. It results in an underestimate of both $\theta$ and $\alpha$, and therefore in an underestimate of n.

The index of a liquid may be measured using a hollow glass prism. The measurement will be accurate if the windows of the prism have parallel faces; in appendix B, I show that this requirement is not stringent. Therefore, all the foregoing remarks refer to liquid-prism techniques as well as to more-common solid-prism techniques.

It is also possible to measure the index of a liquid using a prism spectrometer and a critical-angle method, such as the two described in reference 57. Both methods are in principle the same; the geometry is illustrated in figure A3. The liquid to be measured is in contact with one face of a glass prism whose index is known. The index of the liquid is n and that of the glass is $\mu$. $\mu$ must be greater than n if total reflection is to occur; this is not generally a serious constraint where fiber optics is concerned, because the liquids used will generally have indices less than 1.5.

The index of the liquid is found from the equation,

$$n = N \sin \alpha - \sin \phi \cos \alpha \qquad \text{(A11)}$$

derived in reference 57. $\theta$ is the critical angle, $N^2 = \mu^2 - \sin^2 \phi$, and other parameters are as drawn in figure A3.

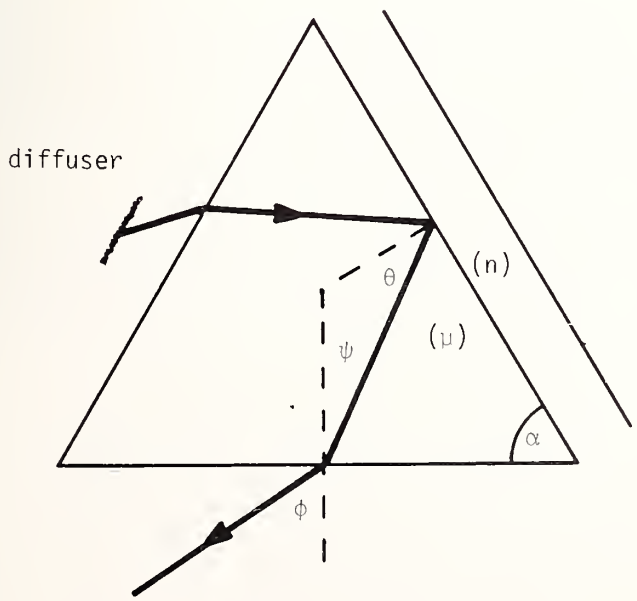


Figure A3. Critical-angle method of determining refractive index of a liquid.

To estimate the precision of the critical-angle methods, we differentiate eq (A11), yielding three equations,

$$\Delta n_\alpha = (N \cos \alpha + \sin \phi \sin \alpha)\, \Delta\alpha, \tag{A12}$$

$$\Delta n_\phi = -[(\sin \alpha \sin \phi \cos \phi)/N + \cos \alpha \cos \phi]\, \Delta\phi, \tag{A13}$$

and

$$\Delta n_\mu = (\mu/N) \sin \alpha\, \Delta\mu, \tag{A14}$$

where the notation is as before.

If we use the same example as above (namely that $\alpha = 60°$ and $\mu = 1.5$), and assume that the index of the liquid is 1.45, we find that $\theta$ is about 75° and $\phi$ about -23°. Therefore,

$$\Delta n_\alpha = 0.4\, \Delta\alpha,$$

$$\Delta n_\phi = -0.2\, \Delta\phi, \tag{A15}$$

and

$$\Delta n_\mu = 0.9\, \Delta\mu.$$

If $\Delta\alpha = 0.15$ mrad (0.5'), then $\Delta n_\alpha + \Delta n_\phi \sim 0.0001$. We learned in connection with eq (A4) that $\mu$ could be determined to 0.0002; using the critical-angle methods adds an additional uncertainty of 0.0001. If a liquid prism is available, the result may in principle be slightly more precise than a determination by the critical-angle method. However, the liquid prism I obtained commercially had such badly warped faces that I decided not to use it.

Equations (A2), (A3), (A12), (A13), and (A14) may be used for estimating the instrumental limit of error only. This represents the greatest precision that can be expected from a particular instrument. A given measurement will have to be carried out several times before the statistical limit of error is as small as the instrumental limit.

Finally, the index of typical liquids varies considerably with temperature, the coefficient being of the order of 0.0004 $K^{-1}$. Therefore, if the index is to be determined to greater precision than the figures assumed in this appendix, the temperature will have to be controlled to within a few tenths of a kelvin.

## APPENDIX B. USE OF THE HOLLOW PRISM

A hollow prism may be used to measure the index of refraction of a liquid, provided that the glass windows have reasonably parallel faces. To determine the imprecision that results from lack of parallelism, we assume that any wedge is shared equally by the two windows through which the light passes. This is, of course, an approximation, but it allows us to draw the ray through the liquid parallel to the base of the prism when the deviation is a minimum. Only half the prism need be drawn, as in figure B1. In that figure, the angles are defined as indicated. The angle labeled $\theta$ is one-half the deviation brought about by the whole prism.

If the window surfaces are parallel, then the angles are as labeled in figure B1. Suppose that we incline the inner face of the window by an angle $\Delta\alpha$, as shown by the dotted line. Then the angles change from $I_3$ to $I_3 + \Delta I_3$ and so on. We wish to calculate the change $\Delta\theta$ in $\theta$ that results from the wedge angle $\Delta\alpha$.

To begin, we apply Snell's law to the refraction at the liquid-glass interface,

$$n \sin I_3 = \mu \sin I_3' . \tag{B1}$$

Differentiating both sides of eq (B1), we find that

$$\Delta I_3' = (n \cos I_3 / \mu \cos I_3')\ \Delta I_3 \tag{B2}$$

where $\Delta I_3$ is equal to $\Delta\alpha$. Similarly,

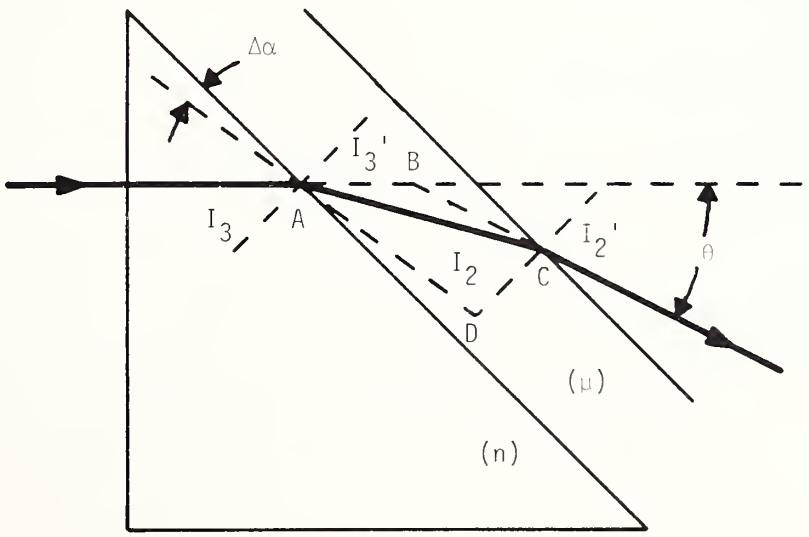


Figure B1. Geometry for calculating effect of wedge in faces of liquid prism.

$$\Delta I_2' = (\mu \cos I_2/\cos I_2')\, \Delta I_2, \tag{B3}$$

but $\Delta I_2$ is not equal to $\Delta\alpha$.

We learn from triangle ABC that

$$\theta = I_3 - I_3' + I_2' - I_2 \tag{B4}$$

and therefore that

$$\Delta\theta = \Delta I_3 - \Delta I_3' + \Delta I_2' - \Delta I_2 \tag{B5}$$

and

$$\Delta\theta = [1 - n \cos I_3/(\mu \cos I_3')]\Delta I_3 + (\mu \cos I_2/\cos I_2' - 1)\Delta I_2. \tag{B6}$$

Using triangle ACD, we find that

$$\Delta I_2 = \Delta I_3' - \Delta\alpha, \tag{B7}$$

which we substitute into eq (B5). Equation (B5) becomes

$$\Delta\theta = [(n \cos I_3/\cos I_3') - \mu](\cos I_2/\cos I_2')\Delta\alpha. \tag{B8}$$

Even if n and $\mu$ differ by 0.1, $\cos I_3'$ is very close to $\cos I_3$, so eq (B8) may be simplified to

$$\Delta\theta = (n - \mu)(\cos I_2/\cos I_2')\Delta\alpha. \tag{B9}$$

If we use the same example as before, and let $n - \mu$ be 0.05, we find that

$$2\Delta\theta \sim 0.15\Delta\alpha \tag{B10}$$

where $2\Delta\theta$ is the total error of measuring the deviation and where $\Delta\alpha$ is the wedge angle of each window. Common optical windows will have wedge of 20" or so; thus, $2\Delta\theta$ is about 3" or 0.05'. Because this error is much smaller than the errors noted in appendix A, wedge in the windows will not be a factor unless we need to know n substantially better than $\pm 0.0002$.

## APPENDIX C. RESOLUTION LIMIT AND DEPTH OF FOCUS

The resolution limit of a microscope objective in air may be expressed as $\lambda/NA$, where NA is the numerical aperture and is equal to sin U; U is the angle formed by the marginal ray and the axis, as shown in figure C1 (see reference 44, chapter 2).

As a rule (except in metallurgical microscopes), the image is projected into a medium whose index n differs from that of air. This is also shown in figure C1. The resolution limit RL' in the medium is equal to $\lambda'/\sin U'$, where $\lambda' = \lambda/n$ is the wavelength in the medium. Using Snell's law at the interface, we find that $\sin U = n \sin U'$. Therefore, RL' = RL. The change of U is precisely compensated by the wavelength shift. This is a well-known result, namely that the resolution limit is $\lambda/NA$, independent of the index of the surrounding material.

The depth of focus DF is given by $\lambda/2(NA)^2 = \lambda/2\sin^2 U$. (That is, the image is in acceptable focus within a distance $\pm DF$ of the image point.) The depth of focus DF' in the medium is therefore $\lambda'/2 \sin^2 U'$, which reduces to $DF' = nDF = n\lambda/2(NA)^2$. The change of wavelength does not compensate the change of angle, and depth of focus is larger in the medium by a factor of n.

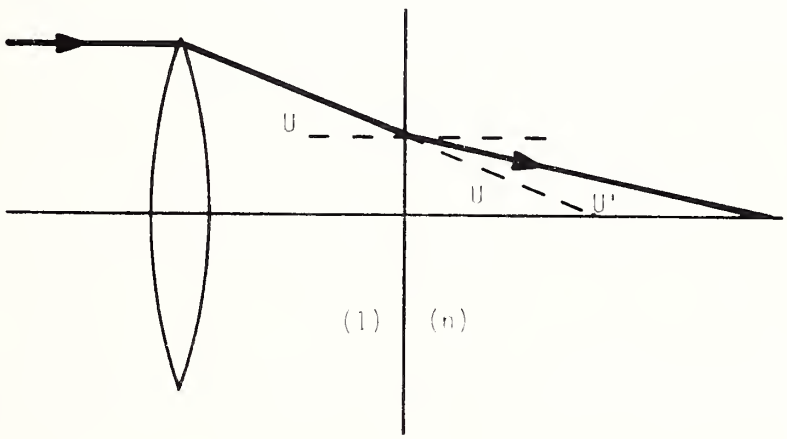


Figure C1. Geometry used for determining the resolution limit in matching fluid.

## APPENDIX D. DESIGN OF MULTIELEMENT GLASS CONDENSER

Single-element glass condensing lenses may be purchased readily with F numbers of 2 or somewhat less. To achieve an effective F number less than 1, we must design a compound lens, the first element of which is operated with the object distance about one half the focal length.

To minimize the aberrations of the lens, we attempt to make the deviation of the ray by each element a constant; likewise, we choose the elements in such a way that the deviation at each surface is about one half the total deviation of the lens.

Figure D1 shows a thin lens whose focal length is f' projecting an image with conjugates $\ell$ and $\ell'$. The angles u and u' are defined as shown, as is the deviation $\delta$. They are related by

$$\delta = u + u'. \tag{D1}$$

This result is true for thick lenses as well as thin. In paraxial approximation,

$$u = h/\ell , \tag{D2}$$

and

$$u' = h/\ell'. \tag{D3}$$

Using eq (D2) and the lens equation, we find immediately that

$$\delta = h/f'. \tag{D4}$$

Now consider a three-element condensing lens (fig. D2). For the moment, consider the lenses to be thin and in contact; all have focal length f'. If we demand a magnification m = 2, then the image distance $\ell_3'$ is equal to $2\ell_1$ where $\ell_1$ is the object distance. If the deviation by each lens is $\delta$, then the total deviation is $3\delta$; therefore, looking at the lens as a whole, we find that

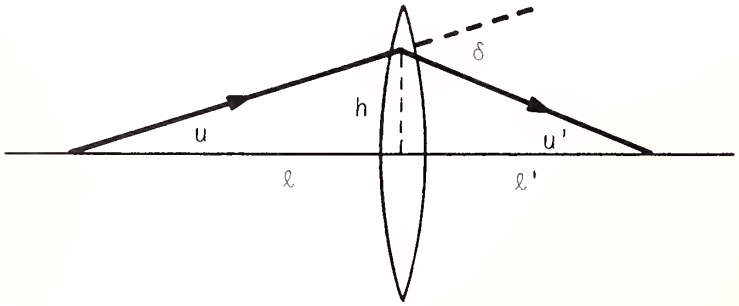


Figure D1. Deviation and other parameters of the condensing lens.

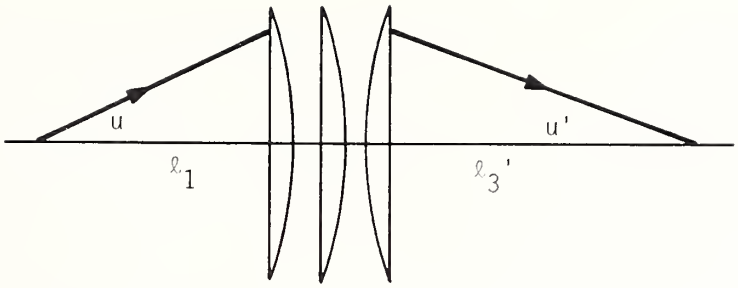


Figure D2. Conjugates of the three-element condensing lens.

$$3\delta = (h/\ell_1) + (h/2\ell_1). \tag{D5}$$

Because $\delta = h/f'$ the object distance $\ell_1$ is $f'/2$.

A simple, paraxial ray trace using the lens equation shows that the first lens projects a virtual object to the primary focal point of the second lens; the second lens projects the image to $\infty$; and the third lens projects the image to its secondary focal point. Thus, to minimize spherical aberration, the lenses should be planoconvex, each oriented with its curved side toward its own long conjugate. (The first element should in principle be meniscus, but such a lens may not be available.) If the lenses have been molded and are to be placed into a barrel, they must be centered and have their edges ground by an optics shop to keep other aberrations to a minimum. Image quality is still poor, as with all condensing lenses, so a uniform, large-area detector is required.

In reality, the elements are comparatively thick with respect to their focal lengths. Therefore, it may be necessary to follow the path of a marginal ray through the lens to be certain that one of the central elements does not act as the aperture stop for the system. Apart from this caveat, the design based on thin-lens elements is probably adequate. The effective focal length of the real lens will exceed the calculated value somewhat.

For most cases, a three-element lens working at the magnification of two will probably be adequate; if not, a four-element lens may be necessary. It is easy to generalize eq (D4) to the case of an N-element lens with magnification m. The result of an analysis exactly similar to the preceding is

$$\ell_1 = (1 + 1/m)\ f'/N, \tag{D6}$$

$$\ell_N' = (1 + m)\ f'/N, \tag{D7}$$

where $\ell_N'$ is the image distance.

# Chapter 4

# Interlaboratory Comparisons on Graded-Index Optical Fibers Using Standard Measurement Conditions

**compiled and edited by**
**D. L. Franzen**
**E M. Kim**

The National Bureau of Standards (NBS), in cooperation with the Electronic Industries Association, has conducted a number of interlaboratory measurement comparisons. Participants include NBS and several fiber manufacturers. Comparisons were limited to telecommunication, multimode, graded-index fibers and covered the main parameters used in specification; namely, attenuation, bandwidth, numerical aperture, and core diameter. The results were reported in Applied Optics and are reprinted here with minor revision to include additional background information.

## CONTENTS

Section 1

# INTERLABORATORY MEASUREMENT COMPARISON TO DETERMINE THE ATTENUATION AND BANDWIDTH OF GRADED-INDEX OPTICAL FIBERS[†]

Douglas L. Franzen, G. W. Day, Bruce L. Danielson,
George E. Chamberlain, and Ernest M. Kim[††]

An interlaboratory measurement comparison was conducted by the National Bureau of Standards in cooperation with the Electronic Industries Association. Participants included NBS and nine optical fiber and cable manufacturers. Four graded-index fibers having lengths of 2, 2, 2 and 0.9 km were used. Measurements of attenuation at 850 nm, using both beam optics and mode filter approaches to achieve a restricted launch, gave one standard deviation spreads of 0.24, 0.12, 0.12, and 0.43 dB/km, for an overall average of 0.23 dB/km. Best measurement agreement was obtained for a fiber having little differential mode attenuation. Measurements of -3 dB bandwidth from time domain acquired data at 900 nm gave an average one standard deviation spread of 12 percent with poorer agreement on the higher frequency portion of the frequency response.

† Applied Optics, 20:2412; 1981.
†† NBS Co-op graduate student on leave from New Mexico State University, Las Cruces, New Mexico.

## 1. INTRODUCTION

Attenuation and bandwidth are important quantities used to specify the transmission properties of optical fibers. For technical and commercial reasons it is useful to assess interlaboratory measurement agreement. Past comparisons of attenuation have indicated discrepancies substantially exceeding the single apparatus precision of participants [1,2]. One would expect these measurement differences to increase in going from intra to interlaboratory comparisons. An earlier NBS sponsored interlaboratory comparison using an overfilled launch for attenuation gave a one standard deviation measurement spread of approximately 0.6 dB/km [1].

Because of differential mode properties in multimode fibers, attenuation and bandwidth values depend on how light is launched into the fiber. The present comparisons used launching conditions specified in measurement procedures pending before standards groups; included are measurement results for restricted launch attenuation and overfilled launch bandwidth [3]. Measurements of overfilled launch attenuation were also included to monitor progress since the previous interlaboratory comparison [1]. A procedure for determining numerical aperture was tested at the same time and results from this are reported elsewhere [4]. Participants include NBS and several manufacturing members of the Electronic Industries Association [5]. This includes most U.S. and some Canadian manufacturers of fiber and fiber cable.

It is desirable to have fiber attenuation values determined in such a manner that they can be added linearly to predict the overall attenuation of joined sections (concatenation). For long lengths of graded index fiber, this means certain high loss modes which do not propagate power far in the fiber must be eliminated at launch. This is accomplished by restricting the launched mode volume in a specified manner [6,7,8,9]. If a typical graded-index fiber is initially overfilled, backscatter measurements show the attenuation rate gradually decreases to a more nearly constant value in several hundred meters (B. L. Danielson, NBS). Higher attenuation for higher-order modes results in a gradual spatial and angular contraction of radiation with fiber length. Figure 1 shows normalized output far- and near-field radiation patterns at 2 m and at 1 km for an overfilled graded-index fiber. After 1 km of propagation, the power in the higher-order modes has been diminished. The restricted launching conditions used for the attenuation comparisons have, in the past, given good results in the prediction of concatenation for long lengths of telecommunciations type, graded index fiber [7,8]. Evaluated in the comparisons were two different measurement philosophies for achieving the necessary restricted launch.

For bandwidth, the launching conditions giving the best prediction for joined sections is not obvious. Nonlinear length scaling and profile compensation effects obscure efforts to recommend a single, universally applicable launching condition. Thus, the present comparisons specified the use of a mode scrambler to produce an overfilled launch to the test fiber [10]. This bandwidth launching condition is presently being used by most fiber manufacturers.

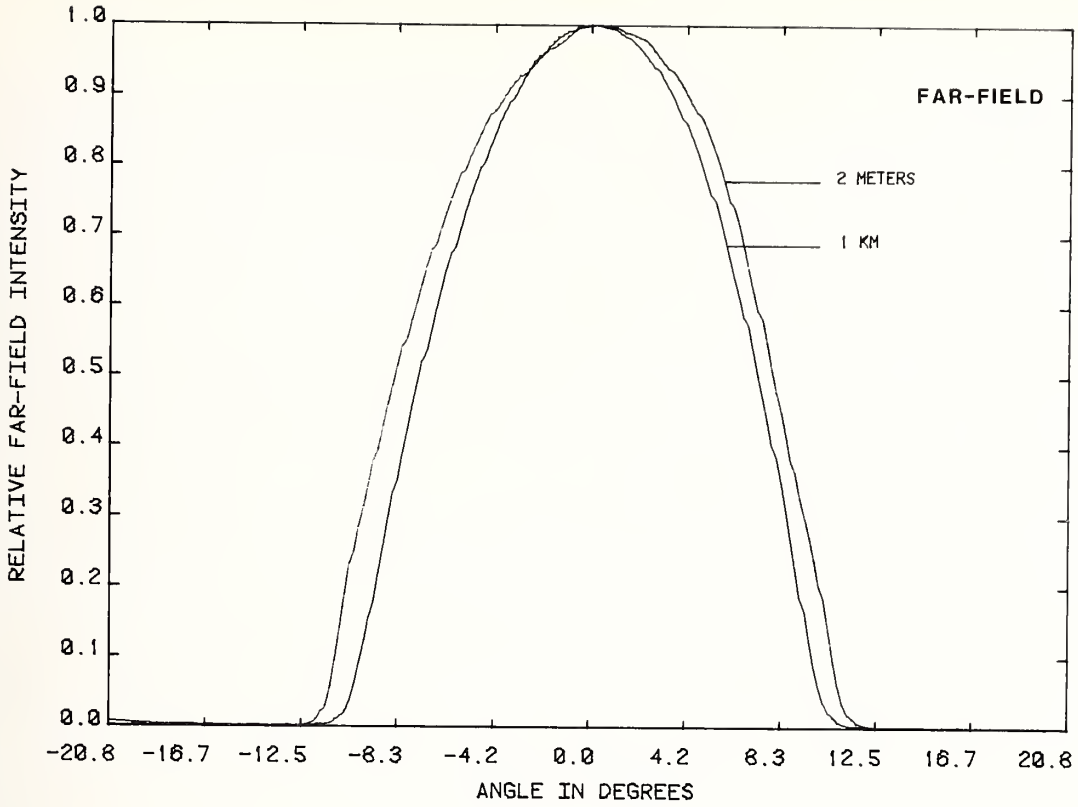


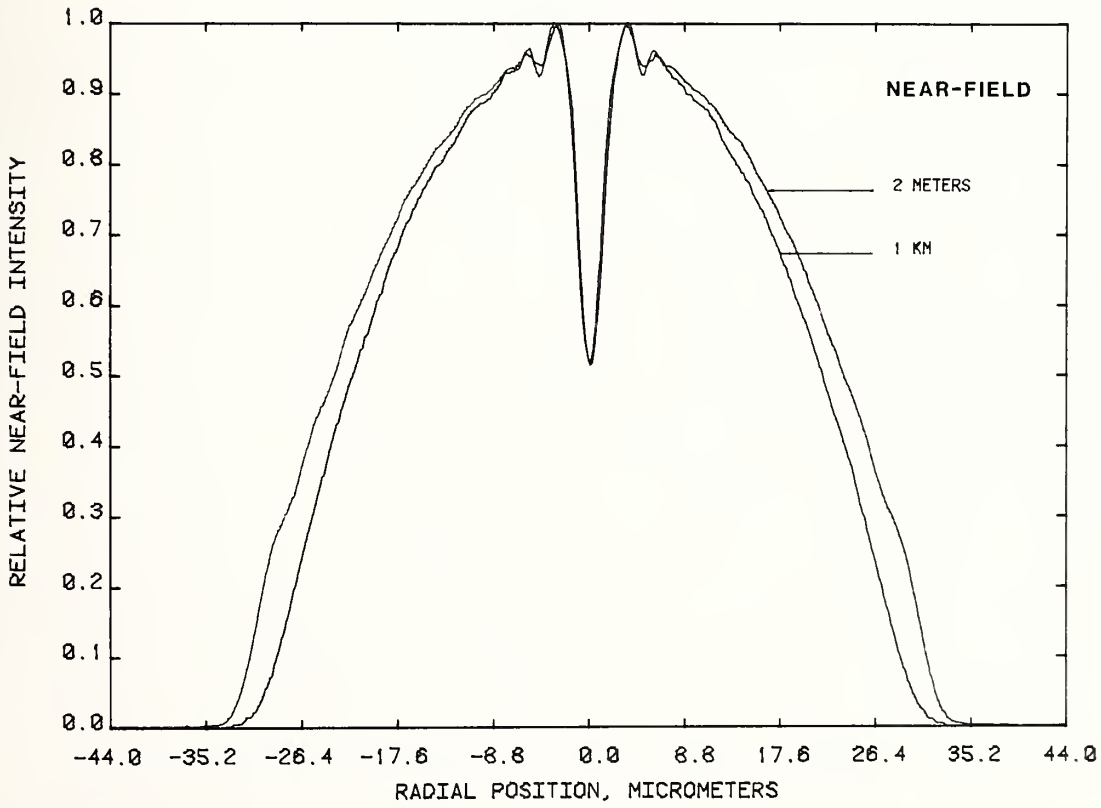


Figure 1. Normalized far- and near-field radiation patterns at 2 m and 1 km from an initially overfilled graded-index fiber. The restriction indicates the loss of power in higher-order modes.

## 2. DESCRIPTION OF COMPARISON FIBERS

Four graded-index fibers designated A, B, C, and D with lengths of 2, 2, 2 and 0.9 km, respectively, were obtained from different manufacturers and chosen to have a mix of properties. Nominal physical parameters are summarized in table 1. Buffering and winding configurations were chosen to enhance fiber stability on the reels by reducing the occurence of unintentional microbending. Fiber A, with a thick plastic buffer coating, was wound on a reel with a minimum of tension; fiber B was wound on a reel whose tension could be released during measurement; fiber C was placed inside a hard plastic buffer tube; and fiber D, also in a buffer tube, was fully cabled with strength members. Reels were shipped to participants inside foam padded, reusable containers.

Fibers were returned to NBS between participants' measurements and attenuation was initially monitored to ascertain stability. Precision of the NBS measurement system was typically 0.1 dB/km at 850 nm. Fibers A, C, and D were stable within system precision (fig. 2); this was verified with another measurement after the seventh participant. One standard deviation spread for the control measurements is 0.06, 0.10, 0.08, and 0.10 dB/km for fibers A, B, C, and D, respectively. Although the spread on fiber B is near the system precision, the trend indicates a decreasing attenuation. However, because of an increasing difficulty with slack occuring in the windings, fiber B was only sent to the first five participants. Stability of all fibers was judged to be adequate for the duration of the comparisons.

Other measurements made on some of the fibers for diagnostic purposes include spectral attenuation, differential mode attenuation (DMA), qualitative mode coupling and backscatter [11]. Spectral attenuation indicates fibers A, B, and C reach attenuation minimums near 1200 nm where the values are 0.9, 0.7, and 0.8 dB/km, respectively. At the comparison wavelength of 850 nm, attenuations for fibers A, B, and C are limited by Rayleigh scattering. Spectral attenuation for these fibers closely follows the $a/\lambda^4 + b$ expression (fig. 3) for wavelengths between 800 and 1150 nm [12]. The values of a and b, 1.2 to 1.4 dB$\cdot\mu m^4$/km and 0.2 dB/km, indicate high quality fibers from an attenuation standpoint. Fiber D has higher attenuation than the others and contains a significant amount of $OH^-$; in fact, the 875 nm absorption line may have affected the comparisons at 850 nm.

Table 1. Nominal properties of comparison fibers

| Fiber | Cladding o.d., μm | Core dia., μm | Buffer coating thickness, μm | Numerical aperture | Reel dia., cm | Length, km |
|---|---|---|---|---|---|---|
| A | 125 | 60 | 170 | 0.24 | 26 | 2 |
| B | 125 | 50 | 70 | 0.16 | 32 | 2 |
| C | 125 | 60 | 70 | 0.18 | 22 | 2 |
| D | 125 | 60 | thin polymer | 0.20 | 30 | 0.9 |

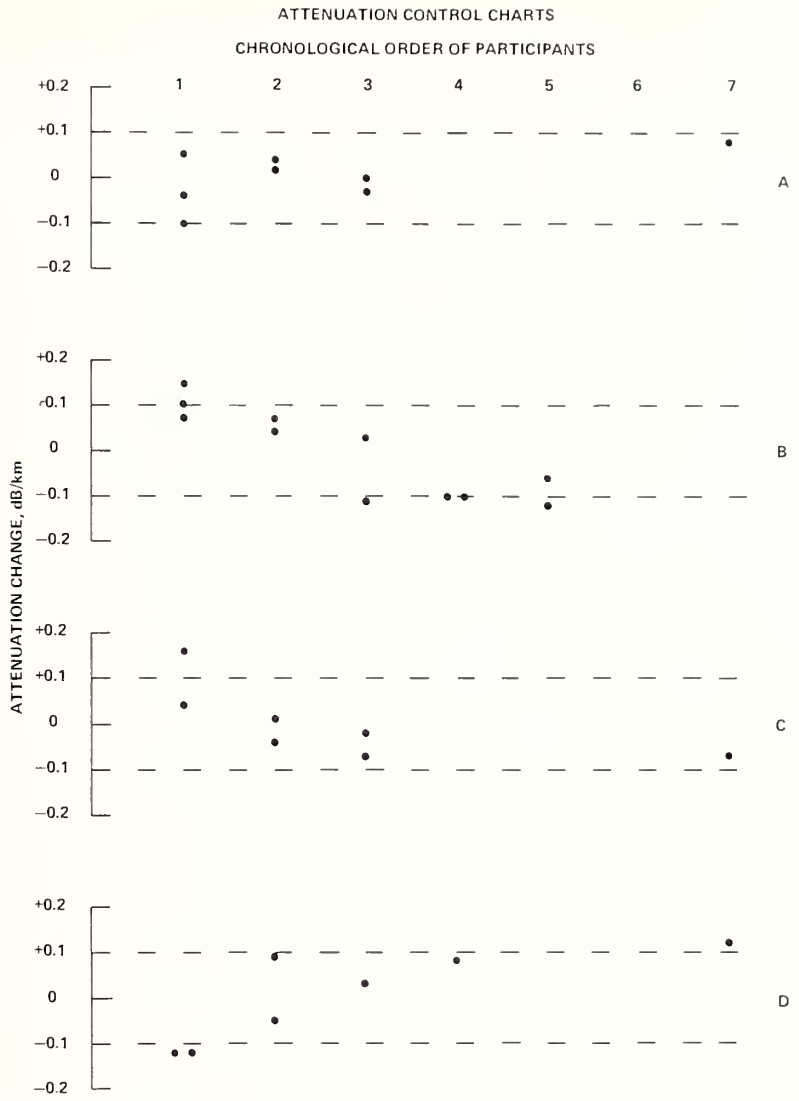


Figure 2. Attenuation stability using an overfilled launch at 850 nm for fibers A, B, C, and D with dotted lines about average indicating typical system precision plus or minus one standard deviation, 0.1 dB/km.

A positive difference between overfilled and restricted launch attenuation values indicates higher attenuation for higher order modes. This occurs in fibers A, B, and D and is the usually observed behavior [13]. Fiber C, however, exhibits also no difference in attenuation between the two launching conditions. A measurement of differential mode attenuation (fig. 4) confirms there is little attenuation difference among modes [14]. Fiber C therefore represents a unique opportunity to compare interlaboratory attenuation results in the absence of differential mode effects.

By comparing the transmitted far-field radiation patterns from various launched mode volumes it was qualitatively determined that little mode coupling occurs in the fibers. This is consistent with recent observations indicating long mode coupling lengths for many presently produced graded-index fibers [8,15].

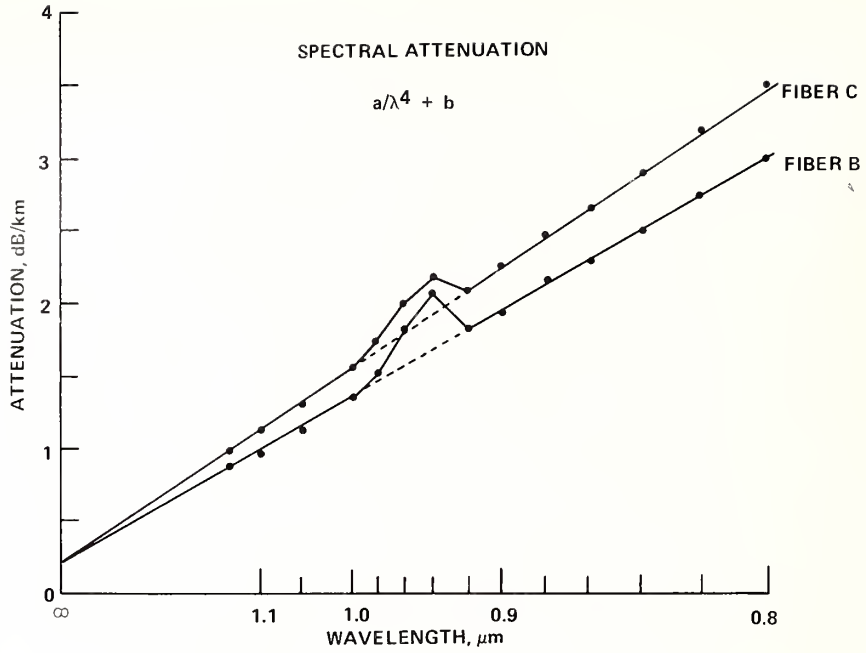


Figure 3. Spectral attenuation of fibers B and C using a restricted launch and plotted as a function of $1/\lambda^4$.

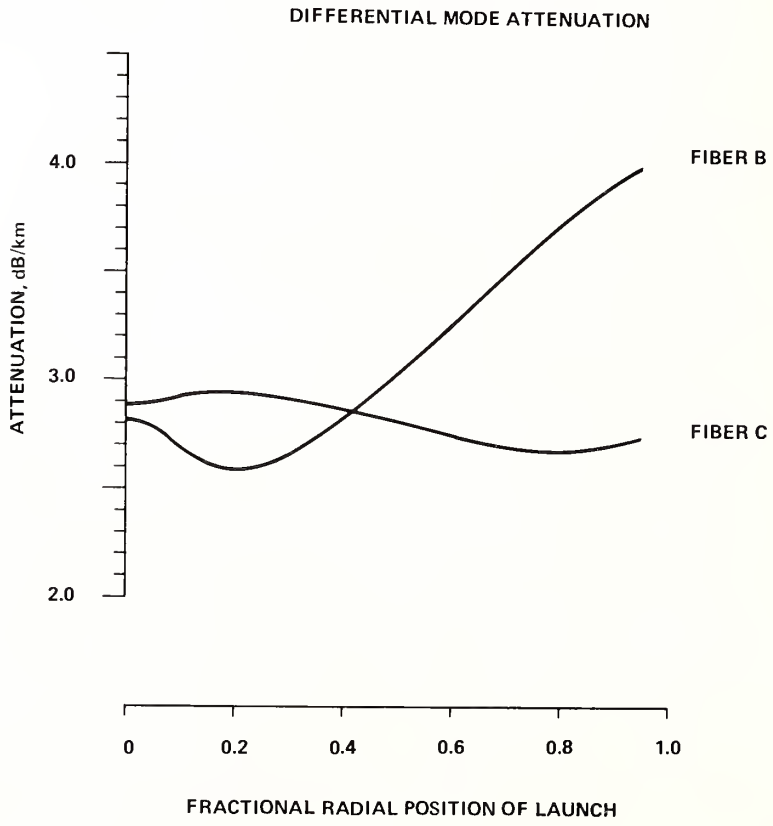


Figure 4. Measurement of differential mode attenuation at 820 nm for fibers B and C.

Backscatter returns obtained for all of the fibers indicate nominally uniform attenuation coefficients. Returns from fibers A and C contain small fluctuations exhibiting a periodicity of 50 to 100 m (fig. 5). Backscatter signatures of this nature are believed to represent core diameter fluctuations along the length. Fibers B and D exhibit smoother backscatter response (fig. 6) with a few small point defects apparent in fiber D which also contained an intentional 0.1 dB loss fusion splice at mid-point.

## 3. ATTENUATION COMPARISONS

Attenuation was measured at 850 nm using the "two point" or "cutback" technique. For the restricted launch measurements, participants could choose either a beam optics or mode filter approach. With properly chosen parameters both are believed to give nearly the same attenuation results [6]. Parameters used with each method have been previously tested through successful concatenation experiments [7,8]. One purpose of the present comparisons is to evaluate systematic differences between the two approaches.

In the beam optics apparatus both the size of the launch spot on the test fiber core and the launch numerical aperture can be independently adjusted. By underfilling the fiber with respect to these parameters, selected high-loss, high-order modes are not initially excited. Participants choosing this method were asked to determine the launch parameters on the fiber entrance face and use the following measurement conditions:

1. A launch spot centered on the test fiber core with a diameter at the 50 percent intensity points of 70 ± 5 percent of the core diameter.
2. A launch numerical aperture at the 5 percent intensity points of 70 ± 5 percent of the fiber numerical aperture.
3. A reference (cutback) length of 1.8 ± 0.1 m.
4. A suitable cladding mode stripper.

In the mode filter approach, certain high angle, high loss modes which have been initially excited in the fiber are stripped out through the action of the mode filter. Mode filter possibilities include mandrel wraps [2,7,9] and dummy fibers. A mode filter can be specified by the effect it has on far-field radiation patterns. It is important for the mode filter to appropriately restrict the high angle portion of the far-field pattern. Participants using the mode filter method were asked to:

1. Overfill the test fiber in both launch spot size and numerical aperture, then determine the far-field radiation pattern exiting the long length at the 5 percent intensity points.

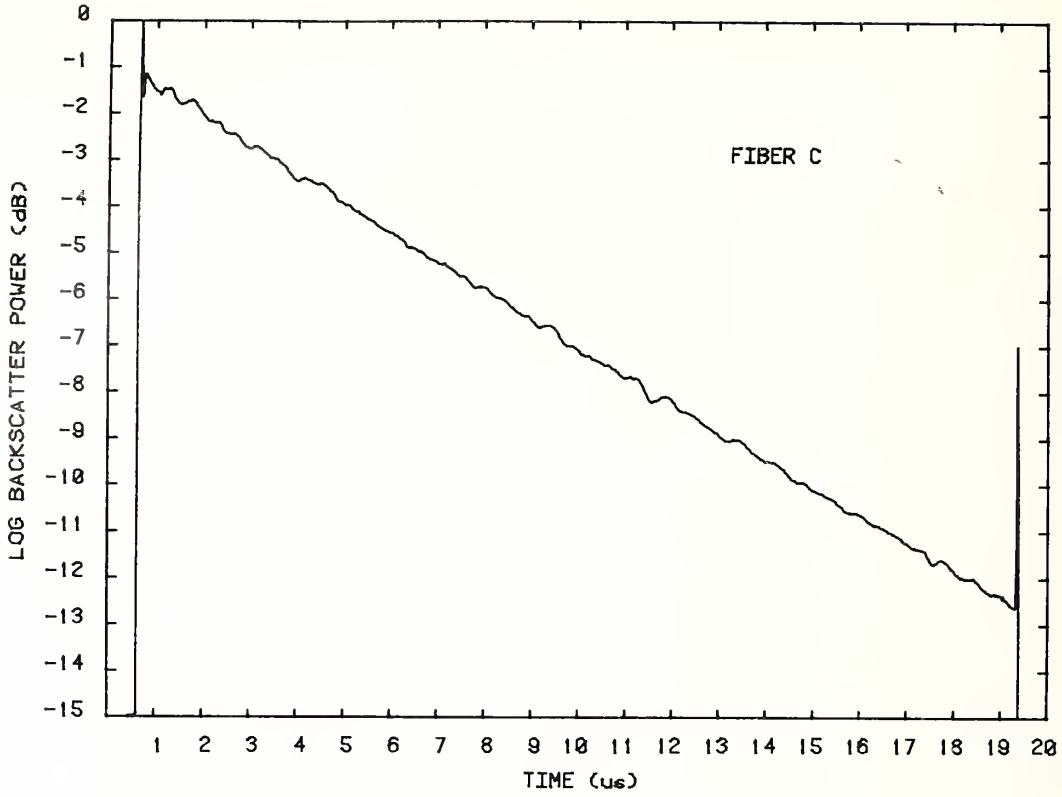


Figure 5. Backscatter return 819 nm, 50 ns resolution from fiber C indicating small fluctuations with length.

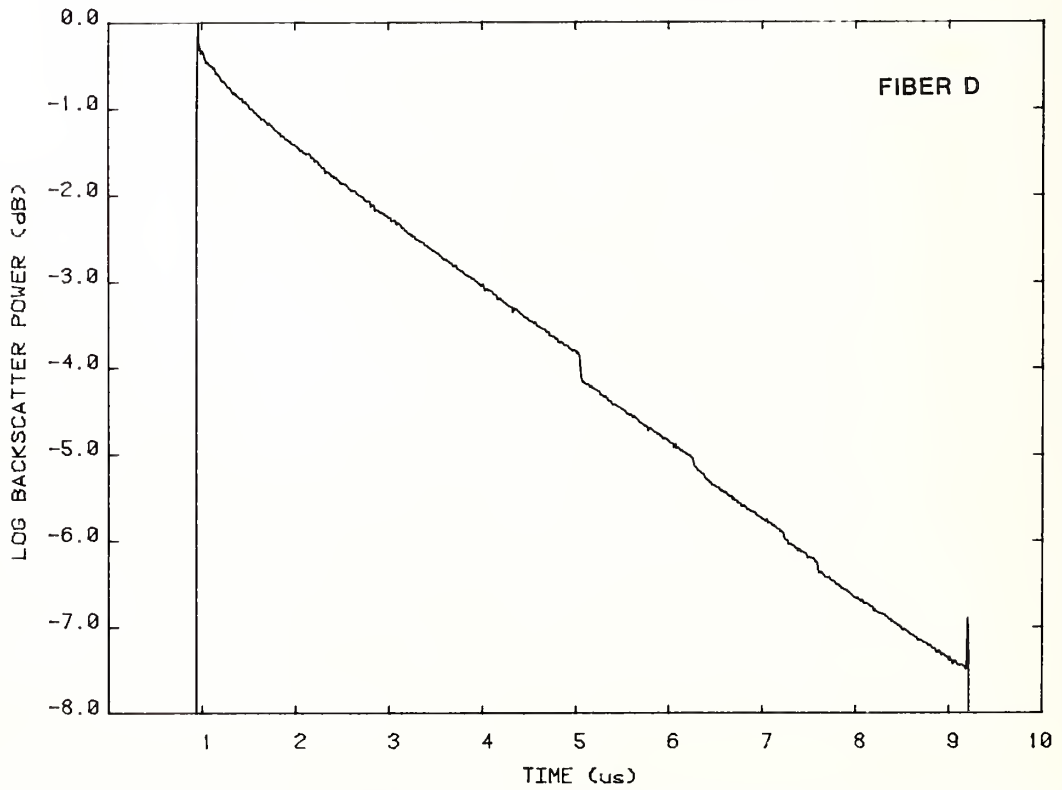


Figure 6. Backscatter return 819 nm, 20 ns resolution from fiber D indicating a smooth response with an intentional 0.1 dB loss fusion splice at mid-point, succeeded by three smaller point defects.

2. Apply a mode filter to the same overfilled test fiber so the far-field pattern at the 5 percent intensity points exiting a 1.8 m length is the same as the above with a tolerance of +0, -7 percent (this procedure qualifies the mode filter).

3. Apply the same overfilled launching conditions and mode filter to the test fiber, then measure attenuation (mode filter is in place and undisturbed for both long and reference length measurements) using a reference (cutback) length of 1.8 ± 0.1 m and a suitable cladding mode stripper.

Attenuation measurements were also made at 850 nm using an overfilled launching condition. Here participants were asked to use a launch spot size exceeding the core diameter and a launch numerical aperture of 0.24 or greater.

Each participant was given fiber length values and results were reported in dB/km. NBS monitored amounts cut off so correct lengths could be provided. Participants typically used 10 m of fiber in completing all measurements and were requested to use no more fiber than needed to make two repeated measurements of a given quantity.

Attenuation results representing contributions from 10 participants are summarized in figures 7 through 10, table 2, and table 3. In compiling these results a few values were clearly outside of the dominant distributions. Out of 58 attenuation values, 3 were eliminated as being unrepresentative. The remaining 55 comprise the data base reported here. In addition to the 3 deleted values, an omission in the tables indicates the participant did not report that particular quantity.

Table 2. Restricted launch attenuation, 850 nm, dB/km

| Participant | Fiber A | Fiber B | Fiber C | Fiber D |
|---|---|---|---|---|
| 726 | 2.91 | 2.44 | 2.51 | 3.77 |
| 833 | 2.87 | 2.38 | 2.77 | - |
| 525 | 2.93 | 2.41 | 2.55 | 3.40 |
| 344 | 2.80 | 2.31 | 2.49 | 3.56 |
| 662 | 2.65 | 2.15 | 2.40 | 4.15 |
| 307 | 3.41 | - | 2.72 | 4.6 |
| 119 | 2.8 | - | 2.6 | 3.8 |
| 129 | 3.19 | - | - | - |
| 038 | 2.7 | - | 2.5 | - |
| 902 | - | - | - | - |
| Mean | 2.92 | 2.34 | 2.57 | 3.89 |
| Standard Deviation | 0.24 | 0.12 | 0.12 | 0.43 |

Table 3. Overfilled launch attenuation, 850 nm, dB/km

| Participant | Fiber A | Fiber B | Fiber C | Fiber D |
|---|---|---|---|---|
| 726 | 3.26 | 2.67 | 2.60 | 4.95 |
| 833 | 3.08 | 2.46 | 2.63 | - |
| 525 | 3.03 | 2.78 | 2.55 | 4.31 |
| 344 | 3.04 | 2.55 | 2.54 | 4.97 |
| 662 | - | - | - | - |
| 307 | 3.38 | - | 2.60 | 4.77 |
| 119 | 3.2 | - | 2.6 | 5.2 |
| 129 | 3.48 | - | - | - |
| 038 | 3.3 | - | 2.66 | - |
| 902 | 4.29 | - | 2.58 | 3.94 |
| Mean | 3.34 | 2.62 | 2.60 | 4.69 |
| Standard Deviation | 0.39 | 0.14 | 0.04 | 0.47 |

Restricted launch results are given in table 2 and figures 7 through 10 for the four fibers. Error bars on data points represent participants' estimates of typical system precision, plus or minus one standard deviation, based on previous experience with other fibers. Reported typical system precision averaged over the ten participants is 0.15 dB/km. One standard deviation measurement spread is 0.24, 0.11, 0.12, and 0.43 dB/km for fibers A, B, C, and D, respectively, with the average being 0.23 dB/km. Approximately two-thirds of the participants used the mode filter procedure while the remainder chose the beam optics. Mode filters which were utilized include mandrel wraps, "S" or serpentine shaped bends, and a dummy fiber. The average of the mode filter determined attenuation values minus the average of the beam optics values is +0.15, -0.02, -0.07, and +0.30 dB/km for fibers A, B, C, and D, respectively. In all cases these offsets are less than the one standard deviation measurement spread of the mode filter values by themselves. Therefore, systematic differences between the two approaches are too small to show up in the present comparisons with a significant level of confidence. One might expect greater differences between the two techniques in fibers which have higher differential mode attenuation than the comparision fibers. The appendix contains measurement results on two fibers having high differential mode attenuation. This data indicates little systematic difference between the two techniques if the mode filter far-field pattern from the reference length is chosen to be in the center of its allowed tolerance. It is interesting to note that the two launching conditions launch different modal distributions in the low- and medium-order mode groups. However, both eliminate the power in the high-order modes and apparently this is sufficient.

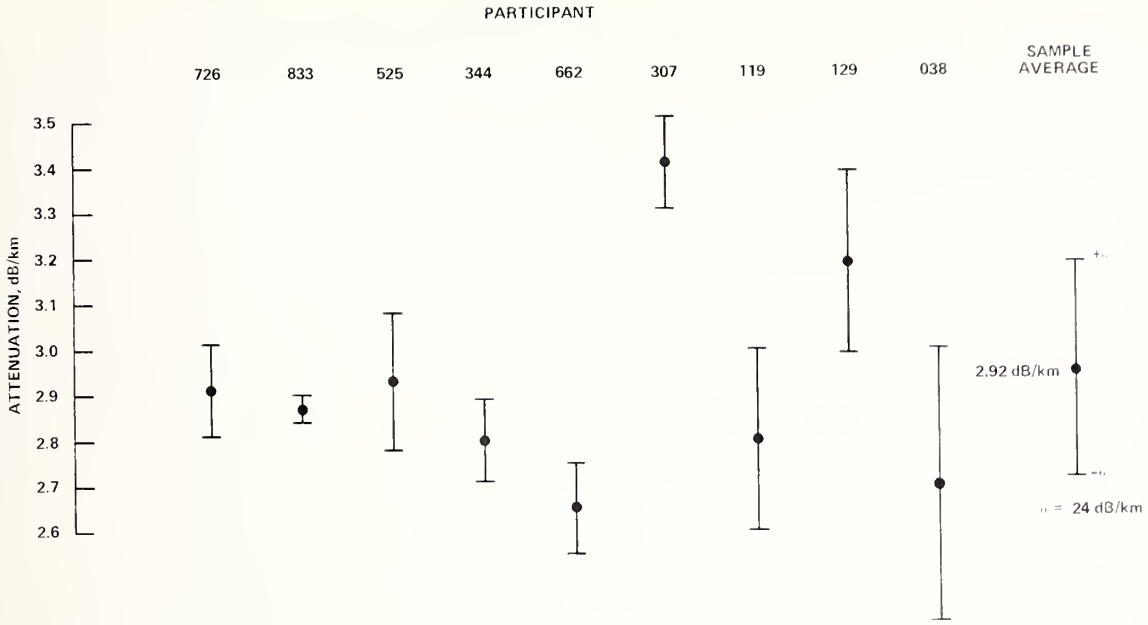


Figure 7. Results of restricted launch attenuation measurements, fiber A, average 2.92 dB/km, one standard deviation 0.24 dB/km.

Overfilled launch results are given in table 3 for the four fibers. Reported launch spots and numerical apertures confirm that participants complied with requested launching conditions. One standard deviation measurement spread is 0.39, 0.14, 0.04, and 0.47 dB/km for fibers A, B, C, and D, respectively, with the average being 0.26 dB/km. Seven participants reported initially aligning the fiber under test for peak transmitted power while two placed the fiber at the center of the launch spot image; results do not indicate any significant difference between the two alignment methods for overfilled launching conditions. Compared to the earlier comparisons having a 0.6 dB/km standard deviation [1], the present overfilled results indicate an improvement. Also, the average of the standard deviations obtained for overfilled launching conditions, 0.26 dB/km, is not very different from the 0.23 dB/km resulting from the restricted launches.

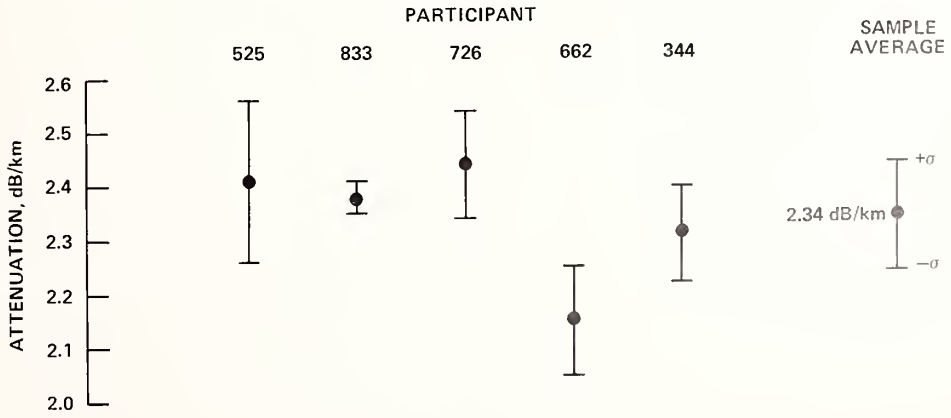


Figure 8. Results of restricted launch attenuation measurements, fiber B, average 2.34 dB/km, one standard deviation 0.12 dB/km.

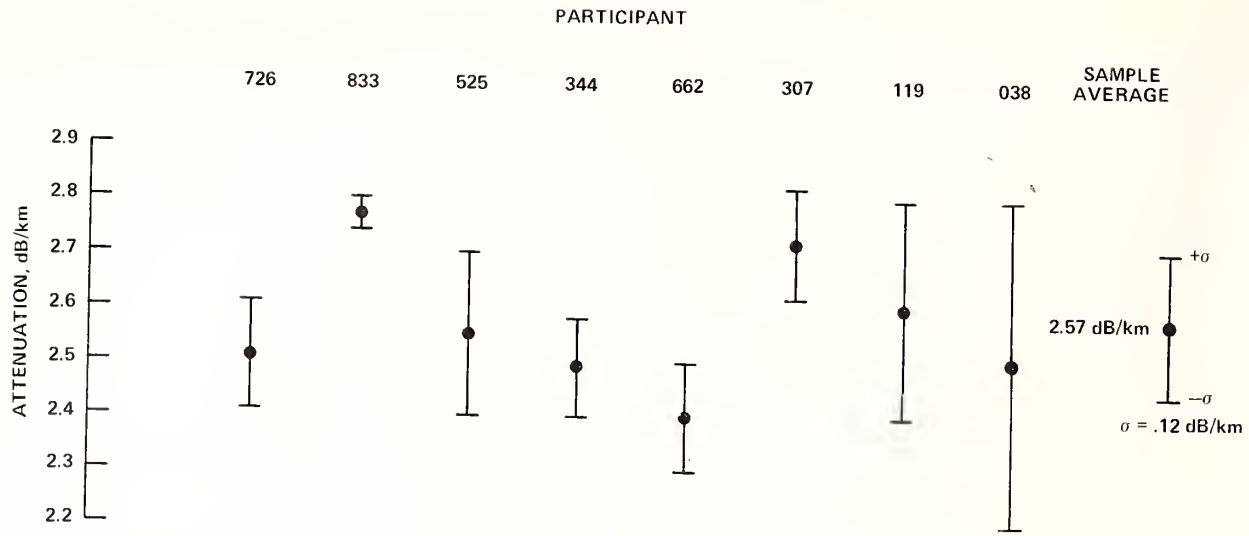


Figure 9. Results of restricted launch attenuation measurements, fiber C, average 2.57 dB/km, one standard deviation 0.12 dB/km.

Participants performed significantly better on some fibers than others. This probably results from differing amounts of differential mode attenuation for the fibers. The smallest measurement spread overall is obtained on fiber C which exhibits almost no differential mode attenuation (fig. 4). The difference between overfilled and restricted launch attenuations is a measure of differential mode attenuation in a fiber; differences based on participants' data for the four comparison fibers in ascending order are 0.03, 0.28, 0.42, and 0.80 dB/km for fibers C, B, A, and D, respectively. This same order occurs when fibers are listed according to increasing measurement spread. As one would expect, the attenuation in high DMA fibers is more sensitive to launching conditions.

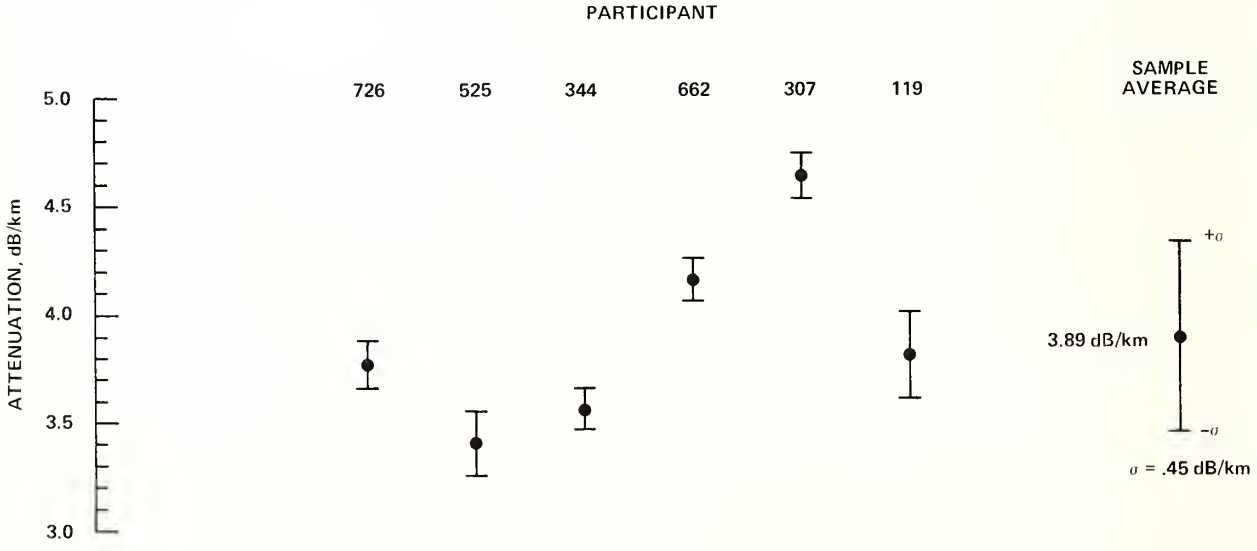


Figure 10. Results of restricted launch attenuation measurements, fiber D, average 3.89 dB/km, one standard deviation 0.43 dB/km.

Fiber D has a high $OH^-$ concentration. The proximity of the 875 nm $OH^-$ absorption line [16] to the 850 nm measurement wavelength may have affected the results. For example, the slope of the spectral attenuation for fiber D at 860 nm is +0.06 dB/nm, whereas in a Rayleigh scattering limited fiber such as C the same slope is -0.01 dB/nm. A small positive offset from the measurement wavelength in addition to a broad source linewidth would result in a higher measured attenuation (fig. 11). Most participants utilized a tungsten lamp source with an interference filter; average reported FWHM linewidth was 12 nm with a maximum of 20 nm. Some results suggest source spectral properties may have had an influence. Participant 662 with a 20 nm source linewidth measured below the average on fibers A, B, and C and above on fiber D.

In summary, the attenuation comparisons yield the following conclusions:

1. Measurement agreement for attenuation has improved industry-wide since the last NBS sponsored comparisons.
2. Uncabled fibers can exhibit good stability as comparison fibers if proper attention is given to buffering and winding configuration.
3. Restricted and overfilled launching conditions for attenuation measurements yield similar standard deviations for comparisons on some types of graded index fiber.

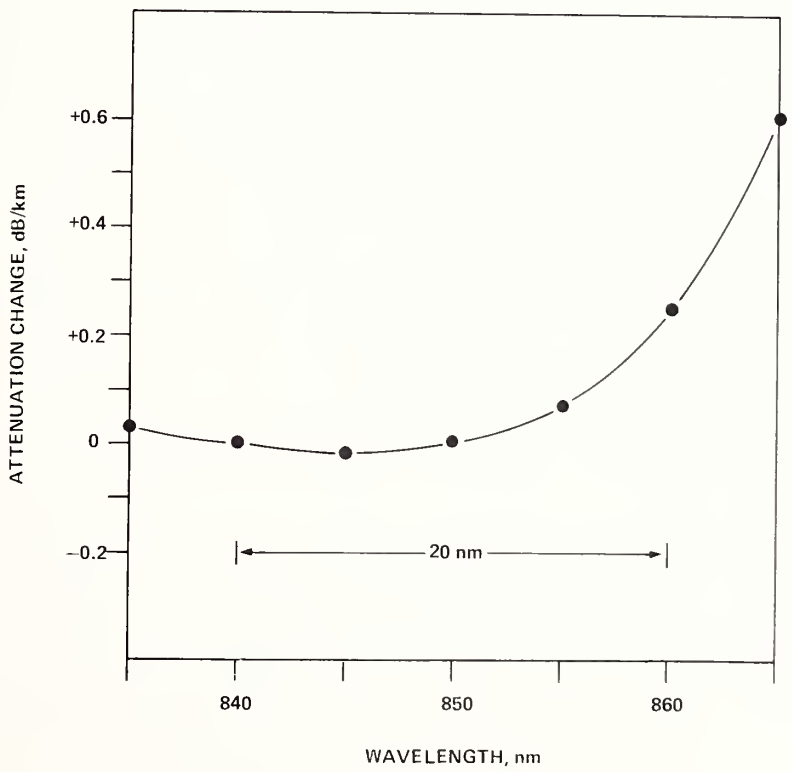


Figure 11. Spectral attenuation change with respect to the comparison wavelength of 850 nm for fiber D. An $OH^-$ absorption occurs at 875 nm.

4. Appropriately specified beam optics and mode filter approaches can give virtually the same results for restricted launch attenuation on many types of long length graded index fiber.

5. The 0.12 and 0.04 dB/km standard deviations obtained for fiber C indicate attenuation systematic differences between participants arising from various non-modal effects such as failure to completely strip cladding light, non-linear detection, incorrect wavelength, etc. are near or less than the average claimed system precision of 0.15 dB/km. As DMA decreases in future high quality fibers, measurement agreement can be expected to improve.

6. The outcome of measurement comparisons is likely to depend on the magnitude of test fiber DMA.

7. Comparison standard deviations on some fibers are presently approaching typical system precisions. Similar observations have been made in preliminary results from a recent European comparison [17]. Further improvements will require better system precisions or the use of many measurements and confidence intervals.

## 4. BANDWIDTH COMPARISONS

Bandwidth comparisons were made using time domain techniques at 900 nm where several participants had pulsed, GaAs laser diodes. Because of significant profile dispersion effects in some of the fibers, it was necessary to specify a single measurement wavelength.

Bandwidth was reported in the frequency domain and defined as the lowest frequency where the magnitude of the baseband frequency response in optical power decreased by 3 dB compared to zero frequency. For the comparisons, participants were asked to:

1. Calculate frequency response from the ratio of Fourier transforms of output to input pulses acquiring the input pulse from a short, 1.8 m length of reference fiber.

2. Use a mode scrambler device to produce launching conditions which overfill the test fiber core and numerical aperture irrespective of the radiation properties of the laser diode.

Fibers A, B, and C which were used for the bandwidth comparisons exhibit different behavior with respect to output pulse shapes [18]. Fiber A has a significant number of late arriving modes (fig. 12); fiber B has a low level front portion with three peaks in the remaining part of the pulse (fig. 12); and fiber C has a single maximum and a fairly symmetrical shape.

Results from the five bandwidth participants are given in figures 13 to 15; -3 dB bandwidths refer to the entire test length which was nominally 2 km. Corrections due to the

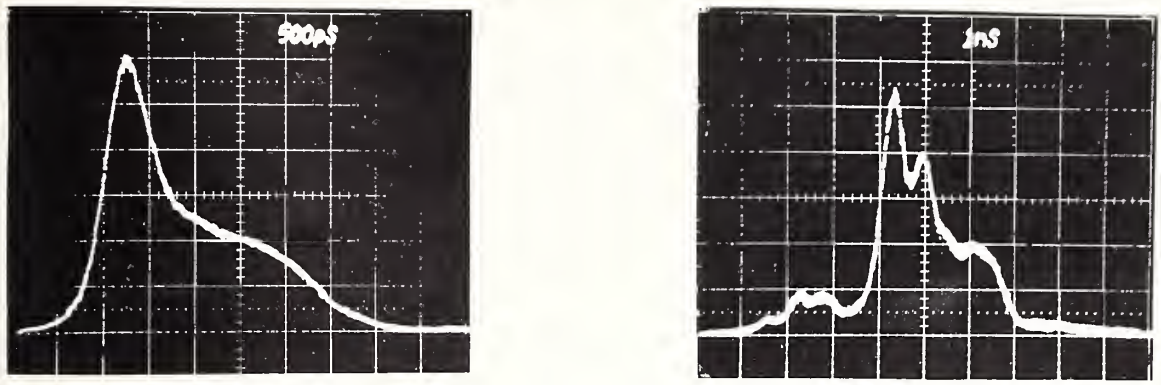


(a) (b)

Figure 12. Output pulse shapes from (a) fiber A, 500 ps per division, and (b) fiber B, 1 ns per division, using an input pulse duration of 320 ps FWHM. Fiber A exhibits late arriving modes and fiber B fine structure within the nominal pulse shape.

small amounts of fiber cut off were negligible and not made. One standard deviation measurement spread for fibers A, B, and C with average -3 dB bandwidths of 280, 214, and 418 MHz is 23, 28, and 53 MHz, respectively, or 8 percent, 13 percent, and 13 percent, expressed as a percentage of the bandwidth. Error bars on the data points represent participants' estimates of typical system precision, plus or minus one standard deviation, based on previous experience with other fibers. Typical system precision averaged over the five participants is 20 MHz. Sufficient data was supplied to also compare at the -6 dB bandwidth. One standard deviation measurement spread for fibers A, B, and C with average -6 dB bandwidths of 796, 482, and 833 MHz is 154 (19 percent), 134 (28 percent), and 78 (9 percent) MHz, respectively.

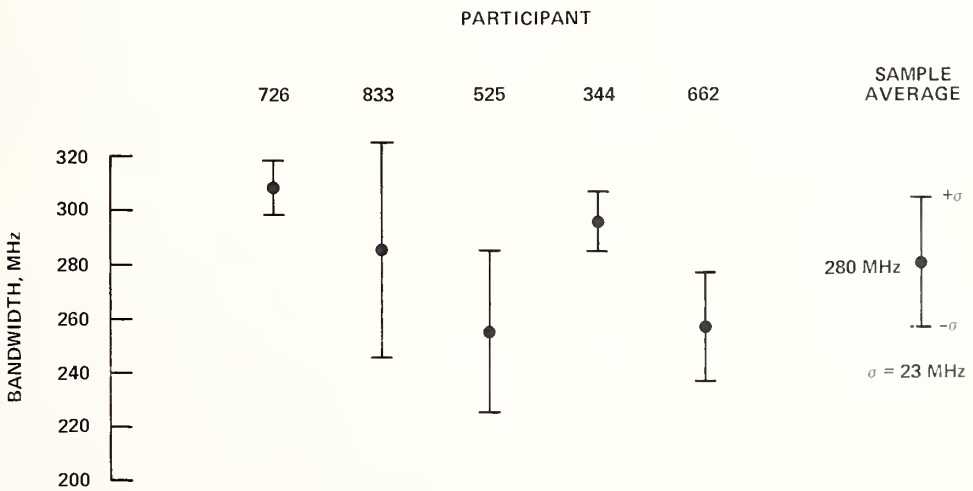


Figure 13. Results of -3 dB bandwidth measurement, fiber A, average 280 MHz, one standard deviation 23 MHz.

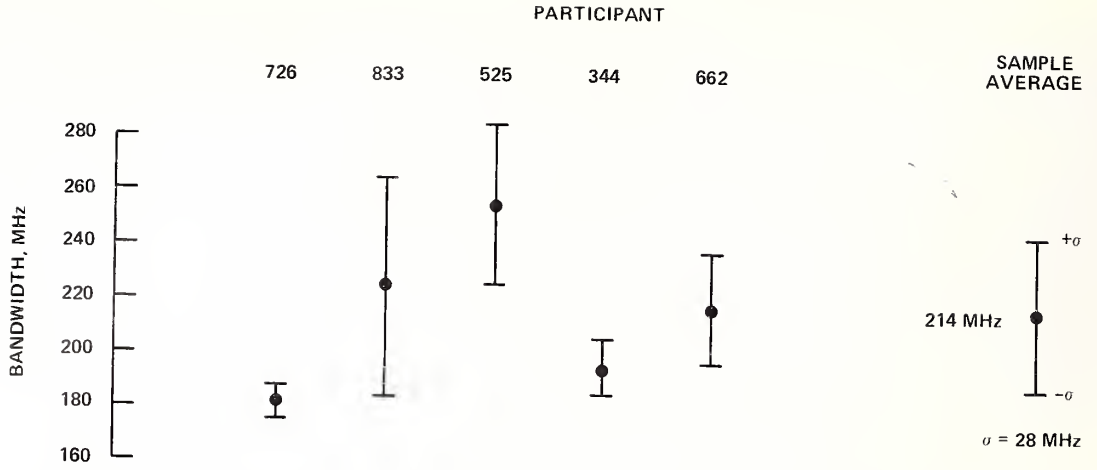


Figure 14. Results of -3 dB bandwidth measurements, fiber B, average 214 MHz, one standard deviation 28 MHz.

Two types of mode scramblers were used in the comparisons. Three participants used short lengths of step, graded, step index fibers fusion spliced together in the manner described by Love [19] while the others used a single length of step index fiber [20] (fig. 16).

Measured bandwidths are primarily a result of intermodal distortion. Intramodal contributions are either negligible or not evident in the data. Laser diode sources used in the comparisons had pulse widths in the 320 to 550 ps FWHM range, and linewidth estimates ranged from 1.5 to 3.5 nm. Bandwidths of fibers A and B are too low to be influenced by intramodal distortion at the maximum source linewidth, while fiber C is marginal. However, the measurements made on fiber C indicate that the highest linewidth sources did not have the lower bandwidth values.

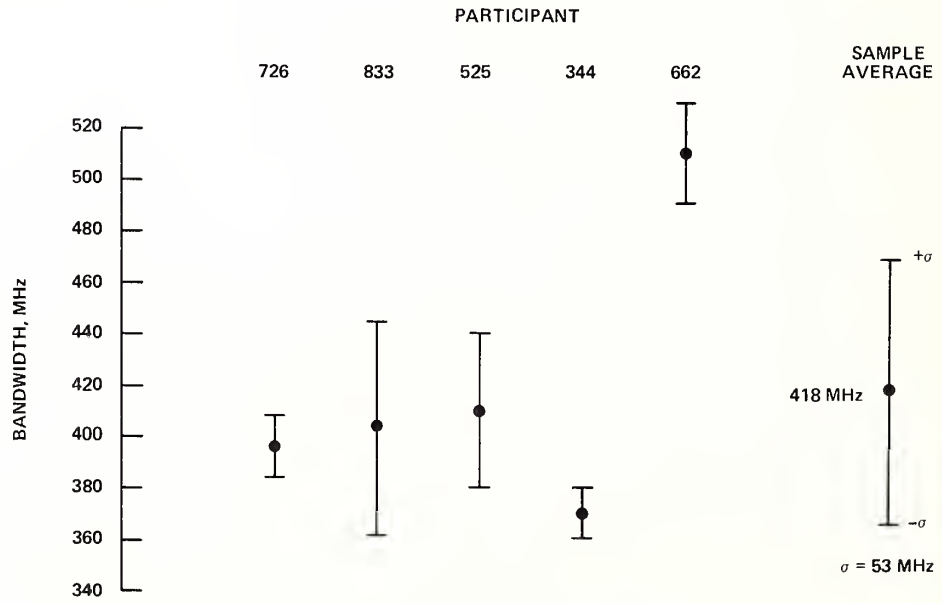


Figure 15. Results of -3 dB bandwidth measurements, fiber C, average 418 MHz, one standard deviation 53 MHz.

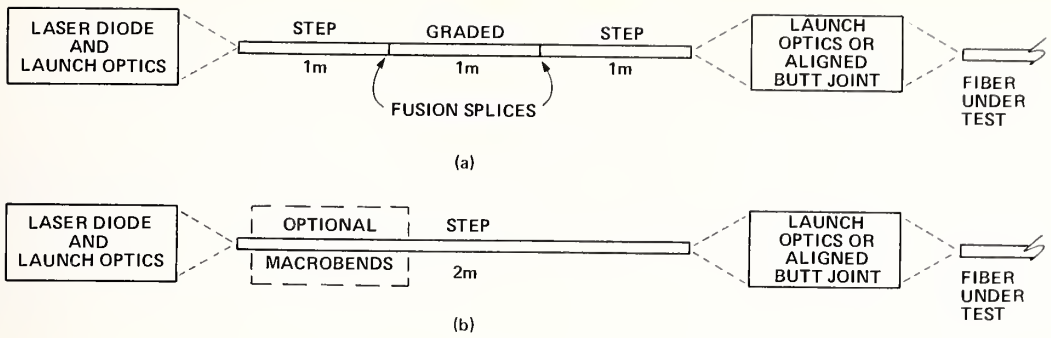


Figure 16. Examples of mode scramblers used by participants.

It is difficult to determine the degree of consistent, systematic offset in the -3 dB bandwidth comparisons. Relative performance of participants on all fibers compared to the average measured values indicates that specific laboratories are not consistently high or low but fluctuate depending upon the fiber. Also, the precision claimed for measurement systems varied by a factor of seven. In light of the average claimed precision of 20 MHz, the measurement spreads for the comparisons are reasonable. Future comparisons should establish measurement precision on the actual test fibers; some estimates are probably too high while others too low.

The higher frequency part of the frequency response (-6 dB) shows poor agreement in fibers A and B. In the time domain, this can indicate differences in the fast components of the acquired output pulses. As might be expected fiber B, with the fine structure in the output pulse (fig. 12), showed the poorest agreement at -6 dB.

---

NBS appreciates the timely cooperation of the following manufacturers for either participating in or supplying fibers for the comparisons: Belden; Bell Laboratories, Atlanta; Bell-Northern, Ottawa; Corning Glass works, Waveguide Products Engineering Laboratory; Galileo; General Cable; ITT; Superior Cable; Times Fiber Communications; and Valtec.

## 5. REFERENCES

[1] G. W. Day and G. E. Chamberlain, Attenuation measurements of optical fiber waveguides: An interlaboratory comparison among manufacturers; National Bureau of Standards Report, NBSIR 79-1608, May 1979.

[2] A. H. Cherin and W. B. Gardner, Laser Focus, 16:60; August 1980.

[3] The launching conditions used for the attenuation (restricted launch) and bandwidth comparisons were those drafted by the Electronic Industries Association (EIA) Working Group on Fibers and Materials (P-6.6). These launching conditions are currently practiced in many laboratories.

[4] D. L. Franzen and E. M. Kim, Applied Optics 20:1218; April 1980.

[5] Participants include NBS and nine members of the EIA Working Group on Fibers and Materials (P-6.6). Comparisons were conducted from April 1980 to Jan. 1981.

[6] M. Eriksrud, et al., Optical and Quantum Electronics 11:517; 1979.

[7] A. H. Cherin and E. D. Head, A fiber concatenation experiment using a standardized loss measurement method; Technical Digest, Symposium on Optical Fiber Measurements, 1980, NBS Special Publication 597, U.S. Govt. Printing Office.

[8] G. T. Holmes, SPIE Vol. 224 Fiber Optics for Communications and Control; 1980. Also G. T. Holmes and R. M. Hawk, Optics Letters 6:55; February 1981.

[9] P. Kaiser, Loss measurements of graded-index fibers: Accuracy versus convenience; Technical Digest, Symposium on Optical Fiber Measurements, 1980, NBS Special Publication 597, U.S. Govt. Printing Office.

[10] The EIA Working Group on Fibers and Materials (P-6.6) is currently recommending the use of mode scramblers with bandwidth measurement light sources to produce overfilled launching conditions to the test fiber.

[11] Several participants supplied additional measurements to more fully characterize the fibers.

[12] K. Inada, Optics Communications 19:437; 1976.

[13] R. Olshansky and S. Oaks, Applied Optics 17:1830; 1978.

[14] DMA measurements were made by launching a small mode volume with a single mode fiber at various points along a core radius and measuring attenuation. These measurements were provided by Bell Laboratories, Atlanta.

[15] Kitayama, K., et al., IEEE J. Quant. Elect. QE-16:356; 1980.

[16] D. B. Keck, Fundamentals of optical fiber communications, M. K. Barnoski, ed. (Academic Press, New York) 28; 1976.

[17] W. Heitmann, et al., Optical and Quantum Electronics 13:47; 1981.

[18] Bandwidth of fiber D was not measured because of short length and unknown bandwidth-length scaling necessary for a correction.

[19] W. F. Love, Paper ThG2, Technical Digest, Topical Meeting on Optical Fiber Communications, March 6-8, 1979, Washington, DC, 118.

[20] T. Tanifuji, et al., Electron. Lett. 7:204; 1979.

## APPENDIX: BEAM OPTICS AND MODE FILTER LAUNCHING CONDITIONS APPLIED TO ATTENUATION MEASUREMENTS IN HIGH DMA FIBERS

The largest discrepancies between beam optics and mode filter approaches to restricted launch attenuation should occur in fibers having high DMA. This appendix gives measurement results contributed by Paul Reitz of the Corning Glass Works on two 1.1 km fibers having higher DMA than the comparison fibers. In these fibers attenuation differences between overfilled and restricted launches at 850 nm are 1.74 and 0.85 dB/km. Attenuation was measured using the same beam optics and mode filter parameters specified for the comparisons. Table 4 shows the difference between the 70 percent core, 70 percent NA beam optics launch and a mandrel wrap mode filter launch implemented at the mid-point and extremes of the specified tolerance on the match of far-field radiation patterns. Mode filters are specified by the fractional restriction, $\Delta$, they produce in the far-field radiation angle at the 5 percent intensity points. If $\theta_L$ is the radiation angle produced using overfilled launching conditions to the test fiber without a mode filter, and $\theta_S$ is the radiation angle from the short (reference) length with the mode filter applied, then $\Delta = (\theta_S - \theta_L)/\theta_L$. For the comparisons, the mode filters had to produce $\Delta$ values between 0 and -7 percent. Notice at both 850 and 1300 nm the mode filter attenuation values at the tolerance extremes (0 and -7 percent) straddle the beam optics values. At -3 percent, near the tolerance mid-point, attenuation values obtained by the two approaches are nearly the same.

## Section 2. INTERLABORATORY MEASUREMENT COMPARISON TO DETERMINE THE RADIATION ANGLE (NUMERICAL APERTURE) OF GRADED INDEX OPTICAL FIBERS*

Douglas L. Franzen
Ernest M. Kim

A procedure for determining the radiation angle (numerical aperture) of graded index optical fibers was tested by an interlaboratory measurement comparison among six fiber manufacturers and the National Bureau of Standards (NBS). Radiation angle was determined using the five percent intensity points on an exit far-field radiation pattern. Measurements on five fibers representing low to high numerical aperture values show standard deviations of 2.9, 2.4, 2.0, 1.5, and 0.9 percent. The overall average, 2.0 percent, is close to the one standard deviation measurement precision reported by most participants.

*Applied Optics, 20:1218-1220; 1981.

## 1. INTRODUCTION

Optical fiber parameters important to system performance include attenuation, bandwidth, core diameter, and numerical aperture. All four are usually given when an optical fiber is specified. Numerical aperture is important in determining the coupling efficiency of LED sources, joint loss when dissimilar fibers are connected, and the susceptibility of the fiber to microbending.

A widely used definition of numerical aperture for an optical fiber is based on the refractive index profile and describes the largest angle meridional ray which can be guided by the fiber. Specifically,

$$NA = \sqrt{n_1^2 - n_2^2} \tag{1}$$

where $n_1$ is the on-axis core index and $n_2$ refers to the cladding. For a fiber with a near parabolic index profile, skew rays and leaky modes are contained within the axial meridionally defined numerical aperture so the maximum radiation angle, with all modes excited, becomes a measure of the numerical aperture [1,2].

Standards groups prefer using the term "radiation angle" to describe the general far-field radiation pattern emitted from a fiber [3]. In the past, many definitions and procedures have been used to measure or quantify far-field patterns, most of which were called "numerical aperture." Some make direct use of the far-field intensity distribution while others integrate to determine the cone angle containing a specified fraction of the total power. Measurement disagreement and confusion has undoubtedly occurred because of the proliferation of different definitions and procedures.

This interlaboratory comparison is intended to determine the measurement agreement when laboratories use the same test procedure. The radiation angle procedure used here is currently pending before the Electronics Industries Association (EIA) and, gives a measure of numerical aperture for a near parabolic index fiber [4]. Briefly, participants were asked to:

(1) Use a specimen length of 1.8 ± 0.1 m having flat, perpendicular ends [5].

(2) Overfill the input to the fiber under test in both launch spot size and numerical aperture.

(3) Use a measurement wavelength of 850 nm with a linewidth of 80 nm or less.

(4) Use a suitable cladding mode stripper.

(5) Obtain the angular intensity distribution exiting the fiber in the far field.

(6) Determine numerical aperture as the sine of the half-angle where the far-field intensity has decreased to 5 percent of its maximum value [6] (fig. 1).

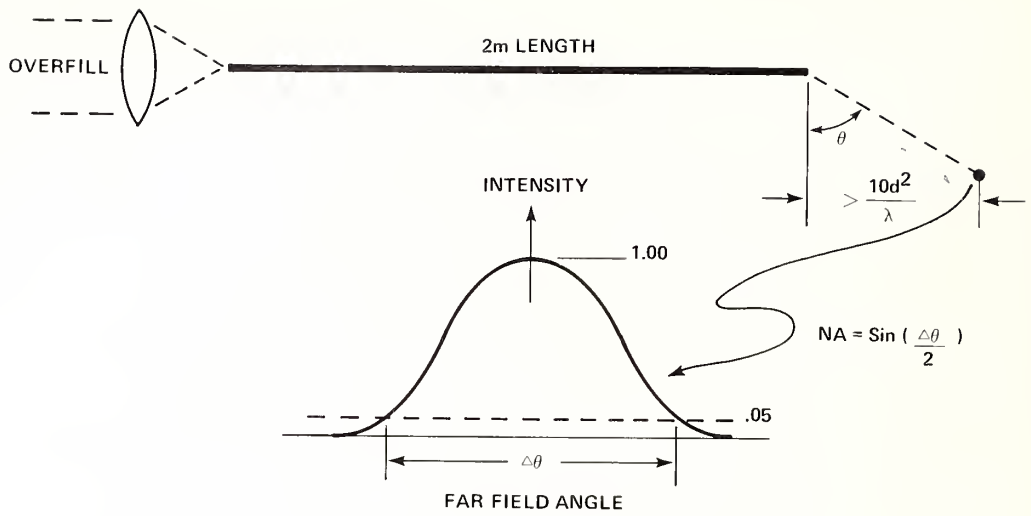


Figure 1. NA determined from far-field radiation pattern.

Participants in the comparisons include several U.S. and Canadian fiber manufacturers and the National Bureau of Standards. Individual laboratories were free to use any experimental technique to implement the above measurement conditions.

## 2. FIBER SAMPLES

Fibers in this comparison came from four different manufacturers. One fiber, E, was chosen to minimize variations in samples sent to participants. This was accomplished by:

(1) Selecting a fiber with smooth backscatter response (backscatter fluctuations can indicate length variations in core or NA) [7].

(2) Cutting adjacent samples from a 1 km length of fiber.

The comparison on fiber E was carried out in parallel; i.e., all participants received samples at the same time.

The remaining fibers, A, B, C, and D, were cutback lengths remaining from a measurement comparison of attenuation and bandwidth among the same participants. These fibers were sent to the participants in series so measured samples were not adjacent in the fiber but separated by nominally 10 m.

Fiber samples are typical of commercial graded index fibers representing low to high numerical aperture values with core diameters in the 50-60 μm range. Fibers A, B, and C exhibited excellent attenuation characteristics with losses of 1, 0.8, and 0.7 dB/km, respectively, at a wavelength of 1.2 μm.

## 3. RESULTS

Various experimental approaches were employed by participants to measure far-field patterns. These include: rotating a detector in the far field, placing a detector array in the far field, and using a lens to obtain a spatial far-field transformation which is scanned by a rotating mirror.

Results for fibers A, B, C, D, and E are given in figures 2, 3, 4, 5, and 6, respectively. Participants were asked to estimate, from previous experience, their precision (one standard deviation) for determining numerical aperture. These values are indicated by the error bars on the data points.

Measurement standard deviations, $\sigma$, for the comparisons are similar for fibers A, B, C, and D; one standard deviations are 2.9, 2.4, 2.0, and 1.5 percent, respectively. Measurements on fiber E display a significantly smaller spread, 0.9 percent for one standard deviation.

Measurement spread indicated in figures 2, 3, 4, 5, and 6 is due in part to systematic differences between participants. This can be seen by plotting the participants' results as a percentage difference from the average measured numerical aperture value for each fiber, figure 7. When results from all five fibers are compared, some participants are consistently high or low.

Refractive index profiles for four of the fibers were measured by M. J. Saunders of Bell Laboratories, Norcross, using the refracted near-field technique. Numerial apertures determined from eq (1) for fibers, A, B, D, and E are 0.262, 0.179, 0.213 and 0.202

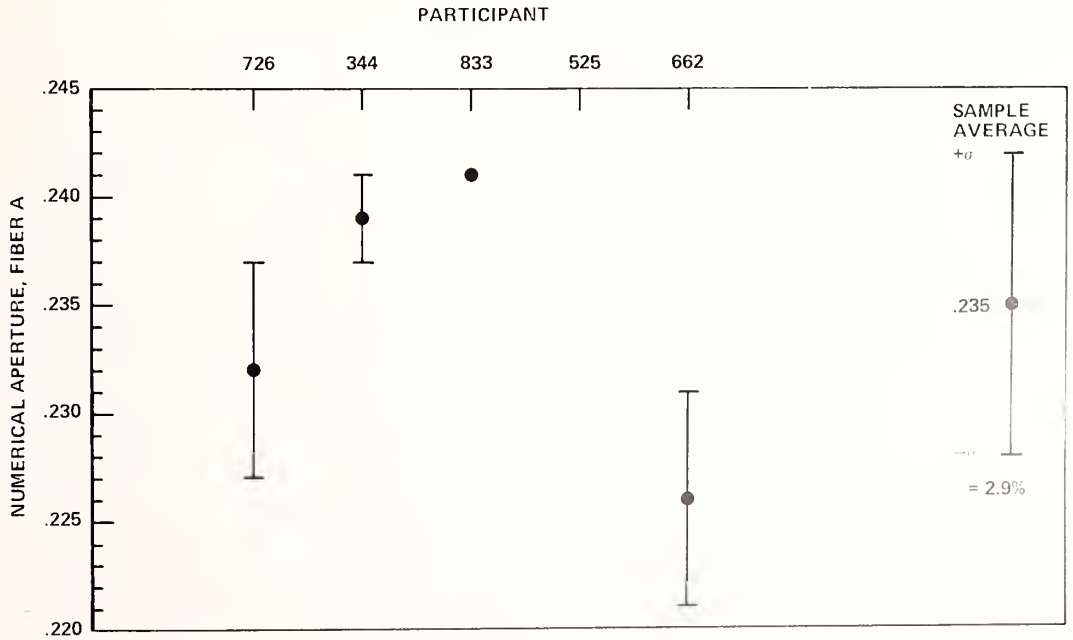


Figure 2. Numerical aperture, fiber A, average 0.235, one standard deviation, 2.9 percent.

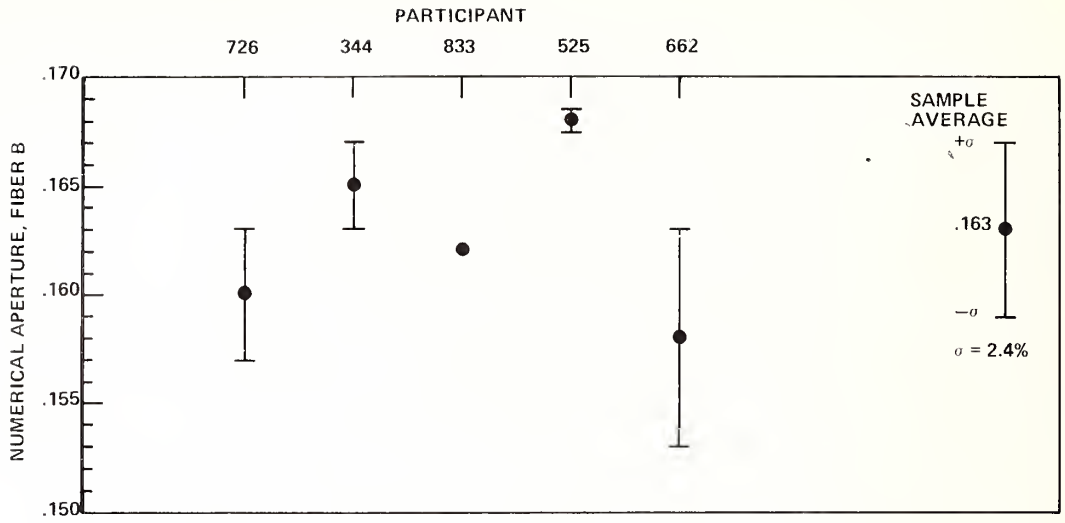


Figure 3. Numerical aperture, fiber B, average 0.163, one standard deviation, 2.4 percent.

respectively. Refractive index profiles for fibers A, B, D, and E, were also determined by M. Young of NBS using again the refracted near-field technique and numerical apertures of 0.244, 0.160, 0.206 and 0.201 were obtained, respectively. The differences between the numerical apertures determined from the average of the far-field comparisons and the average of the index profile measurements are -8, -4, -4, and -4 percent for fibers A, B, D, and E, respectively.

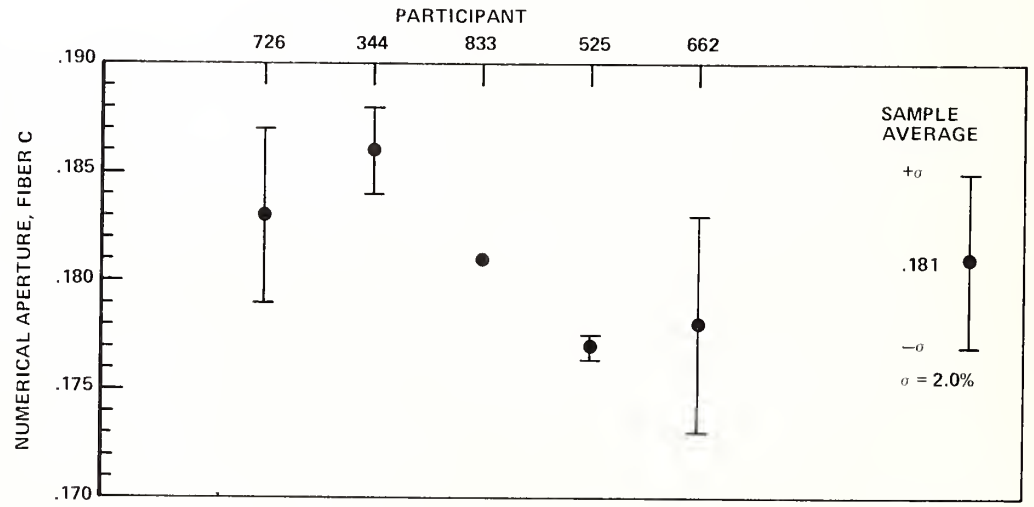


Figure 4. Numerical aperture, fiber C, average 0.181, one standard deviation, 2.0 percent.

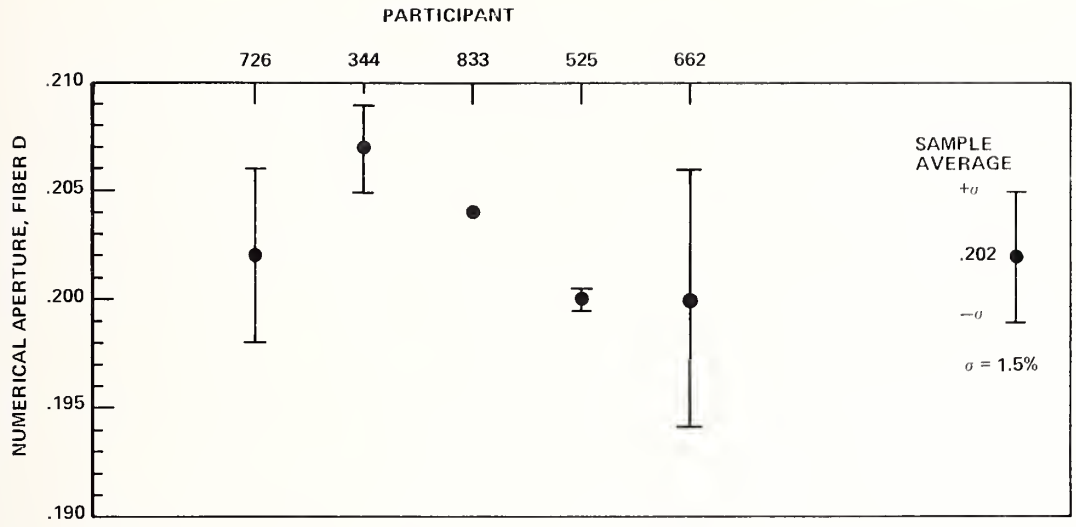


Figure 5. Numerical aperture, fiber D, average 0.202, one standard deviation, 1.5 percent.

Relevant parameters describing participants' measurement systems are given in table 1. This includes launching conditions, angular resolution, and system precision. Launching conditions range from just overfilling the fiber to a substantial overfill. Angular resolution is typically 0.2 to 0.4 degrees and one standard deviation measurement precision is typically a few percent. There may be some uncertainty as to the exact conditions used for determining the precision in table 1 since, for the NBS system, precision depends on whether the fiber end is recleaved and aligned between repeated measurements.

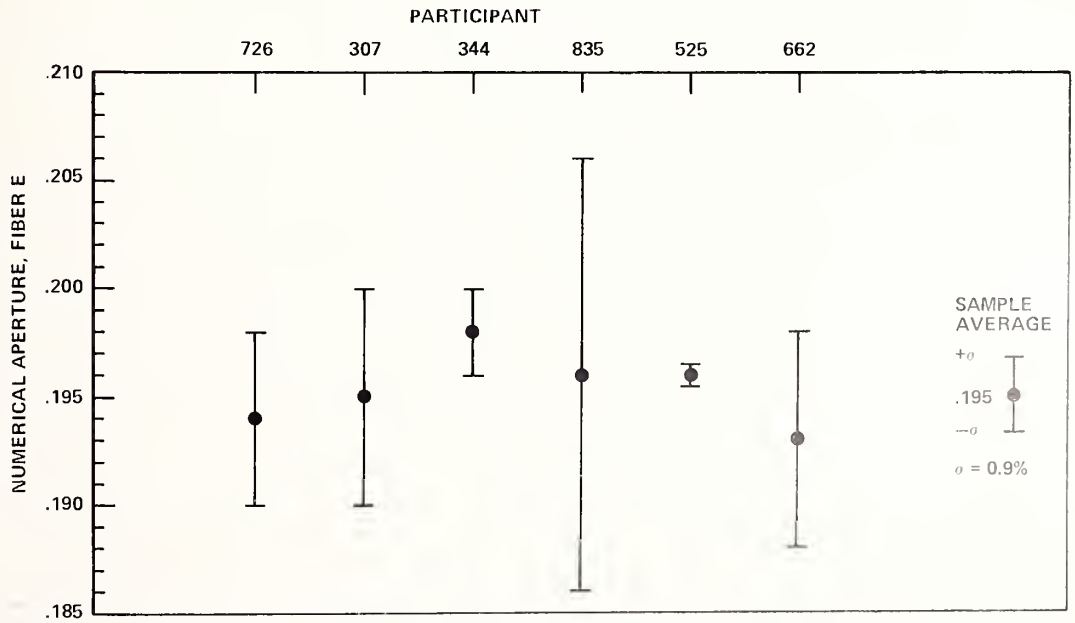


Figure 6. Numerical aperture, fiber E, average 0.195, one standard deviation, 0.9 percent.

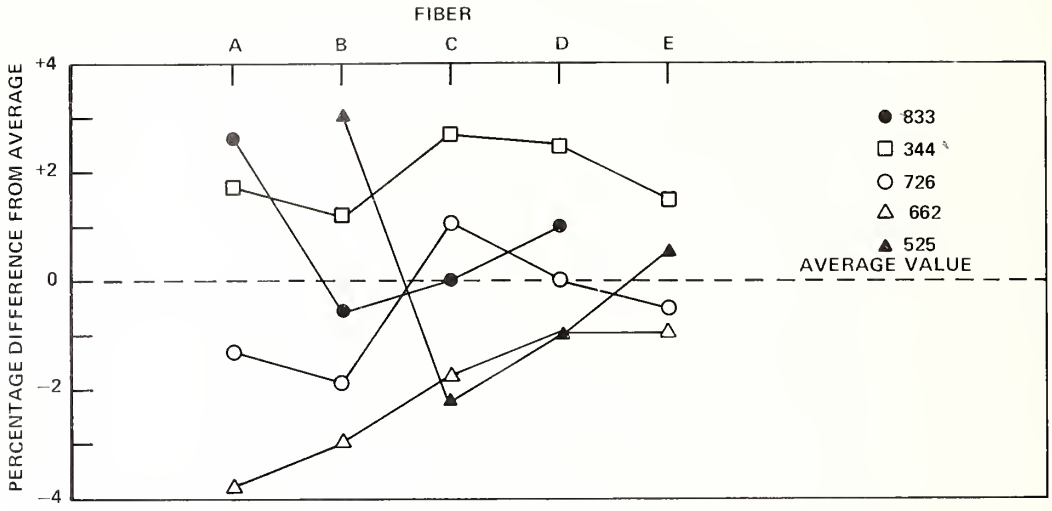


Figure 7. Relative performance of participants on all fibers compared to average measured numerical aperture values.

## 4. CONCLUSIONS

Measurement spread usually increases in going from single apparatus precision to intralaboratory and finally interlaboratory comparisons. This has been the experience in attenuation where single apparatus precision is typically 0.1 dB/km and comparisons yield standard deviations of 0.2 to 0.7 dB/km [8,9]. The present interlaboratory comparison on radiation angle has not shown a noticeable increase in standard deviation over the precision of most individual participants. Thus, relative systematic offsets are not much larger than claimed precisions.

Results indicate a test procedure for radiation angle (numerical aperture) based on the five percent intensity points of the far-field radiation pattern gives good measurement agreement on graded index fibers. Also, measurements are not sensitive to the specific nature of the overfilled launching conditions or to the experimental method of implementation. Standard deviation averaged over the five fibers is 2.0 percent. Some fibers showed better measurement agreement than others. Two participants reported difficulty in removing cladding light from fiber A using their usual cladding mode stripper. For this reason the measurement spread on fiber A may be atypically high. Measurements on fiber E have a smaller standard deviation than most participants report in table 1 for their individual systems, also, all participant's error bars on fiber E mutually overlap. Because of the way the comparisons were conducted, participants spent more time with fiber E. Other than this, we are unable to offer an explanation for the better performance on fiber E. The previously mentioned care given fiber E may be partially responsible.

Numerical aperture determined from index profile measurement shows reasonable agreement to numerical aperture calculated from radiation angle. Systematic differences for the fibers are in the 4 to 8 percent range with the radiation angle measurements giving lower values. Some adjustment is possible by changing definitions. For example, the NBS data gives a 3 to 4 percent increase in radiation angle if 2 percent intensity points on the curve are used rather than 5 percent. A more detailed comparison of index profile determined NA to radiation angle determined NA is needed to establish systematic differences. This should include the affect of low index "barrier" layers commonly used at the core-cladding interface. Fibers A, B, D, and E did not have barrier layers.

---

The authors would like to thank the following laboratories for their participation in this measurement comparison: Bell Laboratories, Norcross; Bell Northern, Ottawa; Corning Glass Works, Waveguide Product Engineering Laboratory; Galite; General Cable; and Valtec.

## 5. REFERENCES

[1] Adams, M. J.; Payne, D. N.; Sladen, F. M. E. Opt. Commun. 17:204; 1976.

[2] Matsumura, H. Opt. Quantum Electron. 7:82; 1975.

[3] Hanson, A. G.; et al. Optical waveguide communication glossary. U.S. Dept of Commerce, NTIA document NTIA-SD-79-4; September 1979.

[4] The procedure came out of EIA Committee P6.6 and was drafted by P. Reitz of the Corning Glass Works.

[5] For fiber E the specimen length was 2.0 ± 0.2 m.

[6] The 5 percent intensity points were chosen as a compromise to reduce requirements on signal-to-noise which could obscure the baseline location.

[7] DiVita P.; Rossi, U. Opt. Quantum Electron. 11:17; 1980. The authors would like to thank B. L. Danielson of NBS for supplying experimental backscatter results.

[8] Day, G. W.; Chamberlain, G. E. Attenuation measurements of optical fiber waveguides: An interlaboratory comparison among manufacturers. Nat. Bur. Stand. (U.S.) NBSIR 79-1608; May 1979.

[9] Cherin, A. H.; Gardner, W. B. Laser Focus 16:60; August 1980.

## Section 3. MEASUREMENT OF THE CORE DIAMETER OF GRADED-INDEX OPTICAL FIBERS, AN INTERLABORATORY COMPARISON*

Ernest M. Kim
Douglas L. Franzen

An interlaboratory measurement comparison of optical fiber core diameter was conducted by the National Bureau of Standards (NBS) in cooperation with the Electronic Industries Association. Participants include NBS and three fiber manufacturers. Six graded-index fibers were measured by all participants using the transmitted near-field method. As a group, the transmitted near-field measurements were consistent and exhibited an average standard deviation of 0.5 μm for 50 μm core fibers. These results were also compared to diameters determined by refracted near-field and transverse interference measurements contributed by other laboratories. For smooth index profiles all three methods agree within approximately 1 μm; substantial differences between the transmitted near-field and the other two methods can exist for fibers having step structure near the core-cladding boundary.

*Submitted to Applied Optics.

## 1. INTRODUCTION

Core diameter is one of the more important geometrical quantities used in optical fiber specification. Diameters of joined sections should be the same to avoid unnecessary splice loss. Dimensions have been standardized permiting the interchange of products from different manufacturers; for multimode graded-index telecommunication fibers, a diameter of 50 μm is internationally accepted.

Core diameter is commonly defined using specified points on the refractive index profile. Figure 1 shows a typical near-parabolic profile having a maximum index of $n_1$ with a homogeneous cladding index of $n_2$. Also shown is an on-axis index dip common to some manufacturing processes and a narrow, low-index region below the cladding that can result from barrier layers deposited at the core-cladding boundary. Core diameter is often defined as that diameter intersecting the points $n_3$ on the profile where

$$n_3 = n_2 + k(n_1 - n_2); \tag{1}$$

k is a constant generally chosen to be between 0 and 0.05 [1].

Several techniques exist to determine the index profile of graded-index fibers [2]. Two techniques reduced to common practice include the Refracted Near Field (RNF), and Transverse Interference (TI) methods. Another technique, the Transmitted Near Field (TNF), gives an approximation to the index profile. TNF is currently used by several fiber manufacturers for quality control measurements. Its main advantages include low cost, ease of implementation, and simple extension to two dimensions. The other two methods give a more direct measure of the index profile with better resolution and are considered more accurate in this respect.

Early work by Sladen, et al. showed for equal mode excitation (Lambertian source) on short lengths of graded-index fiber, the near-field intensity distribution across the output end face (TNF) closely resembles the refractive index profile [3]. Principle deviations include the presence of tunneling leaky modes and the loss of resolution near the core-cladding boundary [4]. Whether a correction should be made for leaky modes is still open to question. Calculations by Petermann suggest a slight core ellipticity can cause leaky modes to attenuate rapidly and a correction should not be necessary for fibers encountered in actual practice [5]. Even if corrections are necessary, the width of the radiation pattern near the baseline is not greatly affected. A more serious limitation of the TNF is the loss of resolution near the core-cladding boundary due to the decrease in local fiber numerical aperture. Figure 2 shows a TNF profile obtained with the NBS system at a wavelength of 850 nm. Superimposed is a normalized least squares fit to the data between the 10 and 80 percent points. The fitted curve is the usual expression for a power law profile,

$$n(r) = n_1\left[1 - 2\Delta(r/a)^g\right]^{1/2} \tag{2}$$

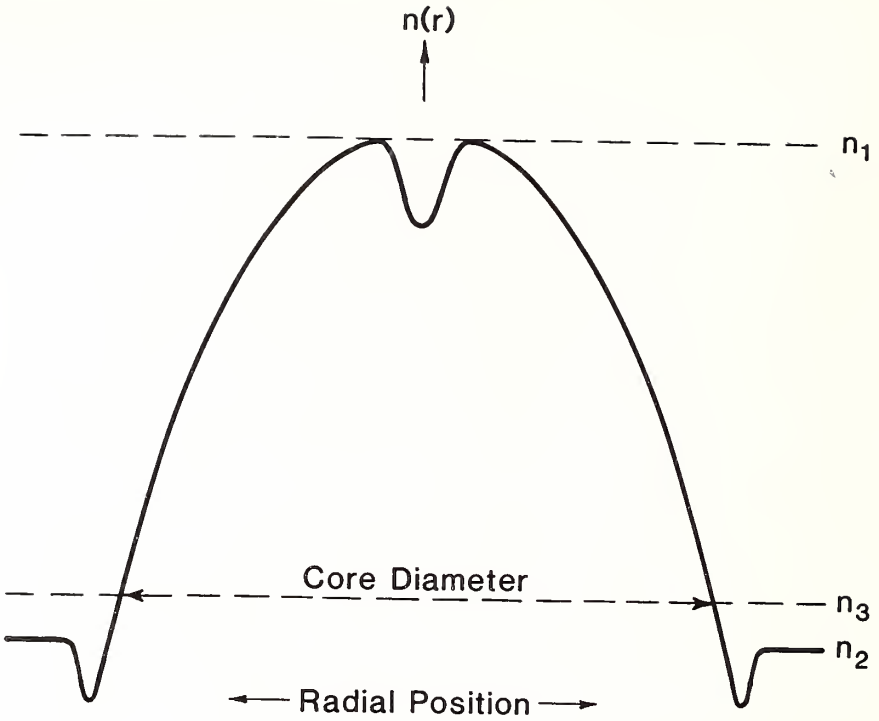


Figure 1. Points on a typical index profile used for determining core diameter. Absolute index values do not have to be known.

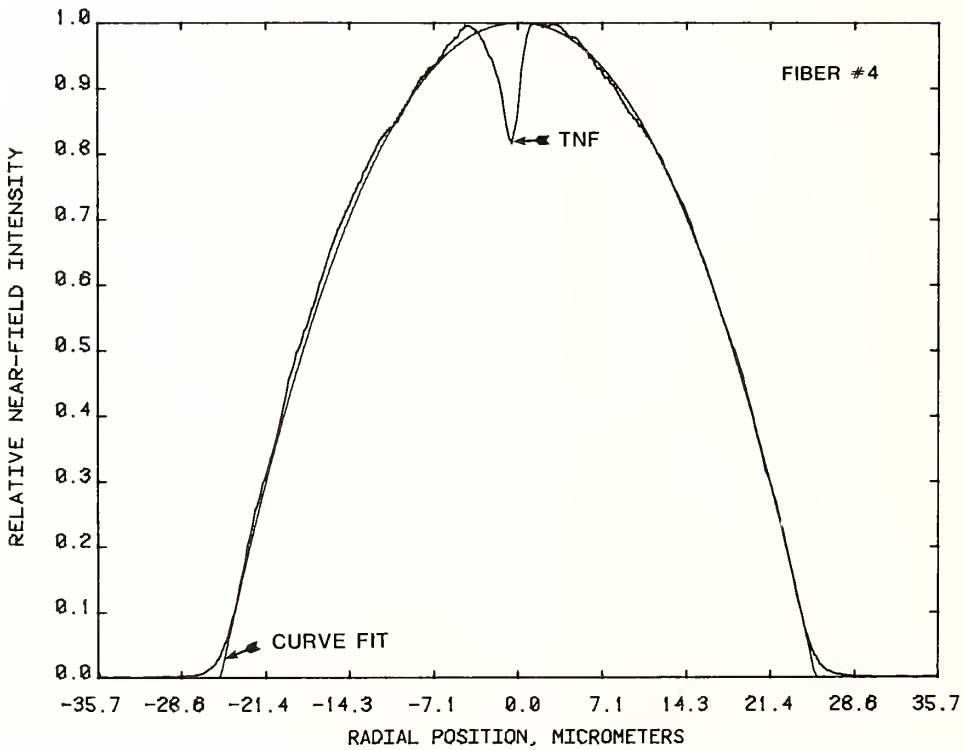


Figure 2. TNF profile for fiber #4 with superimposed least squares fit to a power law profile, NBS.

where n(r) is the radial variation in index, $\Delta$ is approximately $(n_1 - n_2)/n_1$, a is the core radius, and g is the index profile parameter. Variables in the fit include a and g. Figure 2 indicates a good fit down to approximately the 5 percent level where the decrease in resolution causes the TNF profile curvature to reverse. Near the core center the resolution on a 0.2 NA (numerical aperture) fiber is in the 1.5 to 2.0 μm range at a wavelength of 850 nm.

Although technically more complicated to implement, the RNF gives a direct measure of the index profile without the need for a correction [6-8]. Moreover, resolution of RNF systems can easily be in the submicrometer region. TI also gives a direct measure of the index profile by observing fringes with an interference microscope. In general, circular symmetry is assumed and the profile is unfolded by solving an integral equation. Although interference microscopes are expensive, the sample preparation is easy and hence TI finds use in routine measurements. For a complete description of RNF and TI, the reader is referred to other references [2,9]. Similar shapes have been obtained for fiber index profiles measured by both RNF and TI methods [10].

The purpose of the present comparisons is to determine: (1) interlaboratory agreement on core diameter measurements using the TNF technique, (2) how TNF compares to RNF and TI when the same definitions are used for core diameter, and (3) the magnitude of systematic offsets due to differences in interlaboratory dimensional calibrations. Participants in the comparisons include NBS and three manufacturing members of the Electronic Industries Association (EIA) [11]. Two of the participants routinely use TNF for quality control measurements while the other uses both RNF and TI for similar purposes.

## 2. COMPARISON FIBERS

For most of the profiling methods, a single measurement consists of one scan across a diameter. It is therefore important to use test fibers with minimum core ovality so results do not depend on fiber orientation about the axis. Several fibers with nominally 50 μm cores were provided by four different manufacturers. Those fibers were preselected for good core circularity. In other respects the fibers are representative of typical commercial products.

It is also important to use fibers having minimum variation in core diameter with length. Those variations can be related to backscatter fluctuations [12]. NBS determined the backscatter response from candidate fibers using an OTDR with 4 m resolution [13]. Figure 3 is a typical response from one of the six fibers selected for the comparisons. Other selected fibers exhibited fluctuations slightly smaller or larger than figure 3. Fibers were rejected if point defects were present or periodic fluctuations exceeded 0.1 dB peak to peak.

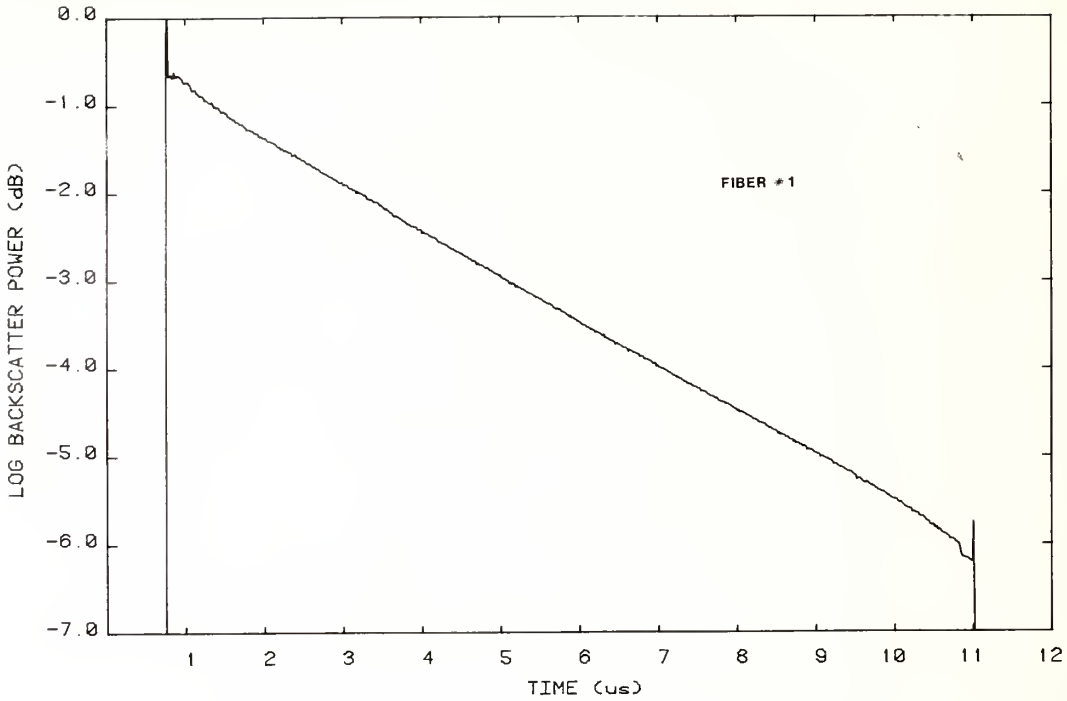


Figure 3. Typical backscatter response for a comparison fiber, fiber #1. Discontinuity at far end results from having a short length of the inside end wound on a second side spool.

NBS measured the core diameter of all samples sent to participants to ascertain sample uniformity. The standard deviation from NBS TNF measurements on seven adjacently cut sample lengths is given in table 1 for each of the six comparison fibers. Each sample was 7 m long and was measured with a random angular orientation. Measurement spread thus reflects a combination of the NBS system precision (0.2 to 0.3 μm), a random sampling of core ovality, and possible length variations. Standard deviations range from 0.2 to 0.8 μm with an average of 0.4 μm. All comparison fibers exhibit better core circularity than most fibers with some being exceptional in this respect.

Table 1. Test sample uniformity,
5 percent TNF core diameter, standard deviation 7 samples

| Fiber number | Standard deviation, μm |
|---|---|
| 1 | 0.4 |
| 2 | 0.2 |
| 3 | 0.6 |
| 4 | 0.8 |
| 5 | 0.2 |
| 6 | 0.4 |
| Average | 0.4 |

Comparison fibers also exhibit a diverse behavior with respect to index profile. Fiber #1 has a step structure near the core-cladding boundary; fibers #2 and #6 have depressed index barrier layers near the core-cladding boundary; fiber #3 has a deep on-axis index dip with deposition layer structure; fiber #4 has a noncircular symmetric index dip-peak; and fiber #5 is made by an outside vapor phase deposition process and exhibits no central index dip. TNF profiles for the comparison fibers are given in appendix 1.

## 3. MEASUREMENT PROCEDURES

The TNF procedures employed are currently pending before the EIA [14]. These procedures, applied at a wavelength of 850 nm, require the following conditions.

1. A test sample length of 2.0 ± 0.2 m having flat, perpendicular end faces.
2. A launch giving a uniform intensity distribution across the core with a launch numerical aperture exceeding 0.3.
3. The use of a cladding mode stripper.
4. A scan of the TNF magnified image with a resolution at least consistent with theoretical limits.

For purposes of this comparison, core diameter was defined using eq (1) and participants determined diameters at the 5 percent intensity points of the TNF distributions. Reported results are the average of three measurements. The first measurement was performed with a random fiber orientation; for the second measurement, a new fiber end was prepared and again the fiber was randomly orientated; for the third measurement, the fiber was rotated 90° about the axis with respect to the second measurement. This measurement sequence thus gives an average over end preparation and orientation.

A. H. Cherin and M. J. Saunders of Bell Laboratories, Norcross and C. Bice of Western Electric determined index profiles by RNF and TI to compare with the TNF results. Specific procedures were not specified for RNF or TI so their normal laboratory methods were used. RNF systems are usually implemented with a HeNe laser so the measurement wavelength was 633 nm; for TI the measurement wavelength was 550 nm. Measurement wavelengths for the various techniques are those used by participants in actual practice. While index profiles exhibit a slight wavelength dispersion which greatly affects fiber bandwidth, the changes are not significant enough to affect core diameters over these ranges. As an example, figures 4 and 5 show only slight differences between normalized, superimposed TNF profiles at 600 and 850 nm from fibers #1 and #5. Table 2 gives the difference between the 5 percent core diameters determined at wavelengths of 600 and 850 nm using the NBS TNF system. For these measurements the fiber end and angular position remained the same so the precision was quite good. The system was calibrated at both wavelengths and a 0.4 percent change in calibration factor due to chromatic aberration in the optics was taken into account.

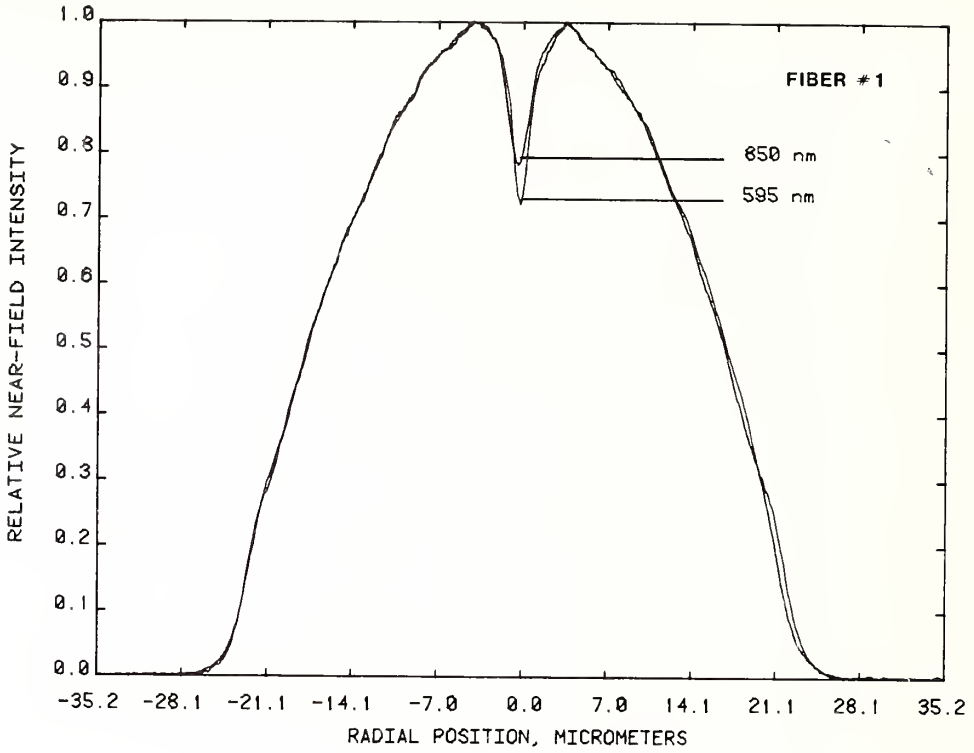


Figure 4. TNF profiles for fiber #1 at 600 and 850 nm, NBS. Note deeper index dip at 600 nm due to improved resolution.

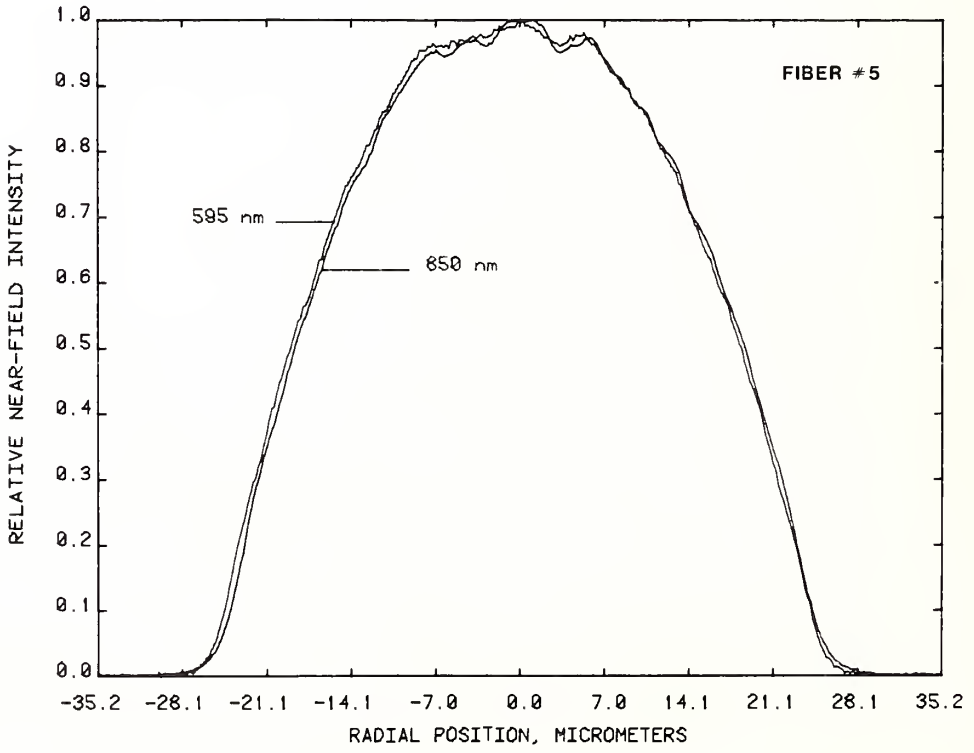


Figure 5. TNF profiles for fiber #5 at 600 and 850 nm, NBS.

Table 2. Dispersion of 5 percent TNF core diameter, 600 nm diameter minus 850 nm diameter

| Fiber number | Difference, μm* |
|---|---|
| 1 | 0.0 |
| 2 | +0.1 |
| 3 | +0.1 |
| 4 | +0.1 |
| 5 | -0.2 |
| 6 | +0.1 |

* Differences are less than the interval between digitized data steps.

## 4. CALIBRATION RETICLE

A device was developed to dimensionally calibrate the scan of TNF systems. It consists of a reticle illuminated by an optical fiber and is intended to fit into a TNF system in place of the fiber under test. Instead of imaging a fiber end, a TNF apparatus images the calibration reticle. Reticles were fabricated using photolithographic techniques. Transparent lines are made on an opaque, 100 nm thick chromium film deposited on a 1.6 mm thick glass substrate. Linewidths were chosen to be consistent with typical theoretical resolution limits which are approximately 1 μm for 0.4 NA imaging optics at a wavelength of 850 nm. The reticle pattern, shown in figure 6, has three 1.2 μm wide vertical lines separated by 50 μm. A pair of horizontal lines 5 μm wide are located 100 μm to either side and aid in obtaining a scan which is perpendicular to the vertical lines. If the scan intersects both horizontal lines, the angle of incidence is within 1° of normal and the central regions of the vertical lines are measured. The reticle, which is placed in a fixture, is illuminated through a diffuser by a 2 m long large core (300 μm), large NA (0.4) plastic fiber.

Analog results of a calibration scan with the NBS TNF system are shown in figure 7. Measured FWHM linewidths are 1 μm in general agreement with expectations. Participants were requested to measure the distance between lines 1 and 3 using their TNF systems and usual calibration procedures, and were not informed a priori of the actual value. By comparing participants' results to the actual value, an indication of systematic offsets due to calibration differences is obtained. Participants were also asked to determine the distances between lines 1 and 2 and 2 and 3 to give a measure of scan linearity.

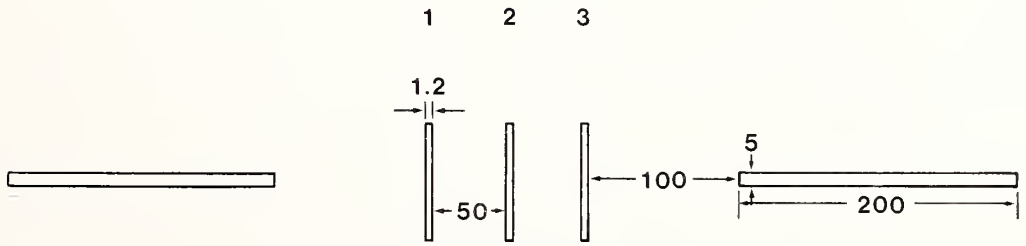


Figure 6. Calibration pattern on NBS reticle, all distances in μm.

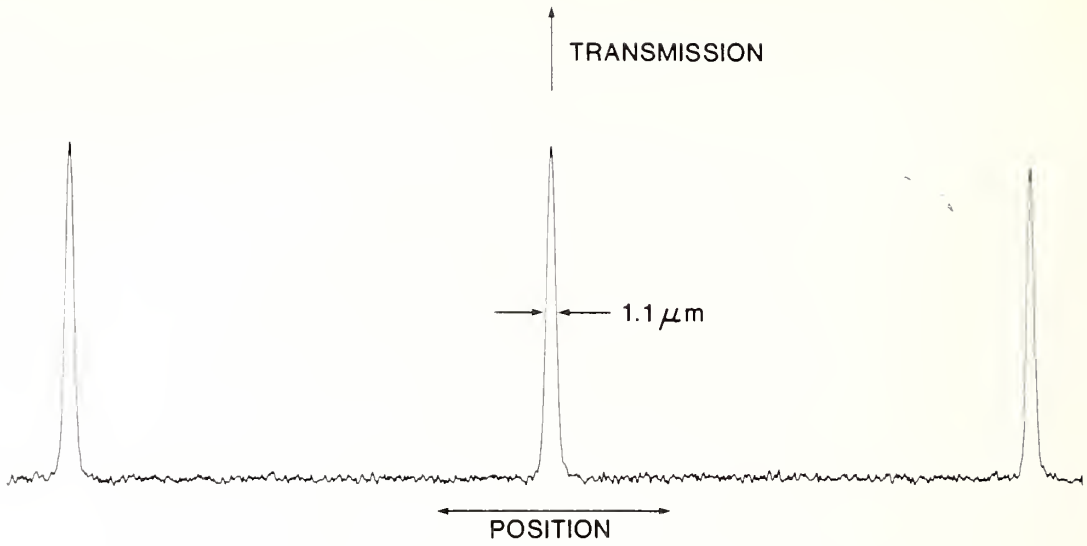


Figure 7. Analog scan of reticle with NBS TNF system.

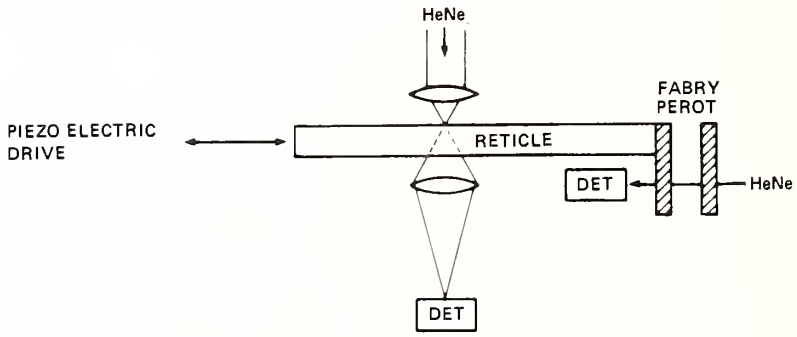


(a)

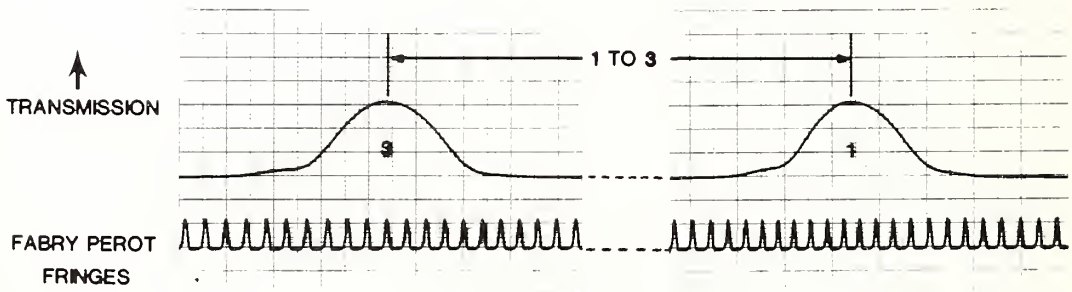


(b)

Figure 8. (a) Method used for placing an absolute calibration on reticle. (b) Line spacing referenced to Fabry-Perot fringes, in this example the 1 to 3 distance is 316.5 fringes.

An absolute calibration of the reticle was accomplished by comparing line separation to the wavelength of the 0.6328 μm laser transition in HeNe. In this technique the reticle is smoothly translated on a piezoelectric-driven stage. Stage displacement is determined by counting transmission fringes from a Fabry-Perot interferometer (fig. 8a). The short Fabry-Perot does not resolve individual cavity modes of the HeNe laser; thus, a transmission fringe appears every half wavelength or 0.316 μm. A second HeNe laser beam is focused to a one micrometer spot size and locates reticle lines as the stage is translated. In this manner, a value of 100.1 μm was obtained for the 1 to 3 distance (fig. 8b). One standard deviation (precision) for 6 measurements was 0.1 μm. Measurements of the 1 to 2 and 2 to 3 distances indicate the difference between them is 0.0 ± 0.1 μm. A second identical reticle, not mounted in a fixture, was also provided to determine calibrations for the RNF and TI systems. Calibrations on the reticles are given in appendix 2.

## 5. RESULTS OF TNF COMPARISONS

Parameters describing participants' TNF systems are summarized in table 3. In all cases launching conditions overfilled the test fibers. Average typical system precision, one standard deviation, is 0.4 μm. All participants had systems designed for a resolution of 1 μm or less.

Results from the 5 percent core diameter measurements are given in table 4 for the six comparison fibers. The values given are those reported by participants and do not include any corrections for calibration error. Uncorrected results are important because they represent the independent capabilities of the laboratories. Standard deviations calculated for fibers 1 to 6 are 0.3, 0.6, 0.6, 0.6, 0.6, and 0.4 μm, respectively, for an overall average of 0.5 μm. This spread is less than twice the average precision claimed by participants.

By comparing relative values, definite offsets between participants are apparent. Figure 9 shows the relative performance of participants compared to the average measured values. Again, uncorrected core diameters are used. Some participants are consistantly high or low with respect to one another. Another analysis of the offsets is given in table 5. Here the relative differences for pairs of participants are calculated for each fiber where the A/B value corresponds to the 5 percent core diameter reported by participant A minus that of participant B. The average of the absolute values of the offsets is 0.5 μm.

Table 3. Parameters of participant TNF systems

| Participant | Spot size dia., μm | Launch NA | Typical precision one standard deviation, μm |
|---|---|---|---|
| 25 | 100 | 0.36 | 0.4 |
| 56 | 200 | 0.3 | 0.4 |
| 83 | --- | 0.6 | 0.1 |
| 47 | >125 | 0.4 | 0.8 |

Table 4. Uncorrected TNF 5% core diameters, μm

| Participant | Fiber number | | | | | |
|---|---|---|---|---|---|---|
| | 1 | 2 | 3 | 4 | 5 | 6 |
| 25 | 47.5 | 44.7 | 50.7 | 49.6 | 50.3 | 47.5 |
| 56 | 46.9 | 44.1 | 49.4 | 48.8 | 49.4 | 46.7 |
| 83 | 47.6 | 44.9 | 50.2 | 49.4 | 49.7 | 47.5 |
| 47 | 47.3 | 43.7 | 49.5 | 48.4 | 50.7 | 47.0 |
| Average | 47.3 | 44.4 | 50.0 | 49.1 | 50.0 | 47.2 |
| Standard deviation | 0.3 | 0.6 | 0.6 | 0.6 | 0.6 | 0.4 |

Results from measurements on the NBS calibration reticle are tabulated in table 6. Values are the measured distances between lines 1 and 3 on the reticle. The right column is the difference between the measurements and the actual separation of 100.1 μm. Average value of the absolute differences is 1.1 percent or 0.6 μm referred to a 50 μm distance. Calibrations were also reported for procedures used with the RNF and TI systems. These calibrations were performed on a second reticle identical for our purposes to the TNF reticle.

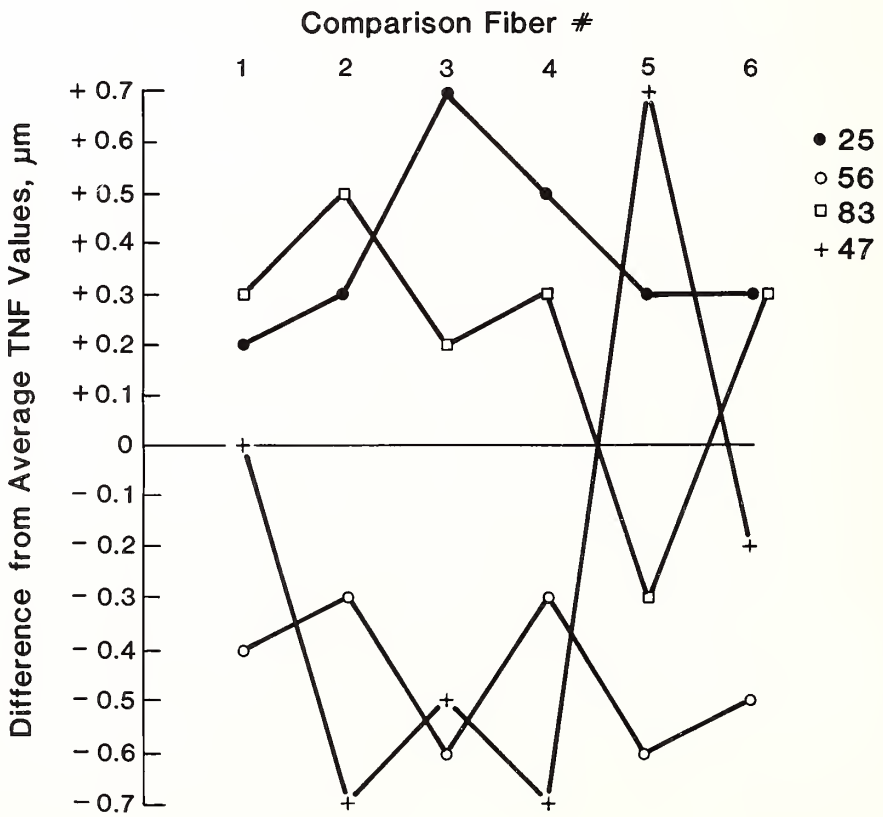


Figure 9. Relative performance of TNF participants compared to the average measured value for each fiber, uncorrected values.

The last row in table 5 gives the average offsets after participants' data has been corrected for calibration error using the data of table 6. After corrections, some participants move closer together while others move further apart. Lower corrected values for participant 83 may have been due to slight modefiltering from their cladding mode stripper which also employed a partial fiber bend along with index matching fluid. The average of the absolute values of the corrected offsets is 0.6 μm.

Scan nonlinearity for participants' TNF systems is indicated by the results reported for the 1 to 2 and 2 to 3 distances on the reticle. Table 7 gives participants' values for the differences between these distances. Nonlinearities vary from 0.2 to 0.7 μm.

The measurements performed beforehand by NBS give insight into the length dependence of TNF results. Measurements on the 7 m sample lengths sent to participants can be compared to the 2 m length measurements specified for the comparisons. Table 8 gives the difference in 5 percent core diameters for the two lengths (2 m minus 7 m). The results are all positive, indicating a gradual spatial contraction of radiation within the fibers due to increased attenuation for higher order modes. The effect differs significantly among fibers but the magnitude is small and justifies the ±0.2 m specification put on test sample length. A comparison of 1 m and 2 m TNF profiles is given in appendix 3.

## 6. COMPARISON OF TNF TO RNF AND TI

The following analysis and RNF measurements were contributed by A. H. Cherin and M. J. Saunders; the TI measurements were contributed by C. Bice.

Profiles determined by TNF can disagree with RNF in two regions which do not appreciably affect core diameter measurements. TNF does not give profile information below the homogeneous cladding level and near the fiber axis TNF has poorer resolution than RNF. Resolution near the axis can be observed on fiber #3 which, according to RNF measurements at 633 nm, has seven resolvable deposition layers of decreasing amplitude with an index dip reaching the 44 percent level (fig. 10). A TNF profile for fiber #3 at a wavelength of 850 nm is given in figure 11; only two layers are resolved but the index dip reaches the 43 percent level in reasonable agreement with RNF. TNF resolution in these situations can be dramatically improved by using shorter wavelengths [15]. Figure 12 is a TNF result at 600 nm; now four deposition layers are clearly visible. For core diameter measurements, the determination of the maximum level $n_1$ is not critical. The more critical portion of the profile is near the core-cladding boundary at the $n_3$ level.

Fibers #2 and #6 have depressed index barrier layers. RNF results on fiber #6 (fig. 13), reveal a 1.5 μm wide barrier layer with a depth approximately 12 percent of the $n_1 - n_2$ value. TNF does not give profile information below the homogeneous cladding level; the TNF profile for fiber #6 smoothly approaches $n_2$ similar to the TNF result in figure 2. Low index barrier layers do not affect the calculation of core diameter since, according to

Table 5. Uncorrected TNF offsets between pairs of participants, μm

| Fiber number | 25/56 | 25/83 | 25/47 | 56/83 | 56/47 | 83/47 |
|---|---|---|---|---|---|---|
| 1 | +0.6 | -0.1 | +0.2 | -0.7 | -0.4 | +0.3 |
| 2 | +0.6 | -0.2 | +1.0 | -0.8 | +0.4 | +1.2 |
| 3 | +1.3 | +0.5 | +1.2 | -0.8 | -0.1 | +0.7 |
| 4 | +0.8 | +0.2 | +1.2 | -0.6 | +0.4 | +1.0 |
| 5 | +0.9 | +0.6 | -0.4 | -0.3 | -1.3 | -1.0 |
| 6 | +0.8 | 0.0 | +0.5 | -0.8 | -0.3 | +0.5 |
| Average offset | +0.8 | +0.2 | +0.6 | -0.7 | -0.2 | +0.5 |
| Corrected average offset | +0.4 | +1.1 | 0.0 | +0.7 | -0.4 | -1.0 |

Table 6. Measured 1 to 3 distance on test reticle

| Participant system | Measured value, μm | % Difference from actual |
|---|---|---|
| 25, TNF | 100.0 | -0.1 |
| 56, TNF | 98.9 | -1.2 |
| 83, TNF | 101.9 | +1.8 |
| 47, TNF | 98.7 | -1.4 |
| BTL, RNF | 99.8 | -0.3 |
| WE, TI | 101.7 | +1.6 |

Table 7. Participant TNF scan nonlinearity, absolute value of 1 to 2 minus 2 to 3 distance

| Participant | Nonlinearity, μm |
|---|---|
| 25 | 0.3 |
| 56 | 0.7 |
| 83 | 0.2 |
| 47 | -- |

Table 8. Length dependance of 5% TNF core diameter

| Fiber # | Diameter from 2m length minus diameter from 7 m, μm |
|---|---|
| 1 | + 0.2 |
| 2 | + 0.3 |
| 3 | + 0.7 |
| 4 | + 0.1 |
| 5 | + 0.7 |
| 6 | + 0.1 |

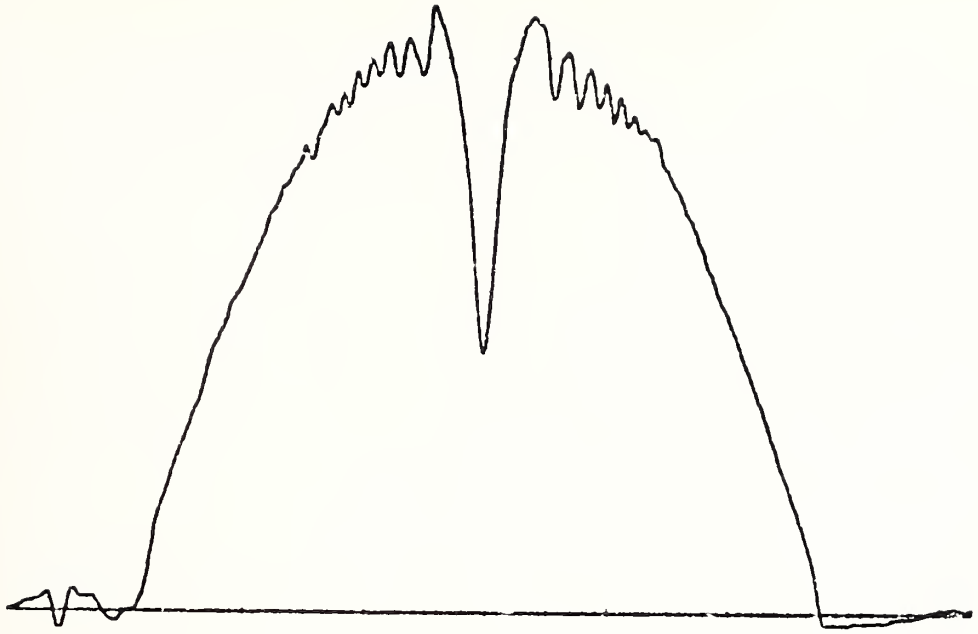

Figure 10. RNF profile for fiber #3 showing a deep index dip with deposition layer structure, M. J. Saunders.

eq (2), the diameter does not depend on the profile below $n_2$. Core diameters determined by TNF and RNF showed good agreement on fibers #2 and #6.

The 5 percent core diameter comparisons between TNF, RNF, and TI are given in figure 14 for all six fibers. A second set of RNF diameters from another apparatus (C. Bice) agreed with those reported here to better than 1 μm for each fiber. The TNF diameters used for figure 14 are from the NBS system at 850 nm and are representative of the corrected TNF diameters. NBS data are on computer files and therefore are readily accessible for scaling and curve fitting. All results given in figure 14 have been corrected for calibration differences using table 6. Corrected RNF and TI diameters agree to better than 1 μm for all six fibers. For TNF, similar agreement is obtained on fibers #2, #3, #4, and #6. Fibers #1 and #5 are notable exceptions. For fiber #1, the disagreement between TNF and the other methods is almost 4 μm. The reason for approximately half of the disagreement is apparent in the RNF profile for fiber #1 (fig. 15). Fiber #1 has an abrupt step in the index profile near the cladding boundary while fiber #5 has a more gradual step nearer the baseline. Another RNF measurement on fiber #1 by M. Young of NBS also reveals the step structure (fig. 16). At about the 8 percent level, the profile diameter of fiber #1 increases abruptly by approximately 3 μm. Figure 17 is a superposition of the TNF and RNF profiles for fiber #1. Using photographic and computer scaling, the curves were normalized and the midpoints of the 5 percent diameters made horizontally coincident. Both curves are accurate with respect to the radial (horizontal) axis. The TNF profile inside the RNF profile in figure 17 goes smoothly to the baseline and because of poor resolution near the cladding

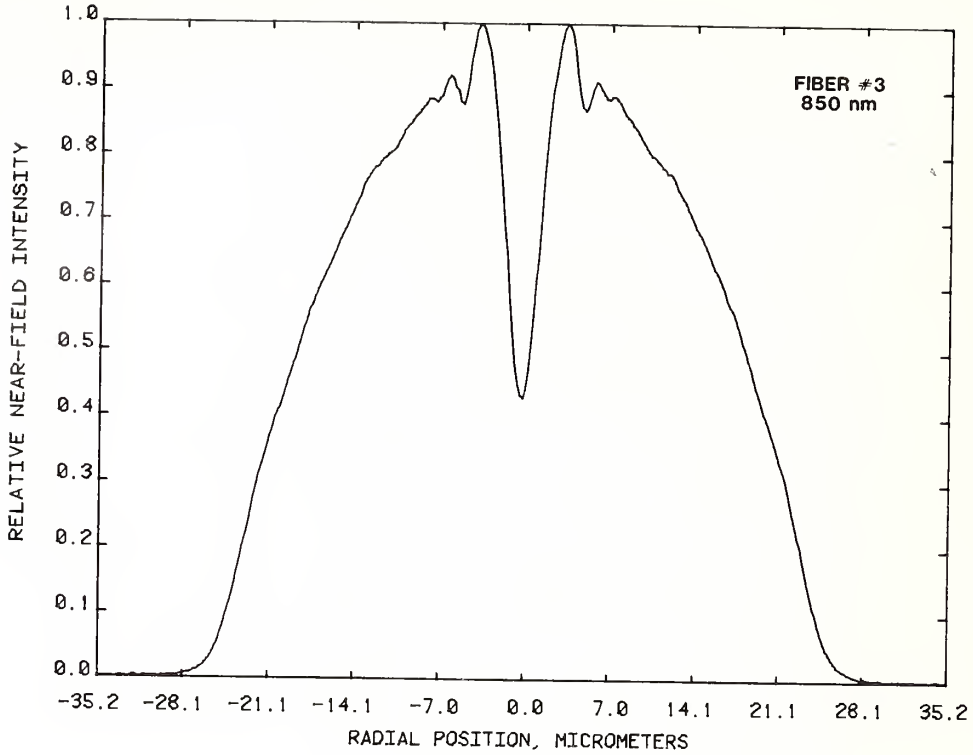


Figure 11. TNF profile for fiber #3 at 850 nm, NBS.

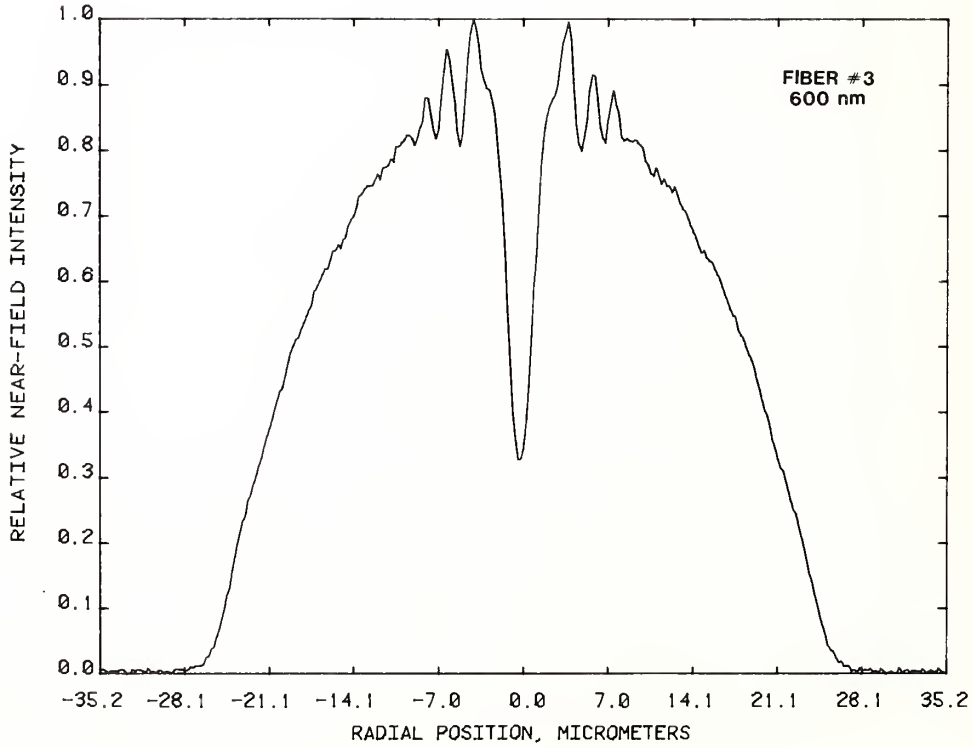


Figure 12. TNF profile for fiber #3 at 600 nm, NBS.

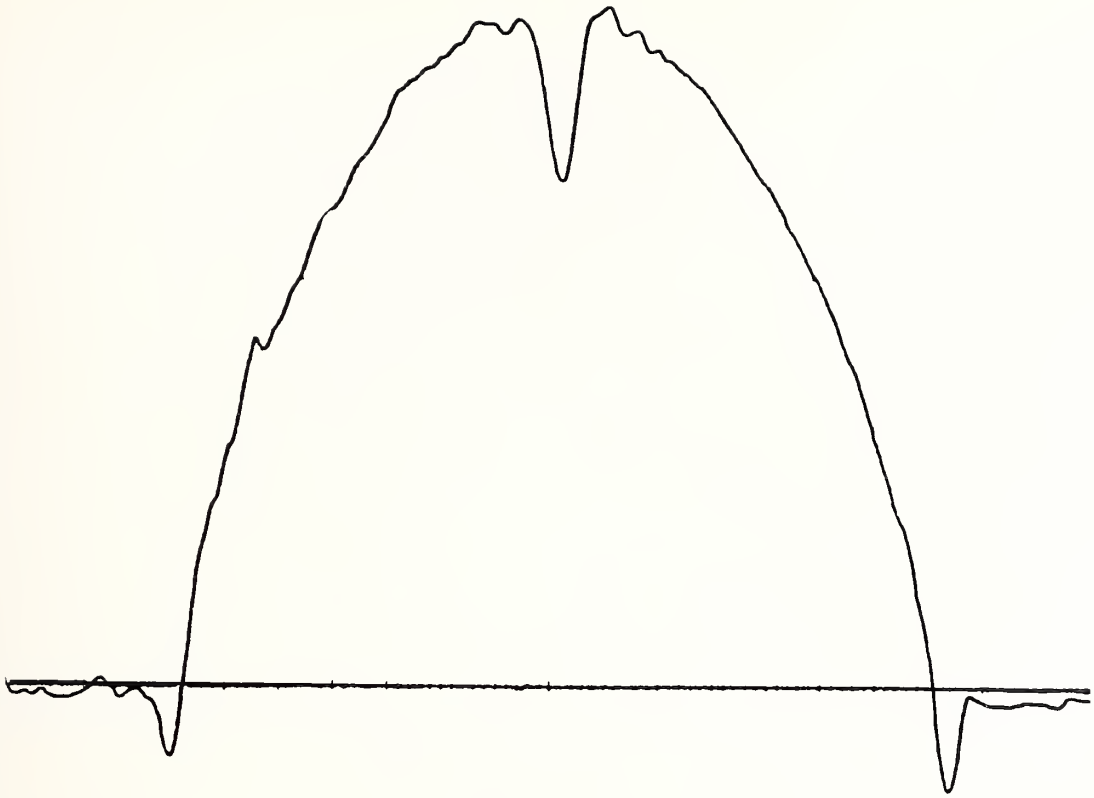

Figure 13. RNF profile for fiber #6 showing a low-index barrier near the core-cladding boundary, M. J. Saunders.

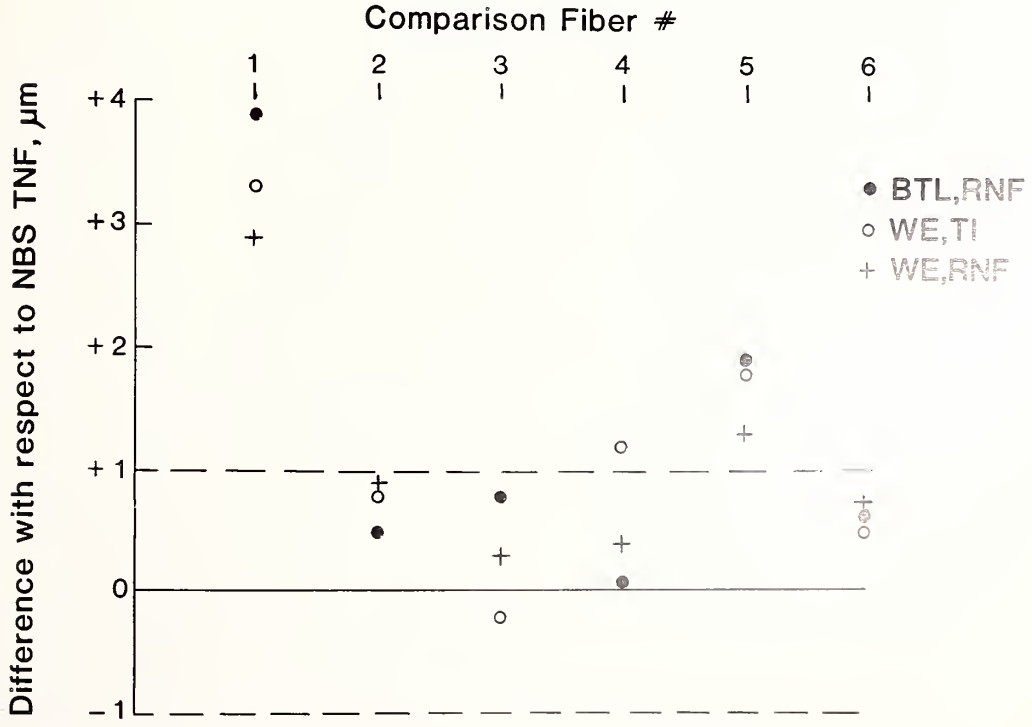


Figure 14. Comparison of 5 percent core diameter determined by TNF, RNF, and TI measurements.

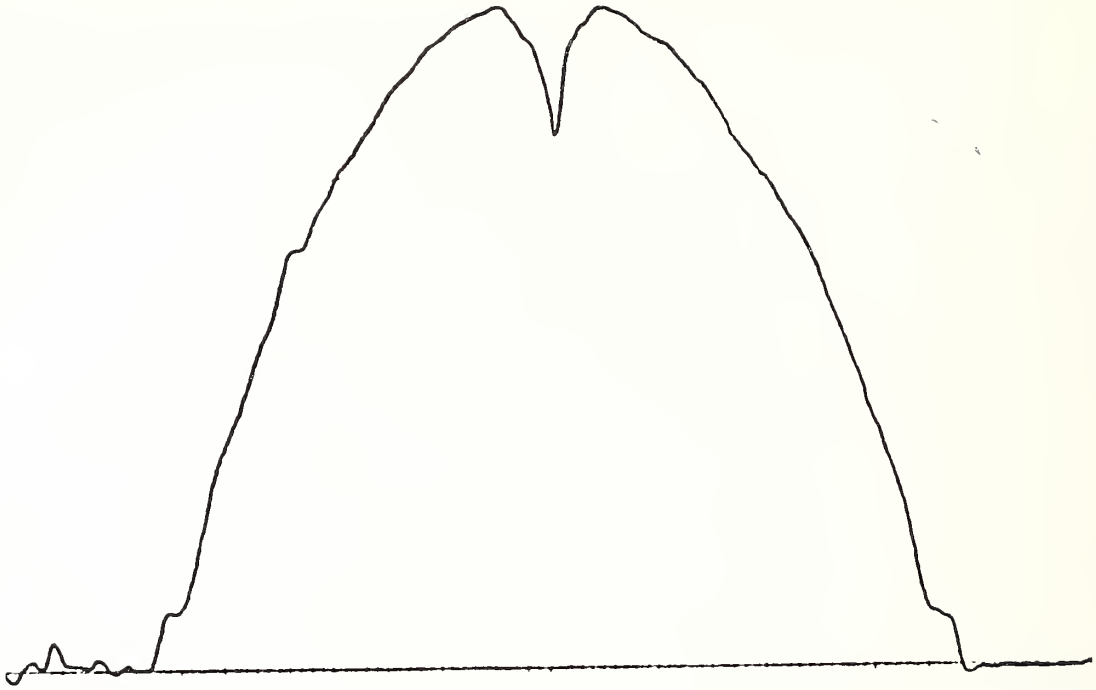

Figure 15. RNF profile for fiber #1 showing a step in the core diameter near the cladding, M. J. Saunders.

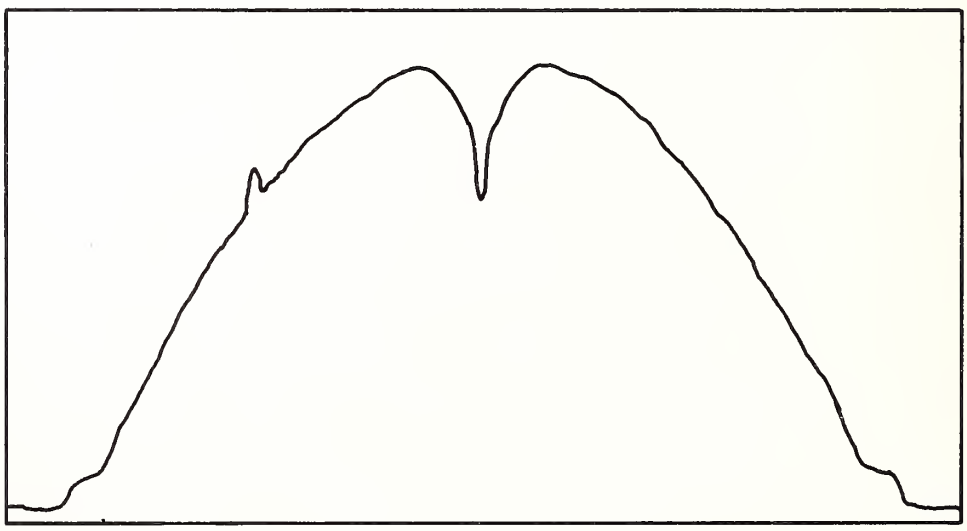

Figure 16. RNF profile for fiber #1 showing a step in the core diameter near the cladding. Glitch to left of center is likely due to contamination by dirt or a shard of glass, M. Young, NBS.

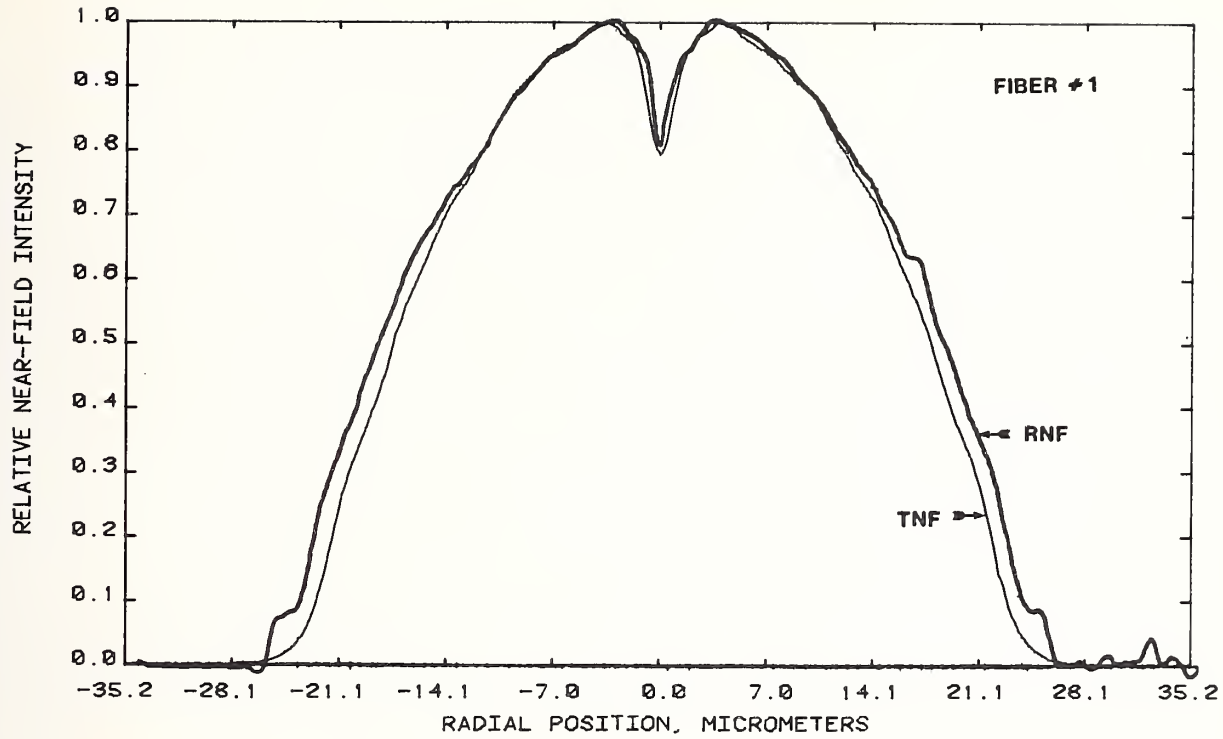


Figure 17. Comparison of RNF (M. J. Saunders) and TNF profiles for fiber #1 which had the largest disagreement in 5 percent core diameter.

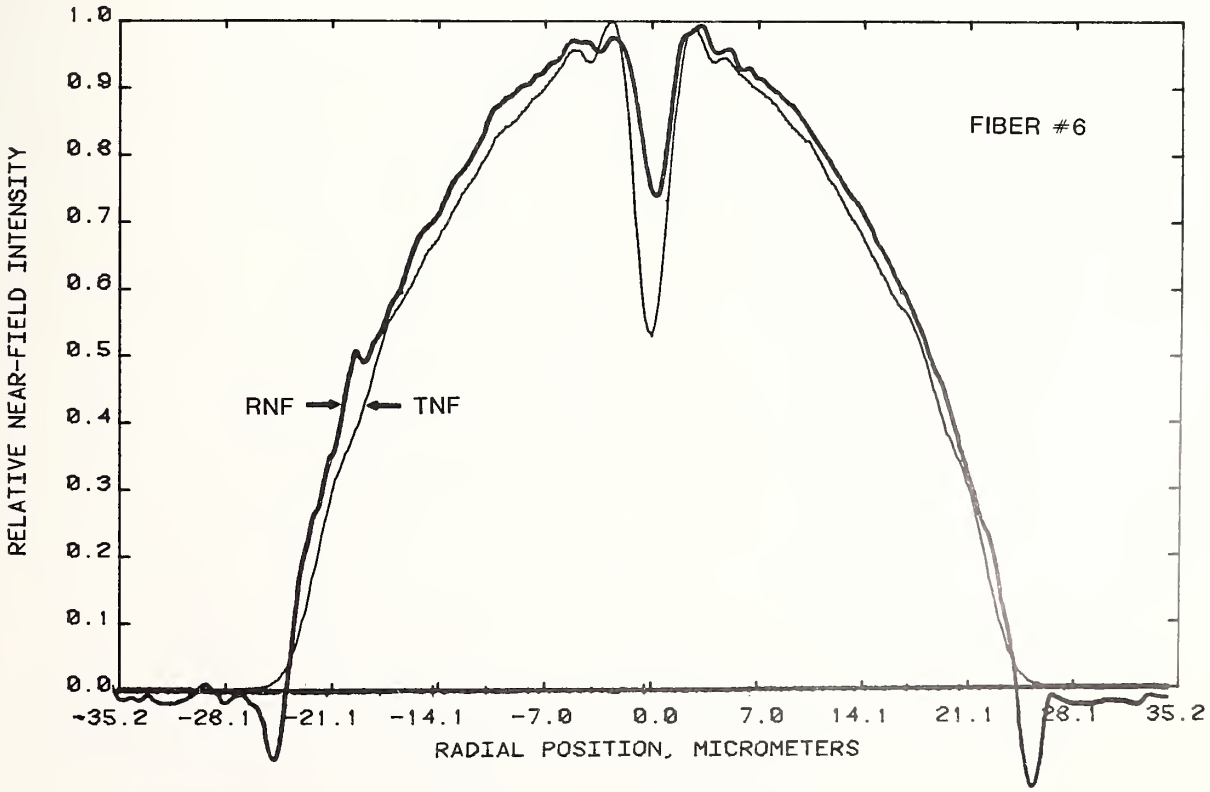


Figure 18. Comparison of RNF (M. J. Saunders) and TNF profiles for fiber #6 which has a low index barrier layer. Good agreement occurs at the 5 percent diameter.

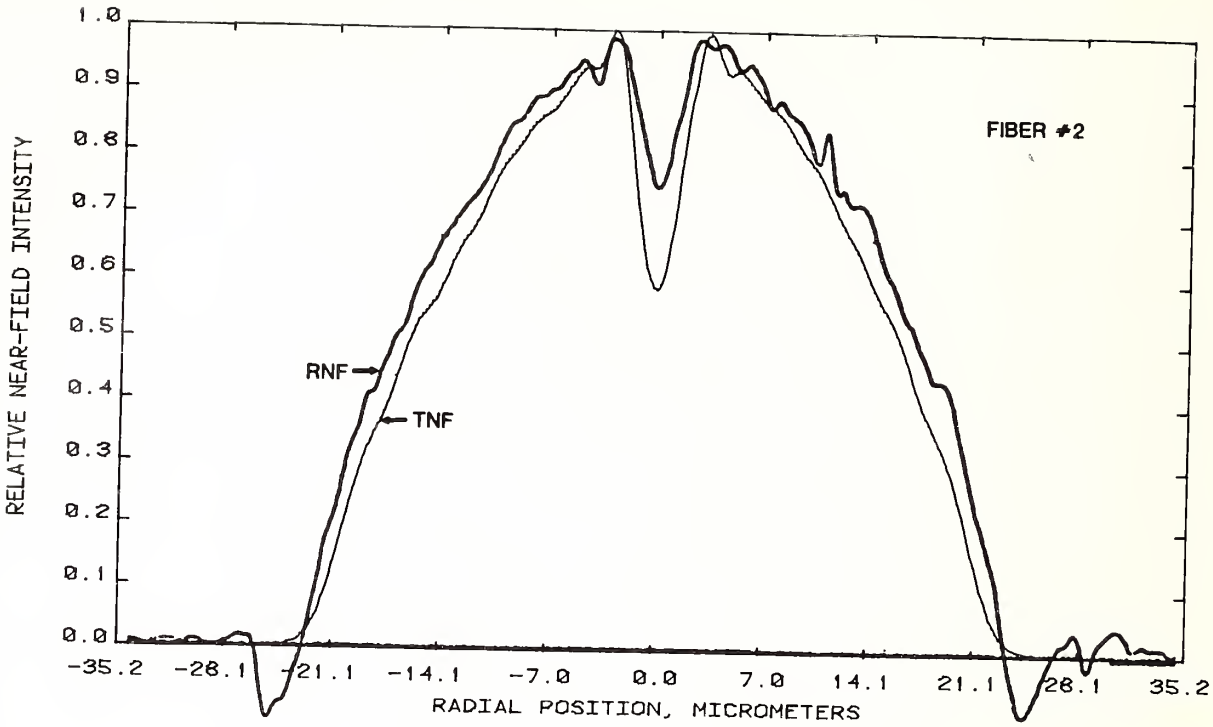


Figure 19. Comparison of RNF (M. J. Saunders) and TNF profiles for fiber #2.

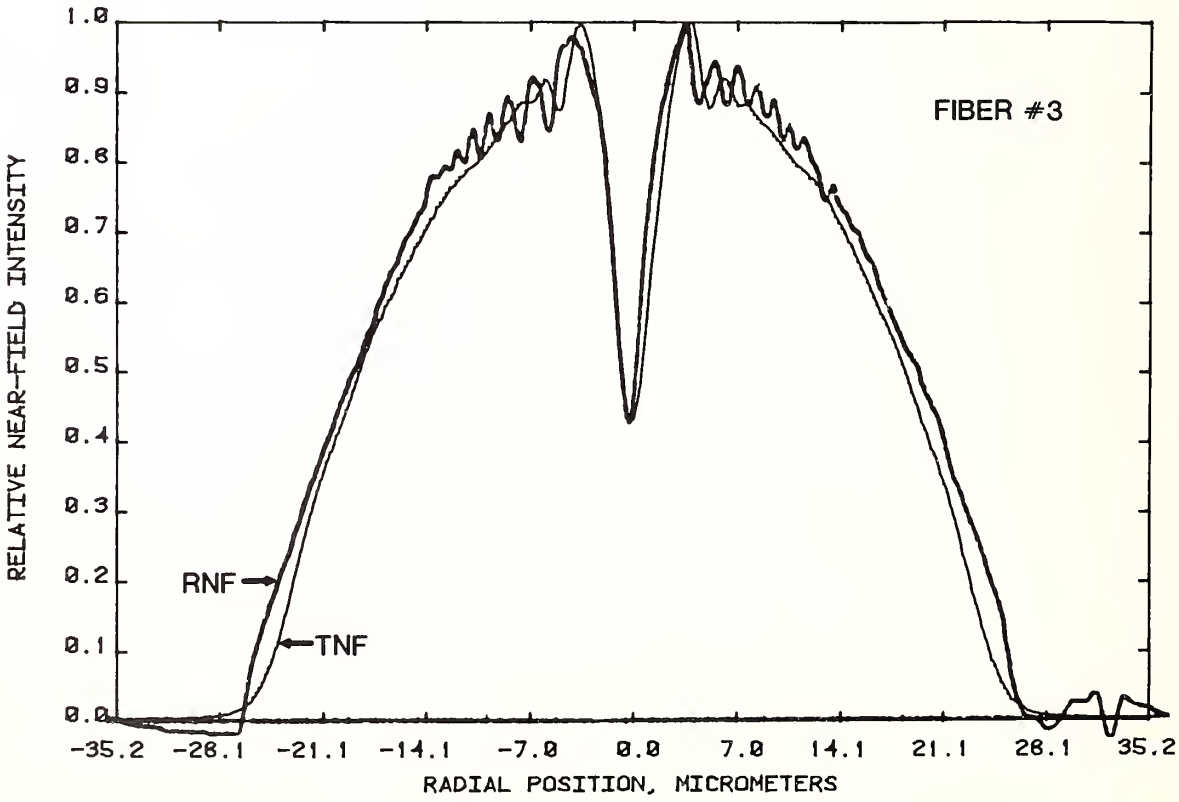


Figure 20. Comparison of RNF (M. J. Saunders) and TNF profiles for fiber #3.

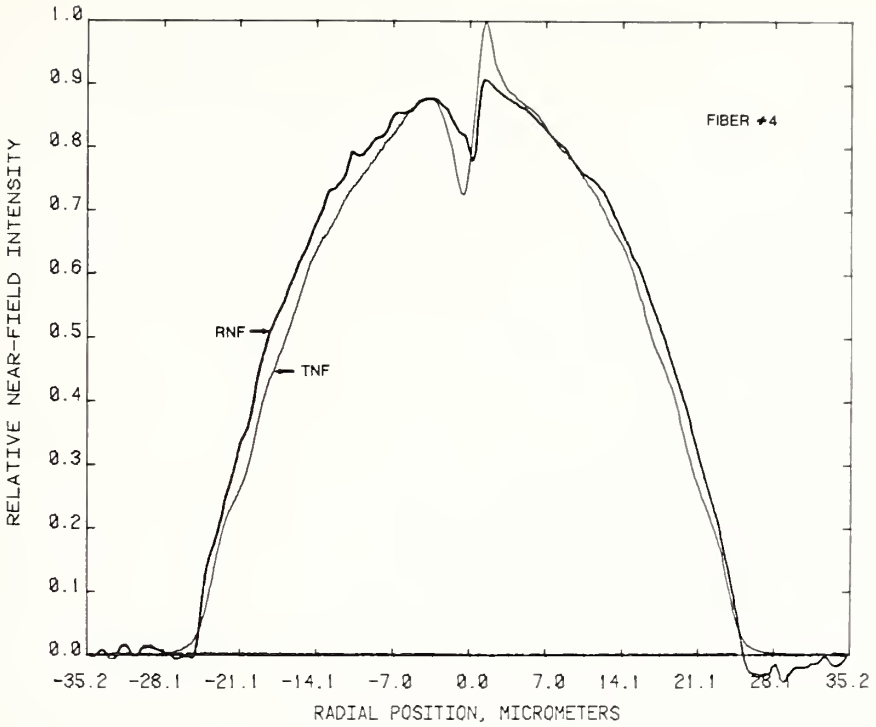


Figure 21. Comparison of RNF (M. J. Saunders) and TNF profiles for fiber #4. Note curves are normalized to left peak. The asymmetric high-intensity peak in the TNF occurs over only a small portion of the core.

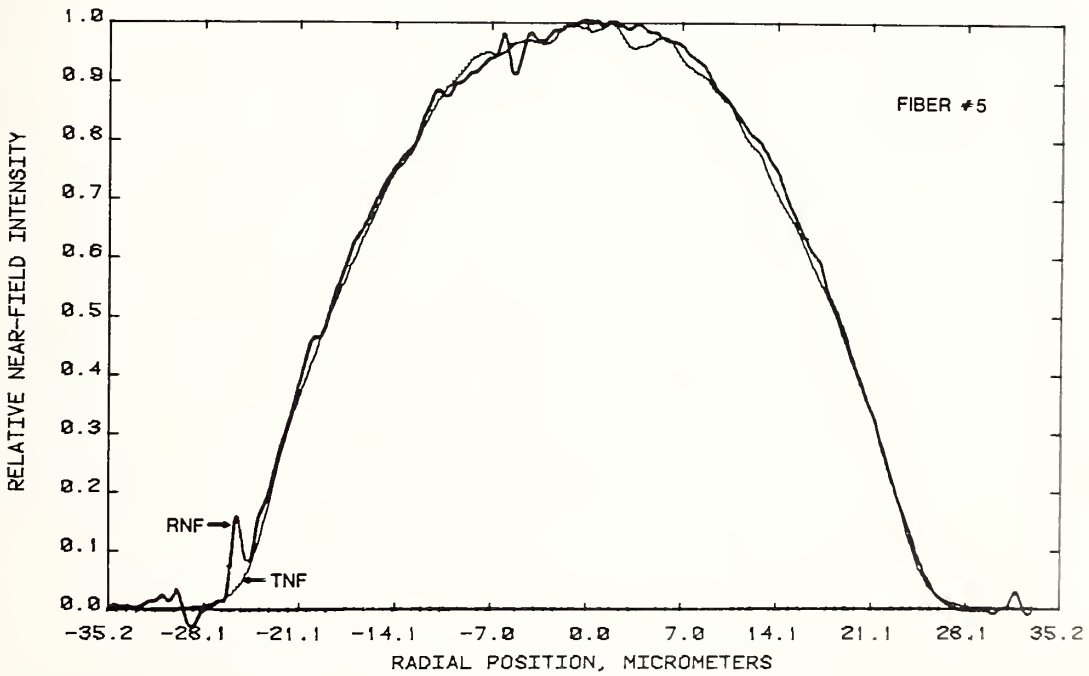


Figure 22. Comparison of RNF (M. J. Saunders) and TNF profiles for fiber #5. A speck of foreign material near the cladding (lower left side of RNF profile) results in an abnormally large value for 5 percent RNF core diameter.

does not indicate the 3 μm step. The RNF profiles for fibers #2, #3, #4, and #6 are smooth near the cladding and the agreement between the various techniques is fairly good. Figure 18 is a TNF/RNF superposition for fiber #6 which has a low index barrier layer. While the TNF is slightly inside the RNF, the agreement is good at the 5 percent diameter. Care should be taken in comparing single measurement profiles since the RNF results are susceptable to end contamination; it appears the RNF result shown in figure 14 (dark circle) for fiber #5 is abnormally high due to a speck of foreign material near the cladding. Figures 19-22 give the TNF/RNF comparisons for the remaining fibers.

## 7. CONCLUSIONS

Core diameter comparisons on a variety of 50 μm core fibers show interlaboratory agreement among TNF systems is within a factor of two of average claimed participant precision. Average one standard deviation is 0.5 μm; the same value is obtained for the average absolute offset between pairs of laboratories. As a percentage of the measured value, the disagreement on TNF is about 1 percent. It is interesting to compare this to similar interlaboratory results for other fiber parameters; 2 percent has been obtained for NA and 0.25 dB (6 percent) for attenuation [16,17].

TNF 5 percent core diameter agrees within 1 μm to RNF and TI diameters when the profiles are smooth near the cladding. If abrupt steps are present, the disagreement can be substantial with nearly 4 μm being observed. If profiles from all techniques are fitted by smooth curves, abrupt changes over small portions can be averaged. Curve fitting the NBS TNF profiles and comparing to curve-fitted RNF profiles gives differences in the core diameters (determined at the baseline, i.e., k = 0) for fibers #1 and #5 of 2.0 and 1.1 μm, respectively. This partially removes some of the discrepancy. However, before curve fitting can be recommended as a standard procedure for all methods, splice loss studies should be done to determine which measurement method best describes fibers having a step near the cladding.

Measurements on the calibration reticle indicate that dimensional calibration errors for TNF, RNF, and TI systems are usually less than 2 percent but interlaboratory differences can exceed 3 percent. This magnitude of interlaboratory offset can be significant since current IEC recommendations call for a tolerance of ±6 percent on core diameter. A systematic offset which is half of the allowed tolerance could affect the statistics of fibers accepted between two parties.

---

The authors would like to thank the following individuals for administering the comparisons in their respective laboratories: Allen Cherin (Bell Laboratories, Norcross), Paul Reitz (Corning Glass Works, Waveguide Product Engineering Laboratory), and William Meixner (Valtec).

## 8. REFERENCES


[1] This definition for core diameter is under consideration by the International Electrotechnical Commission (IEC), CCITT, and Electronic Industries Association (EIA).

[2] Marcuse, D. Principles of optical fiber measurements. New York:Academic Press; 1981.

[3] Sladen, F. M. E.; Payne, D. N.; Adams, M. J. Appl. Phys. Lett. 28:255; 1976.

[4] Hazan, J. P. Electron. Lett. 14:158; 1978.

[5] Petermann, K. Electron. Lett. 13:513; 1977.

[6] One of the first systems based on W. J. Stewart's RNF technique is White, K. I. Opt. Quantum Electron. 11:185; 1979.

[7] Saunders, M. J. Appl. Opt. 20:1645; 1981.

[8] Young, M. Appl. Opt. 20:3415; 1981.

[9] Marcuse, D.; Presby, H. M. Proc. IEEE 68:666; 1980.

[10] Presby, H. M. Bell Sys. Tech. J. 60:1335; 1981.

[11] The participants are members of an EIA P6.6 Subcommittee chaired by D. L. Franzen.

[12] Eriksrud, M. To be published, Appl. Opt.

[13] These measurements were contributed by B. L. Danielson, NBS.

[14] The procedures were drafted by P. Reitz, Corning Glass Works.

[15] Adams, M. J.; Payne, D. N.; Sladen, F. M. E.; Hartog, A. Proc. Third European Conf. Opt. Comm., Munich; 1977.

[16] Franzen, D. L.; Kim, E. M.; Appl. Opt. 20:1218; 1981.

[17] Franzen, D. L.; Day, G. W.; Danielson, B. L.; Chamberlain, G. E.; Kim, E. M. Appl. Opt. 20:2412; 1981.

## APPENDIX 1. TNF PROFILES OF THE SIX COMPARISON FIBERS

TNF profiles for the comparison fibers are given in figures 23 through 29. Fiber #4 is noncircular symmetric and two orthogonal profiles are shown.

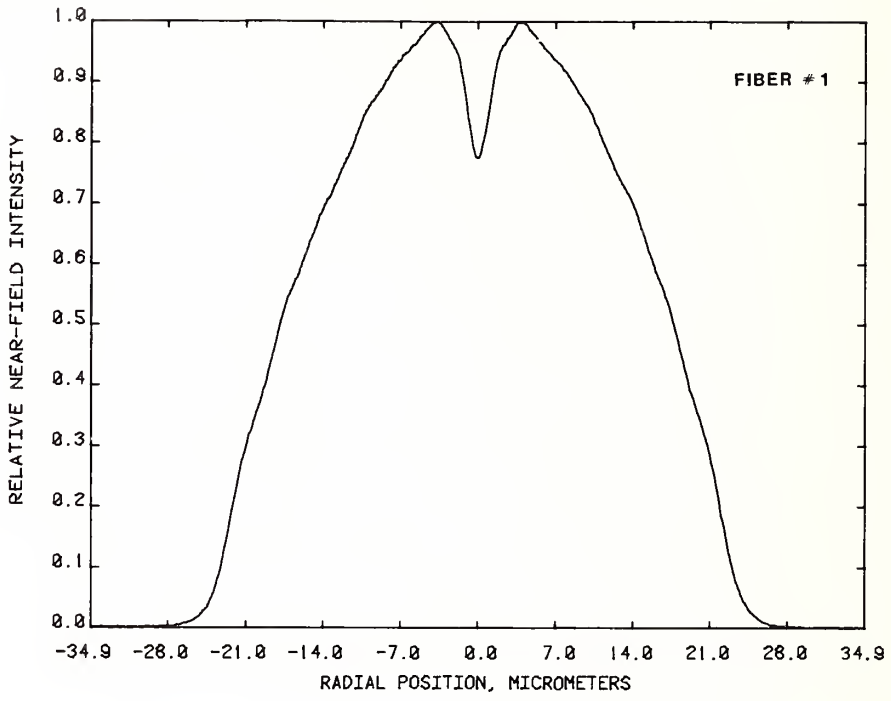


Figure 23. TNF profile of fiber #1, 850 nm.

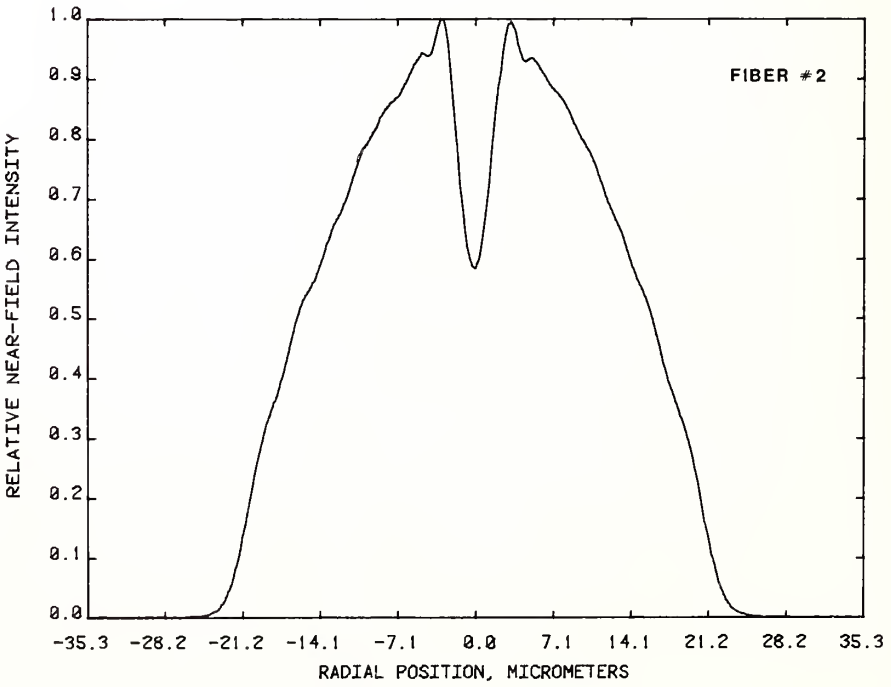


Figure 24. TNF profile of fiber #2, 850 nm.

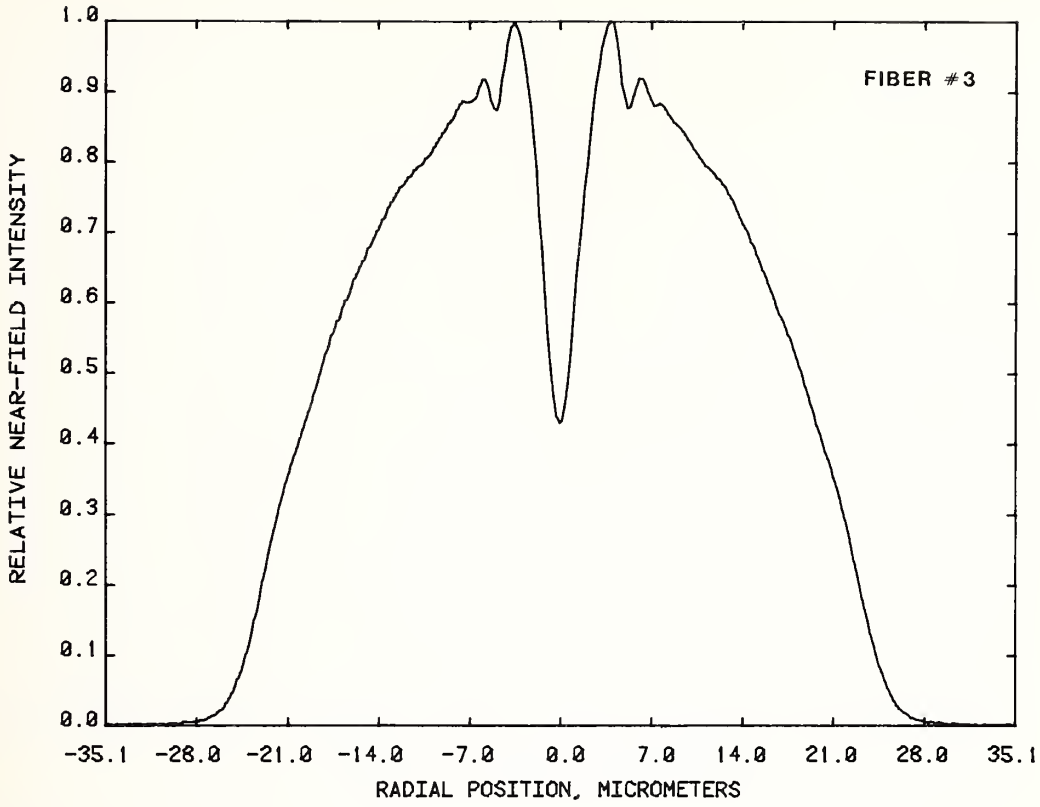


Figure 25. TNF profile of fiber #3, 850 nm.

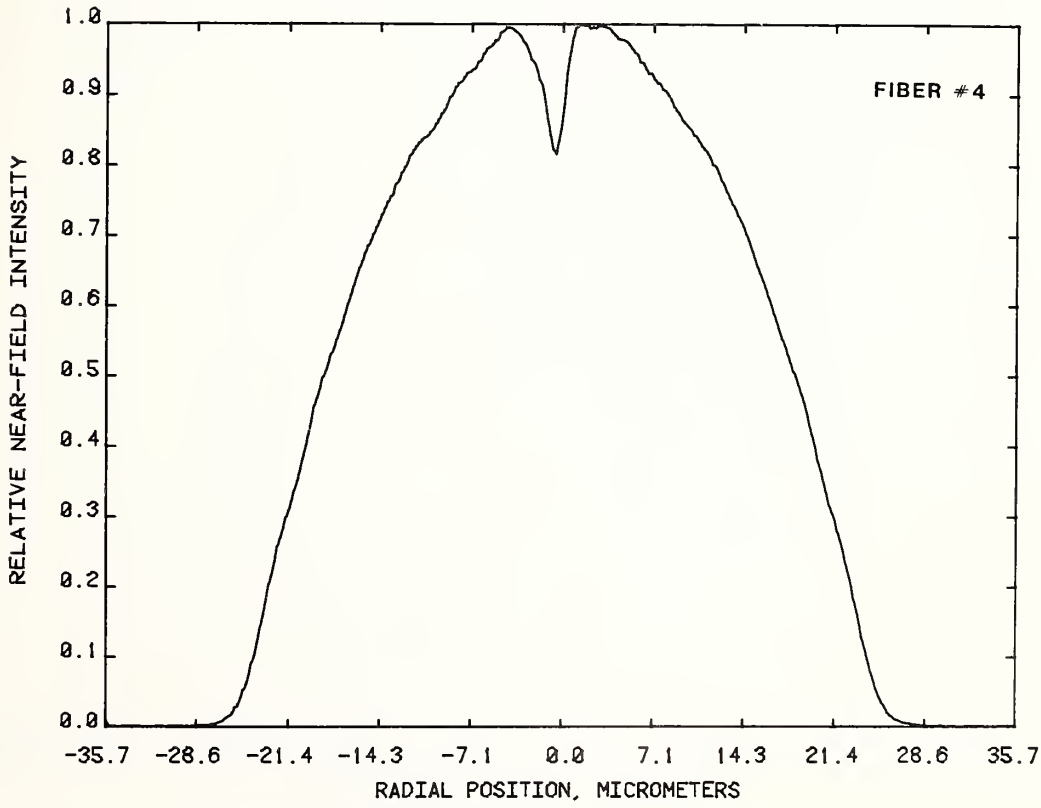


Figure 26. TNF profile of fiber #4, 850 nm.

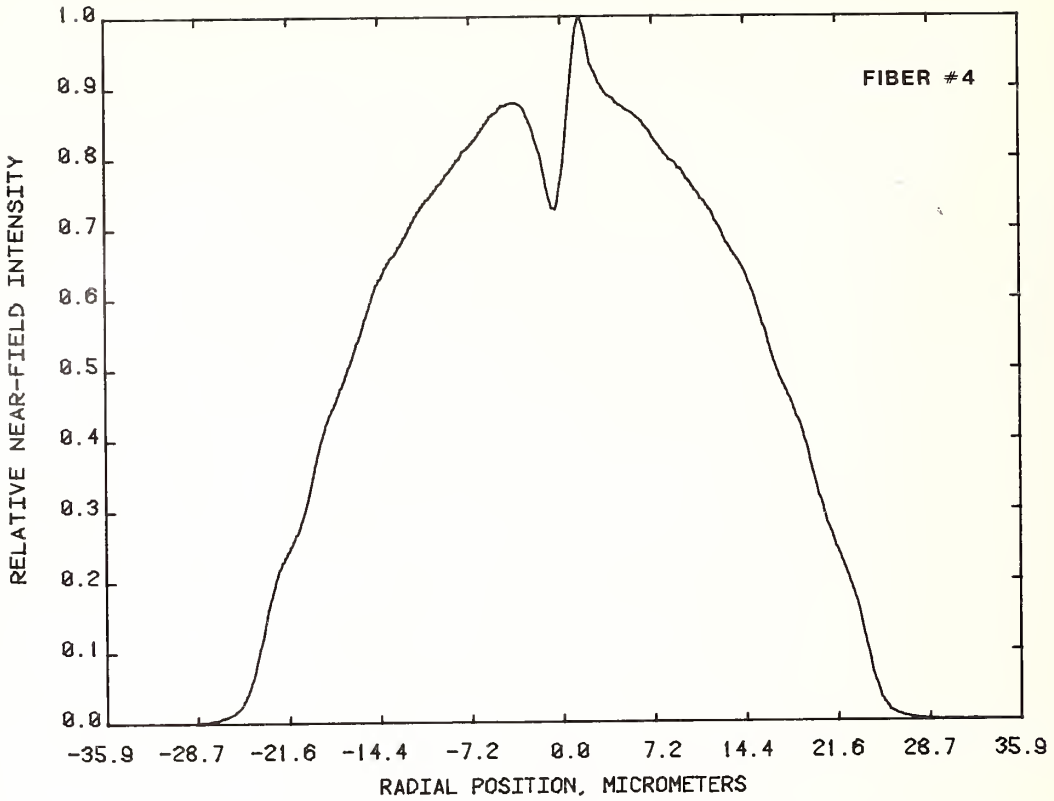


Figure 27. TNF profile of fiber #4, 850 nm. Fiber rotated 90° from figure 26; note lack of circular symmetry at core center.

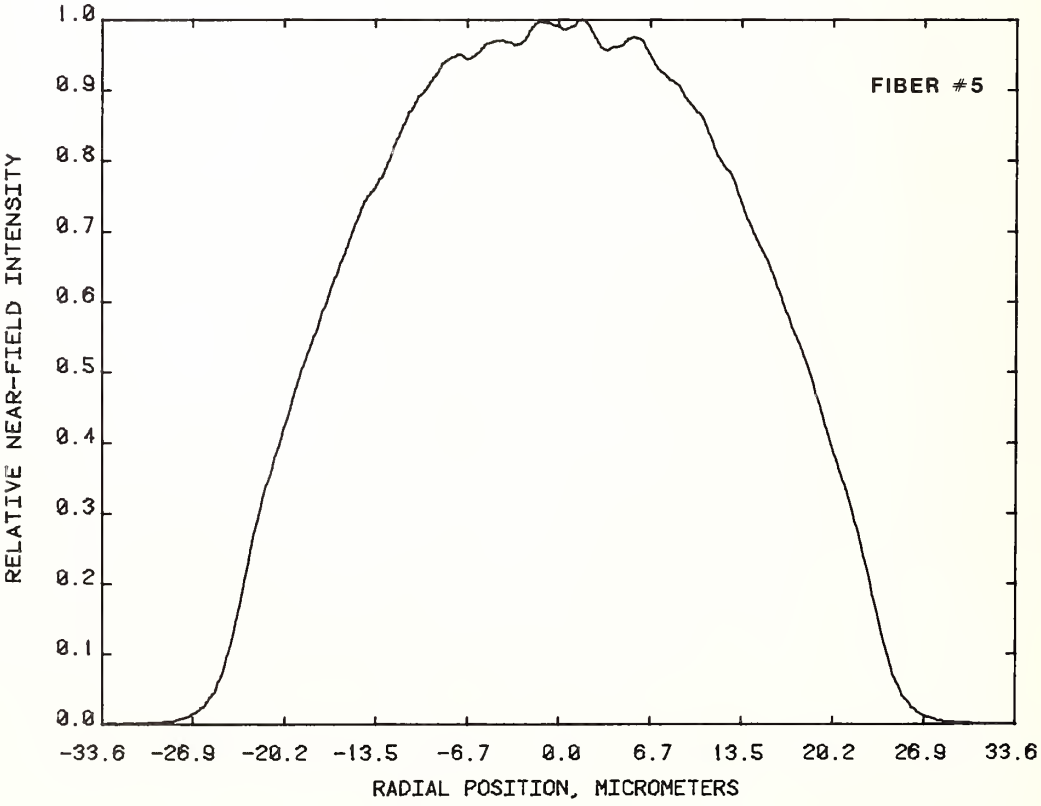


Figure 28. TNF profile of fiber #5, 850 nm.

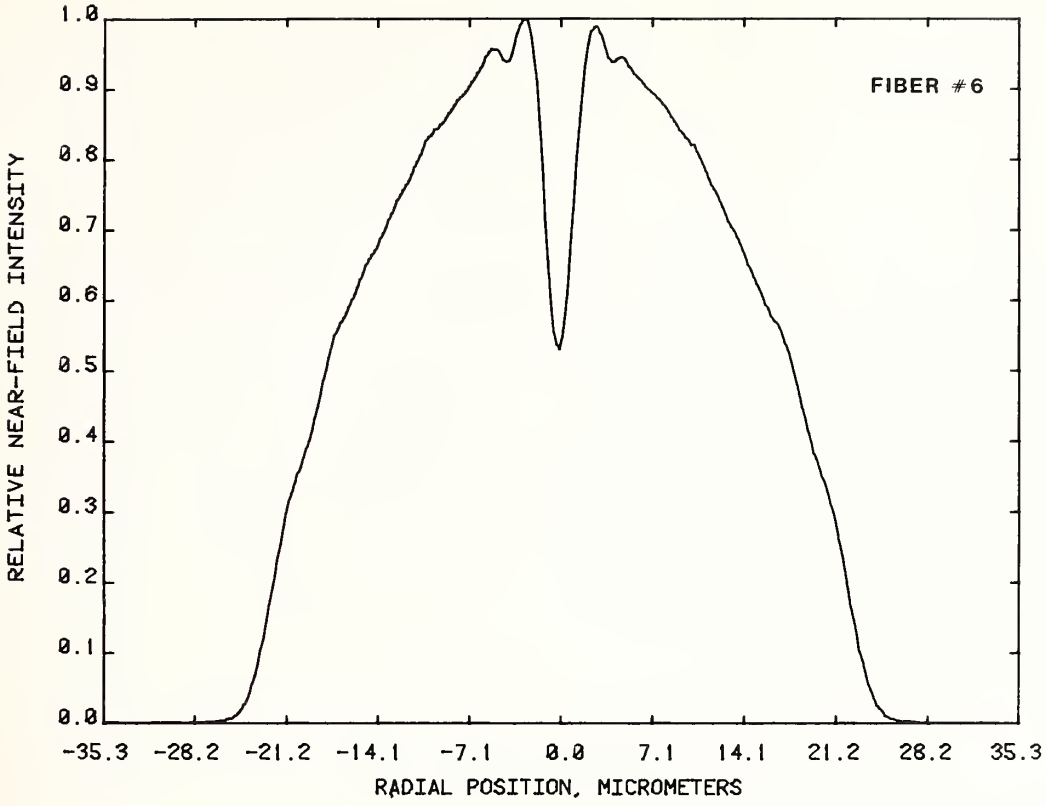


Figure 29. TNF profile of fiber #6, 850 nm.

## APPENDIX 2.

NBS calibrations of the 1 to 3 distance on both reticles #1 and #2 were performed using the apparatus of figure 8. Six measurements were made on #1 while nine measurements were made on #2. Reticle #1 was used on TNF systems while #2 was used on RNF and TI.

| Reticle #1 | | Reticle #2 | |
|---|---|---|---|
| Measurement; | value, μm | Measurement; | value, μm |
| 1 | 100.14 | 1 | 100.36 |
| 2 | 100.14 | 2 | 100.05 |
| 3 | 100.14 | 3 | 100.46 |
| 4 | 99.98 | 4 | 100.33 |
| 5 | 100.24 | 5 | 100.46 |
| 6 | 100.20 | 6 | 100.30 |
| | | 7 | 100.05 |
| | | 8 | 100.17 |
| | | 9 | 100.20 |
| Average | 100.14 | | 100.26 |
| Std. Dev. | 0.09 | | 0.16 |

Average for reticle #2--average for reticle #1 = 0.12 μm.

Reticle #2 was also measured by M. J. Saunders using a Michelson interferometer and a 0.6328 μm HeNe laser. His results rounding off to the nearest quarter fringe were the following.

| Measurement; | value μm |
|---|---|
| 1 | 100.46 |
| 2 | 99.82 |
| 3 | 99.82 |
| 4 | 99.98 |
| 5 | 99.98 |
| 6 | 100.14 |
| 7 | 100.46 |
| 8 | 99.98 |
| 9 | 99.98 |
| 10 | 100.30 |
| Average | 100.09 |
| Std. Dev. | 0.24 |

As far as the fiber comparisons are concerned, the two reticles can be considered identical and the differences not significant.

## APPENDIX 3

A superposition of TNF profiles using 1 m and 2 m specimen lengths is given in figures 30 through 35 for fibers #1 through #6. Launching conditions are the same as those specified for the interlaboratory comparisons. For the 2 m lengths, a single loop 30 to 40 cm in diameter was placed in the fiber. This is intended to simulate bends that could naturally occur between the source and detector on a typical test bench. The 1 m lengths were kept straight between the source and detector. The fiber output end and orientation remained the same for measurements on both specimen lengths. One would expect the 2 m lengths having the loop to give narrower profiles because of possible mode filtering by the bend and additional fiber length. In general, this is observed, but the effect is too small to appreciably affect the TNF profile. The straight 1 m TNF profiles would not come significantly closer to the RNF results. On the average, the 5 percent core diameters from the straight 1 m lengths were 0.4 μm larger than the 5 percent core diameters from the looped 2 m lengths.

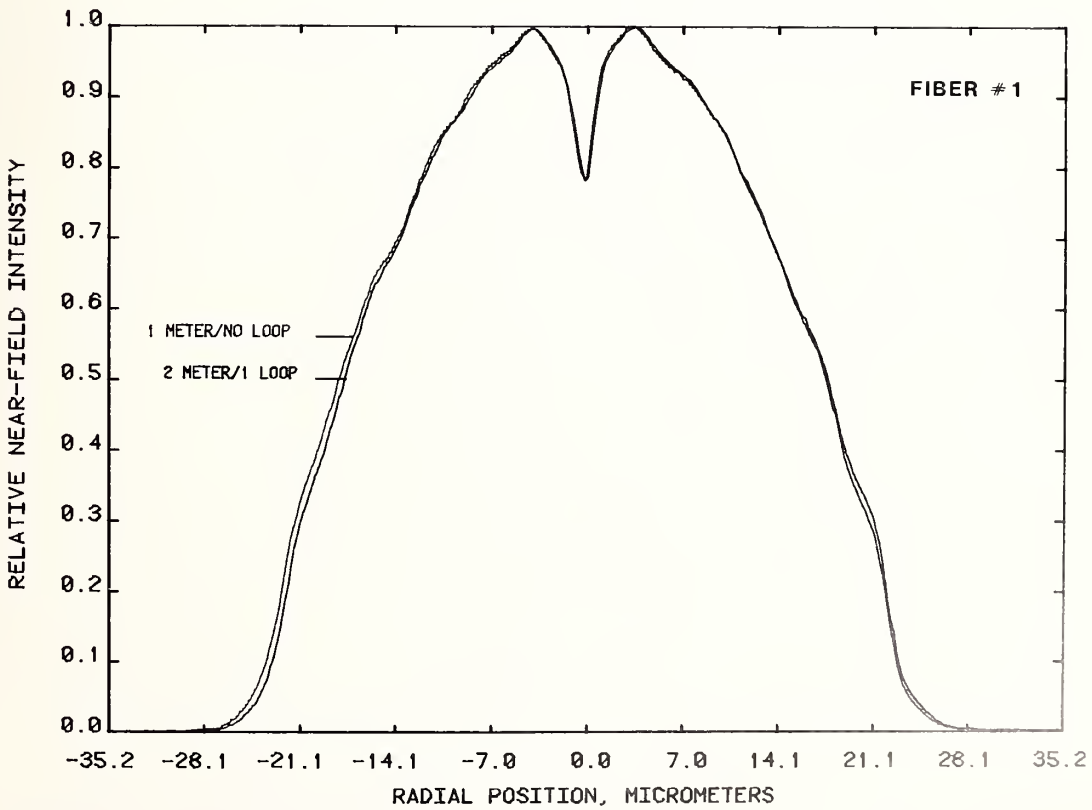


Figure 30. TNF comparisons for 1 and 2 m specimen lengths, 850 nm, fiber #1.

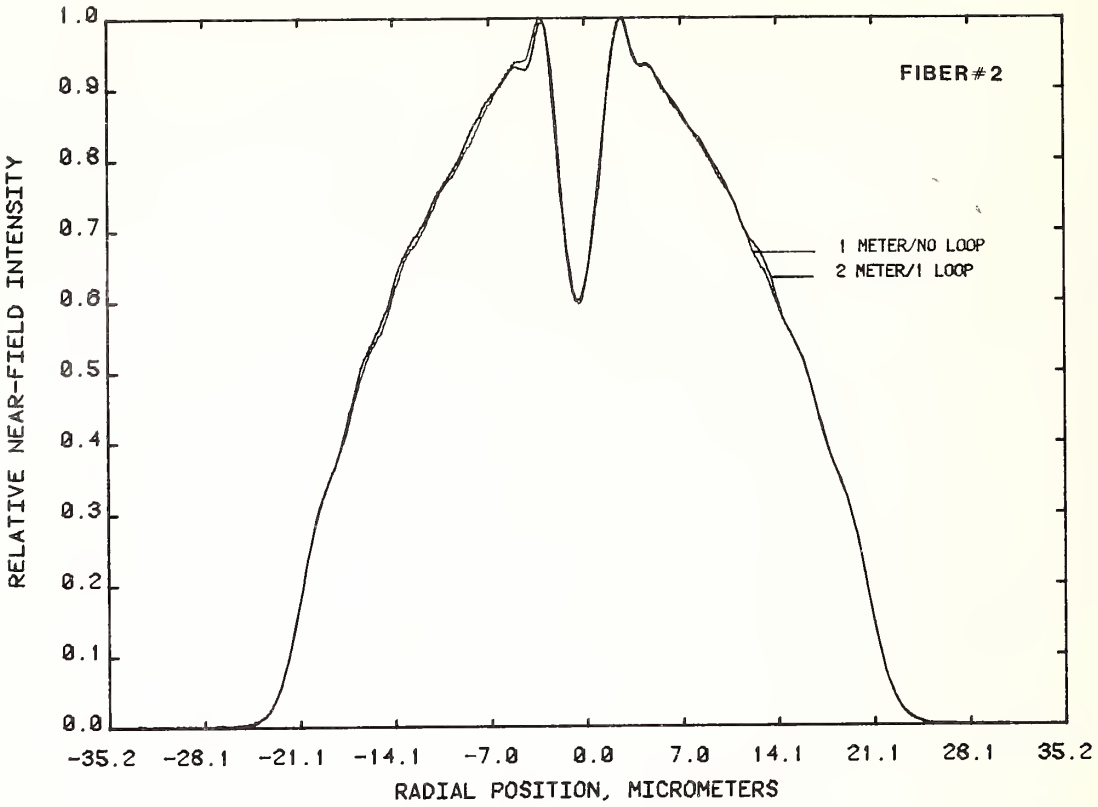


Figure 31. TNF comparisons for 1 and 2 m specimen lengths, 850 nm, fiber #2.

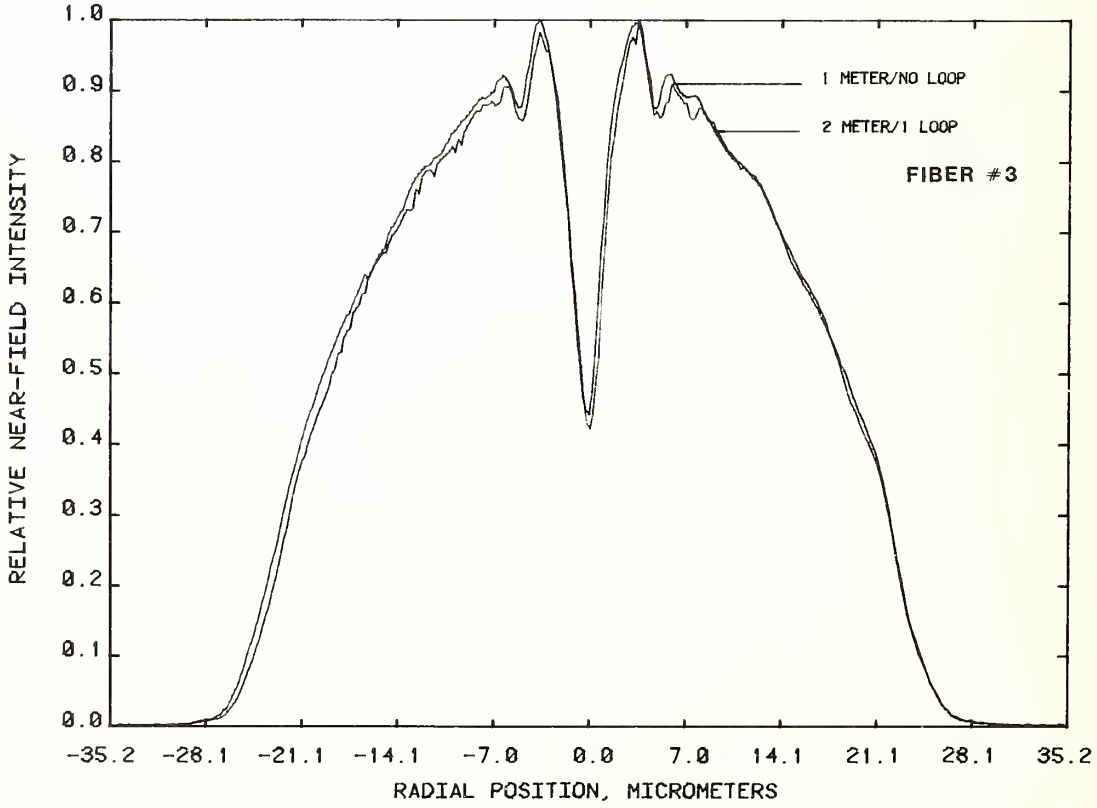


Figure 32. TNF comparisons for 1 and 2 m specimen lengths, 850 nm, fiber #3.

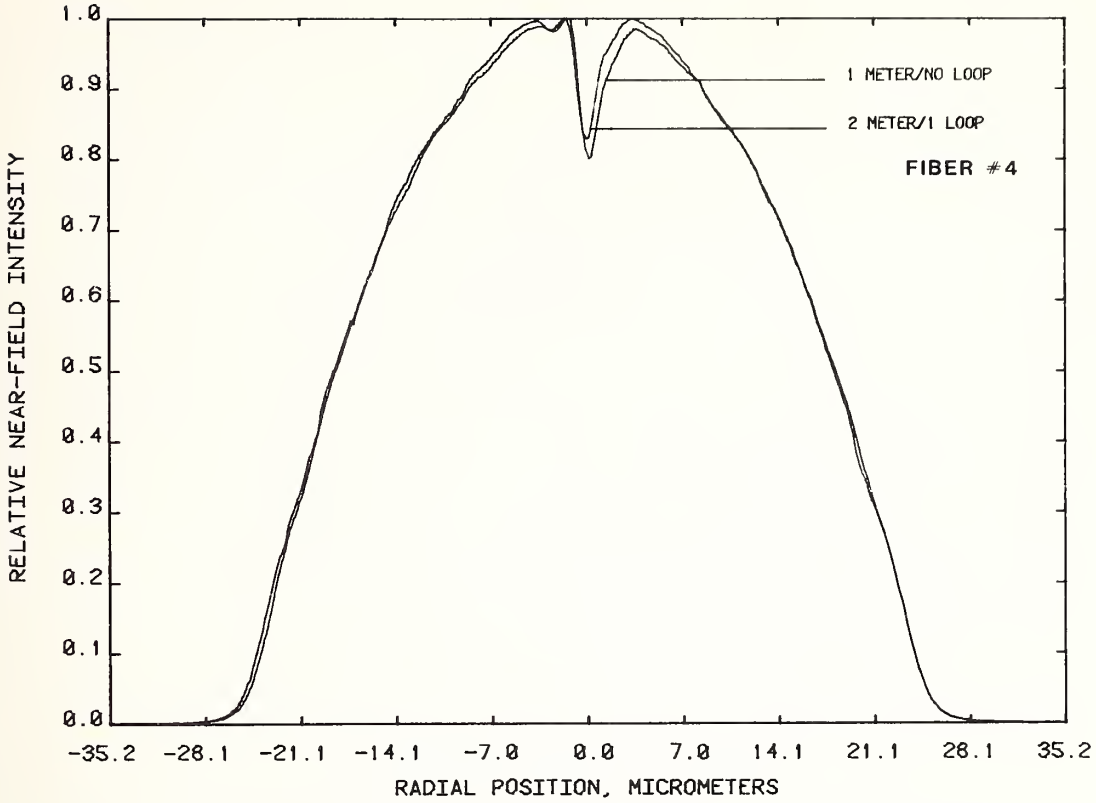


Figure 33. TNF comparisons for 1 and 2 m specimen lengths, 850 nm, fiber #4.

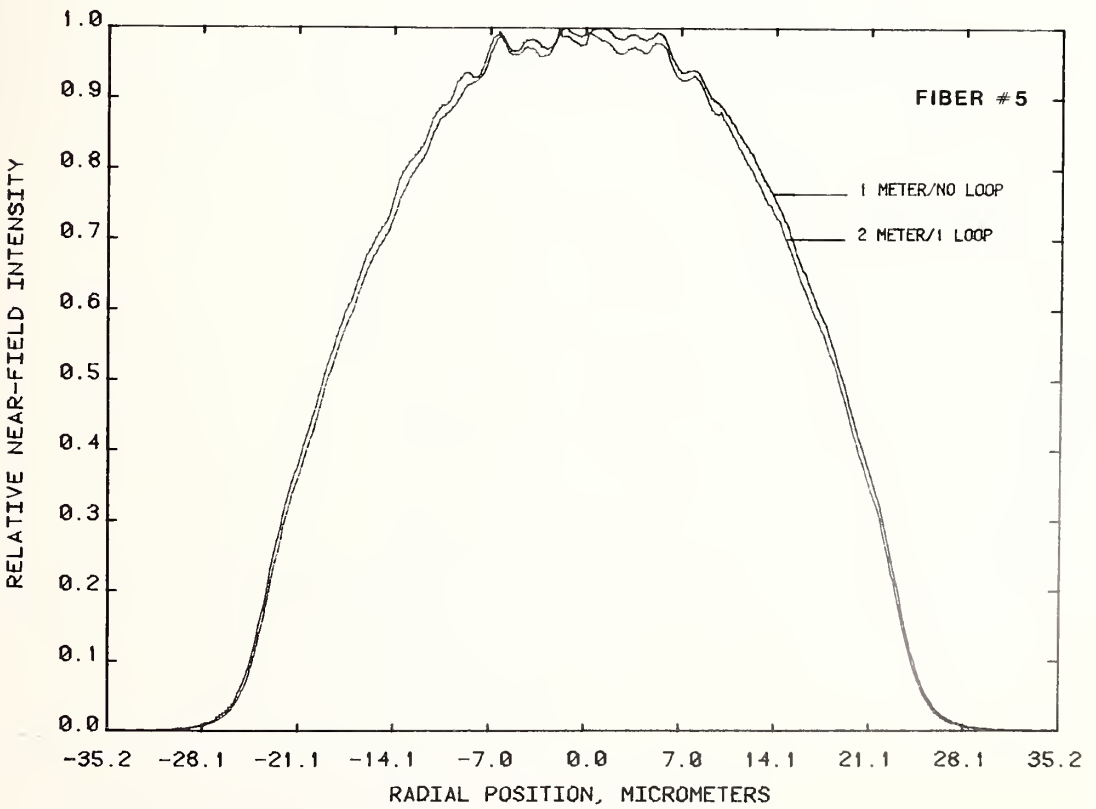


Figure 34. TNF comparisons for 1 and 2 m specimen lengths, 850 nm, fiber #4.

# NBS TECHNICAL PUBLICATIONS

## PERIODICALS

**JOURNAL OF RESEARCH**—The Journal of Research of the National Bureau of Standards reports NBS research and development in those disciplines of the physical and engineering sciences in which the Bureau is active. These include physics, chemistry, engineering, mathematics, and computer sciences. Papers cover a broad range of subjects, with major emphasis on measurement methodology and the basic technology underlying standardization. Also included from time to time are survey articles on topics closely related to the Bureau's technical and scientific programs. As a special service to subscribers each issue contains complete citations to all recent Bureau publications in both NBS and non-NBS media. Issued six times a year. Annual subscription: domestic $18; foreign $22.50. Single copy, $4.25 domestic; $5.35 foreign.

## NONPERIODICALS

**Monographs**—Major contributions to the technical literature on various subjects related to the Bureau's scientific and technical activities.

**Handbooks**—Recommended codes of engineering and industrial practice (including safety codes) developed in cooperation with interested industries, professional organizations, and regulatory bodies.

**Special Publications**—Include proceedings of conferences sponsored by NBS, NBS annual reports, and other special publications appropriate to this grouping such as wall charts, pocket cards, and bibliographies.

**Applied Mathematics Series**—Mathematical tables, manuals, and studies of special interest to physicists, engineers, chemists, biologists, mathematicians, computer programmers, and others engaged in scientific and technical work.

**National Standard Reference Data Series**—Provides quantitative data on the physical and chemical properties of materials, compiled from the world's literature and critically evaluated. Developed under a worldwide program coordinated by NBS under the authority of the National Standard Data Act (Public Law 90-396).

NOTE: The principal publication outlet for the foregoing data is the Journal of Physical and Chemical Reference Data (JPCRD) published quarterly for NBS by the American Chemical Society (ACS) and the American Institute of Physics (AIP). Subscriptions, reprints, and supplements available from ACS, 1155 Sixteenth St., NW, Washington, DC 20056.

**Building Science Series**—Disseminates technical information developed at the Bureau on building materials, components, systems, and whole structures. The series presents research results, test methods, and performance criteria related to the structural and environmental functions and the durability and safety characteristics of building elements and systems.

**Technical Notes**—Studies or reports which are complete in themselves but restrictive in their treatment of a subject. Analogous to monographs but not so comprehensive in scope or definitive in treatment of the subject area. Often serve as a vehicle for final reports of work performed at NBS under the sponsorship of other government agencies.

**Voluntary Product Standards**—Developed under procedures published by the Department of Commerce in Part 10, Title 15, of the Code of Federal Regulations. The standards establish nationally recognized requirements for products, and provide all concerned interests with a basis for common understanding of the characteristics of the products. NBS administers this program as a supplement to the activities of the private sector standardizing organizations.

**Consumer Information Series**—Practical information, based on NBS research and experience, covering areas of interest to the consumer. Easily understandable language and illustrations provide useful background knowledge for shopping in today's technological marketplace.

*Order the* **above** *NBS publications from: Superintendent of Documents, Government Printing Office, Washington, DC 20402.*

*Order the* **following** *NBS publications—FIPS and NBSIR's—from the National Technical Information Services, Springfield, VA 22161.*

**Federal Information Processing Standards Publications (FIPS PUB)**—Publications in this series collectively constitute the Federal Information Processing Standards Register. The Register serves as the official source of information in the Federal Government regarding standards issued by NBS pursuant to the Federal Property and Administrative Services Act of 1949 as amended, Public Law 89-306 (79 Stat. 1127), and as implemented by Executive Order 11717 (38 FR 12315, dated May 11, 1973) and Part 6 of Title 15 CFR (Code of Federal Regulations).

**NBS Interagency Reports (NBSIR)**—A special series of interim or final reports on work performed by NBS for outside sponsors (both government and non-government). In general, initial distribution is handled by the sponsor; public distribution is by the National Technical Information Services, Springfield, VA 22161, in paper copy or microfiche form.

**U.S. DEPARTMENT OF COMMERCE**
**National Bureau of Standards**
Washington, D.C. 20234

OFFICIAL BUSINESS

Penalty for Private Use, $300

POSTAGE AND FEES PAID
U.S. DEPARTMENT OF COMMERCE
COM-215

U.S.MAIL

SPECIAL FOURTH-CLASS RATE
BOOK